

**Climate Change on Mars:
The Nature and History of Non-Polar Ice-Rich Deposits**

BY

Seth Jacob Kadish

B.A., POMONA COLLEGE, 2006
M.S., BROWN UNIVERSITY, 2008

A DISSERTATION SUBMITTED IN PARTIAL FULFILLMENT OF THE
REQUIREMENTS FOR THE DEGREE OF DOCTOR OF PHILOSOPHY IN THE
DEPARTMENT OF GEOLOGICAL SCIENCES AT BROWN UNIVERSITY

PROVIDENCE, RHODE ISLAND
MAY 2011

© Copyright 2011 by Seth J. Kadish

This dissertation by Seth J. Kadish is accepted in its present form by the Department of Geological Sciences as satisfying the dissertation requirement for the degree of Doctor of Philosophy.

Date

James W. Head III, Ph.D., Advisor

Recommended to the Graduate Council

Date

John F. Mustard, Ph.D., Reader

Date

Yongsong Huang, Ph.D., Reader

Date

Timothy D. Herbert, Ph.D., Reader

Date

James L. Fastook, Ph.D., Reader

Approved by the Graduate Council

Date

Peter M. Weber, Ph.D., Dean of Graduate School

Seth Jacob Kadish

Date of Birth: January 2nd, 1984

Place of Birth: Portland, OR, USA

EDUCATION

<u>Brown University, Providence, RI</u>	Sept. 2006-present
Ph.D., Geological Sciences	May 2011
M.S., Geological Sciences	May 2008
<u>Pomona College, Claremont, CA</u>	Aug. 2002-May 2006
B.A., Geology - Earth Planetary Space Science	May 2006
Minor: Environmental Analysis	
<u>Wilson High School, Portland, OR</u>	Aug. 1998-May 2002

HONORS AND AWARDS

Brown University Fellowship	2006-2007
Phi Beta Kappa	2006
Magna Cum Laude Graduation Honors	2006
The D. B. McIntyre – H. Stanton Hill Award in Geology	2006
Sigma Xi	2005
Pomona College Scholar	2003-2006
Department of Geography Prize at University of Edinburgh	2004
The Tileston Physics Prize	2003
Valedictorian, Outstanding Academic Scholar of the Class of 2002	2002
Templeton Scholar at Lewis and Clark College	2001-2002

RESEARCH AND TEACHING EXPERIENCE

Brown University, Graduate Research Appointment	Aug. 2006-May 2011
University of Iceland, NORDVULK Summer School	July 2009
University of Hawaii/NASA, Planetary Volcanology Field Workshop	July 2008
Brown University, Teaching Assistant, Geol 0050	Aug. 2007-Dec. 2007
Northern Arizona University, Research Education for Undergraduates	June 2005-Aug. 2005
Portland State University, Research Education for Undergraduates	June 2004-Aug. 2004
Pomona College, Teaching/Lab Assistant, and Grader for the Physics, Geology, and Astronomy Departments.	Jan. 2003-Jan. 2006

PEER-REVIEWED JOURNAL PUBLICATIONS

- Kadish, S. J.**, and Head, J. W., 2011. Impacts into Non-Polar Ice-Rich Paleodeposits on Mars: Excess Ejecta Craters, Perched Craters and Pedestal Craters as Clues to Amazonian Climate History. *Under review in Icarus*.
- Kadish, S. J.**, and Head, J. W., 2011. Preservation of Layered Paleodeposits in High-Latitude Pedestal Craters on Mars. *Icarus*, doi:10.1016/j.icarus.2011.03.029.

- Fassett, C. I., **Kadish, S. J.**, Head, J. W., Solomon, S. C., and Strom, R. G., 2011. The Global Population of Large Craters on Mercury and Comparison with the Moon. *Accepted to Geophys. Res. Lett.*
- Nunes, D. C., Smrekar, S. E., Fisher, B., Plaut, J. J., Holt, J. W., Head, J. W., **Kadish, S. J.**, and Phillips, R. G., 2011. Shallow Radar (SHARAD), pedestal craters, and the lost Martian layers: Initial assessments. *J. Geophys. Res.*, *in press*, doi:10.1029/2010JE003690.
- Head, J. W., Fassett, C. I., **Kadish, S. J.**, Smith, D. E., Zuber, M. T., Neumann, G. A., and Mazarico, W., 2010. Global Distribution of Large Lunar Craters: Implications for Resurfacing and Impactor Populations. *Science*, *329*, 1504-1507.
- Kadish, S. J.**, Head, J. W., and Barlow, N. G., 2010. Pedestal Crater Heights on Mars: A Proxy for the Thicknesses of Past, Ice-Rich, Amazonian Deposits. *Icarus*, *210*, 92-101.
- Kadish, S. J.**, Barlow, N. G., and Head, J. W., 2009. Latitude Dependence of Martian Pedestal Craters: Evidence for a Sublimation-Driven Formation Mechanism. *J. Geophys. Res.*, *114*, doi:10.1029/2008JE003318.
- Kadish, S. J.**, Head, J. W., Barlow, N. G., and Marchant, D. R., 2008. Martian Pedestal Craters: Marginal Sublimation Pits Implicate a Climate-Related Formation Mechanism. *Geophys. Res. Lett.*, *35*, doi:10.1029/2008GL034990.
- Kadish, S. J.**, Head, J. W., Parsons, R. L., and Marchant, D. R., 2008. The Ascraeus Mons Fan-Shaped Deposit: Volcano-Ice Interactions and the Climatic Implications of Cold-Based Tropical Mountain Glaciation. *Icarus*, *197*, 84-109.
- Penprase, B. E., Berger, E., Fox, D. B., Kulkarni, S. R., **Kadish, S.**, Kerber, L., Ofek, E., Kasliwal, M., Hill, G., Schaefer, B., and Reed, M., 2006. Spectroscopy of GRB 051111 at $z = 1.54948$: Kinematics and Elemental Abundances of the GRB Environment and Host Galaxy. *Astrophys. J.*, *646*, 358-368.

SELECT FIRST-AUTHORED CONFERENCE ABSTRACTS

- Kadish, S.J., and Head, J.W., 2011. Preservation of Layered Paleodeposits in High-Latitude Pedestal Craters on Mars. 42nd Lunar and Planetary Science Conference, Abstract 1003.
- Kadish, S.J., Fassett, C.I., Head, J.W., Smith, D.E., Zuber, M.T., Neumann, G.A., and Mazarico, E., 2011. A Global Catalog of Large Lunar Craters (≥ 20 km) from the Lunar Orbiter Laser Altimeter. 42nd Lunar and Planetary Science Conference, Abstract 1006.
- Kadish, S.J., and Head, J.W., 2010. Impacts into Ice-rich Deposits on Mars: Excess Ejecta Craters, Perched Craters, and Pedestal Craters. 41st Lunar and Planetary Science Conference, Abstract 1017.
- Kadish, S.J., Head, J.W., and Barlow, N. G., 2010. The Formation Timescale and Ages of Mid-Latitude Pedestal Craters on Mars. 41st Lunar and Planetary Science Conference, Abstract 1014.
- Kadish, S.J., Head, J.W., and Barlow, N. G., 2009. Mid-Latitude Pedestal Crater Heights: A Proxy for the Thickness of a Past Climate-related, Ice-rich Substrate. 40th Lunar and Planetary Science Conference, Abstract 1313.
- Kadish, S.J., Head, J.W., and Barlow, N. G., 2009. Pedestal Crater Heights on Mars: Constraining the Thickness of an Ice-Rich, Mid-Latitude Paleodeposit. GSA Annual Meeting, Vol. 41, No. 7, p. 69.
- Kadish, S. J., Head, J. W., and Barlow, N. G., 2008. Determining the Ages of Mid-Latitude Pedestal Craters. 48th Brown-Vernadsky Microsymposium.
- Kadish, S.J., Head, J.W., and Wilson, L., 2008. Subglacial and Synglacial Volcanism Associated with Cold-Based Tropical Mountain Glaciation in the Tharsis Region of Mars. IAVCEI General Assembly, Symposium 3-a.

- Kadish, S.J., Head, J.W., and Barlow, N. G., 2008. Pedestal Craters on Mars: Distribution, Characteristics, and Implications for Amazonian Climate Change. 39th Lunar and Planetary Science Conference, Abstract 1766.
- Kadish, S.J., Head, J.W., Barlow, N. G., and Marchant, D. R., 2008. Pedestal Craters at High Latitudes on Mars: Marginal Sublimation Pits Implicate Ice and Snow in Pedestal Crater Substrate. 39th Lunar and Planetary Science Conference, Abstract 1751.
- Kadish, S.J., Head, J.W., Barlow, N. G., and Marchant, D. R., 2008. Pedestal Craters in Utopia Planitia and Malea Planum: Evidence for a past ice-rich substrate from marginal sublimation pits. 2008 European Planetary Science Congress, Abstract 00156.
- Kadish, S. J., Head, J. W., Forget, F., Fastook, J. L., and Marchant, D. R., 2008. Decoding the Climate Signal in the Tharsis Montes Fan-shaped Deposits: The Dynamics of Tropical Mountain Glaciers. Third International Workshop on the Mars Atmosphere, LPI Contribution No. 1447, p. 9030.
- Kadish, S. J., and Barlow, N. G., 2007. Pedestal Crater Distribution and the Role of a Latitude Dependent Ice-Rich Regolith. 46th Brown-Vernadsky Microsymposium, Abstract 31.
- Kadish, S. J., and Head, J. W., 2007. The Ascraeus Mons Fan-Shaped Deposit: Evidence for Subglacial Volcanism. 46th Brown-Vernadsky Microsymposium, Abstract 32.
- Kadish, S.J., Head, J.W., and Marchant, D. R., 2007. The Age and Morphology of the Ascraeus Mons Fan-shaped Deposit. 38th Lunar and Planetary Science Conference, Abstract 1125.
- Kadish, S.J., and Head, J.W., 2007. Microclimates on the Tharsis Rise and Volcanoes: Orographic Effects and Geological Processes. 38th Lunar and Planetary Science Conference, Abstract 1120.
- Kadish, S. J., and Barlow, N. G., 2006. Pedestal Crater Distribution and Implications for a New Model of Formation. 37th Lunar and Planetary Conference, Abstract 1254.

Acknowledgments

If I were ever to win an Oscar – obviously quite the hypothetical given my current line of work – I would be the guy to take out an excessively long list of people to thank. I would ramble on until the music started playing, cueing me to stop. This would only encourage me to speak louder so that I could be heard over the music. Inevitably, someone would have to drag me off the stage as I reached the section about how I much I appreciate my turtle, Shelly, for teaching me the importance of washing my hands. Sadly, I cannot be as thorough in these acknowledgments as I'd like – it would require an unnecessarily large amount of paper. The following paragraphs, however, highlight some of the more prominent people who have helped me along the way, both academically and socially.

My academic upbringing led me through a series of sorely underfunded Portland Public Schools. Although I remember only a handful of my science classes, Thom Powell's 8th grade earth science course at Robert Gray Middle School certainly stands out. Amidst Mr. Powell's tangents about his wife snaking his Grateful Dead bootlegs, he managed to introduce me to the books of Carl Sagan and gave me my first taste of geology and physics. At Wilson High School, I must thank Ron Zaraza and Barbara Culpepper for strengthening my interest in physics and math, which led to the realization that I just wasn't cut out for my childhood dream of becoming a virologist (well, technically it was of becoming a point guard in the NBA).

At Pomona College, so many incredible professors contributed to my path toward becoming a planetary scientist. In particular, I want to thank the faculty of the Geology Department, who welcomed me with open arms when I began to have doubts about being

a Physics major. Eric Grosfils deserves a special thank you for teaching my first geology course, and advising me throughout much of my college years. Robert Gaines advised my senior thesis and gave me a healthy dose of earth history and research methods, and was very kind in explaining to me the difference between “siliceous” and “salacious”. Rick Hazlett deserves thanks for teaching me that there is more to the environment than rocks, and for showing me the wonders of Joshua Tree. Linda Reinen graciously put up with me during my first hydrology course. And finally, this list couldn’t be complete without a profound thank you to Jerry Irish, my religious studies professor. He attentively listened to my inquisitive atheist thoughts and provided a necessary worldly context for all the science I was learning.

During the summer after my junior year, I took part in the research experience for undergraduates program at Northern Arizona University. I owe thanks to Kathy Eastwood for accepting me into the program. Although I did not know it at the time, this opportunity would substantially influence the course of my research throughout graduate school. My advisor for the summer, Nadine Barlow, showed me my first pedestal crater, and got me started on the global database. She has been a wonderful research colleague and co-author, and has perhaps the sharpest proof-reading eyes of anyone I know. I cannot thank her enough for launching my planetary science research.

At Brown University, I have been supported by so many intelligent and influential professors. First and foremost, my advisor Jim Head deserves a metaphorical standing ovation for guiding my research, for sending me to conferences in parts of the world I had never seen before, and for putting up with my wacky antics over the past five years. He taught me that there is so much more to academia than research. I appreciate Jack

Mustard and Carle Pieters for helping me to realize that my true passion as a geoscientist is remote sensing, and giving me the analytical tools to interpret the bird's eye view. Thanks to Peter Schultz for challenging my thoughts about cratering, to Yongsong Huang for giving me my first true taste of geochemistry, to Tim Herbet for showing me the importance of oceanic cycles, to Lynn Carlson for giving me a pivotal introduction to GIS, to Mike Wyatt for opening my eyes to the many forms of basalt, and to Anne Côté and Nancy Christy for all their administrative help regarding travel logistics and much more. I also want to thank Dave Marchant at Boston University, Jim Fastook at the University of Maine, and François Forget at the University of Paris for collaborating with me on a variety of projects during my time at Brown. Jim H., Jack, Yongsong, Tim, and Jim F. deserve a special acknowledgment for serving on my committee and acting as the readers of this dissertation.

My time at Brown would not have been complete without the influence of my friends and co-graduate students, who made me feel as “at home” as one can in the halls of Lincoln Field. Caleb Fassett and Jay Dickson deserve my unparalleled gratitude. Caleb and Jay are responsible for teaching me all the tricks of the trade; I arrived at Brown making my figures in Microsoft Paint and knowing little more than how to load data into ArcGIS. I leave a self-titled “expert” at Photoshop and a man who dreams about the differences between data projections. They also processed an unhealthy amount of data, which made my research so much easier. My fellow Sagehens, Laura Kerber and Debra Hurwitz, deserve a resounding “Chirp” for their friendship and for reminiscing with me about the days before we had to deal with reviewers' comments. Sam Schon has been driving me around since the day we met at in Flagstaff, and has been a great companion

for discussing everything from beer to stocks. I thank David Baker, Gareth Morgan, Joe Levy, Ailish Kress, and many others who sat in the Mission and Sea Floor rooms with me, listening to my rants about ArcMap's glitches and the limited number of Photoshop licenses.

My dad always tells me to seek the balance. As much as I love planetary geoscience, doing nothing but staring at Mars for eight hours a day without extracurricular activities would have worn on my sanity. As such, I must thank the members of The Bear Necessities for allowing me to continue what has now been almost a decade of collegiate a cappella involvement. I may have been the old man of the group, but they made me feel young. Bear Cheetah Luv. I also appreciate the Brown University Unitarian Universalist Group for spicing up my weekends, and giving a whole new meaning to "House" parties. I am extremely grateful to Mark Harris for getting me involved at The Wheeler School; coaching chess teams and teaching nerdy math students will undoubtedly be among my fondest memories of living in Providence. Finally, my high school buddies, Jim Thorson, Justin Glick, Adam Calhoun, and Bryan Smith provided me with hundreds of hours of distraction in the form of Diplomacy games via email. I hope we wust Sevastopol forever.

Last, but certainly not least, my family deserves an enormous amount of credit for raising me and encouraging me along this long strange trip. To my grandparents, all of whom were teachers in one form or another. They instilled in our family the true value of a good education. To my parents, Josh and Lisa, who were always loving, supportive, and wise. They edited all of my papers, tried to get me to read instead of play video games, and gave me priceless instructions along the way (Dad: Don't let your opponent take your

king. Mom: That should be a C# in the right hand). To my brothers, Nathan and Jonathan, for helping me to chill out at least a little, and for making me realize that, even in pure science, everything really boils down to money, or cost effectiveness, or some sort of equilibrium between supply and demand. Apparently, outer space is a non-excludable, non-rivalrous good. Finally, to my wonderful fiancée, Dana, who has been the most incredible partner I ever could have imagined. After she graduated from Brown, she came back to Providence to live with me, support me, feed me, and make my closets look less empty. She made my time at Brown a truly happy one and I can't thank her enough for that.

In the words of my dear friends Trey and Tom, "I can finally say that this has all been wonderful, but now I'm on my way."

Seth Kadish

March 10th, 2011

Preface

This dissertation explores the recent history of non-polar ice-rich paleodeposits on Mars, primarily through the analysis of pedestal craters. Pedestal craters are a morphology unique to Mars, defined by having their crater bowl perched near the center of a plateau that is surrounded by a marginal outward-facing scarp. The mechanism by which pedestal craters formed has been debated since their initial discovery in Mariner 9 data. Here, we document substantial evidence that pedestal craters are the result of impacts into non-polar ice-rich deposits, which were deposited during periods of climate change resulting from excursions to higher obliquity. The impact armors the proximal surface to a distance greater than the extent of the ejecta. When the obliquity lowers, the icy substrate sublimates and deflates from the intercrater terrain, but it is preserved beneath the indurated pedestal surfaces.

In chapter one, we put forth the basis of our pedestal crater research, detailing the crater database collected and the main lines of evidence that imply a climate-related formation mechanism. This includes the strong latitude-dependent distribution of pedestal craters, which primarily form poleward of $\sim 35^\circ$, as well as a host of physical attributes such as high pedestal to crater radius ratios and marginal sublimation pits located on the scarps of some pedestals.

Chapter two investigates a high-latitude subsample of the pedestal crater population that exhibits layers exposed along the craters' marginal scarps. In the context of their formation mechanism, these examples provide further evidence that pedestal craters are capable of preserving layered ice-rich paleodeposits. This interpretation is confirmed by one example identified on the south polar layered deposit that clearly

preserves a local sequence of ice-rich layers which have been removed in the surrounding area.

Chapter three extrapolates significant implications about the thicknesses of non-polar ice-rich deposits on the basis of the heights of pedestal craters. This study outlines the geographic regions in which pedestals are particularly tall and/or concentrated. These data imply that the thickest paleodeposits were located in Utopia Planitia, Acidalia Planitia, and Malea Planum. We also discuss the presence of pedestal craters that are completely superposed or partially draped on other pedestal craters, and what these incidences suggest about the recurrence of the ice-rich deposits.

In chapter four, we expand the study to two other crater morphologies that are also thought to be the result of impacts into ice-rich substrates. Through a geographic, age, and physical comparison of pedestal craters, perched craters, and excess ejecta craters, we show that the morphologies are genetically related, forming from impacts into the same target materials. These crater types form in the same regions, and have extremely similar excess thicknesses. On the basis of differences in their crater bowl sizes and the appearance of their ejecta, we conclude that only excess ejecta craters and perched craters completely penetrate through the ice-rich surface deposit, excavating regolith material. Perched craters then undergo significant infilling of their crater bowl, differentiating them from excess ejecta craters, which are necessarily fresh.

Chapter five provides a synthesis of the periodicity and pathways that ice-rich material may take from the polar regions to the mid and low latitudes. In this section, we present ages for 50 individual pedestal craters as well as the formation timescale of the entire population. We also date fan-shaped deposits associated with each of the Tharsis

Montes, deriving best-fit ages of 220 Myr, 125 Myr, and 210 Myr for the Ascraeus, Pavonis, and Arsia deposits, respectively. These deposits are the remnants of tropical mountain glaciers, representing periods when large volumes of ice were located near the equator. We also date the series of ridges, interpreted to be drop moraines, which trace the distal margin of the Arsia deposit in order to extract a chronology for the recession of the glacier.

We place these data for both the necessary duration and recurrence of ice-rich material in the context of climate model predictions. This allows us to outline a probable obliquity history for the past 200 Myr on Mars, and to identify significant climatic shifts during the Late Amazonian. Our data suggest that ice is exchanged between the poles and mid latitudes, and between the mid latitudes and low latitudes. In the context of non-polar deposits, the mid latitudes have experienced more frequent glaciations while the low latitudes have maintained ice for a longer overall duration of time. Additionally, we find that large volumes of ice have been present at the low latitudes within the last few hundred Myr, with the last major glaciation ending around ~130 Ma. At the mid latitudes, widespread ice-rich deposits were emplaced within the past tens of Myr and likely within the past few Myr.

Table of Contents

Title Page.....	i
Copyright Page.....	ii
Signature Page.....	iii
Curriculum Vitae.....	iv
Acknowledgments.....	vii
Preface.....	xii
Table of Contents.....	xv

Chapter One:

The Distribution and Geomorphology of Mid-Latitude Pedestal Craters on Mars.....	1
Abstract.....	2
I. Introduction and Background.....	4
II. Methodology.....	5
III. Results.....	7
a. Distribution of Pedestal Craters.....	7
b. Pedestal Crater Attributes.....	7
IV. Discussion.....	10
a. Trends in Pedestal Crater Attributes.....	10
b. Climate Models and Odyssey GRS Experiment Data.....	12
c. Pedestal Craters in the Medusae Fossae Formation.....	15
d. Ages.....	18
e. Hemispheric Asymmetry in Pedestal Crater Distribution.....	23
f. Armoring Mechanism.....	26
g. Related Morphologies.....	30
h. Formation Model and Implications for Ice Preserved under Pedestal Crater Surfaces.....	34
V. Conclusions.....	36
Acknowledgments.....	39
References.....	40
Tables.....	57
Figure Captions.....	59
Figures.....	67

Chapter Two:

Preservation of Layered Paleodeposits in High-Latitude Pedestal Craters on Mars.....	85
Abstract.....	86
I. Introduction.....	87
II. High-Latitude Pedestal Craters.....	88
III. Exposed Layers along Marginal Scarps.....	91
IV. Discussion.....	94
Acknowledgments.....	96
References.....	97
Tables.....	102
Figure Captions.....	103
Figures.....	106

Chapter Three:

Pedestal Crater Heights on Mars: A Proxy for the Thicknesses of Past, Ice Rich,
Amazonian Deposits..... 112

Abstract..... 113

I. Introduction..... 114

II. Methodology..... 115

III. Global Distribution and Trends of Pedestal Heights..... 117

IV. Relationship between Heights and other Pedestal Attributes..... 120

V. Discussion..... 122

 a. Geographic Extent of Ice-Rich Deposit..... 122

 b. Timing and Recurrence of the Ice-Rich Deposit..... 125

 c. Pedestals with Marginal Pits..... 126

VI. Conclusions..... 130

Acknowledgments..... 131

References..... 131

Tables..... 137

Figure Captions..... 138

Figures..... 144

Chapter Four:

Impacts into Non-Polar Ice-Rich Paleodeposits on Mars: Excess Ejecta Craters,
Perched Craters and Pedestal Craters as Clues to Amazonian Climate History..... 155

Abstract..... 156

I. Introduction..... 158

II. Morphological Background..... 159

 a. Excess Ejecta Craters..... 159

 b. Perched Craters..... 161

 c. Pedestal Craters..... 162

III. Formation Mechanisms..... 163

IV. Physical Attribute Comparison..... 168

 a. Crater Diameter and Ejecta/Pedestal Thickness..... 168

 b. Topography and Morphology of Ejecta..... 171

V. Age Comparison..... 173

VI. Geographic Distribution Comparison..... 176

VII. New Examples of Excess Ejecta Craters..... 177

VIII. Discussion..... 180

IX. Conclusions..... 183

Acknowledgments..... 185

References..... 185

Tables..... 191

Figure Captions..... 193

Figures..... 199

Chapter Five:

The Periodicity and Transport Pathways of Amazonian Ice-Rich Paleodeposits at Low to Mid Latitudes on Mars.....	211
Abstract.....	212
I. Introduction.....	214
II. Mid-Latitude Pedestal Craters.....	215
a. Morphologic and Stratigraphic Observations.....	216
b. Population Formation Age.....	218
c. Individual Pedestal Ages.....	219
III. Ages of the Tropical Mountain Glacier Fan-Shaped Deposits.....	211
a. Ascraeus Mons.....	223
b. Pavonis Mons.....	224
c. Arsia Mons.....	225
IV. Discussion.....	227
a. Timing and Periodicity of Ice-Rich Paleodeposits.....	227
b. Transport Pathways for Ice-Rich Material.....	236
c. Implications for Mars' Obliquity History in the Late Amazonian.....	241
V. Conclusions.....	244
Acknowledgments.....	249
References.....	249
Tables.....	259
Figure Captions.....	262
Figures.....	269

CHAPTER ONE:

Latitude Dependence of Martian Pedestal Craters:
Evidence for a Sublimation-Driven Formation Mechanism

Seth J. Kadish¹, Nadine G. Barlow², James W. Head¹

¹Department of Geological Sciences, Brown University, Providence, RI 02912 USA

²Department of Physics and Astronomy, Northern Arizona University, Flagstaff, AZ

86011 USA

Published in:

Journal of Geophysical Research, Vol 114, doi:10.1029/2008JE003318

Abstract:

We report on the results of a survey to document and characterize pedestal craters on Mars equatorward of $\sim 60^\circ\text{N}$ and S latitude. The identification of 2696 pedestal craters reveals a strong latitude dependence, with the vast majority found poleward of 33°N and 40°S . This latitudinal extent is highly correlated with many climate indicators consistent with the presence of an ice-rich substrate and with climate model predictions of where snow and ice are deposited during periods of higher obliquity in the Amazonian. We have measured key physical attributes of pedestal craters, including the farthest radial extents of the pedestals, pedestal heights, and the circularity of the pedestal margins. In conjunction with the geographic distribution, our measurements strongly support a sublimation-related formation mechanism. This is in contrast to previous hypotheses, which have relied on eolian deflation to produce the elevated plateaus. The identification of marginal pits on the scarps of some pedestal craters, interpreted to be sublimation pits, provide direct evidence for the presence of ice-rich material underlying the armored surface of pedestal craters. On the basis of our findings, we propose a formation mechanism whereby projectiles impact into a volatile-rich dust/snow/ice layer tens to hundreds of meters thick, deposited during a period of higher obliquity, overlying a dominantly fragmental silicate regolith. The area surrounding the resulting crater becomes armored. Our measurements show that pedestals extend to a distance of multiple crater radii, farther than typical ejecta deposits. This necessitates an armoring mechanism that is capable of indurating the surface to a distance greater than the reach of the ejecta. Return to low obliquity causes sublimation of the volatile-rich layer from the intercrater plains, lowering the elevation of the regional terrain. This yields generally circular

pedestal craters elevated above the surrounding plains. Observed cases in which one pedestal crater is draped over another suggest that the deposition of latitude-dependent, ice-rich material has been a recurring process. This formation mechanism implies that the armored surfaces of pedestal craters have preserved a significant record of Amazonian climate history in the form of ice-rich deposits. Historical climate reconstructions using global climate models need to account for the presence of significant thicknesses of snow and ice (tens to over a hundred meters) at high-mid-latitudes numerous times during the Late Amazonian. A small population of pedestal craters identified in the Medusae Fossae Formation may suggest the past presence of ice-rich material near the equator. These pedestal craters, however, are physically distinct from those at mid and high latitudes, and could result from a different formation mechanism.

1. Introduction and Background

Pedestal craters are a subclass of impact craters on Mars [Barlow *et al.*, 2000] characterized by a crater perched near the center of a pedestal (mesa or plateau) that is surrounded by an often-circular, outward-facing scarp; the scarp is typically several crater diameters from the rim crest, and tens to over 100 meters above the surrounding plains. First recognized in Mariner 9 data [McCauley, 1973], pedestal craters have been interpreted to form by armoring of the substrate during the impact event, usually by an ejecta covering [e.g., Arvidson *et al.*, 1976]. More recent hypotheses include increased ejecta mobilization caused by volatile substrates [Osinski, 2006], distal impact-melt-rich veneers [Schultz and Mustard, 2004], and/or an atmospheric blast/thermal effect [Wrobel *et al.*, 2006]. Following armoring, a marginal scarp is created by preferential erosion of the substrate surrounding the armored region, historically thought to involve eolian deflation of the fine-grained, non-armored, intercrater terrain [e.g., McCauley, 1973; Arvidson *et al.*, 1976, 1979]. This model, however, is not consistent with the commonly circular planform of pedestal craters; erosion via a predominant wind direction would likely produce asymmetric pedestals [e.g., Head and Roth, 1976; Mutch and Woronow, 1980; Greeley *et al.*, 2001]. Alternatively, the preferential distribution of pedestal craters at latitudes poleward of $\sim 40^\circ$ [Mouginis-Mark, 1979; Kadish and Barlow, 2006], in conjunction with an increased understanding of the role of redistributed ice and dust during periods of climate change [e.g., Jakosky *et al.*, 1995; Head *et al.*, 2003] have led many researchers to suspect that the substrate might have been volatile-rich [e.g., Head and Roth, 1976; Mouginis-Mark, 1987; Schultz and Lutz, 1988; Barlow, 2006; Kadish and Barlow, 2006; Larson, 2007]. Specifically, some [e.g., Kadish and Barlow, 2006]

have called on models of impact into volatile-rich targets to produce pedestal craters during times of higher obliquity, when mid- to high-latitude substrates are thought to have been characterized by thick deposits of snow and ice; return to lower obliquities would cause sublimation of the volatile-rich units, except below the protective cover of pedestal craters, and migration of the volatiles back to the poles [e.g., *Head et al.*, 2003; *Levrard et al.*, 2004]. Thus, this model predicts that thick deposits of snow and ice should underlie the armored pedestal crater surfaces.

Here we report on the results of a comprehensive study using new image and altimetry data that was designed to document and characterize pedestal craters on Mars equatorward of $\sim 60^\circ\text{N}$ and S latitude in order to test these hypotheses for the origin of pedestal craters. We identified 2696 pedestal craters between $\sim 60^\circ\text{N}$ and S latitude; their distribution is strongly latitude-dependent, with the vast majority found poleward of 33°N and 40°S [*Kadish and Barlow*, 2006].

2. Methodology

Pedestal craters were primarily identified through a survey of all Thermal Emission Imaging System (THEMIS) IR images, releases 1 through 23, between $\sim 60^\circ\text{N}$ and S (Figures 1-4). This was supported in certain regions of interest by THEMIS VIS data; THEMIS VIS data were not used for the general survey due to their limited coverage. Additionally, morphological assessments of specific pedestal craters utilized Mars Orbital Camera (MOC), High Resolution Stereo Camera (HRSC), Context Camera (CTX), and High Resolution Imaging Science Experiment (HiRISE) data. Due to the resolution of THEMIS IR images (100 m/pix) (Figure 4), pedestal craters <0.7 km in

diameter were not analyzed. Although numerous pedestal craters are present poleward of 60° latitude, we selected this geographic range because we are particularly interested in how close to the equator pedestal craters are capable of forming; in order to test a sublimation-driven formation hypothesis, we wanted to compare the mid- and low-latitude extent of pedestal craters to where we expect ice-rich material to have been emplaced during periods of high obliquity, based on climate models and other ice-related morphologies. The study was expanded to 70°N and S for pedestal craters with marginal pits [Kadish *et al.*, 2008]. Measurements of pedestal craters, which included the crater diameter, farthest radial extent of the pedestal, and pedestal perimeter, were made using THEMIS IR data, and pedestal heights were derived from Mars Orbital Laser Altimeter (MOLA) data. These measurements allowed for the calculation of pedestal circularity (Γ) values (referred to previously in the literature as “lobateness” values) [Kargel, 1986; Barlow, 1994; Barnouin-Jha and Schultz, 1998] and pedestal to crater radius (P/C) ratios (referred to previously in the literature as “ejecta mobility ratios”) [Mouginis-Mark, 1979; Costard, 1989; Barlow, 2004]. A Γ of 1 represents a perfectly circular pedestal, while higher values correspond to more sinuous/jagged perimeters. These dimensionless attributes are calculated by [Barlow, 2006]:

$$\Gamma = (\text{pedestal perimeter})/[4\pi(\text{pedestal area})]^{1/2} \quad (\text{EQ 1})$$

$$\text{P/C ratio} = (\text{farthest extent of pedestal})/(\text{crater radius}) \quad (\text{EQ 2})$$

3. Results

3.1. Distribution of Pedestal Craters

Pedestal craters are not distributed randomly on Mars (Figures 1-3). In the northern hemisphere, pedestal craters are observed almost exclusively poleward of 33°N, with the majority between 45° and 60°N latitude (Figures 1 and 2, Table 1), and between 70° and 180°E longitude (Figure 3). In the southern hemisphere, pedestal craters are less abundant (Figure 2), occurring almost exclusively poleward of 40°S latitude, between 10° and 90°E longitude (Figures 1 and 3). The highest concentrations occur in Utopia Planitia, east of Acidalia Planitia, and in Malea Planum. We observe a significant hemispherical asymmetry, with more than three times as many pedestal craters located in the northern hemisphere (Figure 2). There is a dearth of pedestal craters equatorward of ~40°N and S latitude, with the exception of one area west of Tharsis (0°-15°N; 190°-235°E) in the Medusae Fossae Formation [*Schultz and Lutz, 1988; Barlow, 1993; Watters et al., 2007*]. All 71 of the pedestal craters with marginal pits are located in Utopia Planitia and Malea Planum, poleward of 48°N and 55°S latitude respectively (white circles in Figure 1) [*Kadish et al., 2008*]. The search for pedestal craters with pits was extended to 70°N and S latitude to improve our understanding of their geographic extent.

3.2. Pedestal Crater Attributes

Images of typical pedestal craters are seen in Figure 4, and additional examples are shown with MOLA data (Figure 5); corresponding topographic profiles are in Figure 6. Pedestal crater attributes measured in this study show several significant trends

(Figures 7-9, Tables 2,3). Diameters of the crater bowls (Figure 7a) are generally <5 km, with a mean of <2 km; because we did not measure pedestal craters with diameters <0.7 km, we cannot define an absolute average diameter. Crater bowl diameters tend to increase toward the equator (Figure 8a), and are largest in the Medusae Fossae Formation. This trend is more prevalent in the southern hemisphere, where pedestal craters tend to be larger. The Γ ranges from ~1 to 2.5 with a mean of 1.1 (Figure 7). Most other types of fresh martian impact craters have distinctly higher marginal sinuosities [Barlow, 2006]; because normal martian craters lack pedestals, these measurements are based on the perimeters of their ejecta deposits. Extremely high Γ values (>1.4) among pedestal craters are generally found in the Medusae Fossae Formation (see section 4.3; Figures 13 and 14). Mean Γ values do not appear to be latitude dependent (Figure 8b).

P/C ratios range from 1.2 to 13; mean values are ~3.3 at northern mid latitudes and ~2.5 at southern mid latitudes (Figure 7). Extremely high P/C ratios (>6) are also usually restricted to the Medusae Fossae Formation (Figures 8c and 13), with the exception of pedestal craters with marginal pits. Pedestal crater P/C values are the highest for any Martian crater type [Barlow, 2006]. Pedestal crater plateaus are typically elevated ~20-80 m above the surrounding plains based on MOLA measurements (Figures 5 and 6). Preliminary measurements of pedestal heights reveal no correlation with crater or pedestal diameter.

The attributes of pedestal craters with marginal pits (Figures 10 and 11) vary somewhat from those without pits. The morphology of pedestal craters with marginal pits is described in detail by Kadish *et al.* [2008]. To summarize, the outward-facing

scarps along the perimeters of some pedestal craters are interrupted by small pits (Figures 10 and 11). Pits often have cusped shapes and alcove-like features, and tend to be elongated along the pedestal crater scarp. In some cases, pits coalesce to form long moat-like troughs along the pedestal perimeter (Figure 10a). Topographic profiles show that pits, which have typical depths of ~ 20 m, form on the scarps themselves, not on the surrounding terrain. Furthermore, pit depths do not extend below the elevation of the adjacent plains (Figure 10c,f). Pit interiors have generally shallow slopes ($<10^\circ$), and slopes are roughly constant around the perimeter of the pit. We have not observed any significant pole-facing or equator-facing trend for the location of pits around the pedestal scarps. Notable differences between pedestal craters with and without marginal pits are that pedestal craters with pits tend to be larger, with an average crater diameter of 5.1 km and an average P/C ratio of 5.6. In other words, both the crater bowl and the farthest extent of the plateau relative to the crater radius are larger. These pedestal craters with marginal pits have a similar average Γ , 1.06, to those without pits. Pedestal heights of those with pits tend to be about twice as high as those without, having an average height of ~ 100 m (compare Figures 5 and 10) [Kadish *et al.*, 2008].

As previously mentioned, pedestal craters in the Medusae Fossae Formation are physically distinct from those at mid and high latitudes (compare Figures 5, 10, and 13). Although the craters themselves, with an average diameter of 2.1 km, are not much larger than pedestal craters without pits at mid to high latitudes, their pedestals extend much farther; the average P/C ratio of pedestal craters in the Medusae Fossae Formation is 5.4 (Figure 8c). The most distinctive quality of pedestal craters in the Medusae Fossae Formation, however, is a jagged pedestal perimeter (Figures 13 and 14), yielding a mean

Γ of 1.64 (Figure 8b). Furthermore, their pedestals are, on average, the tallest of any measured, with mean plateau heights of ~ 200 m (Figure 13), four times the average height of normal mid- to high-latitude pedestal craters.

4. Discussion

4.1. Trends in Pedestal Crater Attributes

The measurements made in this study reveal a number of significant trends regarding the physical attributes of mid-latitude pedestal craters, as well as those within the Medusae Fossae Formation (Figures 7-9). First, pedestal craters tend to have small crater bowl diameters. Greater than 95% of the pedestal craters we observed have diameters of less than or equal to 2.5 km. Second, pedestal perimeters are extremely circular. More than 69% of pedestal craters measured had Γ values of less than or equal to 1.1, and more than 98% had Γ values less than 1.4. As previously mentioned, the outliers from this measurement are restricted almost entirely to the Medusae Fossae Formation. These low Γ values confirm the general circularity of individual pedestals. Third, more than 97% of pedestal craters have P/C ratios greater than 1.5, and more than 67% have P/C ratios above 2.5. These high P/C ratios, which exceed the typical value of ~ 1.7 for mid-latitude, single layer ejecta craters on Mars [Barlow, 2006], strengthen support for an armoring mechanism that is not limited to direct effects from the ejecta deposit, as discussed in section 4.6.

Latitude-dependent trends for the pedestal crater measurements can be seen in Figure 8, where it is apparent that crater bowl diameters tend to increase as latitude

decreases. This trend (Figure 8a) may not be robust due to the small number of pedestal craters in the southern hemisphere, and is less pronounced in the northern hemisphere. Pedestal circularity (Figure 8b) is relatively constant as a function of latitude, with the exception of the Medusae Fossae Formation. Pedestal craters in the Medusae Fossae Formation show consistently higher values for all measurements taken. Our proposed formation mechanism predicts that Γ values should not be affected by latitude, as is confirmed by our measurements. The P/C ratio does not show a strong increasing or decreasing trend as a function of latitude (Figure 8c), although there are notably higher P/C ratios in the northern hemisphere than in the southern hemisphere. This would be expected if an atmospheric blast plays an important role in the armoring mechanism [Wrobel *et al.*, 2006]; the thicker atmosphere in the northern hemisphere, where the impacts occur at lower elevations, would be more capable of propagating the shockwave and thermal pulse, allowing for generally larger pedestals. The data point in the 35 to 40°N bin in Figure 8 includes pedestal craters from 30 to 40°N because so few were present between 30 and 35°N. Even with the lumping of data, these points represent only 24 craters, and thus their deviation from the noted trends is likely due to the statistics of small numbers.

Comparisons of pedestal crater attributes (Figure 9) show a number of interesting results, most notably that the measured characteristics may be largely independent of each other. Pedestal craters tend to have small diameters and low Γ values. However, examination of the extremes for each attribute shows that pedestal craters can have very low Γ values even with large diameters. Conversely, pedestal craters with small diameters can have high Γ values. In addition, pedestal craters in the Medusae Fossae

Formation can have both high Γ values and large diameters. Comparing P/C ratio to crater diameter, a similar trend is observed. Pedestal craters usually have low P/C ratios and diameters, but in some instances have large diameters with low P/C ratios, and high P/C ratios with small diameters. Some examples also have large diameters and high P/C ratios. In other words, regression analyses on these data show low R^2 values, suggesting that there are no statistically significant trends. When Γ values are compared to P/C ratios, a slightly positive correlation is observed, with higher P/C ratios corresponding to higher Γ values. This may suggest that larger pedestals (not necessarily larger crater diameters) may not be homogeneously armored, especially near the distal edge of the pedestal, or that larger pedestals are more prone to differential erosion, resulting in asymmetrical pedestal degradation.

4.2. Climate Models and Odyssey GRS Experiment Data

The strong latitude-dependent distribution of pedestal craters suggests a correlation between pedestal craters and the history of climate on Mars. Although the various Martian climate models do not agree precisely on certain climatic details (e.g. ice accumulation rates), a broad consensus does exist in many areas. The common conclusion is that, during periods of high obliquity ($>35^\circ$), increased insolation to the polar regions during the summer removes volatiles from the polar caps and deposits them at lower latitudes either via precipitation or vapor diffusion into the regolith [e.g., *Forget et al.*, 1999; *Jakosky et al.*, 1995; *Richardson and Wilson*, 2002; *Haberle et al.*, 2003; *Mischna et al.*, 2003; *Mellon et al.*, 2004]. The atmospheric humidity increases, and the latitude at which surface ice is stable moves toward the equator. During periods of low

obliquity, this latitudinal limit is usually around 60°, but at higher obliquities, the ice stability zone moves to ~30°. Most models predict increased wind strength during the higher obliquity eras as well, raising the atmospheric dust content. This dust is incorporated into the ice, potentially yielding fine-grained, ice-rich deposits between 30° and 60° latitude in both hemispheres [Head *et al.*, 2003; Jakosky *et al.*, 1995; Laskar *et al.*, 2004]. When the obliquity decreases, the atmosphere dries and the mid-latitude ice-rich layer desiccates. The sublimated ice eventually returns to the poles, leaving behind an ice-poor regolith, although the generally short durations of low obliquity periods combined with the development of sublimation lags are not likely to result in complete removal of the ice from the mid-latitudes [Head *et al.*, 2003; Mellon *et al.*, 1997; Touma and Wisdom, 1993]. This movement of ice from the polar regions to the mid-latitudes and tropics is expected to operate on timescales of 10⁵–10⁶ years, and current near-surface ice (upper meter of regolith) near the stability boundary (~60° latitude) is expected to have an age of <500 kyr [Haberle *et al.*, 1993; Mellon *et al.*, 2004; Mischna *et al.*, 2003].

The global epithermal neutron data acquired by Mars Odyssey's gamma ray and neutron spectrometer (GRS) provide important information about the current distribution of water ice on Mars [Boynton *et al.*, 2002; Feldman *et al.*, 2002; Mitrofanov *et al.*, 2002], and can thus be used to enhance our understanding of the distribution of pedestal craters. The spectrometer detects to a depth of approximately one meter in the Martian soil, thus measuring the volatile content of the uppermost part of the subsurface. Because pedestals are significantly thicker than one meter, the GRS data cannot directly measure the abundance of volatiles throughout the pedestals. In addition, the GRS data represent

the hydrogen content at the current low Martian obliquity. The pedestal craters, however, were likely emplaced during past higher obliquity periods, and the lateral extent of the ice-rich material has been receding poleward since this time. The thermal, epithermal, and fast neutron data can be used to derive water-equivalent hydrogen concentrations in the form of water-ice or hydrated minerals [Boynton *et al.*, 2002; Feldman *et al.*, 2002; Mitrofanov *et al.*, 2002]. We compare the GRS water-equivalent hydrogen maps with the distribution of pedestal craters (Figure 12). High levels of water-equivalent hydrogen can be indicative of intact, shallowly-buried ground ice covered by desiccated soil [Boynton *et al.*, 2002; Mellon *et al.*, 2004].

Figure 12 reveals a strong latitudinal correlation between the pedestal crater distribution and the concentration of water-equivalent hydrogen. Between 0° and 60°N, the latitudes with the highest hydrogen content (>8 wt% water-equivalent hydrogen) are generally poleward of 50°N, but dip as low as 35°N, matching the pedestal crater distribution in Arcadia Planitia (Figure 12). Between 0° and 65°S, the latitudes with the highest hydrogen content are mostly poleward of 60°S, but reach 50°S near Malea Planum. It is possible that some pedestal surfaces, especially those at higher latitudes, have become re-enriched in water-ice since they formed. We, however, highlight this correlation between high water-equivalent hydrogen and pedestal crater distribution to show that pedestal craters tend to form where water-ice is present near the surface. Note that some small populations of pedestal craters are present in relatively lower water-equivalent hydrogen areas. This is expected during the current low obliquity regime, when the intercrater terrain surrounding some mid-latitude pedestal craters has become desiccated near the surface. However, the locations of these regions coincide with areas

that were likely covered by ice-rich deposits during past periods of higher obliquity [e.g., *Mustard et al.*, 2001; *Head et al.*, 2003]. Thus, the current distribution of water-equivalent hydrogen is consistent with the interpretation of the pedestal craters resulting from obliquity-driven climate change, having formed during periods of higher obliquity.

4.3. Pedestal Craters in the Medusae Fossae Formation

The presence of pedestal craters in an equatorial region (Figures 1, 13, and 14), from about 5°S to 15°N, appears inconsistent with a sublimation-driven model of pedestal crater formation; the closest pedestal craters to the Medusae Fossae Formation population are at 33°N. The formation mechanism for the Medusae Fossae Formation pedestal craters may be closely related to the origin of the fine-grained material that composes the Medusae Fossae Formation. Researchers, however, have been unable to reach a consensus on the exact source of its material [e.g., *Barlow*, 1993; *Bradley et al.*, 2002; *Hynek et al.*, 2003]. If the Medusae Fossae Formation resulted from pyroclastic fall or eolian deposits, it may never have contained ice-rich material [*Scott and Tanaka*, 1982; *Hynek et al.*, 2003]. In this case, pedestal crater formation via sublimation of the surrounding terrain would not be possible. If, however, the Medusae Fossae Formation was created from polar layered deposits during polar wander [*Schultz and Lutz*, 1988] or airborne volatile-rich material deposited locally during a period of high obliquity [*Head and Kreslavsky*, 2004] then it may have had the ice-rich material necessary for sublimation-formed pedestal craters.

The polar layered deposit hypothesis postulates that the deposits formed during a period of polar wander prior to the early stages of Tharsis volcanism [*Schultz and Lutz*,

1988]. The primary evidence for an ice-rich origin came from Viking images of exhumed impact basins and small-scale layering. The opposing argument notes that a polar origin is unlikely based on the timescales required for such an extreme change in spin-axis orientation [Bradley *et al.*, 2002; Tanaka, 2000]. Analyses of observed tectonic features on Mars are also inconsistent with the lithospheric stresses necessary for the magnitude and timing of the proposed polar wandering [Grimm and Solomon, 1986]. Digital elevation models from MOLA data showed that the Medusae Fossae Formation had strikingly similar topography to polar layered terrain [Head, 2000], leading to the interpretation that emplacement took place during periods of higher obliquity [Head and Kreslavsky, 2004]. The hypothesis that the Medusae Fossae Formation contained ice-rich material deposited during high obliquity is based on climate model predictions [Richardson and Wilson, 2002; Haberle *et al.*, 2003; Mischna *et al.*, 2003], gamma-ray spectroscopy (GRS) data showing elevated hydrogen in the region [Boynton *et al.*, 2002; Feldman *et al.*, 2002], and calculations of the obliquity history of Mars [Laskar *et al.*, 2004]. This is further supported by geomorphological, stratigraphic, and surface roughness evidence, which suggest the emplacement of an unusually smooth, ice-rich unit interrupted by periods of erosion and volatile loss [Head and Kreslavsky, 2004].

From the preceding arguments, it is certainly plausible that the Medusae Fossae Formation contained ice-rich material at some point in its past. Recently, Watters *et al.* [2007] used Mars Advanced Radar for Subsurface and Ionosphere Sounding (MARSIS) data to calculate a real dielectric constant and estimate dielectric losses for the Medusae Fossae Formation. The results were consistent with either a substantial water-ice component or an anomalously low-density, ice-poor material [Watters *et al.*, 2007].

From this, we cannot rule out the possibility of a dry pyroclastic fall origin. The distinct geomorphology of pedestal craters in the Medusae Fossae Formation (Figures 13 and 14) suggests that they may have formed through a different process than those in the mid to high latitudes. Not only are the Medusae Fossae Formation pedestal craters more sinuous/jagged and have farther extending plateaus, but they also excavate to much greater depths; Medusae Fossae Formation pedestal crater bowls can extend hundreds of meters below the elevation of the surrounding terrain, whereas the basins of mid- to high-latitude pedestal craters are most often entirely above the elevation of the adjacent plains (compare profiles in Figures 6 and 13). The shallow depths of mid- and high-latitude pedestal crater bowls may be due, in part, to infilling, which likely results from accumulation of material within the crater bowl either from local eolian dust deposits or from subsequent large-scale, ice-rich dust deposits caused by obliquity changes. The extreme excavation depths in the Medusae Fossae Formation apply to all craters, not just pedestal craters; craters in the Medusae Fossae Formation generally have increased depth-diameter ratios. Simple craters are roughly 79% deeper in the Medusae Fossae Formation than craters with the same diameters in other areas [Barlow, 1993]. These high depth-diameter ratios have been attributed to its fine-grained, easily erodible and compactable material [Barlow, 1993]; laboratory experiments confirm that impacts into fine-grained material can have dramatic effects on the resulting impact morphology [Schultz, 1992]. The high P/C ratios of Medusae Fossae Formation pedestal craters may be related to the extreme excavation depths; more material is removed from the crater bowls, which correspond to greater volumes of material in the pedestals. Alternatively, the high P/C ratios may suggest that the armoring mechanism is more efficient in this

fine-grained region. The presence of yardangs and surface textures indicative of eolian erosion adjacent to and contiguous with pedestal craters in the Medusae Fossae Formation suggest that eolian deflation likely played an important role in their formation (Figures 13b and 14c). The Medusae Fossae Formation is also devoid of pedestal craters with marginal pits. If marginal pits do result from sublimation processes in accordance with our model, this complete absence of pits suggests that ice-rich material is not present in the Medusae Fossae Formation pedestals. From this, we conclude that, although it is possible that pedestal craters in the Medusae Fossae Formation formed via the same mechanism as mid- and high-latitude pedestal craters, owing their distinct morphologies to the unique target material of the Medusae Fossae Formation, it is plausible that these features form through a different process based primarily on eolian deflation.

4.4. Ages

Determining the age of a pedestal crater population cannot be done using conventional crater counting techniques [e.g., *Hartmann, 1966; Hartmann and Neukum, 2001; Hartmann, 2005*] that date the surfaces on which the craters are emplaced because the surrounding surface has been repeatedly removed and re-deposited. Despite this limitation, we can place some constraints on the timing of the formation of the pedestal crater population using a combination of methods and observations (Figures 15 and 16). From our survey, we have observed that pedestal craters are generally morphologically fresh (Figures 4 and 5). Crater rims are usually well-preserved (Figure 6), and pedestal surfaces are rarely degraded at THEMIS VIS resolution (18 m/pix).

The geographic distribution of pedestal craters shows that a significant portion of the population is located on Amazonian-aged units in the northern lowlands [*Tanaka et al.*, 2003] and in the north polar region [*Tanaka*, 2005]. This superposition of pedestal craters on young surfaces supports the notion that pedestal craters formed recently. In particular, pedestal craters are concentrated on the Vastitas Borealis Formation (AHvh), as well as smooth (Als₁) and coarse (Alc) lobate materials, which are late Hesperian to early to mid Amazonian in age [*Tanaka et al.*, 2003]. Additionally, *Tanaka et al.* [2003] map a smaller population of pedestal craters at high latitudes, which they note is present on Amazonian materials such as polar layered deposits (Apl₁), as well as Hesperian plains including the Scandia unit (Hs).

If marginal pits form via sublimation, then these features may also support a young age. These pits appear morphologically fresh, with pristine rims and no signs of infilling. Although the sublimation of volatiles is inhibited by the armored pedestal surface, it is not completely prevented. Diffusive exchange of water between ground-ice and the atmosphere at mid latitudes is largely affected by obliquity oscillations, and will result in periodic saturation and desiccation of the upper few meters of soil [*Mellon and Jakosky*, 1995]. During periods of low obliquity, higher soil temperatures and lower atmospheric water content at mid latitudes makes ground ice unstable [*Mellon and Jakosky*, 1993, 1995; *Mellon et al.*, 2004]. Currently, pedestal craters with marginal pits are concentrated around 60° latitude in both hemispheres, which is the latitudinal boundary for stable water-ice, as shown by GRS data – the terrain is hydrogen-rich poleward of 60° latitude [*Feldman et al.*, 2002]. If the indurated pedestal surface drastically restricts the diffusive exchange process, pedestal craters may maintain ground-

ice within the upper few meters of their pedestals. However, the armoring may be weaker near the pedestal margins, as discussed in section 4.8, allowing for more rapid diffusive exchange of volatiles between the pedestal and the atmosphere. As mentioned in section 4.2, *Mellon et al.* [2004] argued that ice in the dynamic saturation/desiccation zone should be relatively young (<500 kyr). It is thus possible that, based on our observations, marginal pits represent an active sublimation process and are still developing, forming connected pits and moat-like structures around pedestal craters. In this case, near-surface ice in the pedestals must be young, and thus the pedestals themselves must be young. We recognize, however, that this evidence is model-dependent, and we cannot, at this time, be certain of the ages of these pits.

Although crater counting cannot provide an absolute age for the pedestal crater population, it can provide a lower limit for how long the population took to form. We used a polygon that delineated the current geographic location of pedestal craters within our survey area to calculate the area on which pedestal craters are capable of forming. This polygon was designed to follow the borders established by the outer geographic reaches of the pedestal crater populations so as to avoid an overestimation of the counting area. Using this area with the measured diameters of 1,363 pedestal craters (1027 from the northern hemisphere and 336 from the southern hemisphere), we find a best fit of approximately 50 Myr (Figure 15) based on isochrons from *Hartmann* [2005]. When considering the northern and southern hemisphere populations separately, taking into account distinct crater counting areas, the best fits derived from the *Hartmann* [2005] isochrons are approximately 65 Myr and 32 Myr respectively. This population of 1,363 pedestal craters, which is ~50% of the total mapped, was identified using THEMIS IR

image releases 1 through 13 (orbit range 816 to 13499), which has >88% coverage between 60°N and 60°S. Measurements of the diameters of the additional 1,333 pedestal craters identified while surveying THEMIS IR image releases 14-23 are currently being acquired. The set of images from THEMIS IR image releases 14-23 increases the coverage between 60°N and 60°S to >96%, and improves the quality of images in many areas. Because we used half of the measured pedestal crater population for the size frequency distribution (Figure 15), our best fit is necessarily an underestimate. However, for young surfaces (<3 Gyr), we can assume a relatively constant crater flux [e.g., *Neukum et al.*, 2001]. Thus, doubling the number of pedestal craters on the surface will double the derived best fit time from 50 Myr to 100 Myr, assuming that the frequency distribution of pedestal crater diameters does not vary significantly between the 1,363 used and the 1,333 being measured.

This derived time implies that the pedestal crater population could have formed in a minimum of ~100 Myr, assuming the continuous presence of the proposed latitude-dependent, ice-rich deposit. However, the time required to form the observed population is necessarily greater than 100 Myr because the deposit is not currently present and a robust solution for the last 20 Myr of Martian obliquity history [*Laskar et al.*, 2004] shows low obliquity periods for the last 3-5 Myr, and potentially widely variable obliquity for the last 250 Myr. Additional work on dating pedestal craters will be possible when more high resolution imagery is available of pedestal surfaces. These images can then be used to perform crater counts on the pedestal surfaces themselves, effectively dating the age of the surface of the ice-rich deposit, and thus of the regional pedestal crater population.

Global climate modeling at a range of obliquities (from 15° to 45°) to investigate the recent formation and evolution of the north polar layered deposits [Levrard *et al.*, 2007] and modeling of the fate of polar water at 45° obliquity [Forget *et al.*, 2006] strongly suggest that polar ice migrates rapidly to the tropics (equatorward of 25° latitude); all the simulations displayed a direct exchange between the northern polar cap and high topography equatorial regions [Forget *et al.*, 2006; Levrard *et al.*, 2004, 2007]. Only with obliquities lower than today (~15° and 20°) and an equatorial source were large-scale accumulations of ice observed poleward of 60° latitude in both hemispheres, with some excursions into the mid-latitude regions [Levrard *et al.*, 2004]. Other models [Mischna *et al.*, 2003; Mischna and Richardson, 2005], however, show significant deposition of ice at increasingly lower latitudes as obliquity increases. In these models, the polar reservoir is eventually exhausted and equatorial ice dominates.

On the basis of the modeled martian obliquity history over the past 20 Myr, and possible histories over the past 250 Myr [Laskar *et al.*, 2004], it is likely that pedestal craters formed during multiple high obliquity events, on successive deposits of ice-rich material at mid and high latitudes. This interpretation is supported by numerous instances of pedestal craters being completely superimposed or partially draped over other pedestal craters (Figure 16). Because these excursions to higher obliquity have likely been common throughout the Amazonian [Laskar *et al.*, 2004], it is plausible that an ice-rich substrate has been emplaced at mid latitudes for much greater than the 100 Myr lower limit, and thus that pedestal craters are more broadly distributed in age throughout the Amazonian.

4.5. Hemispheric Asymmetry in Pedestal Crater Distribution

There is a notable hemispheric asymmetry in the distribution of pedestal craters, with more than three times as many in the northern hemisphere as in the southern hemisphere between 60°N and S latitude. There are two probable factors influencing the observed preferential formation in the northern hemisphere. These include: 1) differences in atmospheric thickness, and thus in the overlying atmospheric water column abundance, defined as the amount of water vapor in the atmosphere above a defined surface area, and 2) the availability/distribution of fine-grained material and variations in surface roughness.

The northern lowlands are, on average, about 6 km lower in elevation than the southern highlands. As such, the low elevation of the northern hemisphere plains is overlain by a thicker atmospheric layer, generally supporting a greater atmospheric water column abundance; this has been empirically confirmed by a number of instruments including: Mars Atmospheric Water Detector (MAWD) on Viking [Farmer *et al.*, 1977], Thermal Emission Spectrometer (TES) on Mars Global Surveyor [Smith, 2002, 2004; Sprague *et al.*, 2006], and Spectroscopy for Investigation of Characteristics of the Atmosphere of Mars (SPICAM) on Mars Express [Fedorova *et al.*, 2006]. Volatiles from the polar regions are suspended in the martian atmosphere and transported to the mid latitudes during periods of high obliquity. Following atmospheric transport, the volatiles are precipitated as ice and snow on the surface, or diffuse into the regolith [e.g., Jakosky, 1983; Fanale *et al.*, 1986; Mellon *et al.*, 2004]. It is possible that, during periods of high obliquity, the thinner atmosphere in the southern highlands is limited in its capacity to transport volatiles to mid latitudes; although the transport process may be equally

efficient in each hemisphere, the greater thickness of the atmosphere overlying the northern hemisphere simply allows for a greater quantity of water vapor to be transported. In the southern hemisphere, this could yield a thinner ice-rich deposit, which may not extend as close to the equator as in the northern hemisphere. This effect would tend to make the northern plains more conducive to pedestal crater formation, and explain why southern pedestal craters do not extend quite as close to the equator as those in the northern hemisphere.

Although the necessity of ice-rich material has been the focus of this research, an important aspect of all pedestal crater formation models that has not been discussed in depth is that the impacts occur in fine-grained material [Arvidson *et al.*, 1976; Barlow, 2006; McCauley, 1973]. This element of the formation hypotheses may play an important role in the preferential formation of pedestal craters in the northern hemisphere. The resurfacing of the northern lowlands occurred via volcanic or sedimentary processes, and may have left a hundreds-of-meters thick deposit overlying much of the northern terrain [Head *et al.*, 2002; Clifford and Parker, 2001; Smith *et al.*, 1999]. Researchers have suggested that the northern lowlands were once submerged under an extensive standing body of water. In this case, the flat northern topography could have resulted from subaqueous volcanism and deposition on the ocean floor [Baker *et al.*, 1991; Parker *et al.*, 1989]. Alternatively, early Hesperian volcanism may have been followed by fine-scale smoothing from the emplacement of outflow channel sediments [Head *et al.*, 2002]. The resulting smoothness has also been interpreted as fine-grained dust. This hypothesis is consistent with the low surface roughness and

regional flatness derived from MOLA data [*Aharonson et al.*, 1998; *Christensen*, 1986; *Kreslavsky and Head*, 2000; *Smith et al.*, 1999].

This low surface roughness has been specifically correlated to the Vastitas Borealis Formation, which covers most of the northern plains with a surface area of $1.8 \times 10^7 \text{ km}^2$ [*Tanaka et al.*, 2005]. This region hosts an extremely high concentration of pedestal craters. The characteristic smoothness of the Vastitas Borealis Formation, suggests a composition of 100 m of sediment overlying volcanic ridged plains [*Kreslavsky and Head*, 2000, 2002; *Tanaka and Scott*, 1987]. Conversely, the southern hemisphere's Noachian terrain may be characterized by coarser material, yielding a much rougher surface, with higher local slopes. Although its ridged plains do form locally flat regions between craters, they are still extremely rough, as shown by interquartile scale surface roughness calculations from MOLA profiles [*Smith et al.*, 1999]. Numerical granular flow models have shown the significant effects of surface roughness on ejecta emplacement and flow; rough surfaces and those with high friction coefficients between ejecta grains restrict ejecta mobility [*Wada and Barnouin-Jha*, 2006], and may be less conducive to armoring. It is thus likely that the southern hemisphere's terrain, having not been resurfaced by dust, sediment, or ash, is too rough and lacks the necessary fine-grained material to form large populations of pedestal craters. The northern hemisphere's younger, smoother deposits, which contain a much higher percentage of fine-grained material, provide a more appropriate setting for pedestal crater formation.

Finally, the atmospheric and the fine-grained material factors may be working in conjunction with one another. It is possible that the concentration of fine-grained material in the northern hemisphere may enhance the dust content in its thicker

atmosphere. A dustier atmosphere provides more nucleation sites for ice to form and precipitate, which could lead to preferential formation of the ice-rich deposit in the northern hemisphere.

At this time, the relative impact of the atmosphere versus the target material in producing four times more pedestal craters between 0° and 60°N than between 0° and 60°S is not fully understood. Both factors, however, could contribute to the observed asymmetry in the hemispheric distribution of pedestal craters. Additional research is necessary to determine which, if either, is dominant.

4.6. Armoring Mechanism

Several possible armoring agents have been suggested, including a coarse ejecta covering or lag deposit [e.g., *Arvidson et al.*, 1976], increased ejecta mobilization caused by volatile substrates [*Kieffer and Simonds*, 1980; *Stewart and Ahrens*, 2005; *Osinski*, 2006], glassy veneers from the distribution of impact melt [*Schultz and Mustard*, 2004], and/or an atmospheric blast/thermal effect [*Wrobel et al.*, 2006]. While our data show clear support for a sublimation-driven formation mechanism, they do not prove which of the above armoring mechanisms is correct. In this section, we offer a brief explanation of each method, and discuss why, based on our geomorphological analyses, we prefer the method proposed by *Wrobel et al.*, [2006].

The hypothesis that coarse material on the surface of the ejecta deposit prevents erosion of the ejecta [*Arvidson et al.*, 1976] applies only to the eolian deflation model, as winds are necessary to create the overlying lag deposit; it is thus not a control for the sublimation model of pedestal crater formation, although the permeability of the material

on the pedestal surface likely has a significant impact on sublimation rates of volatiles within the pedestal. The production of proximal melts, including glassy impactites, that armor the ejecta deposit is plausible [Osinski, 2006; Schultz and Mustard, 2004]. In this scenario, proximal melts are superimposed on the ice-rich material, forming a robust glassy covering that would prevent sublimation of near-surface ice. Another related working hypothesis is based on the theoretical prediction that dust can insulate ground ice for geologically long timescales [Skorov *et al.*, 2001; Mellon *et al.*, 1997]. This notion has been supported by empirical observations in the Antarctic Dry Valleys [Marchant *et al.*, 2002]. This armoring process involves impact into snow and/or ice overlying a fragmental silicate substrate. Impacts excavate to the fine-grained material below the layer of frozen volatiles. The fine-grained material is then mixed with some volatiles and distributed on top of the surrounding snow and/or ice. Even if some sublimation occurs in the upper layers of the ejecta deposit, the interspersed fine-grained material eventually reaches a critical thickness that sufficiently insulates the underlying frozen volatiles during low obliquity periods [Head *et al.*, 2005; Skorov *et al.*, 2001]. While these armoring mechanisms may be capable of preserving volatiles underlying the pedestal crater surface, they seem inconsistent with our measurements of the physical attributes of pedestal craters; none explains why pedestals are anomalously large compared to their associated crater diameters, as confirmed by the high P/C ratio measurements, nor do they account for minimal sinuosity of pedestal circumferences, as confirmed by the low Γ values.

In the scenario proposed by Wrobel *et al.* [2006], the surface proximal to the impact becomes armored via an outwardly-propagating atmospheric blast followed by a

high-temperature thermal pulse. Studies suggest that atmospheric effects play a role both in the emplacement of ejecta, and on the modification of the terrain surrounding the impact site [e.g., *Barnouin-Jha and Schultz, 1996; Schultz, 1992; Schultz and Gault, 1979*]. *Wrobel et al.* [2006] note that the atmospheric blast would likely strip away any loose particulates, allowing the volatile-rich surface to be even more sensitive to the ensuing thermal pulse. Two possible armoring mechanisms could result from these atmospheric effects: (1) "...melting and migration of near-surface water may indurate soil by rapidly dissolving and precipitating salts....," or (2) "...the blast and thermal effects may combine to remove the volatile fraction, leaving behind a protective layer of fine, volatile-poor dust," [*Wrobel et al., 2006*]. In either case, the sublimation rate from volatile-rich material composing the pedestal is reduced compared to the surrounding intercrater terrain upon return to low obliquity. It should be noted that because we are concerned only with sublimation (loss of volume due to removed ice) and not eolian deflation (loss of volume due to removed dust), it is irrelevant whether the ice in the volatile-rich target material was acting to cement the deposit. The only necessary aspect of the armored surface is to reduce the sublimation rate of volatiles from the pedestal material.

Wrobel et al. [2006] calculate geotherms from the thermal response aspect of their model, after *Paterson* [1994]. These geotherms are shown for ice-rich and fine dust layers, and are given based on ambient martian conditions as well as for conditions of increased temperature due to an engulfing hot vapor. On the basis of the geotherms, *Wrobel et al.* [2006] conclude that, "It is evident that lingering temperatures at ~30 s after the passage of the thermal pulse are high enough to produce a thermal wave extending to

depths of several centimeters (temperatures above melting down to ~15 cm) at ~4 apparent crater diameters from impact of an ice-rich substrate. Consequently, if given enough time, temperatures will be sufficient to melt any ice present in the upper layers of a subsurface.” The lateral extent of this heating is increased by considering the radiative effects of elevated temperatures higher in the atmosphere [Rybakov *et al.*, 1997]. By including these effects, significant heating can occur out to a distance of ~10 crater diameters [Wrobel *et al.*, 2006].

The region closer to the impact (2-3 crater diameters) will of course be covered by the subsequent emplacement of ejecta. However, because pedestals extend to a distance much greater than the extent of the ejecta, we do not believe the ejecta plays a primary role in the armoring mechanism. Examples of pedestal craters where the extent of the ejecta is visible and entirely superposed on the farther-reaching pedestal have been identified (e.g. Figures 11b, 16b, 16d). It is likely, however, that ejecta deposits can protect the underlying material. Cases in which the ejecta is solely responsible for preserving the underlying volatile-rich layers have been observed and documented by Black and Stewart [2008]; these morphologies, known as excess ejecta craters, are distinct from pedestal craters, and are discussed in the following section.

The method proposed by Wrobel *et al.* [2006] is thus capable of indurating the surface to a lateral extent of multiple crater radii, and would preferentially yield circular pedestal craters due to the radially symmetric propagation of the atmospheric blast and thermal pulse. As such, we find this armoring mechanism to be consistent with our measurements. Our analyses do not, however, prove this armoring mechanism to be correct, and it is beyond the scope of this paper to provide a quantitative analysis or

review of the atmospheric blast and thermal pulse. We hope that modelers will use the geomorphological constraints that we provide to test further the ability of each of the armoring mechanisms to indurate the surface and to inhibit sublimation of volatiles from the pedestals.

4.7. Related Morphologies

Features similar to the pedestal craters discussed in this paper have been previously identified and associated with sublimation processes. These related morphologies share important traits with pedestal craters, but all differ from the strict definition of pedestal craters [Barlow *et al.*, 2000] in significant ways. Meresse *et al.* [2006] identified a population of “perched craters” in Acidalia and Utopia Planitia between 40°N and 70°N. These degraded features exhibit anomalously high ejecta volumes, in some cases exceeding the volume of the crater cavity. They are also characterized by often fluidized ejecta with low thermal inertia and infilling of the crater bowl. Although both perched craters and pedestal craters are elevated above the surrounding terrain, only perched craters display double-layer ejecta morphologies [Barlow *et al.*, 2000] and have distinctive, nearly constant depth versus diameter values [Boyce *et al.*, 2005]. Meresse *et al.* [2006] propose that these perched craters form via impact into an ice-rich target and subsequent resurfacing of the region. This resurfacing process includes the emplacement of fine-grained material over the ejecta deposits and significant infilling of the crater bowl, followed by erosional processes. Thermal erosion, consisting of weakening and disaggregation of the surface materials, preferentially affects the intercrater plains, which have a higher thermal inertia than the craters and ejecta

deposits. The actual removal of the material begins with cryokarstic processes, including the sublimation of near-surface ice, followed by eolian deflation, lowering the elevation of the intercrater plains. The wind erosion continues to remove parts of the ejecta deposit as well, but the infilled crater cavity is largely resistant, leaving it perched [*Meresse et al.*, 2006].

Meresse et al. [2006] note that, “perched craters have the same morphology as the type 3 craters described by *Boyce et al.*, (2005)...” *Boyce et al.* [2005] identified 414 of these type 3 craters, having a diameter range of 6 to 22.8 km, distinctly larger than the pedestal craters we measured. These type 3 craters, which were first described by *Garvin et al.* [2000], include all craters whose floor is at or above the elevation of the surrounding terrain, and are characterized by their remarkable shallowness and depth to diameter ratio [*Boyce et al.*, 2005]. The craters, which are generally found in the VBF, have floors which are typically ~0 to 250 m above the adjacent plains. *Boyce et al.* [2005] suggest that the distinctive depth to diameter ratios of these craters implies a unique erosional process that requires sublimation to have played a major role in their formation. This erosional style is unique to the VBF on Mars, but is similar to a process that operates in high-latitude permafrost regions on Earth [*Boyce et al.*, 2005].

The pedestal craters described here may have a similar formation mechanism to a population of fresh excess ejecta craters identified by *Black and Stewart* [2008], which are located primarily in Utopia Planitia between 32°N and 44°N. They identified 572 of these with a diameter range of 2.5 to 102 km. The volume of the ejecta material superposed on the preimpact surface is 2.5 to 5.8 times larger than the volume of the crater cavity. *Black and Stewart* [2008] argue that the excess volume cannot be

explained by ejecta bulking alone, and therefore must be a secondary feature. They propose the following formation mechanism: Impact occurs into a rocky target overlain by an ice-rich layer(s) tens of meters thick. The ejecta deposit, which is a combination of rock and ice material, is distributed over the icy layer proximal to the crater cavity. Climate change causes the regional ice to sublimate, yielding a lag deposit, but the ejecta protects the underlying icy layer, prolonging the time over which ice sublimates. Subsequent erosion of the intercrater lag layer deflates the surrounding surface. This lag deposit is preserved under the ejecta, producing the observed excess thickness of 20 to 100 m averaged over the continuous ejecta deposit. They conclude that the excess material may contain some of the original ice, but it could be purely a lag deposit [*Black and Stewart, 2008*]. The similarity between the formation mechanism they propose for excess ejecta craters and the mechanism we propose for pedestal craters suggests that these morphologies may be genetically related. This potential relation is strengthened by their excess thickness calculation (20 to 100 m), which mimics the range of pedestal heights we have measured at mid latitudes (~25 to 150 m).

Morphologies also exist which are similar to the pits we have identified in association with pedestal craters. These related features can form via the sublimation of ice in numerous environments throughout the solar system [*Moore et al., 1996*]. On Mars, these include dissected terrain [*Mustard et al., 2001; Head et al., 2003*], pits on the floors of craters [*Tornabene et al., 2007*] and some outflow channels [*Levy and Head, 2005*], outwash plains and thermokarstic regions [*Costard and Kargel, 1995*], and formerly ice-rich and now beheaded pits in the proximal part of debris-covered glaciers [*Marchant and Head, 2007*]. For example, *Costard and Kargel* [1995] analyzed a similar

pit morphology in western Utopia Planitia, just south of the population we have identified. These morphologically fresh, rimless pits occur in the surrounding substrate. They are interpreted to be due to sublimation and thermokarstic processes [*Costard and Kargel, 1995; Morgenstern et al., 2007; Kargel and Costard, 1993; Soare et al., 2007*]. Although they have similar characteristics and depths to pits in pedestal scarps, unlike pitted pedestal craters they reach depths below the elevation of the adjacent terrain. In particular, *Costard and Kargel [1995]* note that in Utopia Planitia, "...a few 10's of rampart craters or other types of cratered mounds have annular moats around their edges." They argue that the moats have a thermokarstic origin, appearing similar to terrestrial fluvioglacial kettle lakes and alases [*Kargel and Costard, 1993; Costard and Kargel, 1995*]. In their model, "...impact meltwater infiltrated the permeable ejecta and then ponded or drained into rocks around the ejecta blanket. The infiltration of the water into the ground is possible because the impact would have thawed the surrounding ground. Under the cold climate of Mars, the drained water then froze, forming a concentration of segregated ice. During a warmer climate, the subsequent melting of this ice resulted in differential collapse and development of individual alases; slope retreat then resulted in a progressive widening of the thermokarst pits around the ejecta lobe. Finally, the coalescence of the alases produced a complete annular moat," [*Costard and Kargel, 1995*]. They also propose a mechanism in which the craters are not impact craters but mud volcanoes from geothermal liquefaction of frozen silts or slurries [*Costard and Kargel, 1995*].

The pits in pedestal crater margins are also morphologically similar to scallops, which are found in both Utopia Planitia and Malea Planum in the plains between pitted

pedestal craters [Lefort *et al.*, 2005, 2006, 2007; Zanetti *et al.*, 2008]. Scallop pits are thought to form via sublimation of interstitial ice from a volatile-rich mantling layer [Howard, 1978; Lefort *et al.*, 2006; Zanetti *et al.*, 2008]. These scallop pits are 5-20 m deep and can coalesce to form larger pits, much like the pits in the pedestal crater margins. They differ from pedestal crater pits, however, in a few important ways. First, the equator-facing slopes of scallop pits are generally shallower than their pole-facing slopes. Second, scallop pits are generally rounder in planform than pits around pedestal craters; scallop pits are not typically elongated in any given direction. Third, scallop pits can be considerably larger than pedestal crater pits, although this may be due to the fact that pedestal crater pits are confined to the narrow pedestal crater scarp.

4.8. Formation Model and Implications for Ice Preserved under Pedestal Crater Surfaces

On the basis of the evidence discussed throughout this paper, most notably the latitude dependence of pedestal craters, low Γ values and high P/C ratios, and the presence of marginal sublimation pits in some pedestal crater scarps, we favor an origin for pedestal craters based on sublimation of ice-rich deposits (Figure 17). Our model is as follows:

- 1) An impact occurs in a tens to hundreds-of-meters-thick, regional, mid-latitude layer of ice and snow, mixed with dust, which was deposited during a period of higher obliquity.

- 2) The impact distributes ejecta and impact melt around the crater rim, and triggers an atmospheric blast which is followed by a high-temperature thermal pulse

[Wrobel *et al.*, 2006]. The strongest winds and hottest temperatures occur closest to the point of impact.

3) The surface proximal to the crater becomes indurated as a result of the impact process. This armored surface can extend to a distance of multiple crater radii, exceeding the lateral extent of the ejecta deposit. Because the effectiveness of the preferred armoring mechanism lessens moving radially away from the point of impact due to weaker winds from the atmospheric blast and lower temperatures from the thermal pulse, we expect regions at the farthest extent of the pedestal to be weakly armored.

4) During return to low obliquity, climate change causes volatiles to sublime from the unarmored intercrater terrain. The loss of volume lowers the elevation of the surrounding substrate, yielding a symmetrical, circular scarp at the edge of the armored crater. It is important to note that this process does not require eolian deflation which, due to predominant wind directions, would tend to reduce the circularity of pedestals, in contrast to our observations. Armoring inhibits or slows sublimation from beneath the hardened pedestal surface, producing a typical pedestal crater, perched above a locally ice-rich substrate. Continued sublimation at the edge of the armored surface creates the debris-covered, marginal, pedestal scarps. The majority of pedestal craters reach an equilibrium between sublimation and debris cover, which stabilizes the margin of the pedestal.

5) Anomalously tall pedestal craters expose a larger surface area to insolation along their scarps. These higher, more extensive marginal slopes favor downslope movement and the thinning and shedding of any overlying protective regolith. As such, the slopes are preferentially mass-wasted; volatiles within the pedestal material diffuse

and sublimate through the scarp at a faster rate than through the armored surface. This effect may be enhanced by the tapering of the armor strength near the scarp, allowing for more rapid sublimation.

6) This sublimation process produces marginal pits, which appear to reach depths no greater than the vertical extent of the original ice-rich deposit, and do not extend to depths below the elevation of the intercrater, volatile-poor terrain [*Kadish et al.*, 2008]. Regions along the scarp where remnant armoring material inhibits sublimation yield localized preservation of the underlying substrate, producing the isolated mesas observed in some marginal pits.

This sublimation-driven formation mechanism necessarily implies that pedestal craters represent the remnants of a formerly extensive ice/snow layer deposited during a period of higher obliquity. Depending on the age of specific pedestal craters and the rate of sublimation through the pedestal surface, it is likely that volatile-rich material is still preserved underneath many of the armored pedestal crater surfaces [*Kadish et al.*, 2008]. The population density and distribution of pedestal craters identified in this study (Figure 1) suggest that this ice-rich deposit persisted for a significant part of the recent past. For this to be the case, the obliquity of Mars must have been relatively higher than at present during parts of the Amazonian, which is consistent with models of past martian obliquity [*Laskar et al.*, 2004].

5. Conclusions

On the basis of the above findings, we draw the following conclusions about the nature of pedestal craters, and the implications they have for martian climate change:

1) The distribution of 2696 pedestal craters identified in this study is non-random (Figures 1 and 2), occurring in the northern hemisphere almost exclusively poleward of 33°N, with the majority between 45° and 60°N latitude, where 60° represents the latitudinal poleward extent of our survey area. In the southern hemisphere they occur almost exclusively poleward of 40°S. This distribution is highly correlated with the distribution of ice-rich material predicted by climate models at higher obliquity [e.g., *Jakosky et al.*, 1995; *Richardson and Wilson*, 2002; *Mischna et al.*, 2003]. The pedestal crater population also mimics the distribution of a number of morphologies indicative of the presence of an ice-rich substrate at mid latitudes during periods of higher obliquity.

2) The consistently high P/C ratios, revealing that pedestals extend, on average, to a distance of >3 crater radii, and low Γ values, confirming the extreme circularity of the pedestals, support an armoring mechanism that can indurate the surface proximal to the impact to a distance greater than the extent of the ejecta, and that is radially symmetric. The necessity for a far-reaching armoring mechanism is further supported by examples of pedestal craters that have their ejecta deposits completely superposed on their respective pedestal surfaces. Although we have not proven any of the armoring mechanisms discussed in this paper, our geomorphological analyses are consistent with propagation of an impact-induced, symmetrical, atmospheric blast followed by a high temperature thermal pulse [*Wrobel et al.*, 2006]. In this scenario, when an impact occurs into the ice-rich target material, the top few centimeters of the layer are desiccated and indurated, yielding the armored surfaces necessary to form anomalously large, circular pedestals via sublimation of volatiles from the intercrater terrain.

3) The generally small size range of pedestal craters suggests a delicate balance between crater size and the formation of this unique morphology; ejecta from larger craters may overwhelm the volatile substrate layer [Barlow *et al.*, 2001]. Volatiles buried beneath the ejecta of the larger craters may explain the anomalously high crater ejecta volumes observed in related crater morphologies [Garvin *et al.*, 2000; Boyce *et al.*, 2005; Meresse *et al.*, 2006; Black and Stewart, 2008].

4) Our observations strongly support a sublimation-driven formation mechanism for mid-latitude pedestal craters that does not require the role of eolian deflation, which in the past has been a critical aspect of hypotheses for pedestal crater formation. In our model, pedestal craters result from projectiles impacting into a target substrate consisting of a volatile-rich dust/snow/ice layer tens to hundreds of meters thick, overlying a dominantly fragmental silicate regolith. This material is deposited at mid latitudes during periods of higher obliquity. The proximal area becomes armored during the impact process. Climate change from a return to lower obliquity leads to sublimation and removal of the volatile-rich layer from the intercrater plains, which migrates poleward. This lowers the elevation of the regional terrain down to the underlying fragmental silicate-rich regolith, leaving generally circular pedestal craters elevated with armored surfaces overlying the preserved ice-rich material.

5) The characteristics of pedestal craters with pitted margins, interpreted to be sublimation pits, strongly support the current presence of volatiles below the armored surfaces of the pedestals [Kadish *et al.*, 2008].

6) These data and interpretations imply that during the Amazonian, significant climate change occurred. Examples of overlapping pedestal craters show that the

deposition of decameters-thick, latitude-dependent, ice-rich layers has recurred numerous times. The armored surfaces of pedestal craters have therefore preserved a distinctive, accessible record of Amazonian climate history in the form of ice-rich, potentially layered deposits at the surface of Mars.

We are currently: 1) assessing regional variations in the properties of pedestal craters in order to understand the distribution of ancient volatile-rich layers [*Barlow and Perez, 2003*], 2) further analyzing the size-frequency distribution of pedestal craters to constrain the timing of these latitude-dependent volatile-rich layers, 3) targeting prominent pedestal craters with the SHARAD radar instrument [*Phillips et al., 2008*] in order to test for the presence and structure of the proposed volatile-rich deposits, and 4) examining the relationships of these craters to related, sublimation-derived, crater morphologies to assess the links between pedestal formation and the production of perched craters and excess ejecta craters.

Acknowledgments

Initial work on this topic by SJK was supported by the NSF Research Experiences for Undergraduates program at Northern Arizona University (NSF award AST-0453611).

We gratefully acknowledge financial support from the Mars Data Analysis Program (grants NNG04GJ99G and NNX07AN95G to JWH and NAG512510 to NGB), the Mars Fundamental Research Program (grant NNG05GM14G to NGB), and the NASA Mars Express HRSC Guest Investigator Program (to JWH).

References

Aharonson, O., M. T. Zuber, G. A. Neumann, and J. W. Head (1998), Mars: Northern hemisphere slopes and slope distributions, *Geophys. Res. Lett.*, *25*, 4413-4416.

Arvidson, R. E., M. Coradini, A. Carusi, A. Coradini, M. Fulchignoni, C. Federico, R. Funicello, and M. Salomone (1976), Latitudinal variation of wind erosion of crater ejecta deposits on Mars, *Icarus*, *27*(4), 503-516.

Arvidson, R. E., E. Guinness, and S. Lee (1979), Differential aeolian redistribution rates on Mars, *Nature*, *278*, 533-535.

Baker, V. R., R. G. Strom, V. C. Gulick, J. S. Kargel, G. Komatsu, and V. S. Kale (1991), Ancient oceans, ice sheets, and the hydrological cycles on Mars, *Nature*, *352*, 589-594.

Barlow, N. G. (1993), Increased depth-diameter ratios in the Medusae Fossae Formation deposits of Mars, *Lunar Planet. Sci. [CD-ROM]*, *XXIV*, 61-62.

Barlow, N. G. (1994), Sinuosity of Martian rampart ejecta deposits, *J. Geophys. Res.*, *99*(E5), 10927-10935.

Barlow, N. G. (2004), Martian subsurface volatile concentrations as a function of time: Clues from layered ejecta craters, *Geophys. Res. Lett.*, *31*, L05703, doi:10.1029/2003GL019075.

Barlow, N. G. (2006), Impact craters in the northern hemisphere of Mars: Layered ejecta and central pit characteristics, *Meteorit. Planet. Sci.*, *41*, 1425-1436.

Barlow, N. G., and C. B. Perez (2003), Martian impact crater ejecta morphologies as indicators of the distribution of subsurface volatiles, *J. Geophys. Res.*, *108*(E8), 5085, doi:10.1029/2002JE002036.

Barlow, N. G., J. M. Boyce, F. M. Costard, R. A. Craddock, J. B. Garvin, S. E. H. Sakimoto, R. O. Kuzmin, D. J. Roddy, and L. A. Soderblom (2000), Standardizing the nomenclature of Martian impact crater ejecta morphologies, *J. Geophys. Res.*, *E5*(E11), 26733-26738.

Barlow, N. G., J. Koroshetz, and J. M. Dohm (2001), Variations in the onset diameter for Martian layered Ejecta morphologies and their implications for subsurface volatile reservoirs, *Geophys. Res. Lett.*, *28*(16), 3095-3098.

Barnouin-Jha, O. S., and P. H. Schultz (1996), Ejecta entrainment by impact-generating ring vortices: Theory and experiments, *J. Geophys. Res.*, *101*(E9), 21099-21115.

Barnouin-Jha, O. S., and P. H. Schultz (1998), Lobateness of impact ejecta deposits from atmospheric interactions, *J. Geophys. Res.*, *103*(E11), 25739-25756.

Black, B. A., and S. T. Stewart (2008), Excess ejecta craters record episodic ice-rich layers at middle latitudes on Mars, *J. Geophys. Res.*, *113*, E02015, doi:10.1029/2007JE002888.

Boyce, J. M., P. Mouginis-Mark, and H. Garbeil (2005), Ancient oceans in the northern lowlands of Mars: Evidence from impact crater depth/diameter relationships, *J. Geophys. Res.*, *110*, E03008, doi:10.1029/2004JE002328.

Boynton, W. V., et al. (2002), Distribution of hydrogen in the near surface of Mars: Evidence for subsurface ice deposits, *Science*, *297*, 81-85.

Bradley, B. A., S. E. H. Sakimoto, H. Frey, and J. Zimbelman (2002), Medusae Fossae Formation: New perspectives from Mars Global Surveyor, *J. Geophys. Res.*, *107*, 5058, doi:10.1029/2001JE001537.

Christensen, P. R. (1986), Regional dust deposits on Mars: Physical properties, age, and history, *J. Geophys. Res.*, *97*, 13103-13144.

Clifford, S. M., and T. J. Parker (2001), The evolution of the Martian hydrosphere: Implications for the fate of a primordial ocean and the current state of the northern plains, *Icarus*, *154*, 40-79.

- Costard, F. M. (1989), The spatial distribution of volatiles in the Martian hydrolithosphere, *Earth Moon Planets*, 45, 265-290.
- Costard, F. M., and J. S. Kargel (1995), Outwash plains and thermokarst on Mars, *Icarus*, 114(1), 93-112.
- Fanale, F. P., J. R. Salvail, A. P. Zent, and S. E. Postawko (1986), Global distribution and migration of the subsurface ice on mars, *Icarus*, 67, 1-18.
- Farmer, C. B., D. W. Davies, A. L., Holland, D. D. Laporte, and P. E. Doms (1977), Mars – Water vapor observations from the Viking orbiters, *J. Geophys. Res.*, 82, 4225-4248.
- Feldman, W. C., et al. (2002), Global distribution of neutrons from Mars: Results from Mars Odyssey, *Science*, 297, 75-78.
- Feldman, W. C., J. W. Head, S. Maurice, T. H. Prettyman, R. C. Elphic, H. O. Funsten, D. J. Lawrence, R. L. Tokar, and D. T. Vaniman (2004a), Recharge mechanism of near-equatorial hydrogen on Mars: Atmospheric redistribution or sub-surface aquifer, *Geophys. Res. Lett.*, 31, L18701, doi:10.1029/2004GL020661.
- Feldman, W. C. et al. (2004b), Global distribution of near-surface hydrogen on Mars, *J. Geophys. Res.*, 109, E09006, doi:10.1029/2003JE002160.

Feldman, W. C., T. H. Prettyman, S. Maurice, S. Nelli, R. Elphic, H. O. Funsten, O. Gasnault, D. J. Lawrence, J. R. Murphy, R. L. Tokar, and D. T. Vaniman (2005), Topographic control of hydrogen deposits at low latitudes to midlatitudes of Mars, *J. Geophys. Res.*, *110*, E11009, doi:10.1029/2005JE002452.

Forget, F., F. Hourdin, R. Fournier, C. Hourdin, O. Talagrand, M. Collins, S. R. Lewis, P. L. Read, and J. Huot (1999), Improved general circulation models of the martian atmosphere from the surface to above 80 km, *J. Geophys. Res.*, *104*, 24155-24176.

Fedorova, A., O. Korablev, J. Bertaux, A. Rodin, A. Kiselev, and S. Perrier (2006), Mars water vapor abundance from SPICAM IR spectrometer: Seasonal and geographic distributions, *J. Geophys. Res.*, *111*, E09S08, doi:10.1029/2006JE002695.

Garvin, J. B., S. E. H. Sakimoto, J. J. Frawley, and C. Schnetzler (2000), North polar region craterforms on Mars: Geometric characteristics from the Mars Orbiter Laser Altimeter, *Icarus*, *144*, 329-352.

Greeley, R., R. O. Kuzmin, and R. M. Haberle (2001), Aeolian processes and their effects on understanding the chronology of Mars, *Space Sci. Rev.*, *96*, 393-404.

Grimm, R. E., and S. C. Solomon (1986), Tectonic tests of proposed polar wander paths for Mars and the Moon, *Icarus*, *65*, 110-121.

Haberle, R. M., J. B. Pollack, J. R. Barnes, R. W. Zurek, C. B. Leovy, J. R. Murphy, H. Lee, and J. Schaeffer (1993), Mars atmospheric dynamics as simulated by the NASA Ames General Circulation Model. I - The zonal-mean circulation, *J. Geophys. Res.*, *98*, 3093-3123.

Haberle, R. M., J. R. Murphy, and J. Schaeffer (2003), Orbital change experiments with a Mars general circulation model, *Icarus*, *161*, 66-89.

Hartmann, W. K. (1966), Martian cratering, *Icarus*, *5*, 565-576.

Hartmann, W. K. (2005), Martian cratering 8: Isochron refinement and the chronology of Mars, *Icarus*, *174*, 294-320.

Hartmann, W. K., and G. Neukum (2001), Cratering chronology and the evolution of Mars, *Space Sci. Rev.*, *96*, 165-194.

Head, J. W. (2000), Ancient polar deposits in the equatorial region of Mars: Tests using MOLA data, *Eos Transactions AGU*, *81*, Spring Meeting Supplement, P42A-10.

Head, J. W., and M. Kreslavsky (2004), Medusae Fossae Formation: Ice-Rich airborne dust deposited during periods of high obliquity?, *Lunar Planet. Sci. [CD-ROM]*, XXXV, Abstract 1635.

Head, J. W., and R. Roth (1976), Mars pedestal crater escarpments: Evidence for ejecta-related emplacement, *Symposium on Planetary Cratering Mechanics: LPI contribution* 259, 50-52.

Head, J. W., M. A. Kreslavsky, and S. Pratt (2002), Northern lowlands of Mars: Evidence for widespread volcanic flooding and tectonic deformation in the Hesperian Period, *J. Geophys. Res.*, 107, 5004, doi:10.1029/2000JE001445.

Head, J. W., J. F. Mustard, M. A. Kreslavsky, R. E. Miliken, and D. R. Marchant (2003), Recent ice ages on Mars, *Nature*, 426, 797-802.

Head, J. W., et al. (2005), Tropical to mid-latitude snow and ice accumulation, flow and glaciation on Mars, *Nature*, 434, 346-351.

Howard, A. D. (1978), Origin of the stepped topography of the Martian poles, *Icarus*, 34, 581-599.

Hynek, B. M., R. J. Phillips, and R. E. Arvidson (2003), Explosive volcanism in the Tharsis region: Global evidence in the Martian geologic record, *J. Geophys. Res.*, 108, 5111, doi:10.1029/2003JE002062.

Jakosky, B. M. (1983), The role of seasonal reservoirs in the Mars water cycle: I. Seasonal exchange of water with the regolith, *Icarus*, 55, 1-18.

Jakosky, B. M., B. G. Henderson, and M. T. Mellon (1995), Chaotic obliquity and the nature of the Martian climate, *J. Geophys. Res.*, *100*(E1), 1579-1584.

Kadish, S. J., and N. G. Barlow (2006), Pedestal crater distribution and implications for a new model of formation, *Lunar Planet. Sci. [CD-ROM]*, *XXXVII*, Abstract 1254.

Kadish, S. J., J. W. Head, N. G. Barlow, and D. R. Marchant (2008), Martian pedestal craters: Marginal sublimation pits implicate a climate-related formation mechanism, *Geophys. Res. Lett.*, *35*, L16104, doi:10.1029/2008GL034990.

Kargel, J. S. (1986), Morphologic variations of Martian rampart crater ejecta and their dependencies and implications, *Lunar Planet. Sci. [CD-ROM]*, *XVII*, Abstract 28.

Kargel, J. S., and F. M. Costard (1993), Possible occurrence and origin of massive ice in Utopia Planitia, *Workshop on the Martian Northern Plains: Sedimentological, Periglacial, and Paleoclimatic Evolution*, 7-8.

Kieffer, S. W., and C. H. Simonds (1980), The role of volatiles and lithology in the impact cratering process, *Rev. Geophys.*, *18*(1), 143-181.

Kreslavsky, M. A., and J. W. Head (2000), Kilometer-scale roughness of Mars – Results from MOLA data analysis, *J. Geophys. Res.*, *105*(E11), 26695-26712.

Kreslavsky, M. A., and J. W. Head (2002), Fate of outflow channel effluents in the northern lowlands of Mars: The Vastitas Borealis Formation as a sublimation residue from frozen ponded bodies of water, *J. Geophys. Res.*, *107*, 5121, doi:10.1029/2001JE001831.

Larson, S. K. (2007), The origins of four paterae of Malea Planum, Mars, M.S. thesis, 130 pp., Brigham Young University, Provo, UT.

Laskar, J., A. C. M. Correia, M. Gastineau, F. Joutel, B. Levrard, and P. Robutel (2004), Long term evolution and chaotic diffusion of the insolation quantities of Mars, *Icarus*, *170*(2), 343-364.

Lefort, A., P. Russell, and N. Thomas (2005), Ice sublimation landforms in Peneus and Amphitrites Patera, *Lunar Planet. Sci. [CD-ROM]*, XXXVI, Abstract 1626.

Lefort, A., P. Russell, and N. Thomas (2006), Scallop-shaped depressions and mantle sublimation in the mid-latitudes of Mars, *Fourth Mars Polar Science Conference*, Abstract 8061.

Lefort, A., P. Russell, N. Thomas, and the HiRISE Team (2007), Scalloped terrains in Utopia Planitia, insight from HiRISE, *Lunar Planet. Sci. [CD-ROM]*, XXXVIII, Abstract 1796.

Levrard, B., F. Forget, F. Montmessin, and J. Laskar (2004), Recent ice-rich deposits formed at high latitudes on Mars by sublimation of unstable equatorial ice during low obliquity, *Nature*, *431*, 1072-1075.

Levrard, B., F. Forget, F. Montmessin, and J. Laskar (2007), Recent formation and evolution of northern Martian polar layered deposits as inferred from a Global Climate Model, *J. Geophys. Res.*, *112*, E06012, doi:10.1029/2006JE002772.

Levy, J. S., and J. W. Head (2005), Evidence for remnants of ancient ice-rich deposits: Mangala Valles outflow channel, Mars, *Terra Nova*, *17*(6), 503-509.

Marchant, D. R., and J. W. Head (2007), Antarctic dry valleys: Microclimate zonation, variable geomorphic processes, and implications for assessing climate change on Mars, *Icarus*, *192*, 187-222.

Marchant, D. R., A. R. Lewis, W. M. Phillips, E. J. Moore, R. A. Souchez, G. H. Denton, D. E. Sugden, N. Potter Jr., and G. P. Landis (2002), Formation of patterned ground and sublimation till over Miocene glacier ice in Beacon Valley, southern Victoria Land, Antarctica, *Geol. Soc. Am. Bull.*, *114*, 718-730.

McCauley, J. F. (1973), Mariner 9 Evidence for Wind Erosion in the Equatorial and Mid-latitude Regions of Mars, *J. Geophys. Res.*, *78*, 4123-4137.

Mellon, M. T. and B. M. Jakosky (1993), Geographic variations in the thermal and diffusive stability of ground ice on Mars, *J. Geophys. Res.* *98*, 3345-3364.

Mellon, M. T. and B. M. Jakosky (1995), The distribution and behavior of Martian ground ice during past and present epochs, *J. Geophys. Res.*, *100*, 11781-11799.

Mellon, M. T., B. M. Jakosky, and S. E. Postawko (1997), The persistence of equatorial ground ice on Mars, *J. Geophys. Res.*, *102*, 19357-19369.

Mellon, M. T., W. C. Feldman, and T. H. Prettyman (2004), The presence and stability of ground ice in the southern hemisphere of Mars, *Icarus*, *169*, 324-340.

Meresse, S., F. Costard, N. Mangold, D. Baratoux, and J. M. Boyce (2006), Martian perched craters and large ejecta volume: Evidence for episodes of deflation in the northern lowlands, *Meteorit. Planet. Sci.*, *41*, 1647-1658.

Milliken, R. E., J. F. Mustard, and D. L. Goldsby (2003), Viscous flow features on the surface of Mars: Observations from high-resolution Mars Orbiter Camera (MOC) images, *J. Geophys. Res.*, *108*, 5057, doi: 10.1029/2002JE002005.

Mischna, M. A., and M. I. Richardson (2005), A reanalysis of water abundances in the Martian atmosphere at high obliquity, *Geophys. Res. Lett.*, *32*, L03201, doi:10.1029/2004GL021865.

Mischna, M. A., M. I. Richardson, R. J. Wilson, and D. J. McCleese (2003), On the orbital forcing of Martian water and CO₂ cycles: A general circulation model study with simplified volatile schemes, *J. Geophys. Res.*, *108*, 5062, doi: 10.1029/2003JE002051.

Mitrofanov, I., et al. (2002), Maps of subsurface hydrogen from the high energy neutron detector, Mars Odyssey, *Science*, *297*, 78-81.

Moore, J. M., M. T. Mellon, and A. P. Zent (1996), Mass wasting and ground collapse in terrains of volatile-rich deposits as a solar system-wide geological process: The pre-Galileo view, *Icarus*, *122*(1), 63-78.

Morgenstern, A., E. Hauber, D. Reiss, S. van Gasselt, G. Grosse, and L. Schirrmeyer (2007), Deposition and degradation of a volatile-rich layer in Utopia Planitia and implications for climate history on Mars, *J. Geophys. Res.*, *112*, E06010, doi:10.1029/2006JE002869.

Mouginis-Mark, P. (1979), Martian fluidized crater morphology – Variations with crater size, latitude, altitude, and target material, *J. Geophys. Res.*, *84*, 8011-8022.

Mouginis-Mark, P. (1987), Water or ice in the Martian regolith? Clues from rampart craters seen at very high resolution, *Icarus*, 71, 268-286.

Mustard, J. F., C. D. Cooper, and M. K. Rifkin (2001), Evidence for recent climate change on Mars from the identification of youthful near-surface ground ice, *Nature*, 412, 411-414.

Mutch, P., and A. Woronow (1980), Martian rampart and pedestal craters' ejecta-emplacement: Coprates quadrangle, *Icarus*, 41(2), 259-268.

Neukum G., B. A. Ivanov, and W. K. Hartmann (2001), Cratering records in the inner solar system in relation to the Lunar reference system, in *Chronology and Evolution of Mars*, edited by R. Kallenbach, J. Geiss, and W. K. Hartmann, pp. 87-104, International Space Science Institute, Bern.

Osinski, G. R. (2006), Effect of volatiles and target lithology on the generation and emplacement of impact crater fill and ejecta deposits on Mars, *Meteorit. Planet. Sci.*, 41(10), 1571-1586.

Parker, T. J., R. S. Saunders, and D. M. Schneeberger (1989), Transitional morphology in West Deuteronilus Mensae, Mars: Implications for modification of the Lowland/Upland boundary, *Icarus*, 82, 111-145.

Paterson, W. B. (1994), *The Physics of Glaciers*, 3rd ed., 250 pp., Pergamon Press, New York.

Phillips, R. J. et al. (2008), Mars north polar deposits: Stratigraphy, age, and geodynamical response, *Science*, *320*, 1182-1185.

Richardson, M. I., and R. J. Wilson (2002), Investigation of the nature and stability of the Martian seasonal water cycle with a general circulation model, *J. Geophys. Res.*, *107*, doi: 10.1029/2001JE001536.

Rybakov, V. A., I. V. Nemtchinov, V. V. Shuvalov, V. I. Artemiev, and S. A. Medveduk (1997), Mobilization of dust on the Mars surface by the impact of small cosmic bodies, *J. Geophys. Res.*, *102*(E4), 9211-9220.

Schultz, P. H. (1992), Atmospheric effects on ejecta emplacement, *J. Geophys. Res.*, *97*(E7), 11623-11662.

Schultz P. H., and D. E. Gault (1979), Atmospheric effects on Martian ejecta emplacement, *J. Geophys. Res.*, *84*, 7669-7687.

Schultz, P. H., and A. B. Lutz (1988), Polar wandering of Mars, *Icarus*, *73*, 91-141.

Schultz, P. H., and J. F. Mustard (2004), Impact melts and glasses on Mars, *J. Geophys. Res.*, *109*, E01001, doi:10.1029/2002JE002025.

Scott, D. H., and K. L. Tanaka (1982), Ignimbrites of Amazonis Planitia region of Mars, *J. Geophys. Res.*, *87*, 1179-1190.

Skorov, Y. V., W. J. Markiewicz, A. T. Basilevsky, and H. U. Keller (2001), Stability of water ice under a porous nonvolatile layer: implications to the south polar layered deposits of Mars, *Planet. Space Sci.*, *49*, 59-63.

Smith, D. E., et al. (1999), The Global topography of Mars and Implications for Surface Evolution, *Science*, *284*, 1495-1503.

Smith, M. D. (2002), The annual cycle of water vapor on Mars as observed by the Thermal Emission Spectrometer, *J. Geophys. Res.*, *107*, 5115, doi:10.1029/2001JE001522.

Smith, M. D. (2004), Interannual variability in TES atmospheric observations of Mars during 1999-2003, *Icarus*, *167*, 148-165.

Soare, R. J., J. S. Kargel, G. R. Osinski, and F. M. Costard (2007), Thermokarst processes and the origin of crater-rim gullies in Utopia and western Elysium Planitia, *Icarus*, *191*(1), 95-112.

Sprague, A. L., D. M. Hunten, L. R. Doose, R. E. Hill, W. V. Boynton, M. D. Smith, and J. C. Pearl (2006), Mars atmospheric water vapor abundance: 1991-1999, emphasis 1998-1999, *Icarus*, *184*, 372-400.

Stewart, S. T., and T. J. Ahrens (2005), Shock properties of H₂O ice, *J. Geophys. Res.*, *110*, E03005, doi:10.1029/2004JE002305.

Tanaka, K. L. (2000), Dust and ice deposition in the Martian geologic record, *Icarus*, *144*, 254-266.

Tanaka, K. L. (2005), Geology and insolation-driven climatic history of Amazonian north polar materials on Mars, *Nature*, *437*, 991-994.

Tanaka, K. L., J. A. Skinner Jr., and T. M. Hare (2005), Geologic map of the northern plains of Mars, *U.S. Geol. Surv. Sci. Invest. Ser.*, *Map 2888*.

Tanaka, K. L., and D. H. Scott (1987), Geologic map of the polar regions of Mars, *U.S. Geol. Surv. Misc. Invest. Ser. Map I-1802-C*.

Tanaka, K. L., J. A. Skinner Jr., T. M. Hare, T. Joyal, and A. Wenker (2003), Resurfacing history of the northern plains of Mars based on geologic mapping of Mars Global Surveyor data, *J. Geophys. Res.*, *108*(E4), 8043, doi:10.1029/2002JE001908.

Tornabene, L. L., A. S. McEwen, G. R. Osinski, P.J. Mougini-Mark, J. M. Boyce, R. M. E. Williams, J. J. Wray, J. A. Grant, and the HiRISE Team (2007), Impact melting and the role of subsurface volatiles: Implications for the formation of valley networks and phyllosilicate-rich lithologies on early Mars, *Seventh International Conference on Mars*, Abstract 3288.

Touma, J., and J. Wisdom (1993), The chaotic obliquity of the planets, *Science*, 259, 1294-1297.

Wada, K., and O. Barnouin-Jha (2006), The formation of fluidized ejecta on Mars by granular flows, *Meteorit. Planet. Sci.*, 41(10), 1551-1569.

Watters, T. R., et al. (2007), Radar sounding of the Medusae Fossae Formation Mars: Equatorial ice or dry, low-density deposits?, *Science*, 318, 1125-1128.

Wrobel, K., P. H. Schultz, and D. Crawford (2006), An atmospheric blast/thermal model for the formation of high-latitude pedestal craters, *Meteorit. Planet. Sci.*, 41(10), 1539-1550.

Zanetti, M., H. Hiesinger, D. Reiss, E. Hauber, and G. Neukum (2008), Scalloped depressions in Malea Planum, Southern Hellas Basin, Mars, *Lunar Planet. Sci. [CD-ROM]*, XXXIX, Abstract 1682.

Tables

Table 1. Pedestal crater concentration as a function of latitude.

Center of 5° Latitude Band (°N)	Number of Pedestal Craters	Number of Pedestal Craters per km ²
-57.50	366	1.08x10 ⁻⁴
-52.50	154	4.00x10 ⁻⁵
-47.50	62	1.45x10 ⁻⁵
-42.50	26	5.58x10 ⁻⁶
-37.50	2	3.99x10 ⁻⁷
-32.50	0	0
-27.50	0	0
-22.50	0	0
-17.50	0	0
-12.50	0	0
-7.50	0	0
-2.50	4	6.33x10 ⁻⁷
2.50	15	2.38x10 ⁻⁶
7.50	30	4.79x10 ⁻⁶
12.50	15	2.43x10 ⁻⁶
17.50	0	0
22.50	0	0
27.50	0	0
32.50	4	7.50x10 ⁻⁷
37.50	38	7.58x10 ⁻⁶
42.50	186	3.99x10 ⁻⁵
47.50	419	9.81x10 ⁻⁵
52.50	630	1.64x10 ⁻⁴
57.50	745	2.19x10 ⁻⁴

Table 2. Pedestal crater attributes. Because pedestal craters with diameters less than 0.7 km were identified but not included in this study, the mean diameter for mid-latitude pedestal craters without marginal pits is specified as less than 2 km.

Type of Pedestal Crater	Mean Diameter	Mean Pedestal Height	Mean Pedestal Circularity	Mean Pedestal to Crater Radius Ratio
Non-Pitted, Mid to High Latitude	<2 km	~50m	1.10	3.09
Equatorial (Medusae Fossae Formation)	2.1 km	~200 m	1.64	5.36
Pedestals with Marginal Pits	5.1 km	~100 m	1.06	5.62

Table 3. Mean pedestal crater attributes with standard deviations as a function of latitude.

Center of 5° Latitude Band (°N)	Mean Diameter (km)	Standard Deviation	Pedestal Circularity	Standard Deviation	Pedestal to Crater Radius Ratio	Standard Deviation
-67.50	1.26	0.39	1.10	0.07	2.68	0.77
-62.50	1.39	0.72	1.11	0.06	3.03	1.11
-57.50	1.56	0.67	1.10	0.07	2.35	0.83
-52.50	1.75	0.60	1.09	0.07	2.24	0.74
-47.50	1.70	0.57	1.07	0.03	2.23	0.75
-42.50	1.66	0.46	1.08	0.06	2.44	0.90
0.00	2.08	1.25	1.63	0.43	5.36	3.61
37.5	2.02	0.91	1.10	0.06	2.09	0.93
42.5	1.37	0.47	1.10	0.09	3.44	1.37
47.5	1.25	0.45	1.09	0.09	3.30	1.12
52.5	1.25	0.42	1.10	0.09	3.25	1.24
57.5	1.33	0.61	1.12	0.13	3.25	1.04
62.50	1.16	0.21	1.07	0.03	3.06	1.12

Figure Captions

Figure 1 – The geographic distribution of non-pitted pedestal craters (black circles) and pedestal craters with marginal pits (white circles) between $\sim 60^{\circ}\text{N}$ and 65°S on Mars.

Pedestal craters with marginal pits were found in Utopia Planitia (UP) and Malea Planum (MP). The Medusae Fossae Formation (Medusae Fossae Formation) hosted the only population of equatorial pedestal craters.

Figure 2 – Histogram of the pedestal crater latitudinal distribution seen in Figure 1. The northern hemisphere has more than three times as many pedestal craters as the southern hemisphere over the latitudes surveyed. The number of pedestal craters increases as latitude increases. The values of craters/ km^2 , which account for changes in the areas of the latitudinal bands, are shown in Table 1.

Figure 3 – Histograms showing the longitudinal distribution of pedestal craters globally, and within each hemisphere. These emphasize the concentration of pedestal craters between 60° and 180°E in the northern hemisphere (Utopia Planitia) and between 0 and 120°E in the southern hemisphere (Malea Planum). There is a paucity of pedestal craters located in both hemispheres between -150° and 330°E .

Figure 4 – (A) A mosaic of THEMIS IR imagery, with intervening MOLA hillshade data, in Utopia Planitia (101°E , 58°N), displaying a typical pedestal crater field. Black boxes denote the locations of the enlarged regions in parts B-D. (B) Pedestals with very low Γ values. Marginal pits can be readily identified around two pedestal craters on the right-

hand side of the image. (C) Although pedestals are generally circular, this image shows some examples which have sinuous, irregularly-shaped perimeters. (D) A larger area showing additional variation in pedestal size and circularity.

Figure 5 – Examples of typical pedestal craters, shown in THEMIS VIS data with MOLA altimetry data. Each image has a MOLA track consisting of the shot data, corresponding to a topographic profile seen in Figure 6. These small craters are roughly circular in planform and have crater diameters <2.5 km. The pedestals have relatively smooth, flat tops with well-defined marginal scarps (A) A subscene of V21963008 (58.6°N , 110.7°E). (B) A subscene of V13575007 (41.6°N , 153.4°E). (C) A subscene of V18359003 (56.9°S , 43.7°E). (D) A subscene of V19230010 (55.8°N , 107.4°E).

Figure 6 – The topographic profiles for the pedestal craters shown in Figure 5, with visible data points corresponding to the MOLA shot data. Vertical exaggerations for each of the profiles are: A = 65x, B = 55x, C = 50x, D = 47x. Pedestal heights vary from ~ 50 to 75 m. Pedestal surfaces are extremely flat, with slopes generally $<1^{\circ}$, and pedestal scarps have slopes of $<5^{\circ}$. In all cases, the crater cavity is entirely above the elevation of the surrounding plains. In some cases (A and D), infilling of the crater bowl or lowering of the pedestal surface causes the crater floor to be above the height of most of the surrounding pedestal as well.

Figure 7 – Histograms showing the distribution of three pedestal crater attributes: (A) crater diameter, (B) pedestal circularity (Γ), and (C) pedestal to crater radius (P/C) ratio.

For crater diameters, the mode is 1.10 km, with a mean of 1.37 km and a standard deviation of 0.57 km. For Γ values, the mode is 1.04, with a mean of 1.10 and a standard deviation of 0.11. For P/C ratios, the mode is 2.00, with a mean of 3.09 and a standard deviation of 1.22. For each attribute, the values are shown for two pedestal craters, selected to show variation in pedestal morphology. The top crater is in the southern hemisphere, and the bottom is in the Medusae Fossae Formation.

Figure 8 – Graphs showing the latitudinal trends in pedestal crater attributes. Data points represent 5° latitudinal bins. The equatorial data point in each graph represents the Medusae Fossae Formation pedestal crater population. (A) Crater diameters appear to increase as latitude decreases. This trend is weaker in the northern hemisphere, where the majority of pedestal craters exist. (B) Γ values for mid-latitude pedestal craters are independent of latitude. (C) P/C ratios are consistently higher in the northern hemisphere than in the southern hemisphere, but show no significant trend as a function of latitude. It is important to note that standard deviations are significant for all data points in these graphs, and as such, trends derived from latitudinal changes of the mean values may not be statistically significant. The mean values and standard deviations for these graphs are shown in Table 3.

Figure 9 – Plots of pedestal crater attributes, exploring possible relationships among crater size, pedestal size, and pedestal circularity: (A) Crater diameter versus Γ ($R^2 = 0.039$), (B) Diameter versus P/C ratio ($R^2 = 0.001$), and (C) Γ versus P/C ratio ($R^2 = 0.286$). Most pedestal craters plot in the lower left of each graph. There is no identifiable

correlation between crater diameter and Γ or P/C ratio. There may be a small positive correlation between Γ value and P/C ratio.

Figure 10 – Two examples of pedestal craters with marginal pits, shown in THEMIS VIS data (B) and CTX data (A, D, E), with MOLA altimetry data. Corresponding slope maps, derived from the MOLA data, are shown in parts B and E. Profiles of the craters using MOLA shot data are shown in C and F, with corresponding data points on the images in A and D respectively. The vertical exaggerations are: C = 44x and F = 67x. Both the slope maps and profiles reveal that the tops of the pedestals are remarkably flat – as flat as the smooth surrounding terrain. The pits marking the pedestal margins generally have slopes of less than 7° , although these slopes are difficult to measure given the small size of the pits, and the 300 m spacing between MOLA data points.

Figure 11 – Additional examples of pedestal craters with marginal pits shown in THEMIS VIS data. (A) A subscene of V05726010 (58.5°N , 113.7°E). Pits have formed around most of the pedestal margin, some of which contain isolated mesas. (B) A subscene of V13714004 (56.9°N , 106.9°E). The surface of this pedestal crater is contiguous with the surface of a smaller pedestal crater to the east. The ejecta deposit of the larger pedestal crater is completely superposed on the pedestal surface. Pits are primarily located on the northern and western portions of the pedestal margin. Although both examples have high P/C ratios, the extent of the ejecta deposit can be clearly distinguished in this case, making it readily apparent that the armored surface of the pedestal extends more than twice the distance of the ejecta deposit.

Figure 12 – The pedestal crater distribution (black dots) shown on the water-equivalent hydrogen map, derived from the GRS epithermal neutron data [Feldman *et al.*, 2002]. Pedestal craters are primarily located in green, yellow, red, and grey regions, corresponding to greater than 6 wt% water-equivalent hydrogen in the current environment. The general correlation supports the interpretation that pedestal craters form in regions that are likely to contain ice-rich material at higher obliquities [e.g., Head *et al.*, 2003]. Regions of interest are labeled on the map: Utopia Planitia (UP), Arcadia Planitia (AP), the Medusae Fossae Formation (MFF), and Malea Planum (MP). Meridional profiles and zonal averages showing water-equivalent hydrogen as a function of latitude have been previously published [Feldman *et al.*, 2004a, 2004b, 2005], and the raw neutron fluxes as a function of latitude are also available [Boynton *et al.*, 2002].

Figure 13 – Pedestal craters in the Medusae Fossae Formation, shown in CTX data with MOLA altimetry data, each with a corresponding MOLA profile. These pedestal craters are morphologically distinct from typical pedestal craters at mid and high latitudes, as shown in Figures 4 and 5. (A) A subscene of P06_003253_1875_XI_07N163W (7.7°N, 196.2°E). Note the jagged pedestal perimeter, exemplifying the high Δ values of pedestal craters in the Medusae Fossae Formation. Black boxes in this image denote the locations of enlarged images in Figure 14. (B) A subscene of P06_003556_1895_XI_09N156W (9.3°N, 203.8°E). The pedestal crater is surrounded by a field of yardangs, some of which are contiguous with the pedestal surface. These pedestal craters have high Δ values (2.5 and 1.7 for A and B respectively). The crater in

A has a high P/C ratio (6.9), while that of the crater in B is low (2.6). The profiles of the pedestal craters (C and D) show the anomalously deep crater bowls observed throughout the Medusae Fossae Formation, reaching depths hundreds of meters below the surrounding plains. Despite the large pedestal heights (~150-200 m), no marginal pits are present, and none have been observed on any pedestal margins in the Medusae Fossae Formation.

Figure 14 – (A) Enlarged regions from Figure 13, showing the detailed morphology of pedestals in the Medusae Fossae Formation. The locations of parts C and D are outlined. (B) A section of the south-facing pedestal scarp. Small yardangs are present in the surrounding terrain. (C) Erosion of the pedestal is readily apparent at this scale, with dunes present where the pedestal is being eroded. (D) The pedestal scarp appears to have two distinct tiers here, with dunes at the base of the scarp.

Figure 15 – A size frequency distribution using isochrons from *Hartmann* [2005] for 1,363 pedestal craters in THEMIS IR data releases 1 through 13. Error bars were calculated using the 90% confidence interval from an inverse gamma function. Although a typical size frequency distribution is not appropriate for estimating the age of the pedestal crater population, the data do provide a lower limit for the amount of time necessary to form the observed pedestal crater population. Because we used half of the total number of pedestal craters identified in this study for the size frequency distribution, the best fit (BF) of approximately 50 Myr should be doubled to 100 Myr. The best fit line was determined by assigning an isochron to the data and minimizing the misfit. The

result suggests that it would have taken at least ~100 Myr at higher obliquity (with the ice-rich substrate emplaced at mid latitudes) to form the measured pedestal crater population. On the basis of the modeled obliquity variations by *Laskar et al.* [2004], and the state of preservation of these features, it is likely that this amount of time at high obliquity occurred in the Amazonian period.

Figure 16 – Examples of draped and overlapping pedestal craters shown in THEMIS VIS data. These superposition relationships suggest the formation of pedestal craters from multiple episodes of deposition of an ice-rich substrate, possibly from separate high obliquity periods. (A) A subscene of V09959003. Near the bottom of the image, one pedestal crater is draped over another. The margin of the overlying pedestal curves around the crater rim of the underlying pedestal. Another example of overlapping pedestal craters is visible in the top right of the image. (B) A subscene of V21415004 (57.1°N, 78.5°E). This example shows the limited extent of the rough-textured ejecta deposit superposed on the smooth pedestal surface; the pedestal surface has a greater radial extent than the ejecta deposit in all directions. A small marginal pit exists on its eastern scarp. (C) A mosaic from V18046009 and V18358008 (61.0°S, 71.0°E). The larger crater has marginal pits along its eastern perimeter. The smaller crater is draped over this scarp, truncating one of the pits. (D) A subscene of V20142002 (59.0°N, 80.4°E). Multiple overlapping pedestal craters are visible in this image. Similar to the example in ‘b’, the outline of the ejecta deposit of the largest crater in the scene can be identified, and is completely superposed on the pedestal surface.

Figure 17 – A schematic diagram showing the key steps in our conceptual model for the formation of pedestal craters. This sublimation-driven process is as follows: 1) Impact into a volatile-rich deposit, overlying a fragmental silicate regolith. 2) The impact distributes ejecta and triggers an atmospheric blast followed by a high-temperature thermal pulse, desiccating and indurating the surface proximal to the impact. 3) This armors the surface around the crater beyond the margins of the ejecta deposit. 4) Volatiles sublime from the unarmored intercrater terrain during return to lower obliquity, lowering the elevation of the surrounding terrain, producing a scarp at the edge of the armored crater. Armoring inhibits sublimation from beneath the pedestal surface, resulting in a typical pedestal crater. 5) The scarps of taller pedestal craters, where the armoring has tapered off, receive enhanced insolation. Volatiles underlying the pedestal sublime through the scarp at a faster rate than through the armored surface. 6) This preferential sublimation of ice from the scarp produces marginal pits.

Figure 1

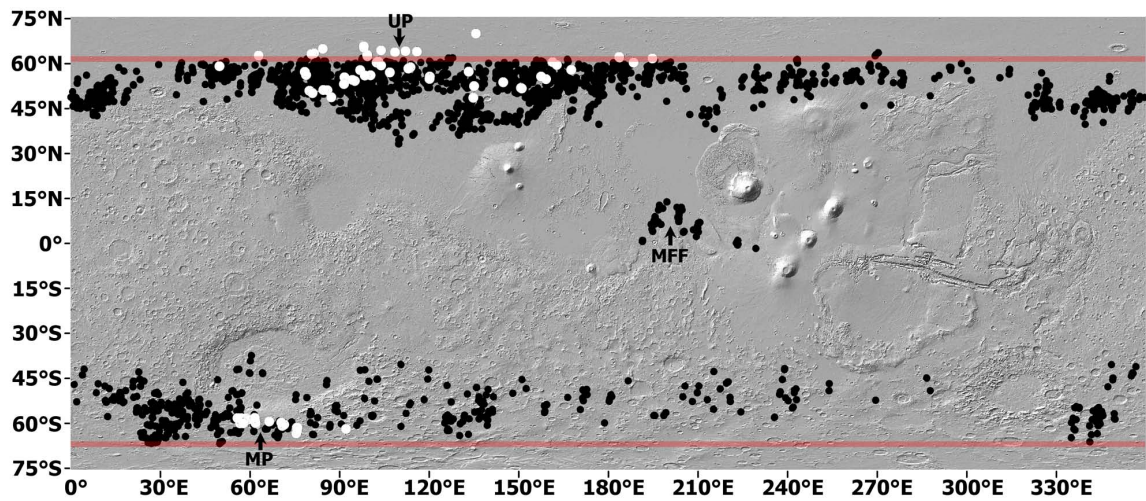


Figure 2

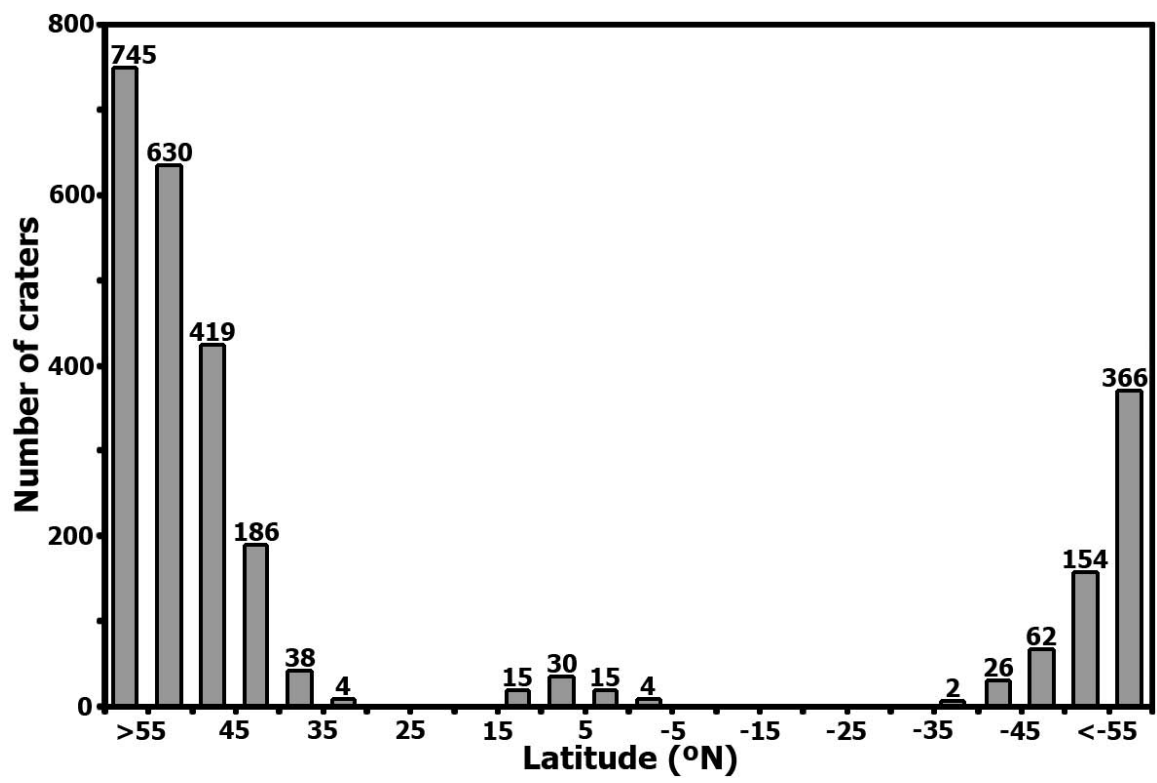


Figure 3

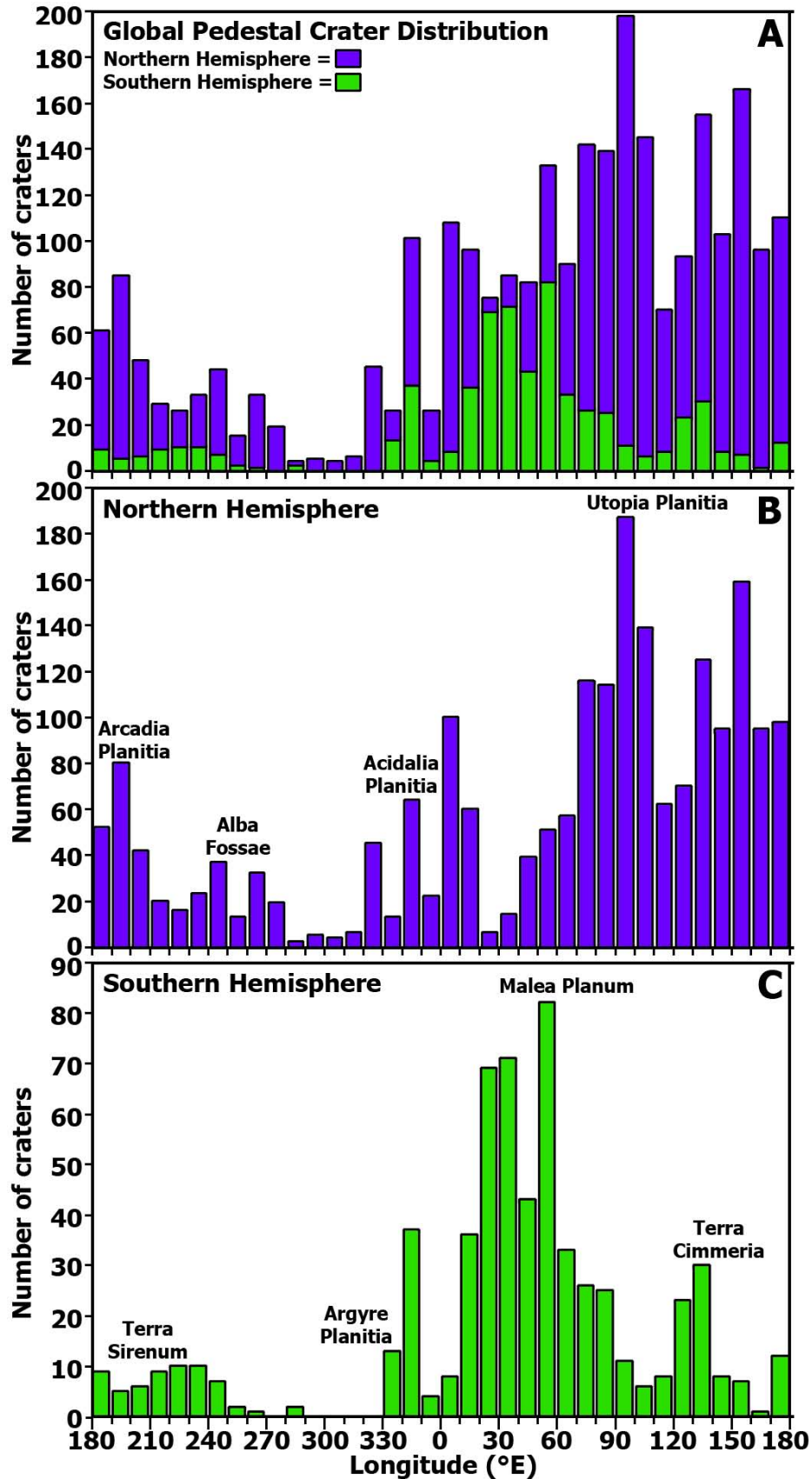


Figure 4

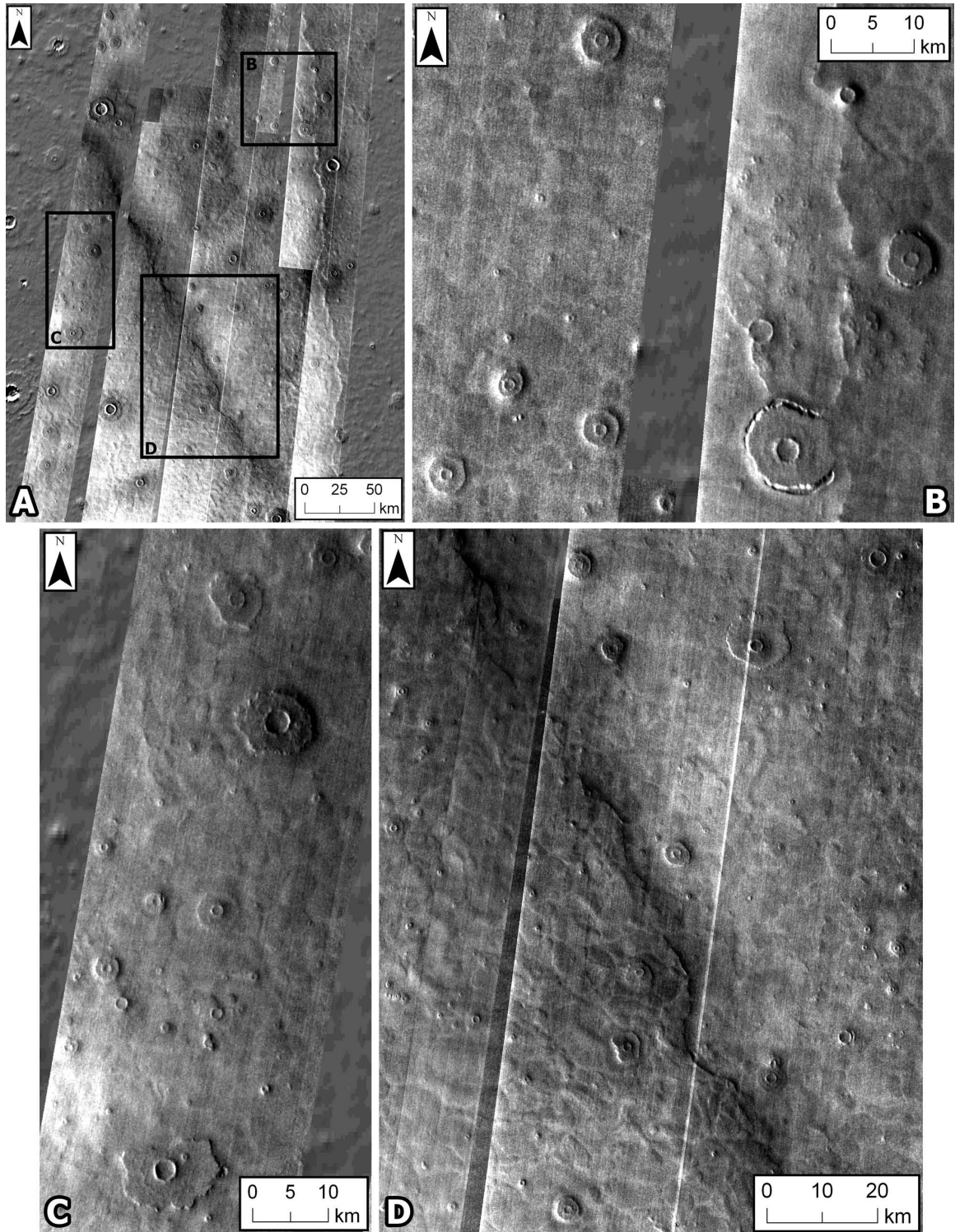


Figure 5

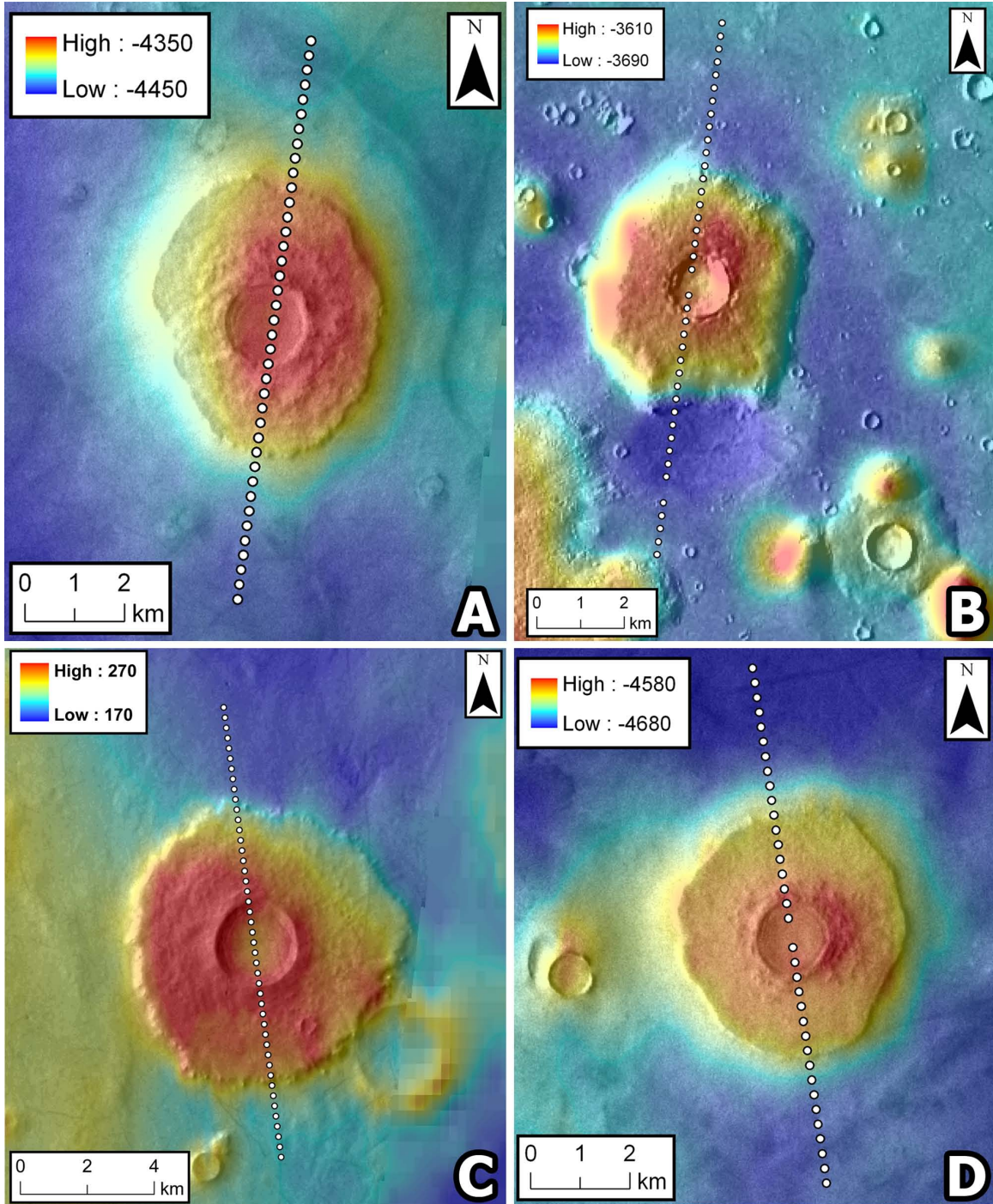


Figure 6

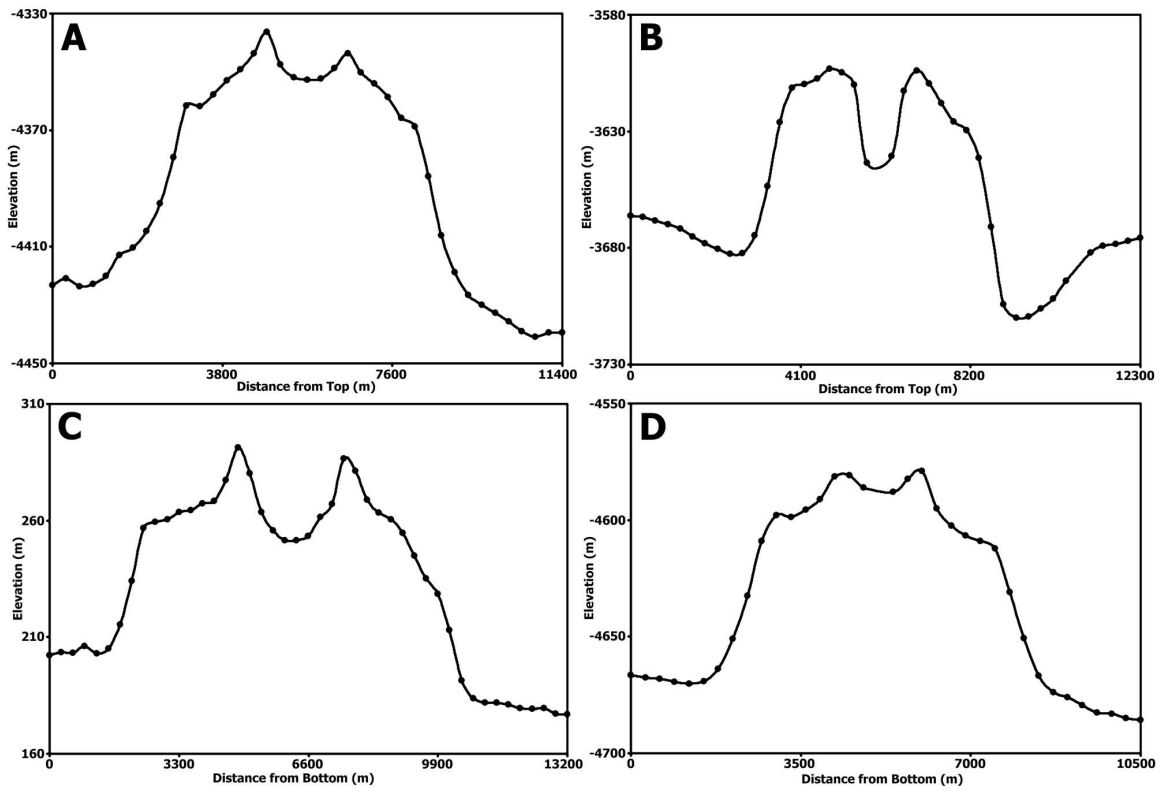


Figure 7

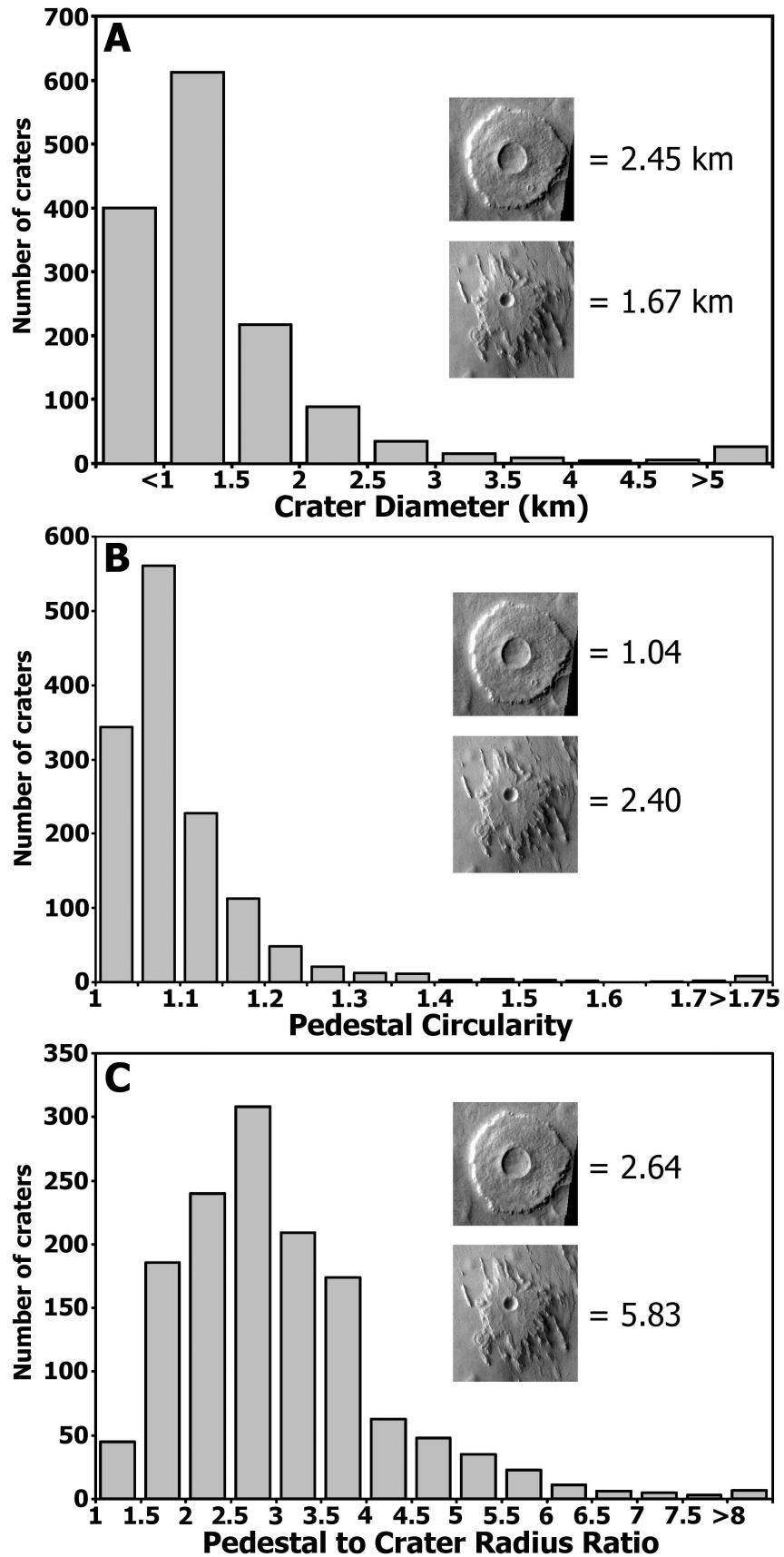


Figure 8

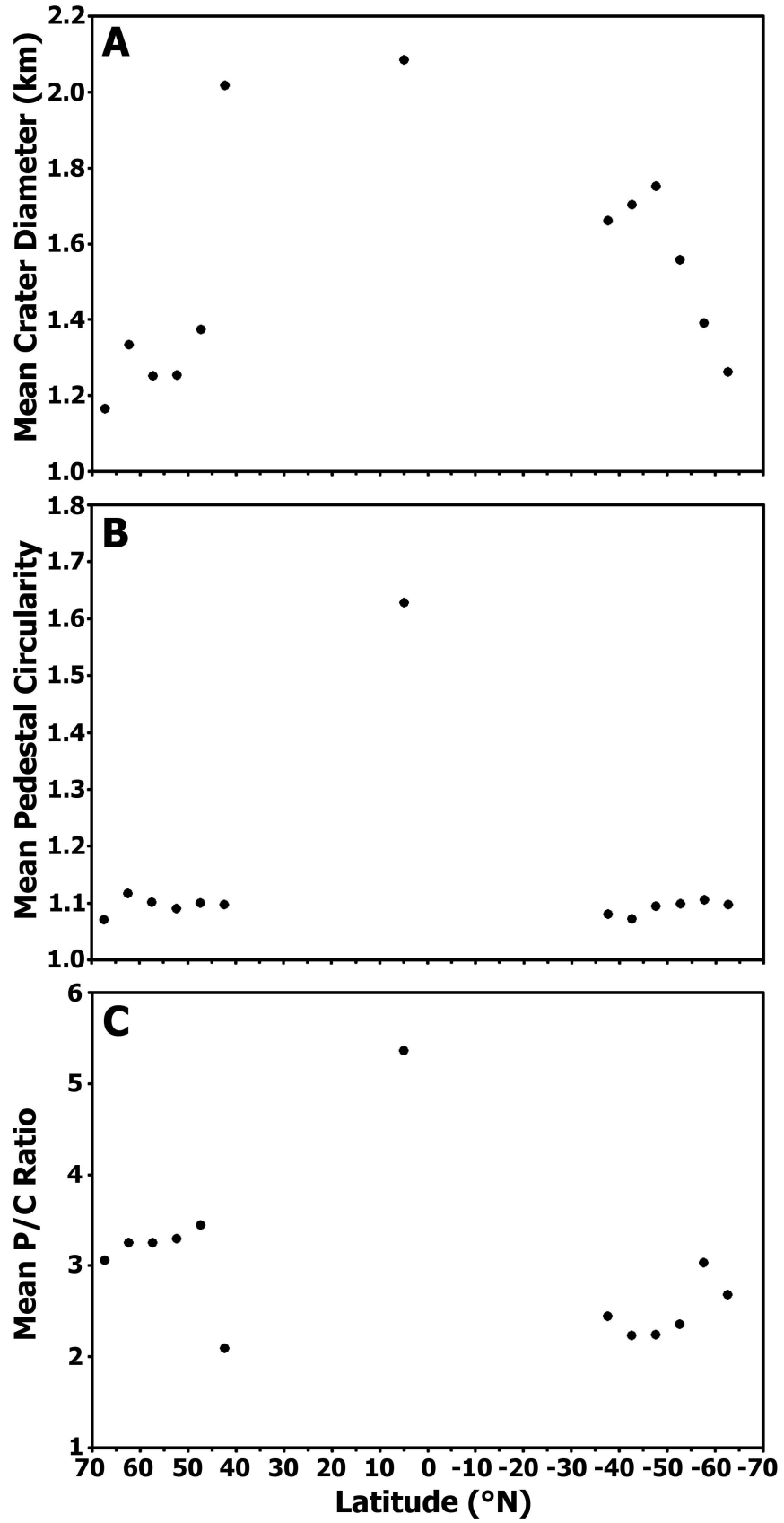


Figure 9

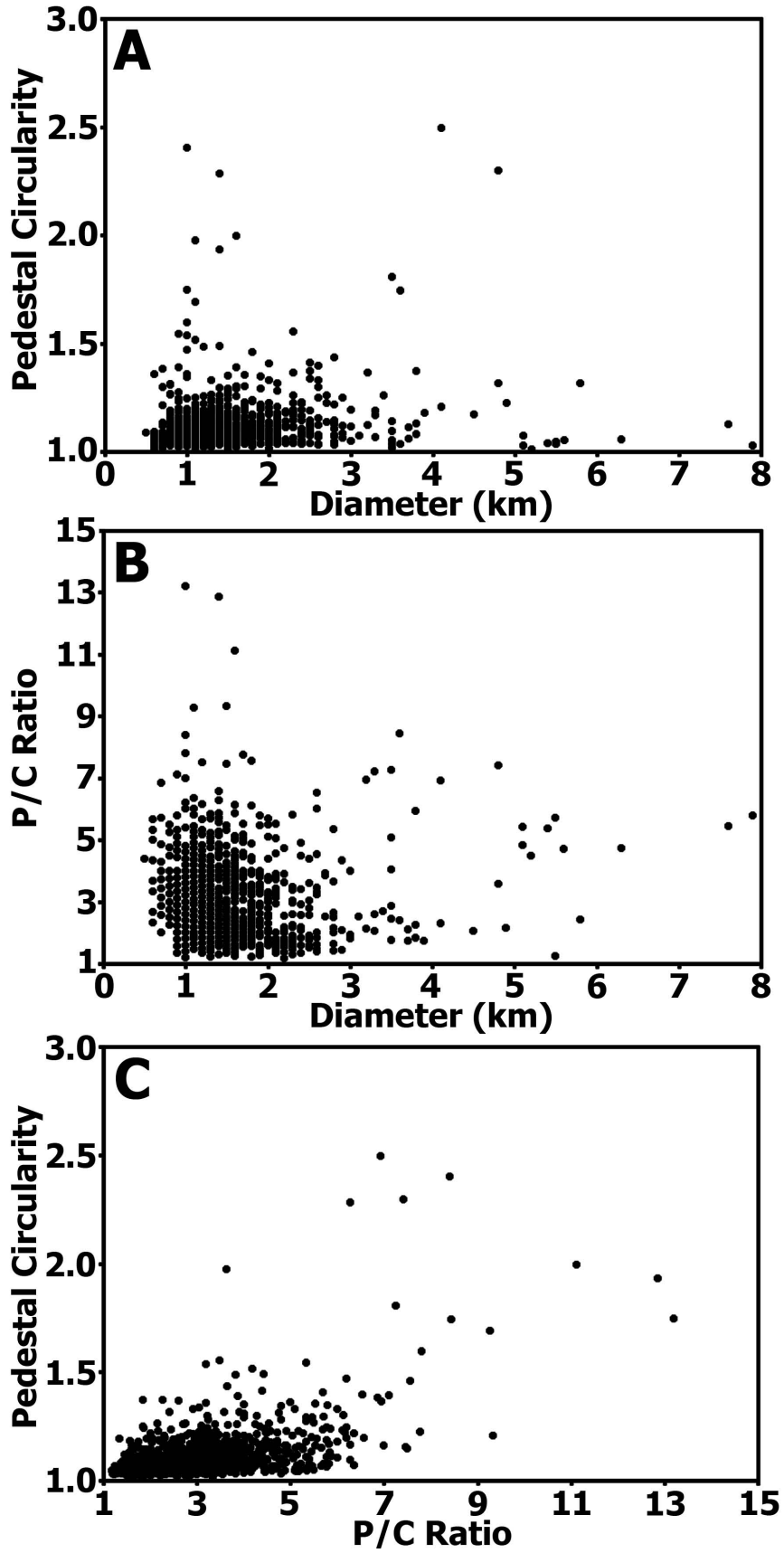


Figure 10

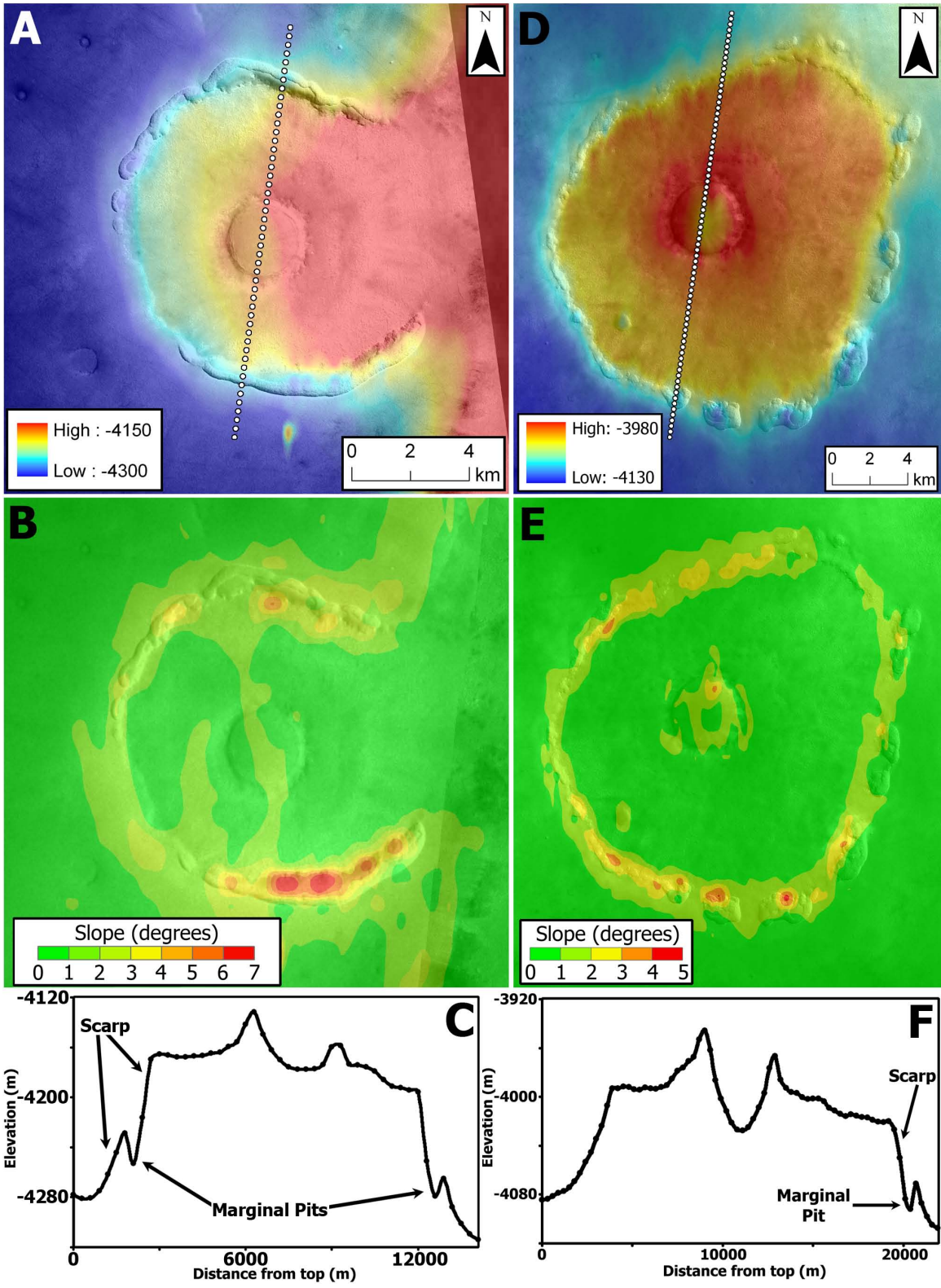


Figure 11

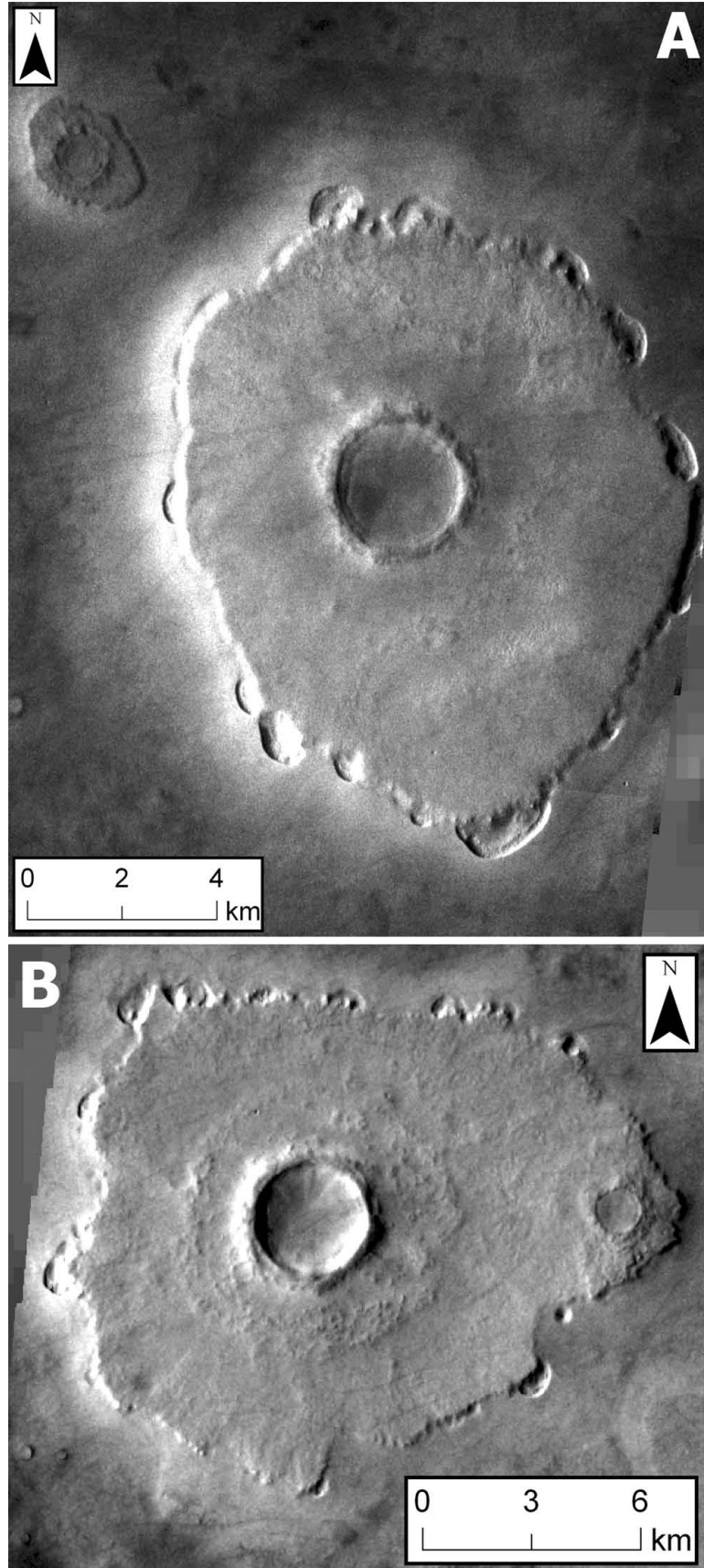


Figure 12

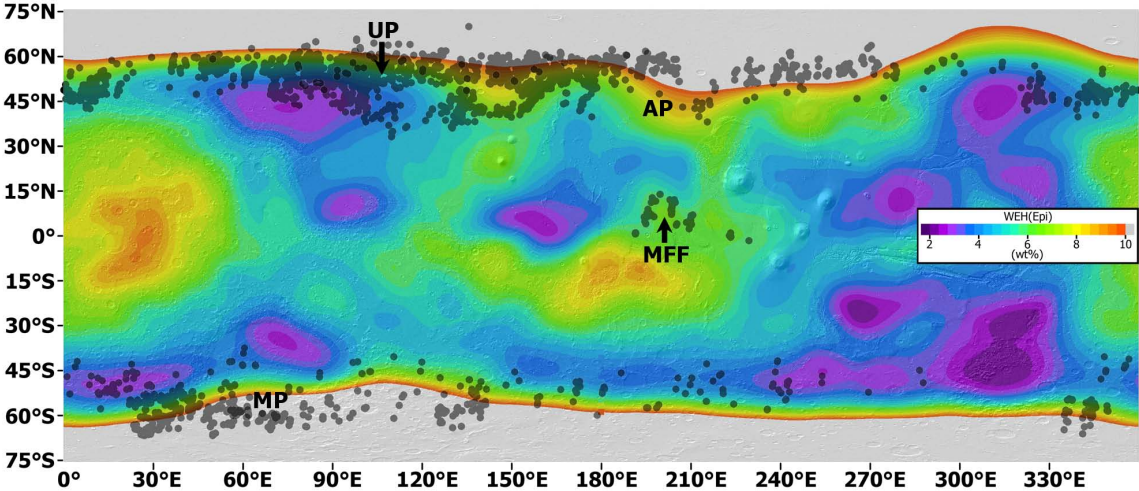


Figure 13

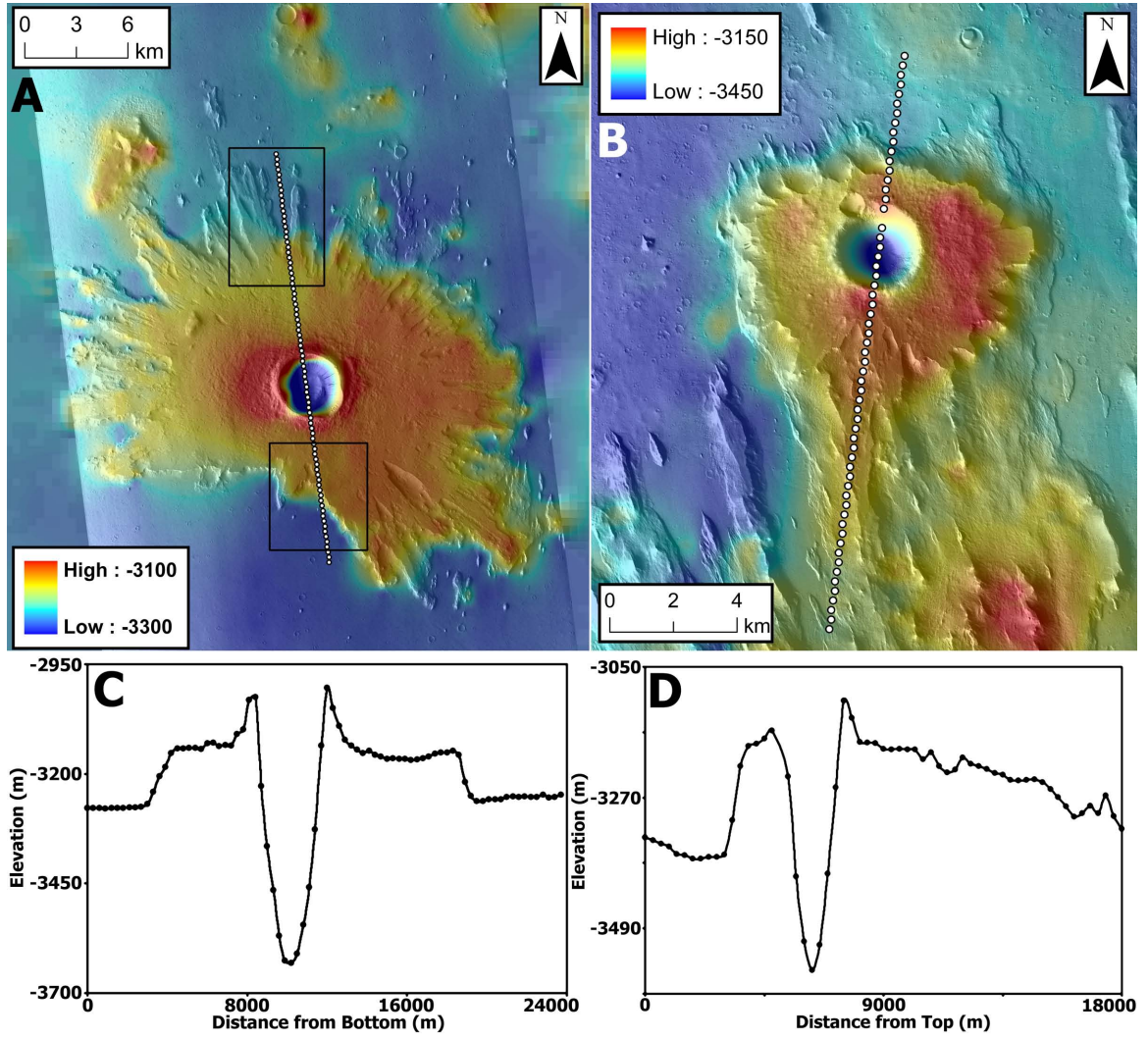


Figure 14

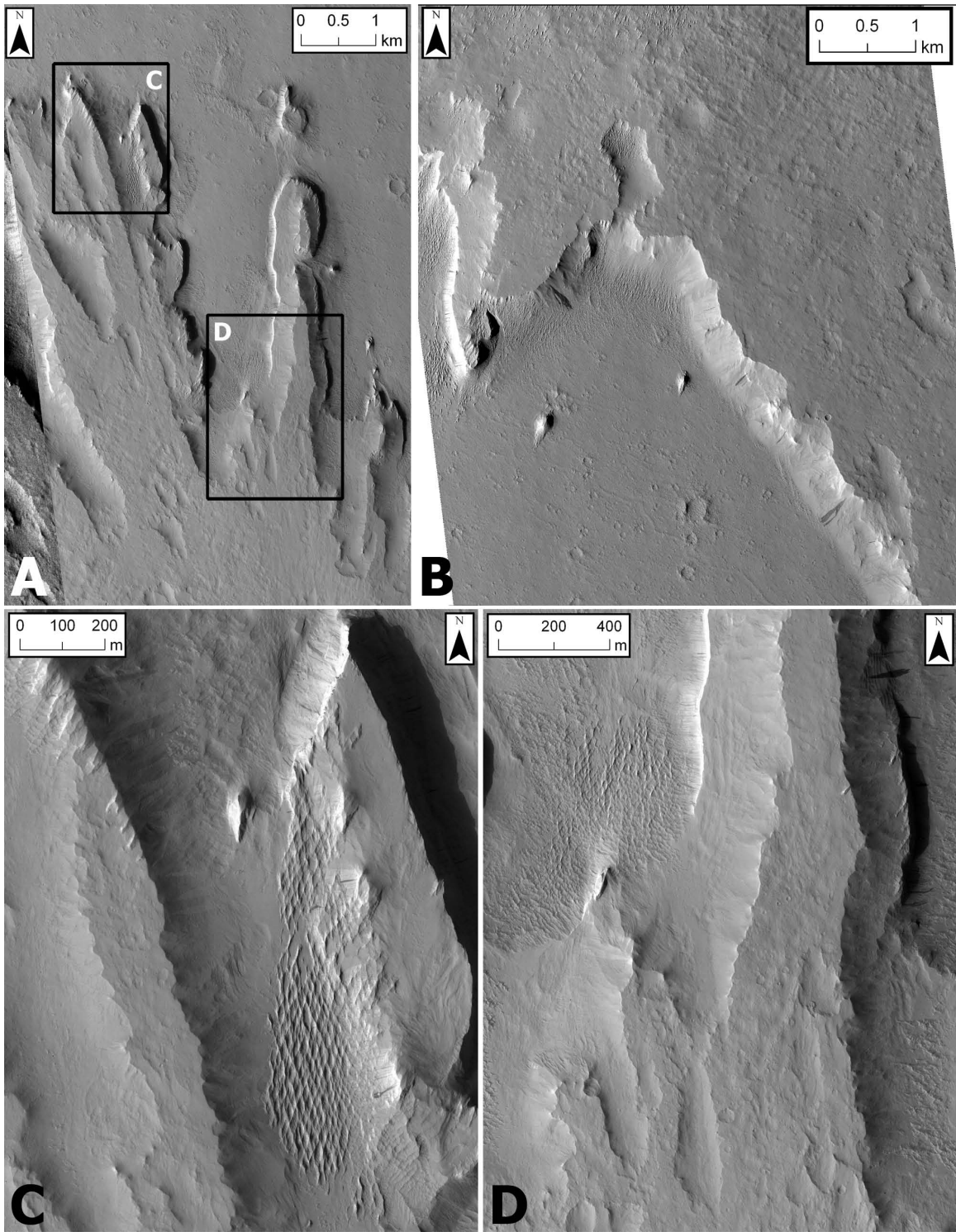


Figure 15

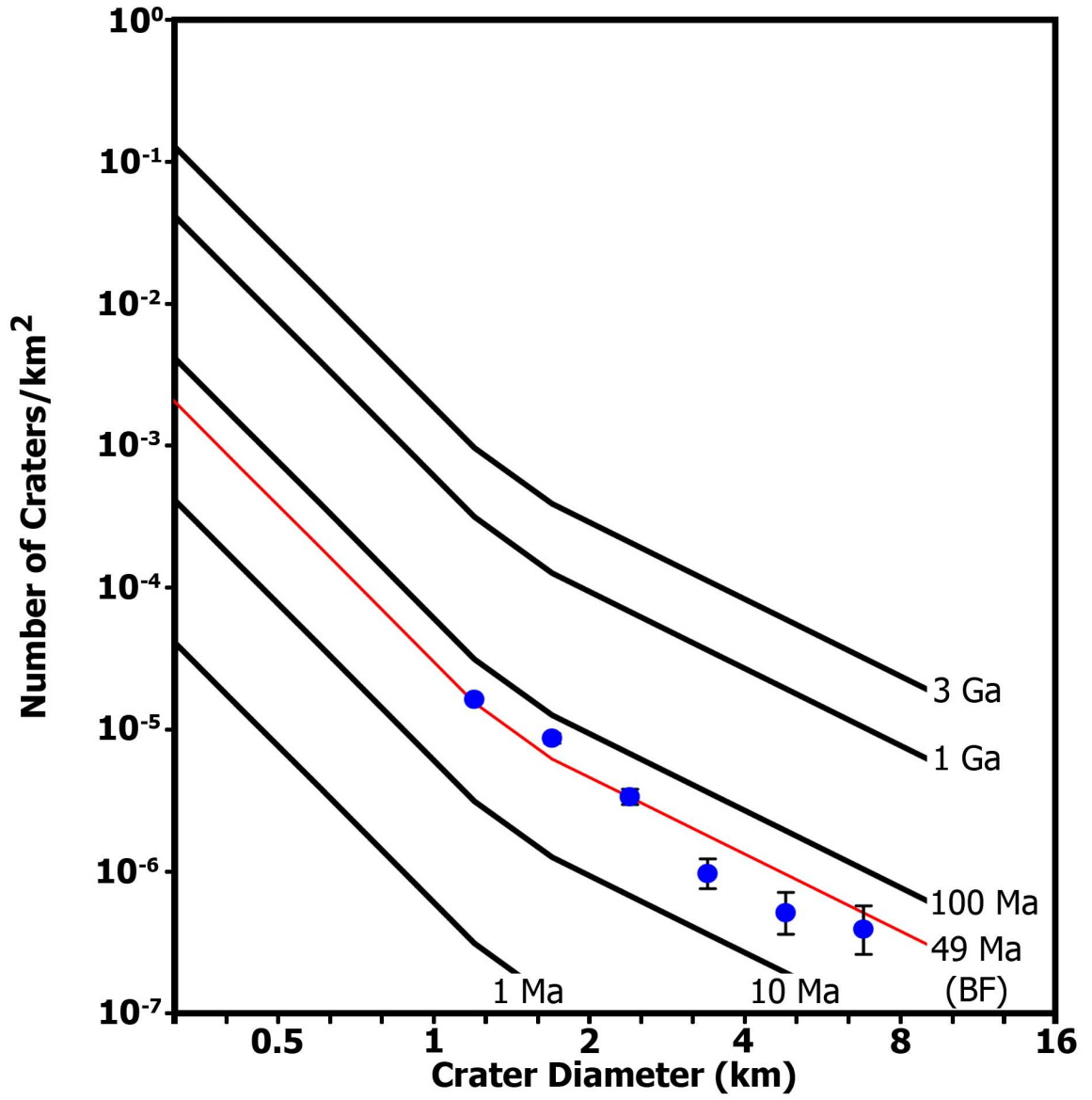


Figure 16

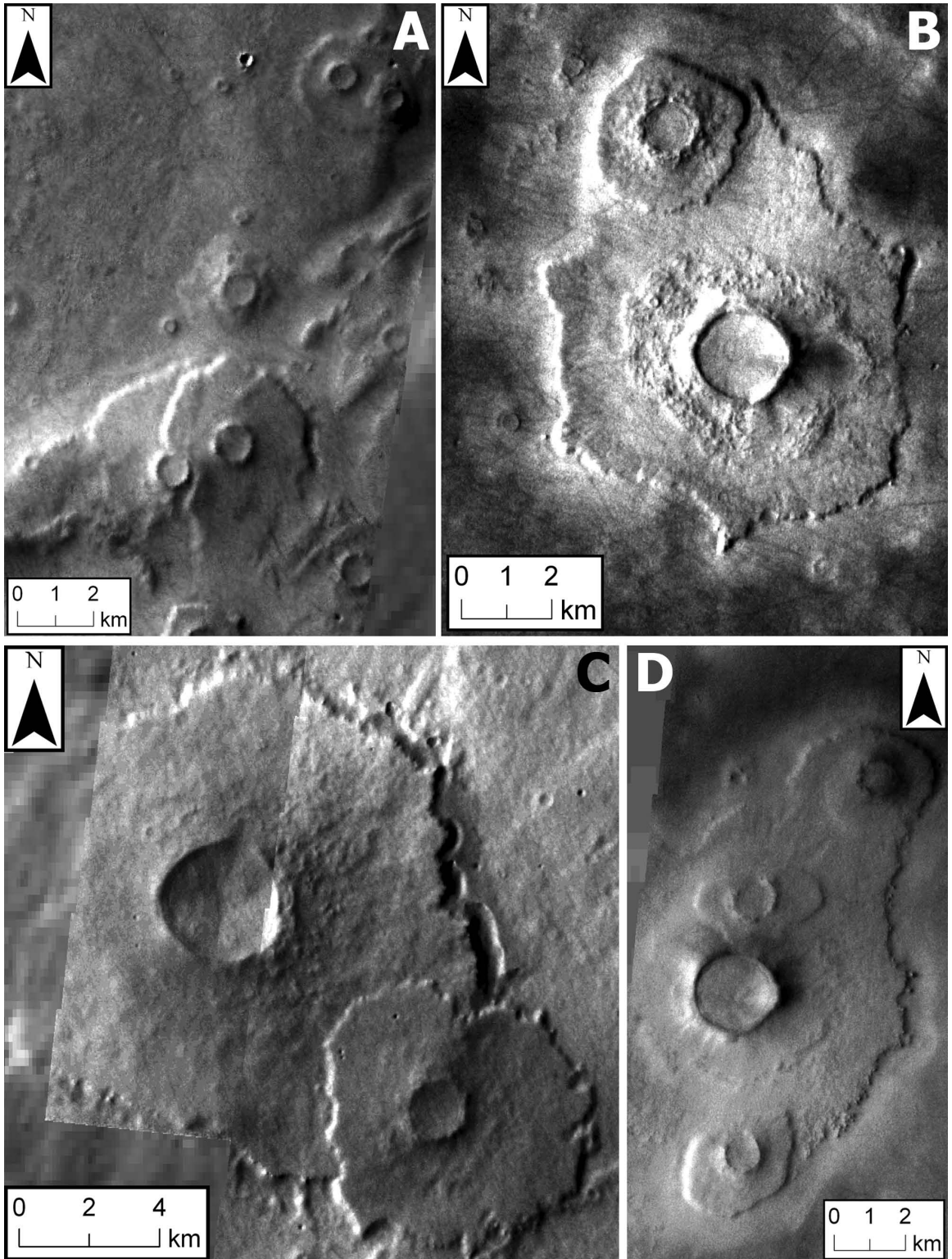
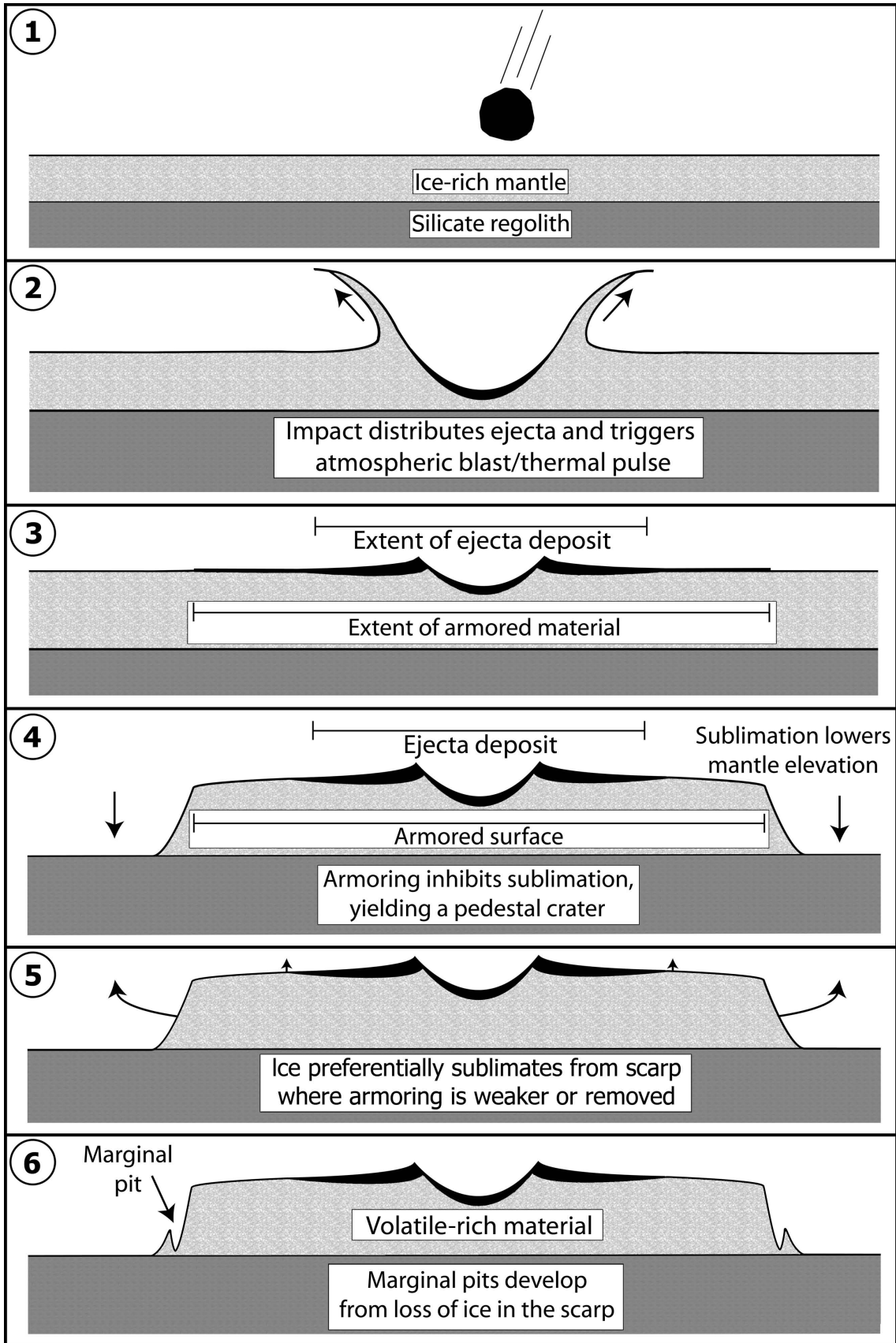


Figure 17



CHAPTER TWO:

Preservation of Layered Paleodeposits in
High-Latitude Pedestal Craters on Mars

Seth J. Kadish^a and James W. Head^a

^aDepartment of Geological Sciences, Brown University, Providence, RI 02912 USA

Published in:

Icarus, doi:10.1016/j.icarus.2011.03.029

Abstract

An outstanding question in Mars' climate history is whether or not pedestal craters represent the armored remnants of ice-rich paleodeposits. We address this question using new high-resolution images; in a survey of several hundred high-latitude pedestal craters, we have identified 12 examples in which visible and/or topographically expressed layers are exposed on the marginal scarp of the pedestal. One example, located on the south polar layered deposits, preserves ice-rich layers that have otherwise been completely removed from the polar cap. These observations provide empirical evidence that the pedestal crater formation mechanism is capable of armoring and preserving ice-rich layered paleodeposits. Although layered exposures have not yet been observed in mid-latitude pedestal craters, high-latitude instances of discontinuous, partially covered layers suggest that layers can be readily concealed, likely through mantling and/or mass wasting processes along the marginal scarp. This interpretation is supported by the observation that high-latitude pedestals with exposed layers along their margins are, on average, taller than mid-latitude examples, and have larger, steeper marginal scarps, which may help to maintain layer exposures. These observations favor the interpretation that mid- to high-latitude pedestal craters represent the armored remnants of ice- and dust-rich paleodeposits, which occurred transiently due to changes in the climate regime. Preservation of fine-scale layering of ice and dust at these latitudes implies that the climate change did not involve regional melting conditions.

1. Introduction

Pedestal craters (Pd) on Mars were first identified almost 40 years ago in Mariner 9 data (McCauley, 1973), and have since been classified as an impact morphology characterized by a crater perched near the center of a plateau, surrounded by a scarp (Arvidson et al., 1976; Barlow et al., 2000). Early studies implicated a formation mechanism based on armoring of fine-grained target material during an impact event, followed by preferential eolian deflation of the non-armored intercrater terrain (McCauley, 1973; Arvidson et al., 1976), yielding pedestals surrounded by marginal scarps. Our recent analyses, however, offer evidence that the target material from which Pd form contains a significant fraction of ice (Kadish et al., 2008, 2009, 2010). These studies highlight the latitude-dependent (poleward of $\sim 35^\circ$) distribution of Pd (Kadish et al., 2009; Mouginis-Mark, 1979), indicating a climate-related formation mechanism, as well as key physical attributes including sublimation pits in the marginal scarps of some Pd (Kadish et al., 2008). The resulting sublimation model for Pd formation posits that impacts occur into ice-rich targets during periods of higher obliquity, when mid to high latitudes were covered by thick deposits of snow and ice (Head et al., 2003, Levrard et al., 2004). The impact arms the proximal surface of the ice-rich deposit. During return to lower obliquity, the deposit sublimates, lowering the elevation of the intercrater terrain. Beneath the armored cover around the crater, however, the ice-rich deposit is preserved, yielding a pedestal. For a more detailed description of this model, see Kadish et al., (2009).

Climate models (e.g. Madeleine et al., 2009) have shown that ice-rich material can gradually accumulate ($\sim 10\text{-}20$ mm/yr) at mid to high latitudes under certain

atmospheric and orbital/obliquity conditions. Madeleine et al. (2009) specifically identify the need for a relatively high dust opacity in order to form such deposits, which accumulate episodically on both short timescales, due to seasonal effects, and longer timescales, due to obliquity cycles. These types of deposits are similar to, but thicker than, the latitude-dependent mantle described by Mustard et al. (2001) and Head et al. (2003), and can lead to glaciation in parts of the mid latitudes (Head et al., 2010). Given the episodicity in accumulation, one might predict deposition of layers of dust and ice, similar to those observed in the polar layered deposits (e.g. Milkovich and Head, 2005; Plaut et al., 1988, 2007) and in more widespread latitude-dependent mantles (e.g. Head et al., 2003; Schon et al., 2009). If Pd formed from armoring of these ice- and dust-rich paleodeposits, which were subsequently removed from the intercrater plains during periods of climate change, then fresh exposures of the margins of the pedestals should reveal evidence of such layering. Here, we provide new evidence for the presence of such layers as identified through our analysis of high-latitude Pd (poleward of 65°) in both hemispheres. These data support our interpretation that Pd result from impacts into ice-rich paleodeposits.

2. High-Latitude Pedestal Craters

Although the geographic distribution and morphology of mid-latitude Pd have been well-documented with a range of new image and altimetry data (e.g. Kadish et al., 2009), there have been no recent studies dedicated to the comprehensive mapping and characterization of Pd at high latitudes. Preliminary analyses of Pd in north polar (e.g. Tanaka, 2005; Tanaka et al., 2008) and south polar regions (e.g. Bleacher et al., 2003;

Head and Pratt, 2001; Plaut et al., 1988) have, however, noted that the presence of Pd on and around the polar caps indicates the removal/erosion of large volumes of material. Although these studies discuss the emplacement, evolution, and erosion of high-latitude units, they do not come to a consensus on the nature of the material composing the pedestals. In the north polar regions, Tanaka et al. (2008) suggest that Pd are the eroded remnants of the Rupes Tenuis unit. They note that this unit may have formed via precipitation and cold-trapping of a dust-ice mixture, with the sediment sourced from eolian erosion of the nearby Scandia region unit during the Early Amazonian. However, they state that the role of volatiles in cementing the Rupes Tenuis unit cannot be established. In the south polar regions, at least one Pd is present on the polar cap (Plaut et al., 1988) and many are superposed on the Hesperian-aged Dorsa Argentea Formation (DAF) (Bleacher et al., 2003). The material composing these pedestals may be preserved remnants of the widespread Noachian-aged cratered units from the plateau sequence (Npl₁ and Npl₂) (Bleacher et al., 2003; Plaut et al., 1988), as mapped by Tanaka and Scott (1987). These units have been interpreted to be primarily volcanic in origin, although they are likely to have been mixed with sedimentary materials and impact breccias. Where Pd are present on the DAF, there is evidence that significant mantling has taken place.

Through an extensive survey using MOLA, THEMIS, CTX, and HiRISE data of more than 200 high-latitude Pd (poleward of 60° in both hemispheres), we have confirmed that, similar to those at the mid latitudes, high-latitude Pd are extremely circular with flat pedestal surfaces, have mean crater diameters of <2 km, mean pedestal heights of <60 m, and have mean pedestal to crater radius (P/C) ratios of ~3 (Kadish et al.,

2009, 2010). The P/C ratio represents the farthest extent of the pedestal as measured from the crater rim crest divided by the crater radius. We have, however, identified a distinct subpopulation of Pd that show visible layering along their marginal scarps (Fig. 1). This layering has not been observed along any pedestal margins equatorward of 65° latitude. Measurements of pedestals that exhibit layering reveal important physical differences compared to those without layers at both mid and high latitudes (Table 1). Most notably, pedestals with exposed layers tend to be taller and larger in lateral extent, and have larger crater diameters. It is important to note that these layers are the armored remnants of paleodeposits, and are morphologically distinct from layered ejecta structures caused by impacts into subsurface volatiles and the subsequent emplacement of ejecta (Barlow, 2004). Although some Pd do exhibit single layer ejecta superposed on the pedestal surface, the pedestal itself is not composed of ejecta as confirmed by the high P/C ratios of Pd and the flatness/smoothness of the pedestal surfaces (e.g. Kadish et al., 2010).

Boola Crater (#1 in Table 1) offers some important observations in regard to the preservation of layers below impact craters. Although Boola does not qualify as a true Pd (Tanaka et al., 2008), it does have a marginal scarp along part of its perimeter that exhibits distinctive layers. Boola does not technically classify as a Pd because half of it is covered by the polar layered deposit, and as such, we have not calculated a value for its pedestal extent or P/C ratio. However, if that part of the deposit were removed, Boola would be a Pd. We thus interpret Boola crater as a clear example of the transition from atmospherically emplaced polar layers below an impact crater to an evolving Pd where the preserved layered are readily exposed; in other words, Boola crater offers a rare view

of the pedestal-forming process and provides insight into the nature of the ice-rich, layered target material from which Pd can form.

3. Exposed Layers along Marginal Scarps

Our high-latitude survey has identified 12 Pd with visible layers, five in the northern and seven in the southern hemisphere (Fig. 2). The presence of layering is typically established on the basis of albedo differences between adjacent layers (Fig. 1c). However, in some cases, layers are primarily expressed topographically, creating stepped pedestal margins, without providing any significant albedo variations (Fig. 1b). The ability to identify this type of layering is more heavily dependent on the lighting geometry of a given image. It should also be noted that layers that appear to have distinct albedos may be the result of preferred sediment/dust deposition where the local slopes are shallower. The layers in most pedestals, however, are expressed both by albedo and topography. Layers are often continuous around the entire perimeter of the pedestal, although some are interrupted by material overlying the scarp (Fig. 3), and may disappear for several kilometers. The number of layers in a pedestal can range from three (e.g. Fig. 1a) to more than thirty (Fig. 4), with the thicknesses varying from layer to layer by as much as twenty meters as measured from Mars Orbiter Laser Altimeter (MOLA) shot data and HRSC high-resolution DTMs. MOLA gridded data are not of sufficient resolution to distinguish the thicknesses of individual layers. As such, we made these measurements by using MOLA shot data and HRSC DTMs in the following manner: 1) Oblique intersections between individual MOLA tracks and pedestal scarps were selected to increase the downslope resolution of the data, allowing us to measure the difference

between the elevation of adjacent layers, and 2) Closely spaced separate MOLA tracks were utilized to measure layer thicknesses directly downslope. This second method confirmed that there was no influence of local slopes on the first method. The HRSC DTMs were then used to confirm the MOLA measurements.

Although our past research strongly supports the interpretation that pedestals are composed of ice-rich material (Kadish et al., 2008, 2009, 2010), efforts to identify directly the structure of the exposed layers using the Shallow Radar Sounder (SHARAD) and composition using the Compact Reconnaissance Imaging Spectrometer (CRISM), both aboard the Mars Reconnaissance Orbiter, have been largely inconclusive. Pd are generally too small to be resolved clearly by SHARAD, which has a variable along-track horizontal resolution of 0.3 to 1 km (Seu et al., 2007). In addition, Pd form almost exclusively in fine-grained terrain where there is an abundant dust source; dust coatings of only tens to hundreds of microns on the pedestal margins can inhibit spectroscopic detections at visible and infrared wavelengths (e.g. Johnson et al., 2002). Two of the Pd in the southern hemisphere (#7 and #9 in Table 1), however, are extremely large compared to typical Pd. The sizes of these pedestals make them good targets because they can be easily resolved by SHARAD. Radargrams clearly show the presence of layered material within these pedestals, but modeling of the dielectric properties yields bulk permittivities that are consistent with either porous silicate or ice-rich material (ϵ ranges from approximately 4 to 5 depending on the pedestal analyzed), and the mixing ratio cannot currently be established (Nunes et al., 2009, 2010). As expected, CRISM data of the pedestal margins (see CRISM observations FRT0001461F and FRT000145A8)

suggest that the region is likely dusty, having no strong mineralogical or water ice signature.

Despite the paucity of direct evidence for ice-rich material from SHARAD and CRISM, we can confirm that the process that forms Pd is readily capable of maintaining ice-rich material. There is a Pd (see #12 in Table 1) on the south polar layered deposits (SPLD), first noted by *Plaut et al.*, (1988), that has armored the proximal surface. The surrounding intercrater terrain has since partially sublimated/eroded, exposing a clear sequence of layers along the marginal scarp of the pedestal (Fig. 4). The SPLD are known to be ice-rich, with dielectric properties consistent with a bulk composition of nearly pure water ice (Plaut et al., 2007). The stratigraphically lower layers in this pedestal are contiguous with surrounding layers of the SPLD, but the pedestal has preserved some layers just beneath the armored surface which are no longer present in the proximal region (Fig. 4). Although there is no CRISM coverage of this specific Pd, observations of morphologically similar layers in the SPLD within 150 km show evidence of water ice based on the BD1500 and/or BD1900 spectral parameter products (Pelkey et al., 2007) (e.g. CRISM observations FRT00004ECD, HRS0001132A, and HRS00011035). The BD1500 product is indicative of water ice, while the BD1900 product corresponds to water ice and/or hydrated sulfates, clays, or glass. As such, this example offers empirical evidence of the ability of Pd to preserve ice-rich layers.

One additional noteworthy example is that of Pd #4 in Table 1 (see Figs. 1b and 5). As previously mentioned, the layers in this Pd are expressed only topographically, possibly due to mantling of the marginal scarps. Despite this covering, the pedestal margins do show the presence of water ice, as confirmed by CRISM data; these ribbons

of ice are also visible in High Resolution Imaging Science Experiment (HiRISE) color data, appearing extremely bright (Fig. 5). The water ice is located primarily on the north-facing scarp, and is also present on the north-facing side of the crater bowl. However, small amounts also exist on the south-facing scarp. While this is likely to be frost (e.g. Langevin et al., 2008), its presence in the northern hemisphere summer ($L_s = 129^\circ$) in the late afternoon – HiRISE image PSP_010074_2540 was acquired at 2:57 pm local Mars time – argues against a diurnal coating that sublimates completely. The persistence of this surficial ice may imply the presence of near-surface ground ice. Ice buried within the pedestal would maintain lower surface temperatures via conduction, due to the second law of thermodynamics, allowing frost or other ice on the surface to remain stable throughout the day.

4. Discussion

The existence of high-latitude Pd with exposed layers, where thick deposits of snow and ice have been repeatedly deposited throughout the Amazonian (Head et al., 2003; 2010), supports the model that Pd form from impacts into ice-rich target material. Although the ice-rich material does not need to be layered for Pd to form, the episodicity in ice accumulation on both seasonal and obliquity-cycle timescales, in conjunction with the need for a high dust opacity (Madeleine et al., 2009), supports the interpretation that the target deposits could be layered. The small size of our subpopulation raises the question of why the vast majority of pedestals do not have exposed layers, particularly those located at mid latitudes. The paucity of Pd with exposed layers might be expected, given the ease with which layers can be buried. In order for pedestal layers to be visible,

a fresh face of the marginal scarp must be exposed, but it is likely that most scarps have been modified by: 1) sublimation of the ice and the subsequent retention of a lag deposit, 2) deposition (e.g. mantling) of a younger deposit, or 3) degradation through mass wasting (e.g. slumping and downslope movement of debris).

At mid latitudes, the terrain has undergone episodic mantling and subsequent dissection due to recent obliquity variations; the dissected texture, indicating the presence of mantling, has been identified primarily between 30° to 70°N and 25° to 65°S (Mustard et al., 2001). The layered exposures that we have identified exist poleward of 69°N and 66°S (Table 1). Eolian deposition of this meters-thick mantling unit at mid latitudes would be sufficient to mute the topographic expression of layers and prevent them from being visible in high resolution images on the basis of albedo contrasts. Eolian deposition of material also occurs at high latitudes, and consequently, the scarps of most high-latitude Pd appear no different than those at mid latitudes. Based on the measurements reported here, we propose that larger pedestals, specifically those that are taller (Table 1), are more capable of preserving fresh scarp faces due to having larger scarp surface areas and steeper margins, making it more difficult for mantling to accumulate. Additionally, these Pd have distinctly higher P/C ratios, suggesting they have been more efficiently and/or thickly armored. A more indurated pedestal surface would be less susceptible to erosion, and would therefore inhibit mass wasting of the marginal slopes, leading to preferential exposure along the scarps. Finally, it should be noted that because both mass wasting and mantling are cumulative processes, younger pedestals would be more likely to have exposed layers.

Although additional evidence is needed to establish whether all Pd contain ice-rich layers, the data in this study show that pedestals are capable of preserving ice-rich paleodeposits and that exposures of these layers on pedestal margins can readily be modified and covered. The presence of a Pd that is composed of the SPLD confirms that the armored surface can preserve ice-rich layers (Fig. 4; crater #12 in Table 1). The morphologic similarity and geographic proximity of this crater to other high-latitude Pd that also show layered exposures along their marginal scarps supports the interpretation that non-polar pedestals are also capable of preserving ice-rich paleodeposits. Finally, examples of discontinuous layers that have been partially covered via mantling and/or mass wasting supports the notion that Pd that initially have layered exposures can be modified to conceal these exposures. The tendency for layers to be visible only on the marginal scarps of Pd that are anomalously large and tall suggests that the process of covering layers occurs readily and repeatedly. These observations favor the interpretation that mid- to high-latitude pedestal craters represent the armored remnants of ice- and dust-rich paleodeposits, which occurred transiently due to changes in the climate regime. Future work will focus on utilizing new CRISM and HiRISE data to identify water ice signatures along pedestal scarps, and to look for subtle expressions of partially buried layers in order to understand better the relative roles of mantling and mass wasting.

Acknowledgments

The authors would like to thank the HiRISE, CTX, and CRISM teams, without whom this study could not have been possible. The authors are grateful for financial

support from NASA Mars Data Analysis Program (MDAP) grant NNX09A14GG to JWH.

References

Arvidson, R.E., Coradini, M., Carusi, A., Coradini, A., Fulchignoni, M., Federico, C., Funicello, R., Salomone, M., 1976. Latitudinal variation of wind erosion of crater ejecta deposits on Mars. *Icarus* 27(4), 503-516.

Barlow, N.G., 2004. Martian subsurface volatile concentrations as a function of time: Clues from layered ejecta craters. *Geophys. Res. Lett.* 31, L05703, doi:10.1029/2003GL019075.

Barlow, N.G., Boyce, J.M., Costard, F.M., Craddock, R.A., Garvin, J.B., Sakimoto, S.E.H., Kuzmin, R.O., Roddy, D.J., Soderblom, L.A. 2000. Standardizing the nomenclature of Martian impact crater ejecta morphologies. *J. Geophys. Res.* 105(E11), 26733-26738.

Bleacher, J.E., Sakimoto, S.E.H., Garvin, J.B., Wong, M., 2003. Deflation/erosion rates for the Parva Member, Dorsa Argentea Formation and implications for the south polar region of Mars. *J. Geophys. Res.* 108, doi:10.1029/2001JE001535.

Head, J.W., Pratt, S., 2001. Extensive Hesperian-aged south polar ice sheet on Mars: Evidence for massive melting and retreat, and lateral flow and ponding of meltwater. *J. Geophys. Res.* 106(E6), 12275-12299.

Head, J.W., Marchant, D.R., Dickson, J.L., Kress, A.M., Baker, D.M.H., 2010. Northern mid-latitude glaciation in the Late Amazonian period of Mars: Criteria for the recognition of debris-covered glacier and valley glacier landsystem deposits. *Earth Planet. Sci. Lett.* 294, 306-320, doi: 10.1016/j.epsl.2009.06.041.

Head, J.W., Mustard, J.F., Kreslavsky, M.A., Milliken, R.E., Marchant, D.R., 2003. Recent ice ages on Mars. *Nature* 426, 797-802.

Johnson, J.R., Christensen, P.R., Lucey, P.G., 2002. Dust coatings on basaltic rocks and implications for thermal infrared spectroscopy of Mars. *J. Geophys. Res.* 107, doi: 10.1029/2000JE001405.

Kadish, S.J., Head, J.W., Barlow, N.G., Marchant, D.R., 2008. Martian pedestal craters: Marginal sublimation pits implicate a climate-related formation mechanism. *Geophys. Res. Lett.* 35, L16104, doi:10.1029/2008GL034990.

Kadish, S. J., Barlow, N.G., Head, J.W., 2009. Latitude Dependence of Martian Pedestal Craters: Evidence for a Sublimation-Driven Formation Mechanism. *J. Geophys. Res.* 114, E10001, doi:10.1029/2008JE003318.

Kadish, S.J., Head, J.W., Barlow, N.G., 2010. Pedestal Crater Heights on Mars: A Proxy for the Thicknesses of Past, Ice-Rich, Amazonian Deposits. *Icarus*, doi:10.1016/j.icarus.2010.06.021.

Langevin, Y., Vincendon, M., Poulet, F., Bibring, J-P., Gondet, B., Douté, S., Encrenaz, T., 2008. Weak Signatures of Water Ice at High Northern Latitudes: Aerosols, Frosts and Ice Outcrops. *Lunar Planet. Sci. Conf. XXXIX*, abstract #2134.

Levrard, B., Forget, F., Montmessin, F., Laskar, J., 2004. Recent ice-rich deposits formed at high latitudes on Mars by sublimation of unstable equatorial ice during low obliquity. *Nature* 431, 1072-1075.

Madeleine, J.-B., Forget, F., Head, J.W., Levrard, B., Montmessin, F., Millour, E., 2009. Amazonian northern mid-latitude glaciation on Mars: A proposed climate scenario. *Icarus* 203, 390-405.

McCauley, J.F., 1973. Mariner 9 Evidence for Wind Erosion in the Equatorial and Mid-latitude Regions of Mars. *J. Geophys. Res.* 78, 4123-4137.

Milkovich, S.M., Head, J.W., 2005. North polar cap of Mars: Polar layered deposit characterization and identification of a fundamental climate signal. *J. Geophys. Res.* 110, doi:10.1029/2004JE002349.

Mouginis-Mark, P., 1979. Martian fluidized crater morphology – Variations with crater size, latitude, altitude, and target material. *J. Geophys. Res.* 84, 8011-8022.

Mustard, J.F., Cooper, C.D., Rifkin, M.K., 2001. Evidence for recent climate change on Mars from the identification of youthful near-surface ground ice. *Nature* 412, 411-414.

Nunes, D.C., Smrekar, S.E., Fisher, B., Plaut, J.J., Holt, J.W., Head, J.W., Kadish, S.J., Phillips, R.J., 2010. SHARAD, Pedestal Craters, and the Lost Martian Layers – Initial Assessments. *J. Geophys. Res.*, in press.

Nunes, D.C., Fisher, B., Smrekar, S.E., Plaut, J.J., Holt, J.W., Phillips, R.J., Seu, R., Head, J.W., 2009. Pedestal crater deposits as seen by SHARAD, American Geophysical Union, Fall Meeting 2009, abstract #P13B-1277.

Pelkey, S.M, et al., 2007. CRISM multispectral summary products: Parameterizing mineral diversity on Mars from reflectance. *J. Geophys. Res.* 112, doi: 10.1029/2006JE002831.

Plaut, J.J., Kahn, R., Guinness, E.A., Arvidson. R.E., 1988. Accumulation of sedimentary debris in the south polar region of Mars and implications for climate history. *Icarus* 76(2), 357-377.

Plaut, J.J., et al., 2007. Subsurface Radar Sounding of the South Polar Layered Deposits of Mars. *Science* 316, 92-95.

Schon, S.C., Head, J.W., Milliken, R.E., 2009. A recent ice age on Mars: Evidence for climate oscillations from regional layering in mid-latitude mantling deposits. *Geophys. Res. Lett.* 36. L15202, doi:10.1029/2009GL038554.

Seu, R., et al., 2007. SHARAD sounding radar on the Mars Reconnaissance Orbiter. *J. Geophys. Res.* 112, doi: 10.1029/2006JE002745.

Tanaka, K.L., 2005. Geology and insolation-driven climatic history of Amazonian north polar materials on Mars. *Nature* 437, 991-994.

Tanaka, K.L., Scott, D.H., 1987. Geologic map of the polar regions of Mars. *US Geol. Surv. Misc. Inv. Ser. Map I-1802-C*.

Tanaka, K.L., Rodriguez, J.A.P., Skinner Jr., J.A., Bourke, M.C., Fortezzo, C.M., Herkenhoff, K.E., Kolb, E.J., Okubo, C.H., 2008. North polar region of Mars: Advances in stratigraphy, structure, and erosional modification. *Icarus* 196, 318-358.

Tables

Table 1. Geographic locations and measurements of the physical attributes of Boola Crater (#1) and 12 high-latitude Pd (#2-13) that have layers exposed along their marginal scarps. Values for Boola Crater were not included in calculating the median, mean, and standard deviation.

Crater #	Latitude (°N)	Longitude (°E)	Height (m)	Crater Diameter (km)	Pedestal Extent (km)	P/C Ratio
1	81.3	-105.2	N/A	17.9	N/A	N/A
2	74.7	107.1	88	2.8	8.1	5.8
3	74.2	78.3	126	4.7	15.7	6.7
4	74.1	67.0	172	2.9	6.7	4.6
5	70.9	93.2	81	3.0	6.6	4.4
6	69.5	74.9	139	2.3	7.2	6.3
7	-66.4	62.0	167	15.3	59.8	7.8
8	-71.3	54.7	102	2.0	3.5	3.5
9	-71.7	55.5	265	14.6	37.1	5.1
10	-72.1	-9.2	434	3.1	5.1	3.3
11	-78.6	-7.5	105	1.5	3.9	5.2
12	-79.2	124.3	173	3.1	4.6	3.0
13	-80.8	86.3	96	5.4	10.8	4.0
Median			132.5	3.1	7.0	4.9
Mean			162.3	5.1	14.1	5.0
Standard Deviation			100.0	4.7	17.1	1.5

Figure Captions

Figure 1 – Three examples of Pd that show layers along their marginal scarps. A) Crater #6 in Table 1, shown in CTX image P17_007516_2496. Layers are continuous around the base of the marginal scarp, but are not visible in the light-toned material that forms a halo around the edge of the pedestal surface. B) Crater #4 in Table 1, shown in CTX image B01_010074_2564. The layers, which occur near the top of the marginal scarp, are expressed topographically. C) Crater #11 in Table 1, shown in CTX image B08_012702_1012. The white box outlines the location of the image seen in part “D”. The dark discontinuous layers surround a very rough-textured pedestal surface. D) An enlarged view (MOC image s1101636) of the layers along the crater in part “C”. The four visible layers have a distinctly lower albedo than the rest of the scarp, and create a stepped pedestal margin.

Figure 2 – The distribution of Pd with exposed layers mapped in north (left) and south (right) polar projections. The numbers on the maps correspond to the crater numbers listed in Table 1. Note that the pedestals are primarily located in the eastern hemisphere. In the northern high latitudes, they are clustered just north of Utopia Planitia.

Figure 3 – Three distinct segments of the marginal scarp of a massive Pd (#7 in Table 1), each showing discontinuous layering at different scales. In each image, the lobes of material overlying the layered scarp are usually contiguous with the surrounding plains material, and in some cases are contiguous with the pedestal surface as well. Because of this, when a sequence of layers is only partially covered, the layers that are

stratigraphically on top are usually the ones that remain exposed. This situation is apparent in part “C” of the figure. A) A section of Thermal Emission Imaging System (THEMIS) VIS image V17859015. B) A section of CTX image B12_014321_1131. C) A section of HiRISE image ESP_014031_1125. D-F) Sketch maps of the scenes shown in parts “A”, “B”, and “C”. These illustrate the striking discontinuity of the layers. Grey arrows point in the downslope direction along the marginal scarps.

Figure 4 – An example of a Pd that is superposed on the south polar cap (Crater #12 in Table 1). The armored surface is preserving the local SPLD sequence. A) A CTX and THEMIS mosaic with MOLA topography showing the geologic context of the Pd in the Promethei Lingula region. B) A CTX mosaic (images B11_013884_1011 and P06_003520_1009) of the Pd. The black box outlines the image in part “C”. The layers are particularly clear along the south-facing section of the marginal scarp, where they closely mimic the curvature of the pedestal perimeter. C) An enlarged view of the layers, showing that the pedestal is responsible for preserving the ice-rich SPLD.

Figure 5 – A) Crater #4 in Table 1, shown in CTX image B01_010074_2564. The black box outlines the location of the image in part “D”. B) The enhanced visible color product from CRISM image FRT0000C969. Note the bright material highlighting the topographically expressed layers, particularly along the northern margin of the pedestal. The black box outlines the location of the image in part “C”. C) An enlargement of the northern margin of the pedestal, shown as the *ir_ice* summary product. In this image, the colors correspond to spectral parameter products, with red as BD1900, green as BD1500,

and blue as BD1435. The strong green signal mimicking the curvature of the layers is indicative of water ice, suggesting the presence of frost or trapped snow/ice. Image credit for parts B and C goes to NASA/Johns Hopkins University Applied Physics Laboratory.

D) An enlargement of a portion of the south-facing marginal scarp, shown in HiRISE image PSP_010074_2540. The black box delineates the location of the image in part “E”.

E) A view of the corresponding color HiRISE image, showing patches of bright material, as indicated by the black arrows. This material is likely snow/ice which has been maintained on the pedestal scarp despite its south-facing orientation, and the fact that the image was taken during a summer afternoon.

Figure 1

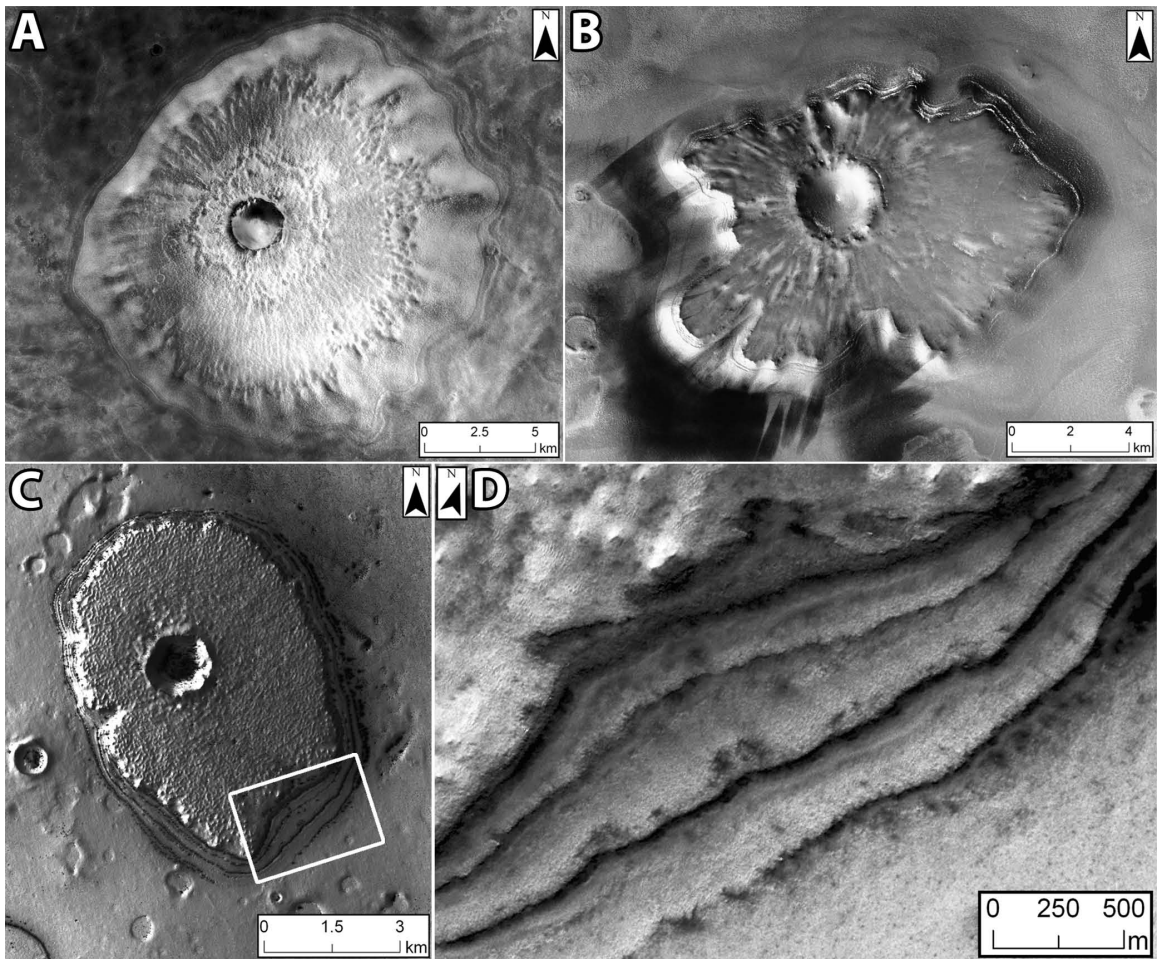


Figure 2

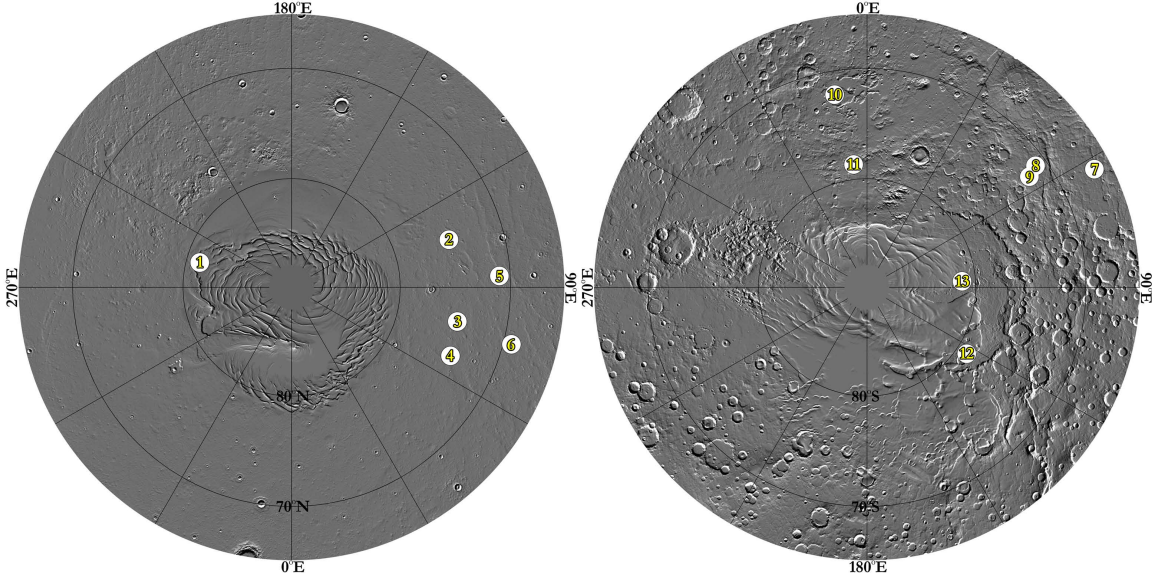


Figure 3

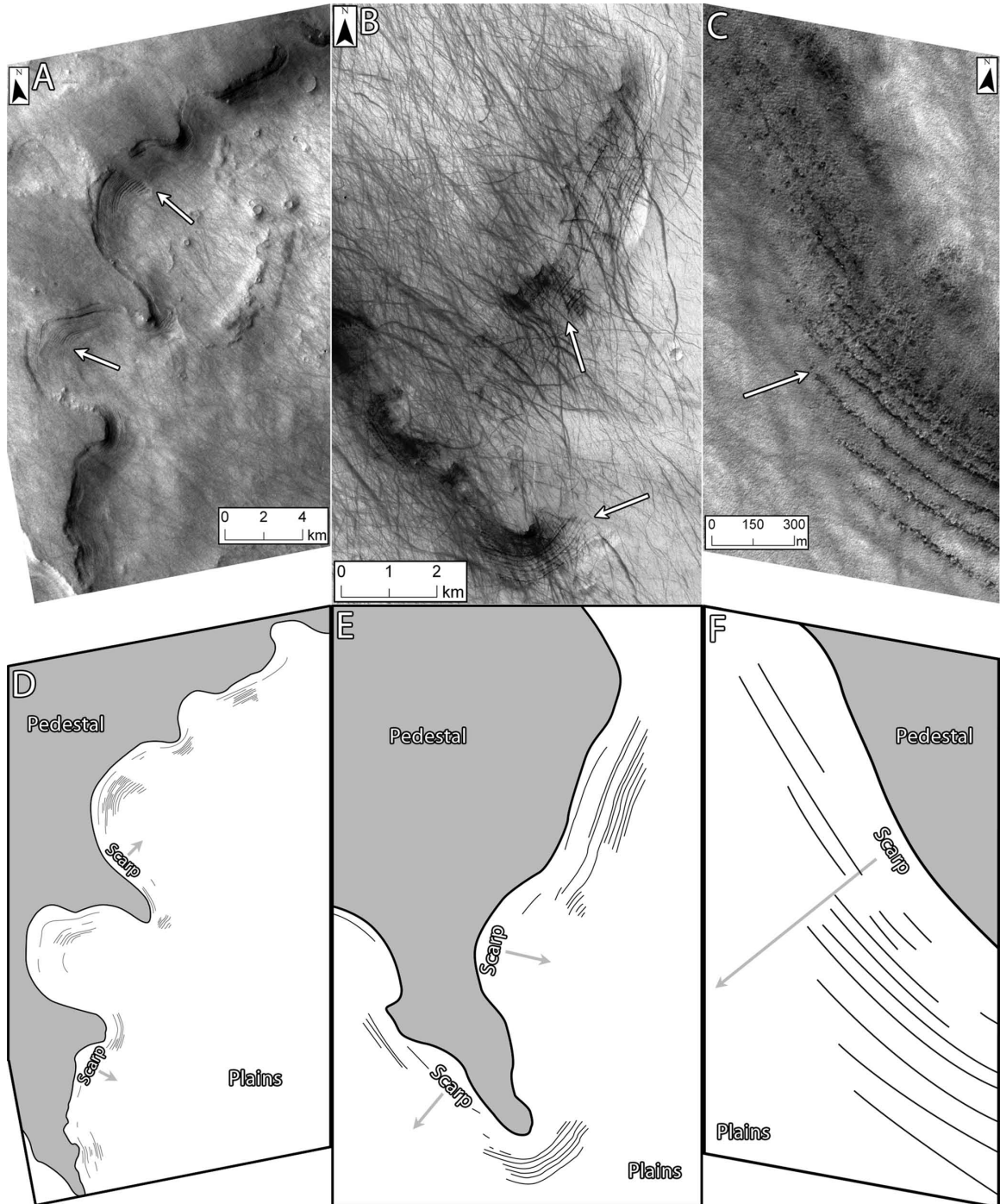


Figure 4

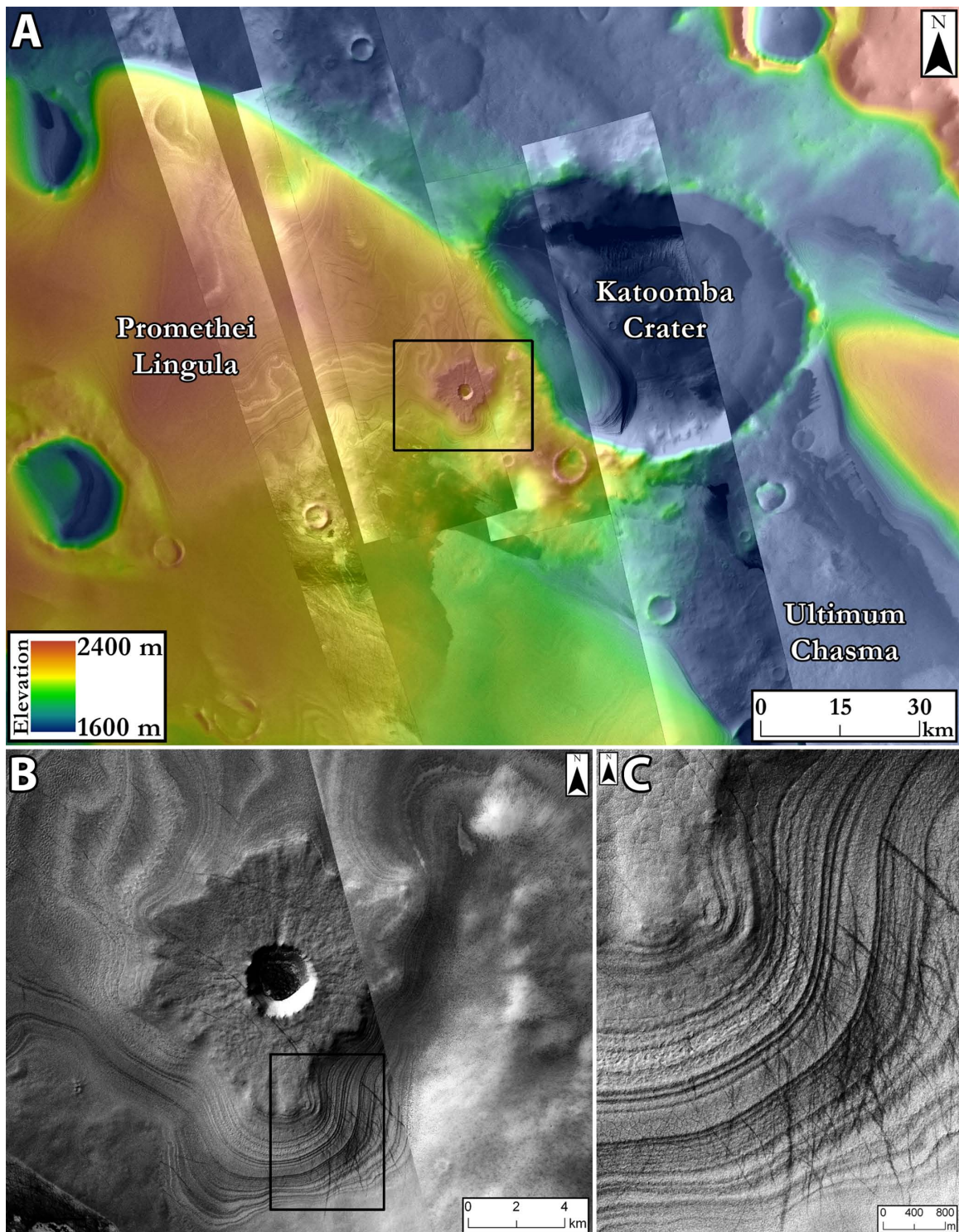
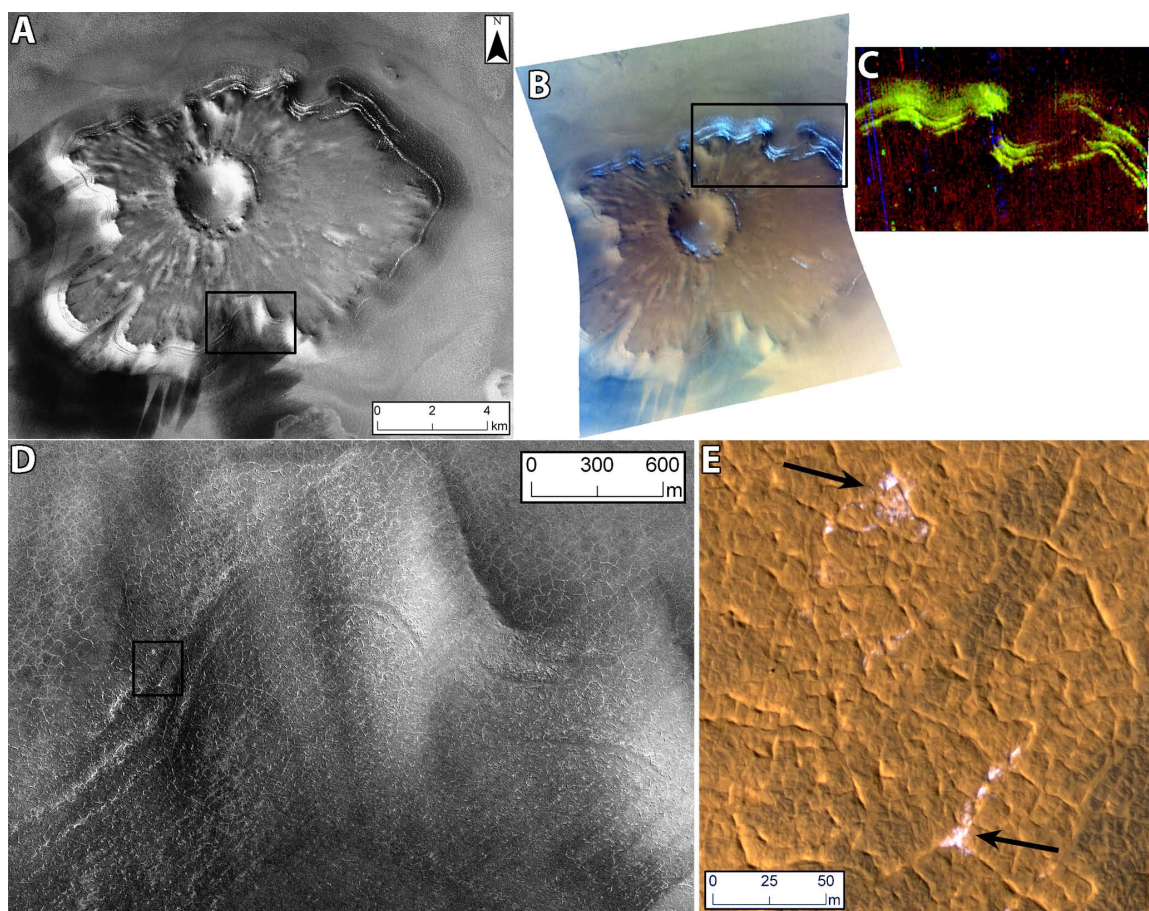


Figure 5



CHAPTER THREE:

Pedestal Crater Heights on Mars:

A Proxy for the Thicknesses of Past, Ice-Rich, Amazonian Deposits

Seth J. Kadish¹, James W. Head¹, and Nadine G. Barlow²

¹Department of Geological Sciences, Brown University, Providence, RI 02912 USA

²Department of Physics and Astronomy, Northern Arizona University, Flagstaff, AZ

86011 USA

Published in:

Icarus, Vol 210, 92-101

[112]

Abstract

Mid-latitude pedestal craters on Mars offer crucial insights into the timing and extent of widespread ice-rich deposits during the Amazonian period. Our previous comprehensive analysis of pedestal craters strongly supports a climate-related formation mechanism, whereby pedestals result from impacts into ice-rich material at mid latitudes during periods of higher obliquity. The ice from this target deposit later sublimates due to obliquity changes, but is preserved beneath the protective cover of the armored pedestal. As such, the heights of pedestals act as a proxy for the thicknesses of the paleodeposits. In this analysis, our measurement of 2300 pedestal heights shows that although pedestals can reach up to ~260 m in height, ~82% are shorter than 60 m and only ~2% are taller than 100 m. Mean pedestal heights are 48.0 m in the northern mid latitudes and 40.4 m in the southern mid latitudes, with the tallest pedestals located in Utopia Planitia, Acidalia Planitia and Malea Planum. We use these data in conjunction with prior climate model results to identify both regional and global trends regarding ice accumulation during obliquity excursions. Our data provide evidence for multiple episodes of emplacement and removal of the mid-latitude ice-rich deposit based on stratigraphic relationships between pedestal craters and the close proximity of pedestals with significantly different heights.

1. Introduction

We have recently presented a range of evidence for a sublimation-driven formation mechanism for pedestal craters on Mars (Kadish et al., 2008, 2009). First recognized in Mariner 9 data (McCauley, 1973), pedestal craters are an impact crater morphology on Mars characterized by a crater perched near the center of a plateau, surrounded by an often-circular, outward-facing scarp (Arvidson, 1976; Barlow et al., 2000). We have mapped 2300 pedestal craters from 60°N to 65°S to establish the latitude-dependent distribution and have physically characterized the pedestal craters' attributes (Kadish et al., 2009). We also have identified pedestal craters in Utopia Planitia and Malea Planum that have marginal pits, providing evidence for the sublimation of volatiles from the scarps of the pedestals (Kadish et al., 2008). This work further supports a model that calls on impact into ice-rich targets to produce pedestal craters during periods of higher obliquity, when mid to high latitudes were covered by thick deposits of snow and ice (Fig. 1). During return to lower obliquity (e.g. Head et al., 2003; Levrard et al., 2004), the regional volatile-rich unit sublimated, lowering the elevation of the surrounding terrain and removing its exposed snow and ice. Beneath the armored cover of the pedestals, however, the ice-rich deposit is preserved (Fig. 2).

It is important to note that the armoring and the ejecta are not the same feature. The armoring is the result of sintering and induration of the region proximal to the impact event. The exact mechanism by which the surface becomes armored remains debated, and several processes have been proposed. These include a coarse ejecta covering or lag deposit (Arvidson et al., 1976), increased ejecta mobilization caused by volatile-rich target substrates (e.g. Osinski, 2006), impact melt distribution that produces a glassy

veener (Schultz and Mustard, 2004), an atmospheric blast followed by a high temperature thermal pulse (Wrobel et al., 2006), and a turbulent, dust-laden, density-driven flow (Boyce et al., 2008). Although we have identified instances of single-layer ejecta distributed on pedestal surfaces, consistent with past observations (Mutch and Woronow, 1980; Barlow, 2004, 2006), the ejecta is always much more limited than the extent of the armoring that produces the pedestal surface. As such, the primary constraint that our empirical observations has on the armoring mechanism is that it must be capable of affecting an anomalously large lateral area. This suggests that the armoring mechanism is unlikely to be ballistic in nature. For a discussion of the proposed armoring mechanisms and of the pedestal extent as measured by the pedestal to crater radius ratio, see sections 3.2, 4.1, and 4.6 of Kadish et al., 2009.

In this sublimation model, the heights of pedestal craters are a proxy for the thickness of the paleodeposit and provide information as to how it may have varied regionally. These data can be used to establish where snow and ice preferentially accumulated during periods of higher obliquity. Here, we provide results on the measurements of mid-latitude pedestal heights, and discuss the implications for the timing and extent of a past latitude-dependent, ice-rich deposit.

2. Methodology

Pedestal height measurements in this study used gridded Mars Orbiter Laser Altimeter (MOLA) data (463 m/pix). Pedestal surfaces are not always level; their slopes are influenced by the topography of their surroundings (Fig. 3). As such, it is not valid to calculate a pedestal height as the difference between the highest elevation of the pedestal

and the lowest elevation of the immediately adjacent terrain. To account for this, we made four measurements of each pedestal's elevation, one in each quadrant (NW, NE, SW, and SE), halfway between the pedestal margin and the crater rim. Most pedestal surfaces are smooth, with no remaining topographic or morphologic evidence of the ejecta deposit. As previously mentioned, in cases where the ejecta is preserved, it never covers the entirety of the pedestal surface, and is usually much smaller in its radial extent. In these cases, we took precautions to avoid taking elevation data on the ejecta, ensuring that we were only measuring the elevation of the pedestal surface and not the combined elevation of the pedestal and the ejecta. We then made four measurements of the elevation of the surrounding terrain along the same radial lines extending from the crater center. These were taken within two kilometers of the pedestal margin, avoiding topographic aberrations like pits or mounds that would provide spurious results. The average of the four elevations of the surrounding terrain was then subtracted from the average of the four pedestal elevations to get the pedestal height.

This method provides reasonable averages for the heights of the pedestal craters, and works to eliminate the influence of local slopes and uneven terrain. It is possible that the current elevation of the intercrater terrain in some regions is not the same as it was prior to emplacement of the latitude-dependent deposit due to local mantling and/or erosion subsequent to the pedestal crater formation. Although we cannot account for these potential changes to the elevations of the surrounding surfaces, they are likely negligible compared to the heights of the pedestals and should not affect our results on a global scale.

3. Global Distribution and Trends of Pedestal Heights

Pedestal heights (Figs. 3,4) have important implications for the surface conditions that existed at the time of impact. Previous researchers (e.g. Bleacher et al., 2003; Thomson and Schultz, 2007; Tanaka et al., 2008) have noted that the heights of pedestal craters offer information concerning the elevation of the paleosurface; pedestal craters represent the remnants of a paleodeposit that has since been removed, leaving the craters perched above the surrounding terrain. Our interpretation is that these paleodeposits were emplaced directly on the martian regolith, persisted for some duration of time and were then removed. Given this interpretation, the heights of pedestal craters can act as a proxy for the thicknesses of these paleodeposits. Impacts that occurred into the paleodeposit during its accumulation or removal would produce pedestals that are shorter than the maximum thickness of the deposit. Consequently, some pedestal heights may provide minima for the thicknesses of the regional paleodeposits rather than the full thicknesses.

The use of pedestal heights as a proxy for paleodeposit thickness is valid regardless of which armoring mechanism is eventually proven to be correct, and is consistent with both the eolian deflation model and the climate-related sublimation model for pedestal crater formation. Historically, pedestal craters were thought to form by armoring of a dry, fine-grained target material during the impact event, followed by eolian deflation of the intercrater terrain. This preferential erosion of the non-armored material would yield the perched pedestals surrounded by marginal scarps (e.g. McCauley, 1973; Schultz and Lutz, 1988). However, as previously mentioned, we have provided substantial evidence supporting a formation mechanism involving sublimation of an ice-rich paleodeposit (Kadish et al., 2008, 2009).

Support for the sublimation model includes, but is not limited to, the following:

(1) The latitude-dependent distribution of pedestal craters (Fig. 4), with the majority found poleward of 45° (Mouginis-Mark, 1979; Kadish et al., 2008, 2009). The distribution also mimics that of several other surface morphologies that are indicative of a mid-latitude ice-rich substrate, and coincides with the regional and latitudinal extent of where martian climate models predict snow/ice accumulates during periods of higher obliquity (e.g. Richardson and Wilson, 2002; Mischna et al., 2003; Madeleine et al., 2009). This latitude-dependent distribution is at odds with the eolian deflation model, which allows pedestals to form in any region with fine-grained material on Mars. (2) The paucity of pedestal craters larger than 5 km in diameter. The deflation model does not predict any size limitation for pedestal crater formation, but under the sublimation model, large impacts would likely overwhelm an ice-rich unit, melting and/or vaporizing its volatiles upon impact (Barlow et al., 2001). Under the sublimation model, the small size of most pedestal craters may also explain why they rarely have ejecta deposits. Impacts into ice-rich material would distribute the dust/ice mixture on top of the armored surface. When the obliquity lowers and the intercrater terrain sublimates, yielding the pedestal relief, the ejecta would also sublimate and any remaining fines would be prone to deflation. Only in cases where there was a particularly high dust to ice ratio, or the impact excavated and distributed the underlying regolith, would there be enough material to maintain an ejecta deposit on the pedestal surface. (3) Physical measurements of the pedestal craters' attributes (Kadish et al., 2009), as discussed in section 4. Most importantly, pedestals are extremely circular, which is an expected result from the sublimation model. Eolian deflation of the surrounding terrain would produce elongated

pedestals due to predominant wind directions. (4) Pits in the scarps of some pedestal craters, as discussed in section 5.3, indicating a loss of material from the pedestal itself (Kadish et al., 2008). These pits are morphologically similar to scallops and other sublimation depressions, and they never excavate below the elevation of the surrounding terrain. This suggests that pedestals are composed of ice-rich material overlying a dry/desiccated regolith.

Given this evidence for a sublimation-driven formation mechanism and the notion that pedestal heights are reasonable proxies for the thicknesses of the paleodeposits, we can use our measurements in conjunction with other pedestal crater attributes to constrain the distribution, volume, and timing of ice accumulation at mid latitudes during periods of higher obliquity. The geographic distribution of pedestal heights on Mars reveals four important trends (Figs. 4,5; Table 1): (1) Pedestals tend to be <60 m in height (Fig. 5a). Although we measured pedestals as tall as 256 m, only 43 of 2300 (~2%) were >100 m, while 1885 of 2300 (~82%) were <60 m. Pedestals <20 m in height were not analyzed in this study due to the uncertainty in distinguishing them from regular craters with thick ejecta deposits. (2) Although pedestals are, on average, slightly taller in the northern hemisphere (48.0 m) than the southern hemisphere (40.4 m), the average height of mid-latitude pedestals does not show any statistically significant variation as a function of latitude (Fig. 5b). As we will discuss later, this result is most likely due to the high population density of short pedestals (20 to 50 m) at both mid and high latitudes, masking the tendency of the less populous tall pedestals (>80 m) to form at higher latitudes. The small equatorial population, located exclusively in the Medusae Fossae Formation (MFF), is composed of much taller pedestals; the mean height is 114.4 m compared to

47.7 m at mid latitudes in both hemispheres. It is important to note that MFF pedestal craters are morphologically distinct from those at mid latitudes, and may result from an entirely different formation mechanism (Kadish et al., 2009). (3) Within each hemisphere, there are variations in pedestal height as a function of longitude (Fig. 5c-d). The mapped distribution of pedestals >80 m in height (Fig. 4d-f) shows that the tallest mid-latitude pedestals are concentrated in Utopia Planitia and Acidalia Planitia in the northern hemisphere and Malea Planum in the southern hemisphere. As a result, the average pedestal height in Acidalia Planitia and Malea Planum is slightly greater than the average in the rest of their respective hemispheres. Utopia Planitia, however, also contains the highest concentration of shorter pedestals, resulting in a lower average height for the region compared to the rest of the northern hemisphere. (4) Pedestals in close proximity to each other can have significantly different heights; we see examples of pedestal craters less than 20 km apart that have a height difference of more than 80 m. This is especially common in Utopia Planitia. As will be discussed later, this heterogeneity in regional pedestal heights suggests that pedestals are likely forming from multiple distinct episodes of obliquity excursions.

4. Relationship between Heights and other Pedestal Attributes

In addition to pedestal heights, we have measured three other key pedestal crater attributes (Kadish et al., 2009). These include the diameter of the crater bowl, pedestal to crater radius ratio (P/C ratio – similar to “ejecta mobility ratio” for layered ejecta morphologies) (e.g. Mougini-Mark, 1979; Barlow, 2004), and pedestal circularity value (equivalent to “lobateness” for layered ejecta morphologies) (e.g. Barlow, 1994), where:

$$\text{P/C ratio} = (\text{farthest extent of pedestal})/(\text{crater radius}) \quad (\text{EQ 1})$$

$$\text{Pedestal Circularity} = (\text{pedestal perimeter})/(4\pi(\text{pedestal area}))^{1/2} \quad (\text{EQ 2})$$

These three attributes are established by the impact and armoring processes. The P/C ratio is dependent on the size of the crater and the radial extent of the armoring, while the pedestal circularity is solely dependent on the radial symmetry of the armoring. If the pedestal height is determined exclusively by the thickness of the ice-rich target material, then the height should be independent of both the impact and armoring process, and therefore be independent of the P/C ratio and the pedestal circularity.

To test these potential relationships between pedestal crater traits, we have plotted pedestal heights against each of the other three attributes (Fig. 6). The correlation coefficients of these graphs are all positive values less than 0.09; we observe no statistically significant relationship between the pedestal height and the crater size, pedestal size, or pedestal shape. While this does not guarantee that pedestal height is solely the result of the thickness of the target deposit, it greatly reduces the possibility that our data have any bias from the cratering and/or armoring processes. It should be noted that these results do not favor one pedestal crater formation mechanism over another. Both the eolian deflation model and the sublimation model predict that the pedestal height is determined by the thickness of the target layer and not the impact process. We thus present these data not to further our support for the sublimation model,

but to provide additional support for our fundamental assertion that pedestal heights can be used to approximate the thicknesses of regional paleodeposits.

5. Discussion

5.1. Geographic Extent of the Ice-Rich Deposit

We have shown that the heights and locations of pedestal craters can provide insight into both the geographic extent and thickness of the mid-latitude ice-rich deposit from which the pedestals formed. Given the sublimation-driven formation mechanism, we would expect that the highest concentrations of pedestal craters delineate regions where the ice-rich deposit persisted for the longest period of time, and the tallest pedestal craters highlight where the deposit reached the greatest thickness.

In our study region, there are approximately 3.6 times more pedestal craters in the northern hemisphere than in the southern hemisphere. If the regional concentration of pedestal craters is viewed as an estimate of the duration of snow/ice cover, then the geographic distribution (Fig. 4) suggests that the ice-rich deposit persisted for longer in the northern mid latitudes. Within the northern hemisphere, the ice-rich deposit was widespread and persisted for the longest in Utopia Planitia. Acidalia and Arcadia Planitia were likely also covered by long-standing ice-rich deposits. The deposit was present for a much shorter duration of time in the Alba Fossae region. In the southern hemisphere, the deposit remained for the longest period of time in Malea Planum, which has roughly the same population density as Arcadia Planitia. The deposit was emplaced for much shorter durations near Terra Cimmeria and Terra Sirenum.

The distribution of pedestal heights, however, suggests that the emplacement duration and maximum thickness are not directly correlated. The locations of mid-latitude pedestals taller than 80 m (Fig. 4d-f) reveal that the thickest deposits accumulated in Utopia Planitia, Acidalia Planitia, and Malea Planum. The maximum pedestal heights in these regions are 131 m, 152 m, and 192 m respectively. These data show that, although the ice-rich material may have been present the longest in Utopia Planitia, the thickest accumulations may have been briefly present in Malea Planum, and to a lesser extent, Acidalia Planitia. In addition, Arcadia Planitia, which has a higher concentration of pedestal craters than Acidalia, has no pedestals taller than 100 m, suggesting a long-standing deposit formed by steady but low accumulation rates. The Alba Fossae region, which has a low pedestal crater population density, also lacks pedestals taller than 100 m, but has more pedestals that are 50-80 m tall than 20-50 m tall. This implies a short-lived ice-rich deposit that accumulated rapidly, remained at maximum thickness for the majority of its lifetime, and then quickly sublimated.

The absence of a latitude-dependent change in average pedestal height, as mentioned in section 3, may have important implications for the nature of the ice-rich paleodeposits. This trend, in conjunction with noted variations in longitudinal thickness, may suggest that the deposits that produced the pedestal crater population are not the result of simple migration of volatiles from the poles to the mid latitudes during periods of higher obliquity (Head et al., 2003), which might produce taller pedestals at higher latitudes. Rather, these deposits could be regional in nature, with peak accumulation zones occurring due to mesoscale changes in topography and wind, resulting in deposits centered across a variety of latitudes. We find this to be unlikely, however, given the

dominant latitude-dependence of climatic factors. Instead, we interpret this trend to be a statistical result of averaging the heights of a large population of short pedestals (20 to 50 m) with a small population of tall pedestals (>80 m); short pedestals outnumber tall pedestals by 1508 to 126, or a ratio of ~12:1. A qualitative assessment of the geographic distribution suggests that short pedestals have a high population density at all latitudes where pedestal craters can form, excluding the MFF, while tall pedestals tend to be restricted to the higher latitudes within our study boundaries (Fig. 4). This distribution is consistent with a climate scenario where the thickest paleodeposits accumulated and were maintained for the longest periods of time poleward of ~50° latitude in both hemispheres, while thinner, more transient deposits accumulated between 35° and 50° latitude (e.g. Head et al., 2003).

Climate modeling research can be used in tandem with our empirical data to strengthen our interpretations regarding mid-latitude accumulations of ice-rich material. Recent climate modeling research (Madeleine et al., 2009) using an equatorial source of ice on the flanks of the Tharsis volcanoes (Forget et al., 2006) has shown that glaciations can readily occur in the northern mid latitudes. The model produces ice accumulation rates of ~10 mm/yr given a moderate obliquity (25-35°) (Madeleine et al., 2009). This result is supported by previous climate modeling research, which has shown that during periods of moderate obliquity (35°), the zone of water-ice stability extends to the mid latitudes, and at higher obliquities (45°), water-ice is stable at tropical latitudes (Richardson and Wilson, 2002; Mischna et al., 2003). We must be cautious when comparing our results to any given modeling output due to the high number of variables; the parameter space used by Madeleine et al. (2009) includes the orbital eccentricity,

obliquity, areocentric longitude of the Sun at perihelion, dust optical depth, and location of the surface water-ice reservoir. Our pedestal crater distribution does, however, closely match the regions in the northern mid latitudes predicted to have highest accumulation rates under dusty conditions at 35° obliquity. This output used an eccentricity of 0.1 and an aphelion during the northern summer, and yields net ice accumulation of 10-16 mm/yr in western Utopia Planitia and rates of 8-12 mm/yr in Acidalia and Arcadia Planitia (see figure 7 in Madeleine et al., 2009). Continued modeling work will further constrain the orbital and atmospheric conditions necessary to form the deposits that produced the pedestal crater population.

5.2. Timing and Recurrence of the Ice-Rich Deposit

The geographic distribution of the pedestal craters and the proximity relationships between pedestals of different heights constrain the timing and recurrence of the mid-latitude ice-rich deposit. As discussed, we commonly observe pedestals in close proximity (10s of km) that are up to 80 m different in height. In addition to these examples, we have identified more than 30 instances of pedestal craters that are partially draped over the scarps or completely superposed on the surfaces of other pedestal craters (Figs. 3b,7-9; also see figure 16 in Kadish et al., 2009). While pedestals in close proximity that have extremely different heights could potentially form from the same deposit at different times – one during the early stage of accumulation or late stage of sublimation and another during maximum thickness of the deposit – it is much more difficult to explain draped pedestals, which show the topographic influence of the underlying pedestal scarp. These cases of draped pedestals require one pedestal to form

completely, followed by an impact into a subsequent deposit that contours to the topography of the underlying pedestal (Fig 8,9). In the context of this evidence for recurring depositions of a mid-latitude ice-rich deposit, it is highly likely that the pedestal crater population measured in this study formed from multiple episodes of accumulation and sublimation.

The recurrence of this mid-latitude ice-rich deposit is supported by the known variations in Martian obliquity over the past 20 Myr (Laskar et al., 2004). The obliquity of Mars over the last 5 Myr has oscillated between 15° and 35°, and during the previous 15 Myr, it oscillated between 25° and 45°. Given the modeled exchange of volatiles between the poles, mid latitudes, and equatorial regions at these obliquities (e.g. Forget et al., 2006; Madeleine et al., 2009) and the high frequency of the recent obliquity variations (e.g. Laskar et al., 2004; Levrard et al., 2004), it is expected that ice-rich material has been repeatedly emplaced and removed at mid latitudes throughout the Late Amazonian. Assuming an accumulation rate of 10 mm/yr (Madeleine et al., 2009), it would take only 5 kyr to form a 50 m deposit, which is thick enough to produce an average pedestal. Even the tallest mid-latitude pedestals (<200 m) could form from deposits that accumulated in under 20 kyr.

5.3. Pedestals with Marginal Pits

Some mid-latitude pedestal craters, concentrated in Utopia Planitia and Malea Planum, have pits along their marginal scarps (Figs. 7,8; also see figure 2 in Kadish et al., 2008). As mentioned, these pits represent a loss of material from the pedestal itself; the pits occur in the scarps and do not excavate to depths lower than the surrounding terrain

(Kadish et al., 2008). Contrary to recent research on morphologically similar pits in Utopia Planitia (Soare et al., 2008), we see no evidence for melting associated with these pits that would lead us to identify them as thermokarst lakes/alases.

The relatively even distribution of pits around pedestals – no preferred slope-facing orientation– provides important information about the sublimation process and the evolution of scarp formation and retreat. The even distribution indicates that asymmetric warming from insolation is not the primary factor responsible for where sublimation occurs. The slopes of pedestal margins are shallow, ranging from only 3° to 7°. For comparison, martian gullies, which exist predominantly on pole-facing slopes of crater walls, form on surfaces with an average slope of 26.5° (Dickson et al., 2007). The effect of uneven warming of pedestal scarp slopes is further diminished by the fact that pedestals with pits are located almost exclusively poleward of 50°N and 60°S, where the latitude-dependent temperature gradient is much less pronounced.

Although the sublimation rate of buried ice depends primarily on temperature (e.g. Mellon and Jakosky, 1993), it also is influenced by other factors, including atmospheric humidity, wind speed, till thickness, and surface albedo (e.g. Schorghofer and Aharonson, 2005; Kowalewski et al., 2006). As such, insolation is a contributing factor, but may not always be the dominant one. While the rate of diffusion of volatiles has important implications for the preservation of pedestal craters, it is not currently possible to constrain it quantitatively. Atmospheric conditions and regional temperatures have not been robustly established during the obliquity excursions necessary to produce pedestals. We also do not know the permeability of the armoring and how it varies as a

function of distance from the crater rim. Future work using 1-D modeling and a better understanding of paleoclimatic conditions will help to assess these sublimation rates.

The presence of the pits guarantees that local meteorological conditions are conducive to sublimation, and insolation likely contributes to this. However, the radially symmetric distribution suggests that geologic factors play a more important role in establishing where the pits form. Specifically, the tapering or absence of the armoring along pedestal margins likely allows volatiles within the pedestal to diffuse into the atmosphere. In addition, the absence of pits on the pedestal surface supports the notion that the armoring is capable of significantly inhibiting sublimation of the underlying volatiles. If pits can form on both the equator- and pole-facing slopes of pedestal scarps, but not on the flat pedestal surfaces, which receive more insolation than the pole-facing scarps, then the thickness and/or degree of induration of the armoring must inhibit vapor diffusion, and thus drastically reduce the sublimation rate.

Although we do not frequently see evidence for significant mass wasting along pedestal margins, perhaps due to the shallowness of their slopes, it is likely that pit formation leads to scarp retreat, reducing the size of the pedestal (Fig. 7,10). Loss of volatiles from the edges of the pedestal results in downslope movement of material, which could degrade the integrity of the armoring along the perimeter of the pedestal. This would result in a positive feedback loop, allowing further pit formation, leading to continued scarp retreat. While it is difficult to assess the degree to which a pedestal's size has been reduced due to sublimation along the margins, we do see examples of pit coalescence, resulting in moat-like structures that represent a substantial loss of volume from the pedestal (Kadish et al., 2008). In addition, we have observed examples of highly

degraded, non-circular pedestals that contain pits, providing evidence that repeated pit formation via sublimation is capable of completely removing pedestals (Fig. 10).

In cases where we see stratigraphic relationships between pedestals, the overlying pedestal often preserves the underlying pedestal at the point of overlap, truncating pits or preventing pit formation along that portion of the underlying pedestal's margin. While superposed pedestals are themselves subject to sublimation and erosion (Figs. 3b, 7c), the additional armoring they provide is clearly effective in increasing the longevity of the underlying pedestal. This results in pedestal morphologies that appear to have been much larger, but have since sublimated and been eroded except where the overlying pedestals preserve their initial extents (Fig. 7).

The average height of pedestals with pits is 82.5 m, greatly exceeding the average height for the overall population. This indicates that having a greater scarp surface area is more conducive to sublimation from the margins of the pedestal, further supporting our interpretation that sublimation is limited by the geologic properties of the pedestal surface; if sublimation were controlled solely by insolation, then pedestals with pits should have the same average height as those without pits. The geographic restriction of these taller, pitted pedestals to Utopia Planitia and Malea Planum implies that these regions are unique in the timing and/or thickness of accumulation of the ice-rich deposit. Continued work in these geographic areas will explore whether these regions are more conducive to thicker deposits, which is consistent with the discussion in section 5.1, or perhaps maintained deposits more recently than other regions and are thus still undergoing active sublimation.

6. Conclusions

On the basis of the sublimation-driven formation mechanism for pedestal craters, the current heights of the pedestals offer direct evidence for the approximate elevation of the icy paleosurface at the time of impact. The pedestal heights act as a proxy for the thickness of the paleodeposit, perhaps modified somewhat by subsequent effects including compaction, erosion, mantling, and sublimation. We measured the heights of 2300 pedestals between 60°N and 65°S using MOLA data (Fig. 4). Through the analysis of these data, in conjunction with previously measured pedestal crater attributes (Kadish et al., 2009), we conclude that: (1) While pedestals can reach up to ~260 m in height, 82% are <60 m and only ~2% are >100 m (Fig. 5a). (2) The mean mid-latitude pedestal heights are 48.0 m in the northern hemisphere and 40.4 m in the southern hemisphere (Table 1). (3) Neither hemisphere shows any significant variation in average pedestal height as a function of latitude. However, taller pedestals (>80 m) tend to be restricted to latitudes poleward of 50°, whereas shorter pedestals (20 to 50 m) have high population density throughout the mid latitudes. Longitudinal variations in average pedestal height are present (Fig. 5b-d), with the tallest pedestals located in Utopia and Acidalia Planitia and Malea Planum. (4) Pedestal height has no statistically significant correlation with pedestal crater diameter, P/C ratio, or pedestal circularity (Fig. 6). This supports the interpretation that the final height of a pedestal is determined by the thickness of the ice-rich target deposit and not the impact process. (5) Pedestal craters with significantly different heights are found in close proximity to each other. Pedestals can also be partially draped or completely superposed on other pedestals (Figs. 7,8). This implies multiple distinct episodes of the deposition of a mid-latitude, ice-rich layer. (6) Pedestal

craters with marginal sublimation pits have a mean height of 82.5 m. These tall craters, which are located exclusively in Utopia Planitia and Malea Planum, indicate that these geographic regions may be more conducive to the accumulation of ice-rich material, or may have experienced more recent emplacement of an ice-rich deposit.

Acknowledgments

The authors are grateful for financial support from NASA Mars Data Analysis Program (MDAP) grant NNX07AN95G and NASA Applied Information Systems Research Program NNX08AC63G to JWH, and MDAP grant NAG512510 to NGB. SJK would like to thank Jay Dickson and Caleb Fassett for productive dialogue on sublimation processes, as well as Joseph Boyce and an anonymous reviewer for constructive comments that strengthened this manuscript.

References

- Arvidson, R.E., Coradini, M., Carusi, A., Coradini, A., Fulchignoni, M., Federico, C., Funicello, R., Salomone, M., 1976. Latitudinal variation of wind erosion of crater ejecta deposits on Mars. *Icarus* 27, 503-516.
- Barlow, N.G., 1994. Sinuosity of Martian rampart ejecta deposits. *J. Geophys. Res.* 99, 10927-10935.

Barlow, N.G., 2004. Martian subsurface volatile concentrations as a function of time: Clues from layered ejecta craters. *Geophys. Res. Lett.* 31, doi:10.1029/2003GL019075. L05703.

Barlow, N.G., 2006. Impact craters in the northern hemisphere of Mars: Layered ejecta and central pit characteristics. *Meteorit. Planet. Sci.* 41(10), 1425-1436.

Barlow, N.G., Boyce, J.M., Costard, F.M., Craddock, R.A., Garvin, J.B., Sakimoto, S.E.H., Kuzmin, R.O., Roddy, D.J., Soderblom, L.A., 2000. Standardizing the nomenclature of Martian impact crater ejecta morphologies. *J. Geophys. Res.* 105, 26733-26738.

Barlow, N.G., Koroshetz, J., Dohm, J.M., 2001. Variations in the onset diameter for Martian layered ejecta morphologies and their implications for subsurface volatile reservoirs. *Geophys. Res. Lett.* 28, doi:10.1029/2000GL012804.

Bleacher, J.E., Sakimoto, S.E.H., Garvin, J.B., Wong, M., 2003. Deflation/erosion rates for the Parva Member, Dorsa Argentea Formation and implications for the south polar region of Mars. *J. Geophys. Res.* 108, doi:10.1029/2001JE001535.

Boyce, J.M., Barlow, N.G., Tornabene, L.L., 2008. Lonar Crater on Mars: Implications of its Unusual Morphology. *Lunar Planet. Sci.* [CD-ROM], XXXIX, Abstract 1406.

Dickson, J.L., Head, J.W., Kreslavsky, M., 2007. Martian gullies in the southern mid-latitudes of Mars: Evidence for climate-controlled formation of young fluvial features based upon local and global topography. *Icarus* 188, 315-323.

Forget, F., Haberle, R.M., Montmessin, F., Levrard, B., Head, J.W., 2006. Formation of glaciers on Mars by atmospheric precipitation at high obliquity. *Science* 311, 368-371.

Head, J.W., Mustard, J.F., Kreslavsky, M.A., Milliken, R.E., Marchant, D.R., 2003. Recent ice ages on Mars. *Nature* 426, 797-802.

Kadish, S.J., Head, J.W., Barlow, N.G., Marchant D.R., 2008. Martian pedestal craters: Marginal sublimation pits implicate a climate-related formation mechanism. *Geophys. Res. Lett.* 35, doi:10.1029/2008GL034990. L16104.

Kadish, S.J., Barlow, N.G., Head, J.W., 2009. Latitude Dependence of Martian Pedestal Craters: Evidence for a Sublimation-Driven Formation Mechanism. *J. Geophys. Res.* 114, doi:10.1029/2008JE003318. E10001.

Kowalewski, D.E., Marchant, D.R., Levy, J.S., Head, J.W., 2006. Quantifying low rates of summertime sublimation for buried glacier ice in Beacon Valley, Antarctica. *Antarct. Sci.* 18(3), doi:10.1017/S0954102006000460.

Laskar, J., Correia, A.C.M., Gastineau, M., Joutel, F., Levrard, B., Robutel, P., 2004. Long term evolution and chaotic diffusion of the insolation quantities of Mars. *Icarus* 170(2), 343-364.

Levrard, B., Forget, F., Montmessin, F., Laskar, J., 2004. Recent ice-rich deposits formed at high latitudes on Mars by sublimation of unstable equatorial ice during low obliquity. *Nature* 431, 1072-1075.

Madeleine, J.-B., Forget, F., Head, J.W., Levrard, B., Montmessin, F., Millour, E., 2009. Amazonian northern mid-latitude glaciation on Mars: A proposed climate scenario. *Icarus* 203, 390-405.

McCauley, J.F., 1973. Mariner 9 Evidence for Wind Erosion in the Equatorial and Mid-latitude Regions of Mars. *J. Geophys. Res.* 78, 4123-4137.

Mellon, M.T., Jakosky, B.M., 1993. Geographic Variations in the Thermal and Diffusive Stability of Ground Ice on Mars. *J. Geophys. Res.* 98, 3345-3364.

Mischna, M.A., Richardson, M.I., Wilson, R.J., McCleese, D.J., 2003. On the orbital forcing of Martian water and CO₂ cycles: A general circulation model study with simplified volatile schemes. *J. Geophys. Res.* 108, doi:10.1029/2003JE002051.

Mouginis-Mark, P., 1979. Martian fluidized crater morphology – Variations with crater size, latitude, altitude, and target material. *J. Geophys. Res.* 84, 8011-8022.

Mutch, P., Woronow, A., 1980. Martian rampart and pedestal craters' ejecta-emplacement: Coprates quadrangle. *Icarus* 41(2), 259-268.

Osinski, G.R., 2006. Effect of volatiles and target lithology on the generation and emplacement of impact crater fill and ejecta deposits on Mars. *Meteorit. Planet. Sci.* 41(10), 1571-1586.

Richardson, M.I., Wilson, R.J., 2002. Investigation of the nature and stability of the Martian seasonal water cycle with a general circulation model. *J. Geophys. Res.* 107, doi:10.1029/2001JE001536.

Schorghofer, N., Aharonson, O., 2005. Stability and exchange of subsurface ice on Mars. *J. Geophys. Res.* 110, doi:10.1029/2004JE002350.

Schultz, P.H., Lutz, A.B., 1988. Polar wandering of Mars. *Icarus* 73, 91-141.

Schultz, P.H., Mustard, J.F., 2004. Impact melts and glasses on Mars. *J. Geophys. Res.* 109, doi:10.1029/2002JE002025.

Soare, R.J., Osinski, G.R., Roehm, C.L., 2008. Thermokarst lakes and ponds on Mars in the very recent (late Amazonian) past. *Earth Planet. Sci. Letters* 272, 382-393.

Tanaka, K.L., Rodriguez, J.A.P., Skinner Jr., J.A., Bourke, M.C., Fortezzo, C.M., Herkenhoff, K.E., Kolb, E.J., Okubo, C.H., 2008. North polar region of Mars: Advances in stratigraphy, structure, and erosional modification. *Icarus* 196(2), 318-358.

Thomson, B.J., Schultz, P.H., 2007. The geology of the Viking Lander 2 site revisited. *Icarus* 191(2), 505-523.

Wrobel, K., Schultz, P., Crawford, D., 2006. An atmospheric blast/thermal model for the formation of high-latitude pedestal craters. *Meteorit. Planet. Sci.* 41(10), 1539-1550.

Tables

Table 1. Statistics for pedestal heights on Mars (meters).

	Median	Mean	Standard Deviation
All Mid-Latitude	44.0	47.7	22.5
Northern Mid-Latitude	45.0	48.0	18.8
Southern Mid-Latitude	35.0	20.4	19.2
Equatorial (MFF)	95.0	114.4	53.0

Figure Captions

Figure 1 – A schematic diagram of the primary steps in the sublimation model of pedestal crater formation (altered from Kadish et al., 2009), highlighting that the thickness of the target material, which is an ice-rich deposit, is the eventual height of the pedestal. The steps are: 1) Impact into an ice-rich deposit that has accumulated at mid latitudes during a period of higher obliquity over the martian silicate regolith. 2) The impact distributes ejecta and triggers an armoring process. 3) This results in a radially-symmetric armored surface around the crater rim that exceeds the extent of the ejecta deposit. 4) During return to lower obliquity, volatiles sublimate from the unarmored intercrater terrain, lowering the elevation of the surrounding terrain. Armoring inhibits sublimation from beneath the pedestal surface, preserving the ice-rich deposit. This results in a typical pedestal crater that is as tall as the initial thickness of the target deposit.

Figure 2 – A perspective view of a pedestal crater. This illustration highlights that: 1) Pedestal craters are elevated above the intercrater plains, with the pedestal height equivalent to the thickness of a past ice-rich paleodeposit. 2) The pedestal interior preserves the paleodeposit under its armored surface, and thus maintains ice-rich material. 3) The ejecta deposit resulting from the impact is much smaller in radial extent than the armored pedestal surface.

Figure 3 – Examples of pedestal craters shown in CTX images with MOLA topography and corresponding profiles from MOLA shot data. A) A 2.1-km-diameter crater located in western Utopia Planitia at 48.1°N, 101.3°E (P18_008214_2288). B) A 2.8-km-

diameter crater located west of Malea Planum at 57.2°S, 36.0°E (P15_007004_1222).

Note the remnants of a smaller pedestal crater, 0.9 km in diameter, completely superposed on the northern end of the larger pedestal. C) A profile of the pedestal crater in (A), showing the individual MOLA points (VE = 67x). The surrounding topography is uneven, resulting in heights of 49 m and 72 m on the northern and southern sides of the pedestal respectively. The calculated height of the pedestal is 62 m. D) A profile of the pedestal crater in (B), showing the MOLA shot data (VE = 40x). The local topography slopes downhill from SW to NE. This slope produces greater pedestal heights on the downhill (northern) side, as shown by the measurements of 113 m and 97 m on the northern and southern sides respectively. The calculated height of the pedestal is 107 m.

Figure 4 – The geographic distribution of pedestal heights. Pedestal craters were primarily identified through a survey of all THEMIS IR images with center coordinates equatorward of 60°N and 65°S (Kadish et al., 2009). As such, pedestal craters poleward of these latitudes were generally not analyzed in this study – lines on the maps indicate the boundaries of the study region. The populations have been divided into six groups to show where populations of specific heights are concentrated: A) 20-40 m, B) 40-60 m, C) 60-80 m, D) 80-100 m, E) 100-120 m, and F) 120-260 m. Regions discussed in this paper are labeled on map (F), with the following abbreviations: AcP = Acidalia Planitia, AF = Alba Fossae region, ArP = Arcadia Planitia, MFF = Medusae Fossae Formation, MP = Malea Planum, TC = Terra Cimmeria, TS = Terra Sirenum, and UP = Utopia Planitia.

Figure 5 – The quantitative results of this study in the form of: A) A histogram of the pedestal height distribution for all 2300 pedestals measured. The median, mean and standard deviation of the pedestal heights for the population are shown. B) Mean pedestal heights as a function of latitude. Pedestals are slightly taller in the northern than in the southern hemisphere, but neither shows significant variations as a function of latitude. Equatorial pedestals, located in the MFF, have much greater heights than those at mid latitudes. Error bars in B, C, and D are +/- one standard deviation. C) Mean mid-latitude pedestal heights in the northern hemisphere as a function of longitude. D) Mean mid-latitude pedestal heights in the southern hemisphere as a function of longitude. Because equatorial pedestal craters are confined to the MFF, we have not shown their variations as a function of longitude.

Figure 6 – Plots of pedestal height versus: A) crater diameter, B) P/C ratio, and C) pedestal circularity. These attributes, measured and described by Kadish et al. (2009), are the result of the impact/armoring process. The correlation coefficients for linear fits to the data are shown in the top right corner of each plot. These extremely low values confirm that there is no statistically significant correlation between the pedestal heights and the impact size or extent of the armoring.

Figure 7 – Examples of pedestal craters that have marginal pits on their scarps and smaller pedestal craters draped or superposed on their margins. These cases show that superposed pedestal craters, which form from subsequent ice-rich deposits, are capable of partially preserving the radial extent of the underlying pedestal. The underlying pedestals

gradually recede via the formation of sublimation pits, but are preserved due to subsequent armoring from the emplacement of the superposed pedestals. In all examples, the farthest extents of the underlying pedestals are directly adjacent to the superposed pedestals, as indicated by white arrows. A) Pedestal craters (60.3°N, 188.6°E) shown in CTX image B02_010584_2407 with MOLA topography. The black arrow identifies possible mass wasting of the pedestal margin, where blocky material is contained in a shallow marginal pit. B) Pedestal craters (57.1°N, 78.5°E) shown in THEMIS VIS image V21415004 with MOLA topography. Black arrows point to the distal rim of the ejecta deposit, which is clearly less extensive than the armored pedestal surface. C) Pedestal craters (56.9°N, 106.9°E) shown in a THEMIS VIS (V13714004 and V28315004) and HiRISE (ESP_016600_2370) mosaic with MOLA topography. Black arrows identify the distal margin of the ejecta deposit superposed on the pedestal surface.

Figure 8 – An example of a draped pedestal crater. The smaller pedestal crater partially overlaps the larger pedestal crater, truncating the marginal pits in the larger pedestal's eastern scarp. A) A mosaic of THEMIS VIS images V18046009 and V18358008 (61.0°S, 71.0°E). The black box delineates the area shown in part (B). Note that, on both craters, the ejecta deposits are faintly visible, and have radial extents that are less than half of their respective pedestals. B) A mosaic of CTX image B08_012857_1187 and HiRISE image ESP_012857_1185, with MOLA topography. The MOLA data reveal the distinct topographic influence that the larger pedestal has on the smaller, draped pedestal; the buried scarp of the larger pedestal can be readily traced along the surface of the smaller pedestal, as shown by the black dashed line.

Figure 9 – A schematic diagram of the steps necessary to produce a pedestal crater draped over the marginal scarp of another pedestal crater, as seen in figure 8, where the smaller pedestal shows the topographic influence of the larger underlying pedestal. The steps are: 1) The presence of a pre-existing pedestal, which forms via the process shown in figure 1. 2) An obliquity excursion leads to the accumulation of a new ice-rich deposit that contours to the topography of the buried pedestal. 3) An impact occurs into this deposit at a point near the marginal scarp of the buried pedestal. This distributes ejecta and armors the proximal surface, as shown in steps 2 and 3 of figure 1. 4) The fresh crater bowl and armored surface are situated on the ice-rich deposit, stratigraphically above the margin of the underlying pedestal crater. 5) Return to a lower obliquity leads to sublimation of the regional ice-rich deposit, as shown in step 4 of figure 1. The armoring from the fresh crater, however, preserves some of the deposit, yielding a draped pedestal crater that contours to the topography of the underlying pedestal scarp.

Figure 10 – The remnants of what was likely once a much larger pedestal crater, located at 58.2°N, 113.2°E. The CTX mosaic (P20_008754_2395 and P22_009822_2399) with MOLA topography shows that small portions of the pedestal remain preserved to the NW and SE of the infilled crater bowl. The pedestal is still perched more than 80 m above the surrounding terrain, and is surrounded by a halo of material that slopes gradually down to the plains. This supports the interpretation that pedestals sublime and erode from their marginal scarps inward to their crater rims. In this instance, there is a marginal pit located

on the SE portion of the pedestal scarp, and the pedestal surface is lower in elevation in that area.

Figure 1

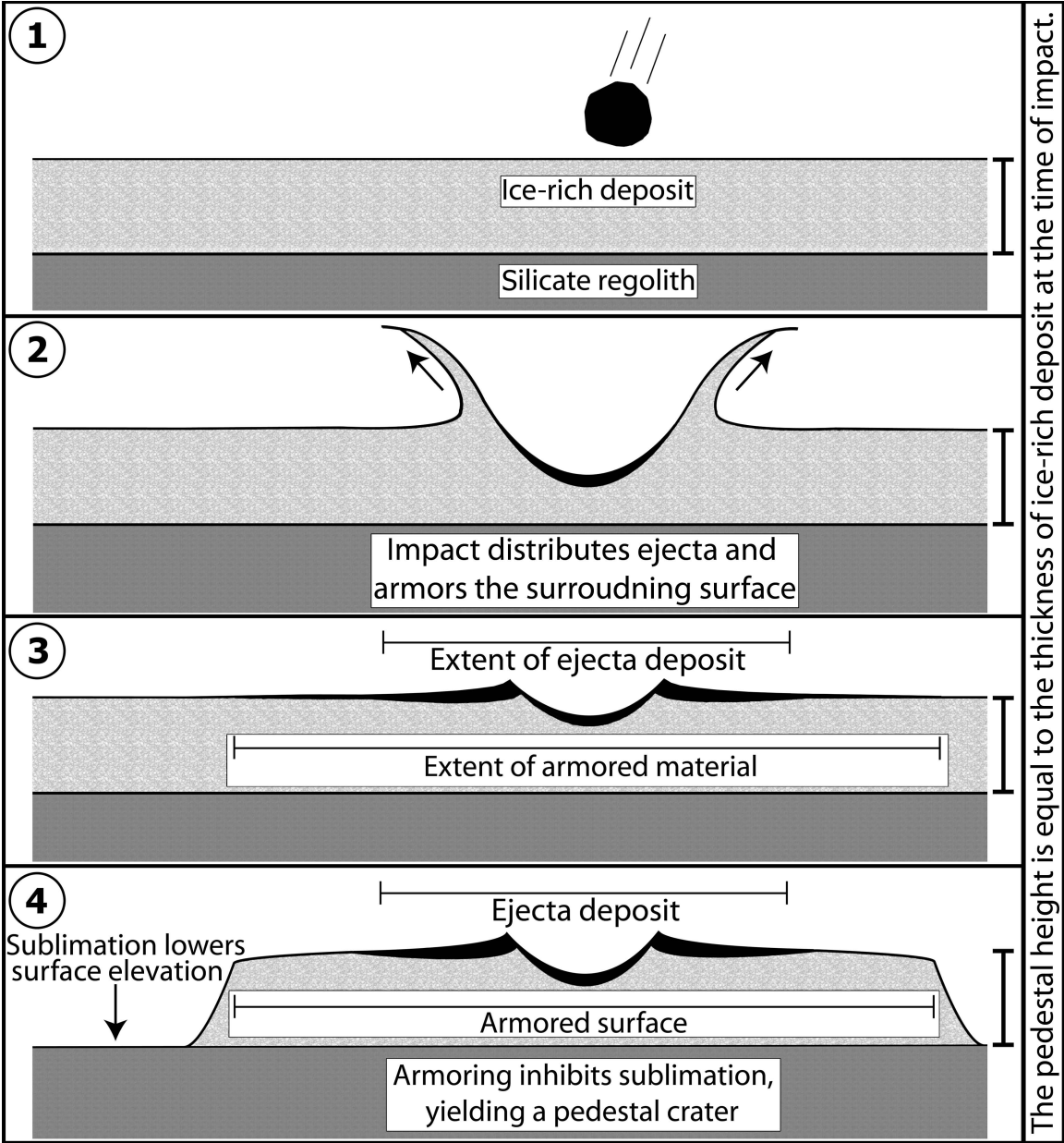


Figure 2

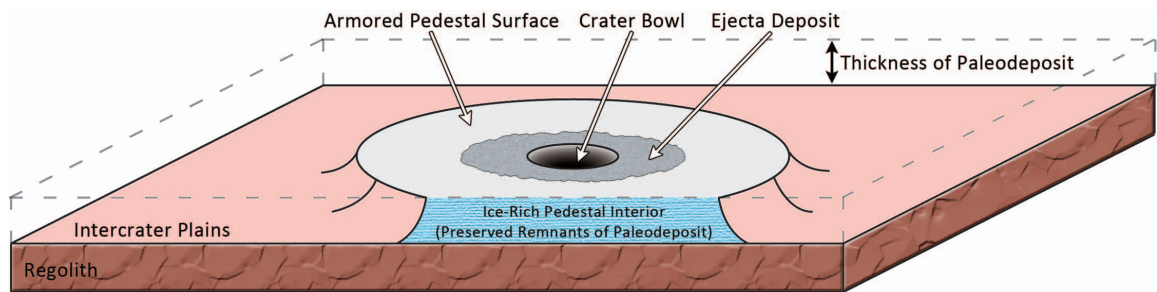


Figure 3

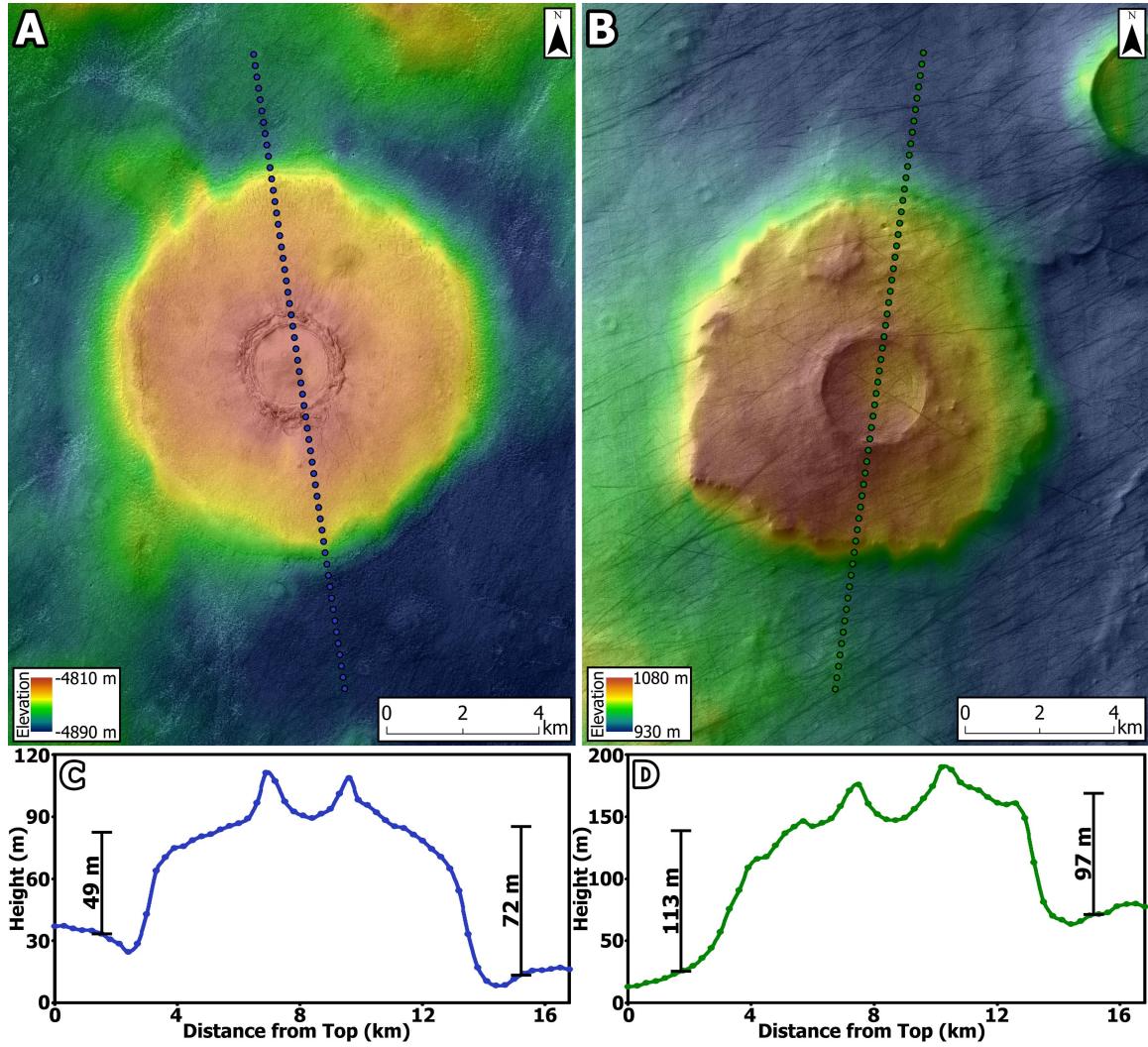


Figure 4

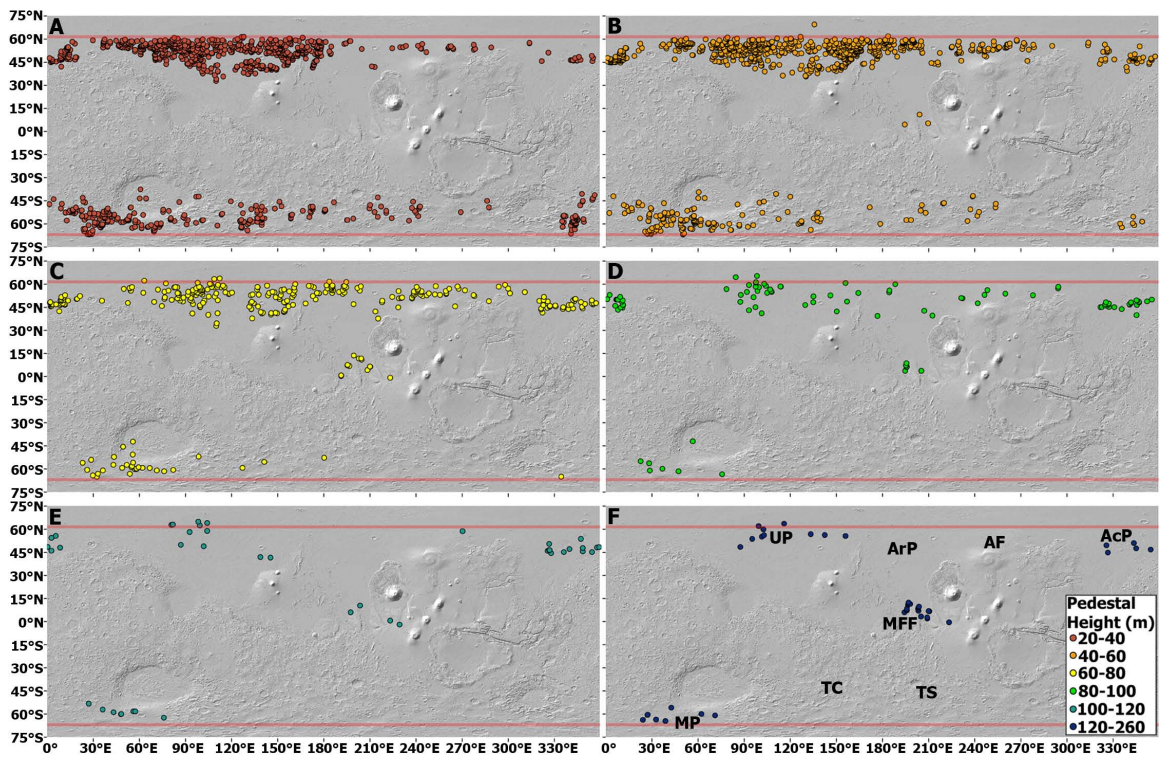


Figure 5

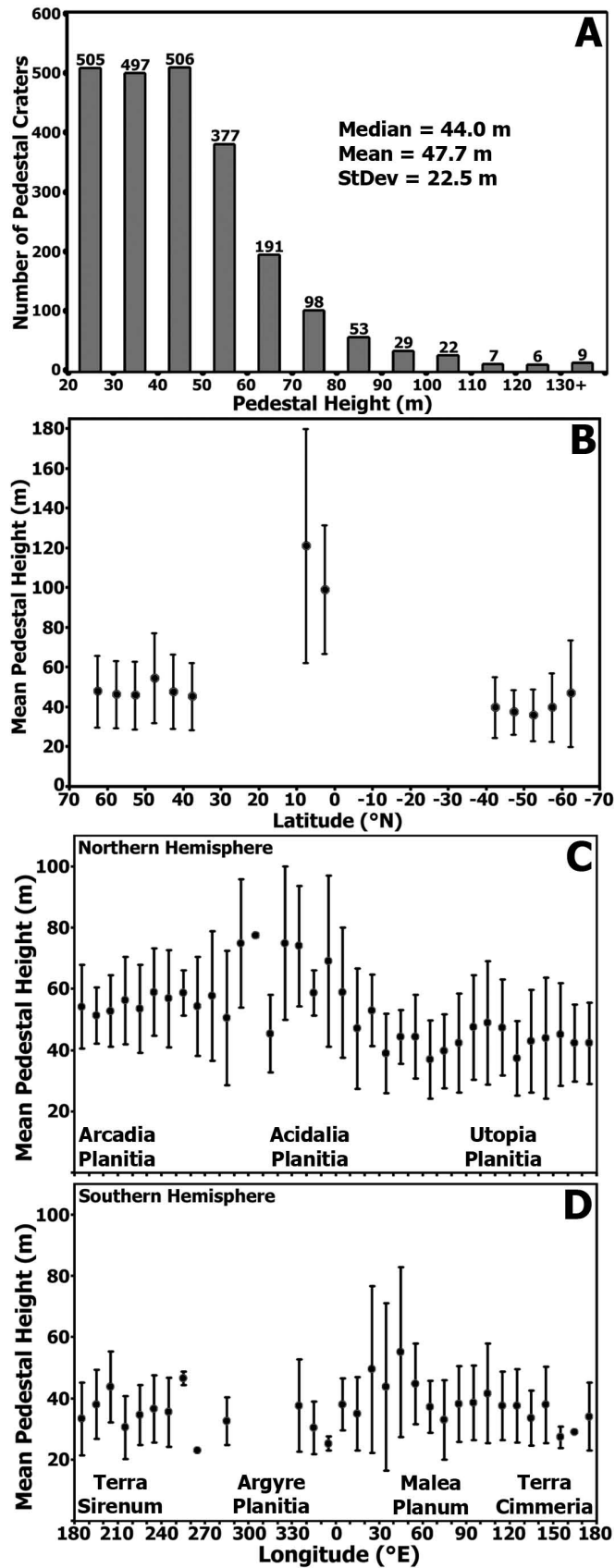


Figure 6

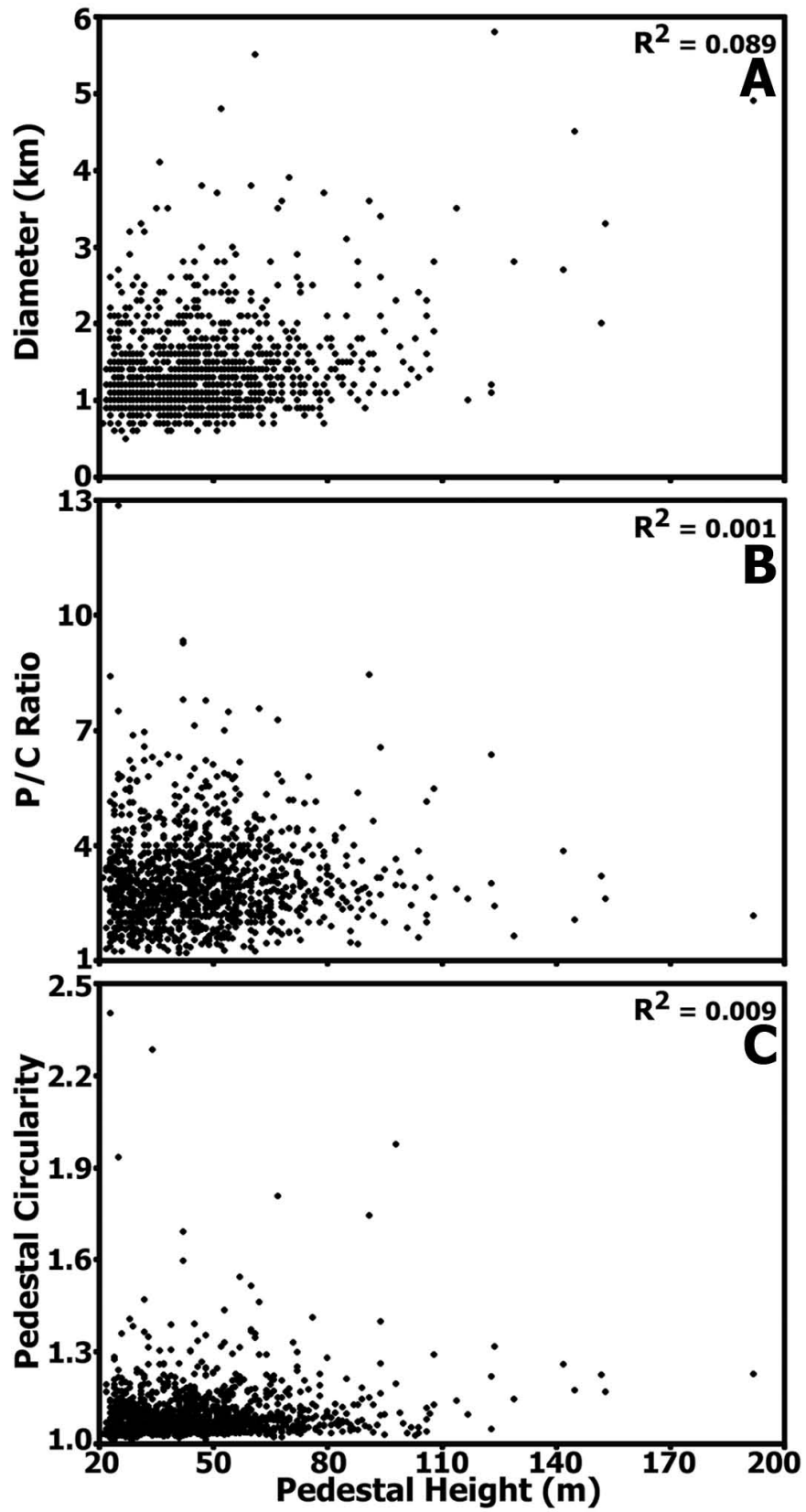


Figure 7

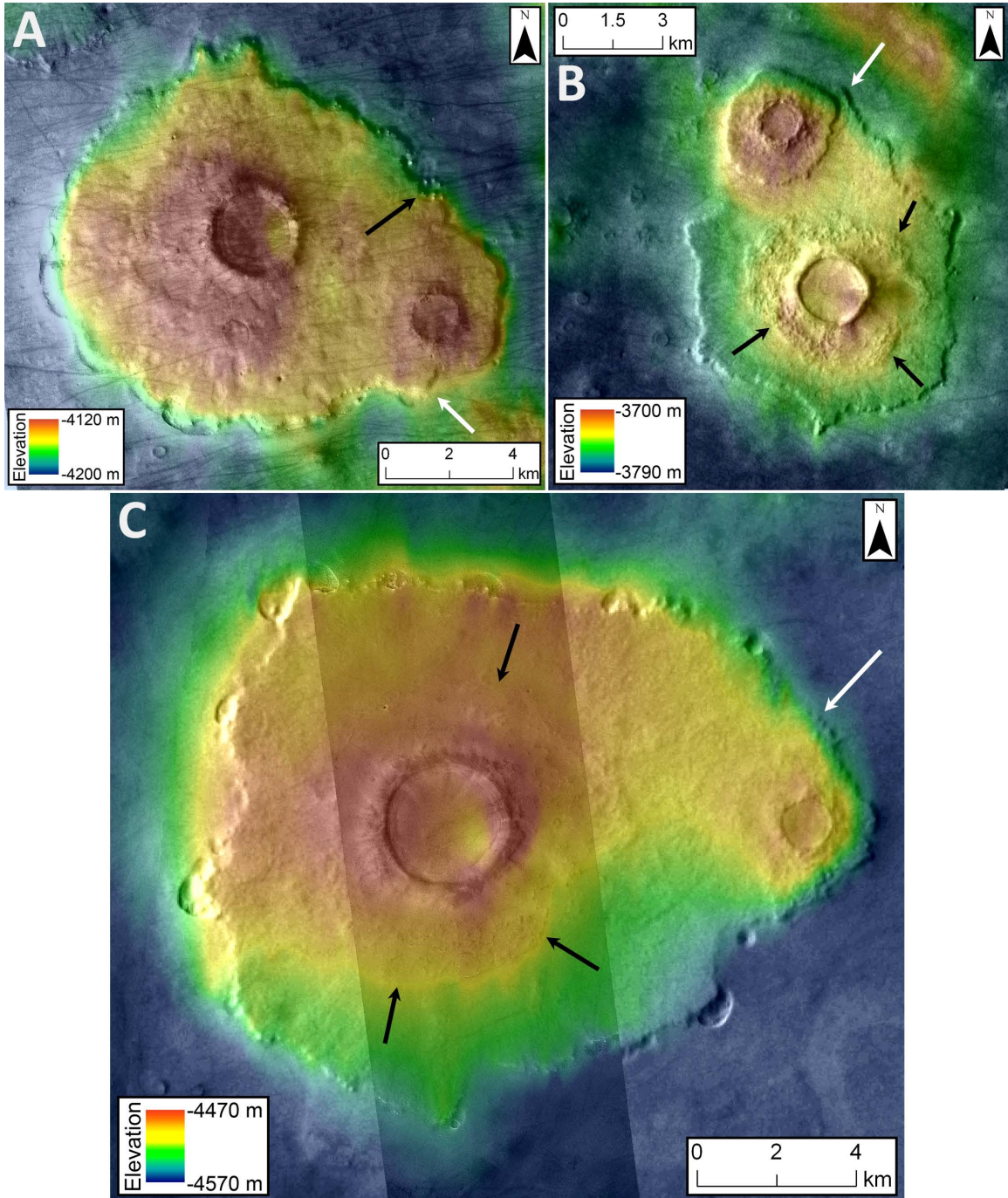


Figure 8

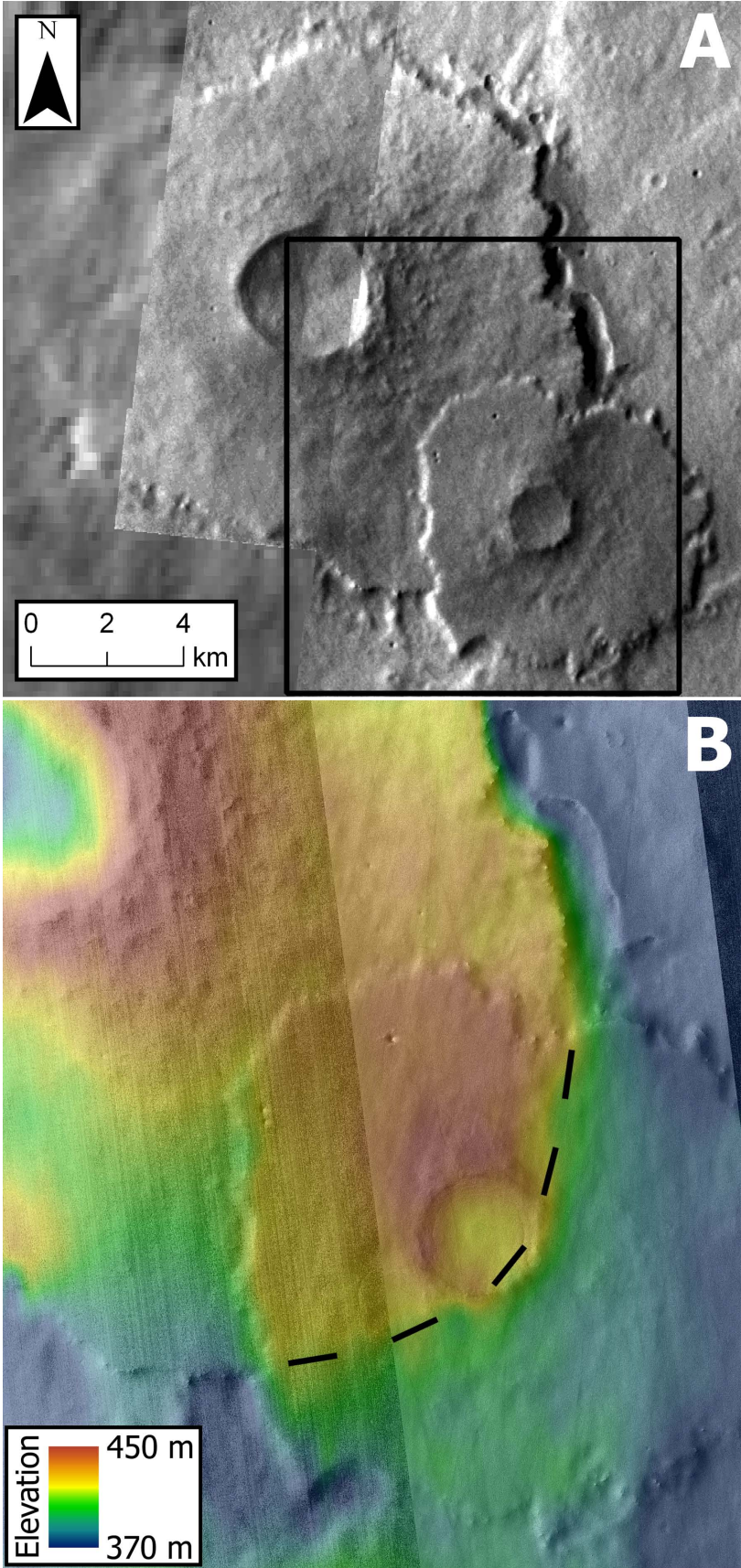


Figure 9

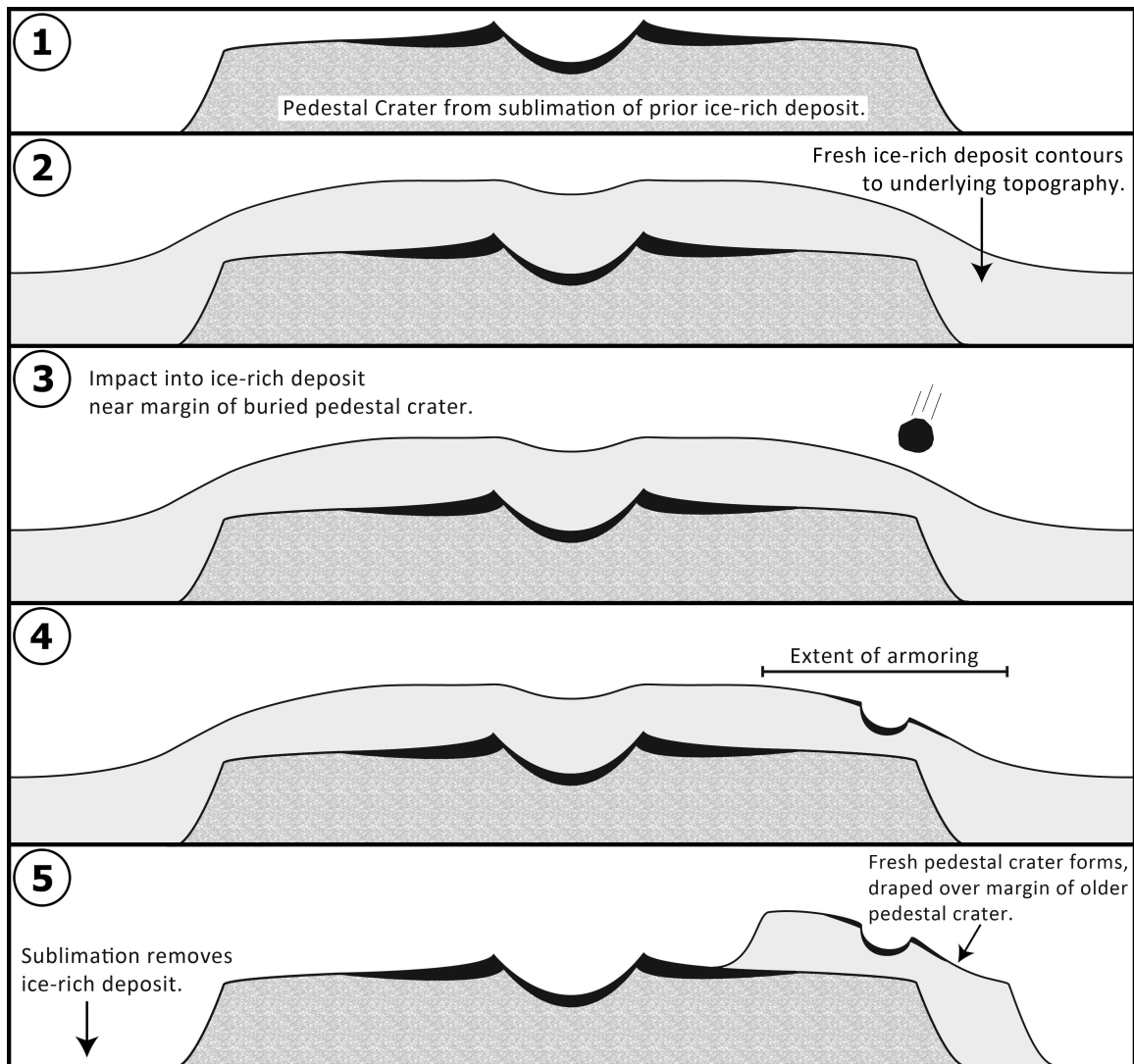
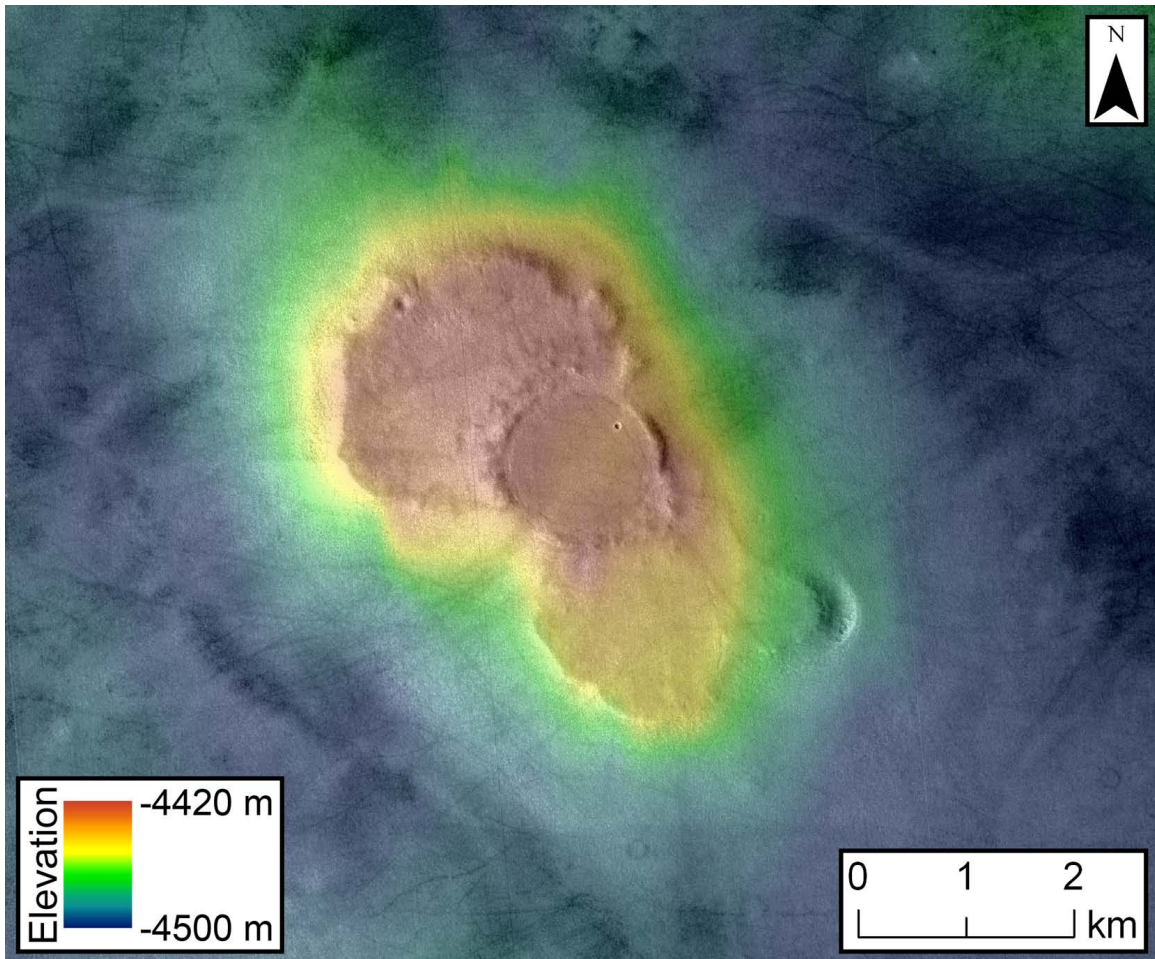


Figure 10



CHAPTER FOUR:

Impacts into Non-Polar Ice-Rich Paleodeposits on Mars:
Excess Ejecta Craters, Perched Craters and Pedestal Craters
as Clues to Amazonian Climate History

Seth J. Kadish^a and James W. Head^a

^aDepartment of Geological Sciences, Brown University, Providence, RI 02912 USA

Under Review In:

Icarus, February 2011

[155]

Abstract

We compare three previously independently studied crater morphologies – excess ejecta craters, perched craters, and pedestal craters – each of which has been proposed to form from impacts into an ice-rich surface layer. Our analysis identifies the specific similarities and differences between the crater types; the commonalities provide significant evidence for a genetic relationship among the morphologies. We use new surveys of excess ejecta and perched craters in the southern hemisphere in conjunction with prior studies of all of the morphologies to create a comprehensive overview of their geographic distributions and physical characteristics. From these analyses, we conclude that excess ejecta craters and perched craters are likely to have formed from the same mechanism, with excess ejecta craters appearing fresh while perched craters have experienced post-impact modification and infilling. Impacts that led to these two morphologies overwhelmed the ice-rich layer, penetrating into the underlying martian regolith, resulting in the excavation of rock that formed the blocky ejecta necessary to armor the surface and preserve the ice-rich deposits. Pedestal craters, which tend to be smaller in diameter, have the same average deposit thickness as excess ejecta and perched craters, and form in the same geographic regions. They rarely have ejecta around their crater rims, instead exhibiting a smooth pedestal surface. We interpret this to mean that they form from impacts into the same type of ice-rich paleodeposit, but that they do not penetrate through the icy surface layer, and thus do not generate a blocky ejecta covering. Instead, a process related to the impact event appears to produce a thin, indurated surface lag deposit that serves to preserve the ice-rich material. These results provide a new basis to identify the presence of Amazonian non-polar ice-rich deposits, to map their

distribution in space and time, and to assess Amazonian climate history. Specifically, the ages, distribution and physical attributes of the crater types suggest that 10s to 100s of meters of ice-rich material has been episodically emplaced at mid latitudes in both hemispheres throughout the Amazonian due to obliquity-driven climate variations. These deposits likely accumulated more frequently in the northern lowlands, resulting in a larger population of all three crater morphologies in the northern hemisphere.

1. Introduction

The classification of crater and ejecta morphologies (Barlow, 2000) in the mid latitudes on Mars has led to the identification of three crater types that have been interpreted as impacts into an ice-rich surface layer. These morphologies include (Table 1): (1) Excess ejecta craters (EE), which are fresh craters that have anomalously voluminous ejecta deposits (Black and Stewart, 2008), (2) Perched craters (Pr), which include all craters that have their ejecta and crater interiors completely elevated above the elevation of the surrounding terrain (e.g. Boyce et al., 2005; Garvin et al., 2000; Meresse et al., 2006), (3) Pedestal craters (Pd), which have their crater interiors perched near the center of a plateau surrounded by an outward-facing marginal scarp (e.g. Barlow, 2005; Kadish et al., 2009).

Each of these morphologies has either ejecta or a pedestal that has a volume greater than that of the interior of the crater below the rim crest. Consequently, a formation mechanism has been proposed for each that involves the presence of a thick ice-rich surface unit at the time of impact, and the eventual preservation of parts of the ice-rich deposit via armoring of the surface or superposition of ejecta. When ice eventually sublimates from the intercrater terrain, most likely due to climate change from obliquity variations (e.g. Head et al., 2003; Levrard et al., 2004), the protective covering inhibits the loss of ice in the region proximal to the crater. This process lowers the elevation of the surrounding terrain, yielding craters that are either topographically perched or that have excessively voluminous ejecta.

The similarities between these morphologies and their proposed formation mechanisms suggest a potential genetic relationship among them. Although the crater

types are not necessarily mutually exclusive from a morphological standpoint – many pedestal craters fit the technical definition of a perched crater – they do exhibit several key distinguishing features that may offer insight into the process of impacting into ice-rich material. In order to address these questions, we undertook new surveys and morphological analyses using recently released high-resolution images. Specifically, we discuss evidence for the possible genetic relationship among EEC, Pr, and Pd based on our new crater size, morphology, and geographic distribution database. In addition, using these new data, we identify and document the key similarities and differences in the characteristics of the three distinct crater types and assess the implications for their formation processes.

2. Morphological Background

2.1. Excess Ejecta Craters

Excess ejecta craters (EE) are, by definition (Black and Stewart, 2008), fresh craters (Figs. 1,2). This criterion is established on the basis of the cavity depth and rim height of a particular crater, which must exceed specified cutoff values for a given region (Black and Stewart, 2008). In addition, EE have a distinct thermal inertia pattern in nighttime infrared images, with bright exposures (rocky material) on the crater walls, and a dark, low-thermal inertia signature from the unconsolidated ejecta material. By definition, EE have ejecta volumes above the pre-impact surface that are at least 2.5 times the volume of the crater cavity (Black and Stewart, 2008). Precise measurements of the ejecta volume are complicated by uncertainties in the profile of the structurally uplifted

terrain on which the ejecta is superposed (Stewart and Valiant, 2006). As such, the value used for calculations includes the total integrated volume of the material above the pre-impact surface. This is compared to the volume of the pristine crater cavity below the elevation of the pre-impact surface. The ratio of these values, neglecting changes in the bulk density of the material, should be approximately equal to one. Using a set of fresh craters, Black and Stewart (2008) calculate the average $V_{\text{above}}/V_{\text{cavity}}$ to be 0.99 with a standard deviation of 0.44. This means that, in order for a crater to be classified as an EE, its $V_{\text{above}}/V_{\text{cavity}}$ value must be more than three standard deviations (3σ) from the mean (>2.5), completely separating it from the natural variability of typical fresh craters.

The initial survey for EE identified the highest concentration in Utopia Planitia (Black and Stewart, 2008). This survey was, however, geographically limited to 18-55°N, 86-163°E. Fresh craters from several smaller regions were used for morphological comparison, including part of Acidalia Planitia (27-54°N, 308-355°E). Classification of the ejecta revealed that EE tend to have double-layer ejecta (DLE) (Fig. 1), although examples with single-layer ejecta (SLE) exist (Fig. 2; Table 1). Barlow et al. (2000) define SLE craters as those surrounded by only a single layer of material. DLE craters are those surrounded by two layers of material, where the inner layer has a smaller diameter than the outer layer and is usually superposed on the outer layer (Barlow et al., 2000). In either case, a morphological analysis of an EE ejecta deposit reveals minimal differences from that of normal ejecta; both normal and EE ejecta exhibit similar textures, and the margin of the outer layer ejecta merges relatively seamlessly with the topography of the surrounding plains. In some EE there exists a concentric topographic depression on the inner layer ejecta, just outside of the crater rim (Fig. 1). The EE measured by Black and

Stewart (2008) range from ~5 to 18 km in diameter, although only craters from 4 to 50 km were included in the survey. The crater interiors, which may contain central peaks and pits, reach 600 to 1400 m depth below the elevation of the surrounding surface. Given the radii of the craters and the radial extents of the ejecta, the ejecta volumes correspond to excess thicknesses of 27 to 108 m (Black and Stewart, 2008).

2.2. Perched Craters

The set of perched craters (Pr) includes all craters whose current cavity floors and ejecta deposits are at or above the elevation of the surrounding terrain (Boyce et al., 2005; Garvin et al., 2000; Meresse et al., 2006) (Figs. 3-5). These crater interiors have necessarily undergone significant infilling, decreasing the depths of the cavities; in extreme cases, the crater floor can be situated hundreds of meters above the intercrater plains. This process results in Pr having nearly constant depths regardless of the crater diameters (Boyce et al., 2005; Meresse et al., 2006). Through a survey of rectangular-shaped test areas (defined by the MOLA 1/128° DEM) in the northern lowlands, Boyce et al. (2005) found that Pr exist below an elevation of -2400 m. They tend to be located north of 40°N, although they are present as far south as 25°N, with the highest concentration in Utopia Planitia. Out of 2279 craters measured, Boyce et al. (2005) identified 414 examples of Pr with diameters ranging from ~6 to 23 km. However, their study did not include craters smaller than 6 km in diameter. A subsequent study by Meresse et al. (2006) found several examples that were 3 to 10 km in diameter.

The ejecta and crater rims of Pr often show evidence of degradation or erosion (Figs. 3-5). The ejecta can be SLE or DLE (Barlow et al., 2000), and always exhibits a

low thermal inertia in THEMIS nighttime images (Meresse et al., 2006). The texture of the ejecta is highly variable; it may be smooth or rough, and can exhibit radial lineations and/or pits. Measurements of the ejecta of Pr and normal DLE craters in Utopia Planitia have been used to estimate the excess thickness of the Pr ejecta, which is typically 60-80 m for the outer ejecta layer and 150-200 m for the inner ejecta layer. These ranges suggest an excess thickness of 35-140 m of material (Meresse et al., 2006). Despite Pr having inflated ejecta, the margins of the ejecta deposit usually slope gradually down to the elevation of the surrounding terrain, but do exhibit terminal ramparts in some cases. The material within the crater interiors is often concentric crater fill (Levy et al., 2010) (Figs. 3,4), but in some cases appears quite smooth with no evidence of cracks or flow. Additionally, the fill can be heavily pitted with depressions resembling scallops (Fig. 5), a feature interpreted to be due to sublimation (e.g. Lefort et al., 2009).

2.3. Pedestal Craters

By definition, pedestal craters (Pd) are an impact morphology characterized by having the crater interior located near the center of a pedestal (mesa or plateau) that is surrounded by an outward-facing scarp (Barlow, 2000) (Figs. 6,7). The marginal scarp is generally located several crater diameters from the rim crest, which implies that the pedestal surface has a radial extent (Kadish et al., 2009) that exceeds that of a typical ejecta deposit (Barlow et al., 2000; Melosh, 1989). Some marginal scarps are marked by pits that represent loss of material from the pedestal; pit formation has been attributed to sublimation of the icy substrate below the protective veneer (Kadish et al., 2008) (Fig. 7).

Pd are generally small, with crater diameters less than 6 km (Fig. 6). The crater floors of mid-latitude Pd are usually but not always above the elevation of the surrounding terrain. In rare cases, the crater floor is above the elevation of the pedestal surface (Kadish et al., 2009) (Fig. 6a). Pedestals tend to be ~20 to 110 m in height. Although evidence of ejecta is uncommon, the pedestal surface can sometimes be superposed by SLE, which never reaches the pedestal margins (Kadish et al., 2010). A global survey revealed that the highest Pd concentrations are in Utopia and Acidalia Planitia, and Malea Planum (Kadish et al., 2009). For a more detailed description of the physical attributes and geographic distribution of Pd, see Kadish et al. (2008, 2009, 2010, 2011).

3. Formation Mechanisms

The fundamental commonality among these three crater types is the interpretation that each morphology is the result of an impact into ice-rich surface deposits (Black and Stewart, 2008; Kadish et al., 2009; Meresse et al., 2006) (Fig. 8). As discussed in detail by Kadish et al. (2009, 2010), these ice-rich deposits must be similar to, but thicker than, recent icy mantling units that have been repeatedly emplaced at mid latitudes during periods of higher obliquity in the last several million years (e.g. Head et al., 2003; Kreslavsky and Head, 2002; Mustard et al., 2001).

Climate model results (e.g. Levrard et al., 2004; Madeleine et al., 2009) show that the necessary thicker deposits can accumulate over geologically-short time periods given the proper orbital and atmospheric conditions. These include an equatorial source of ice, such as the Tharsis tropical mountain glaciers (e.g., Forget et al., 2006; Head and

Marchant, 2003), a moderate obliquity (35°), and high dust opacity. Variations on these constraints do change the quantity and geographic distribution of ice deposited at mid latitudes. However, this study shows that accumulation rates can readily exceed 10 mm/yr at the same locations in which we identify the highest populations of EE, Pr, and Pd. Furthermore, the predicted history of martian obliquity variations during the past 10s to 100s of Myr (Laskar et al., 2004) suggests that the ice-rich material that leads to the formation of these crater morphologies is likely to have been emplaced episodically. This scenario would lead to multiple generations of ice-rich layers that were tens of meters thick, and to the production of these crater types upon impact of projectiles into this substrate, which is consistent with our observations (Kadish et al., 2010, 2011). Further, this sequence of events is necessary in order to maintain the presence of EE, which lose their classification as EE upon significant degradation or burial by mantling.

Formation mechanisms for EE, Pr, and Pd have been proposed on the basis of their topography, morphology, and distribution. The specific process models for EE, Pr, and Pd, which have been schematically detailed by Black and Stewart (2008), Meresse et al. (2006), and Kadish et al. (2009) respectively (Fig. 8), each begin with an ice-rich unit overlying a silicate regolith. This ice-rich material is interpreted to be the result of obliquity-driven climate change, and the redistribution of polar ice to lower latitudes (Head and Marchant, 2009). In the EE model, the ejecta, which is a mixture of ice and the underlying regolith, is distributed over the icy layer surrounding the crater cavity (Figure 8a). During return to lower obliquity, the ice from the intercrater terrain sublimates, and the remaining dusty lag deposit is susceptible to erosion. The silicate-rich ejecta deposit, however, preserves the ice-rich layer surrounding the crater by insulating the ice fraction

and inhibiting sublimation (Black and Stewart, 2008; Kadish et al., 2009; Meresse et al., 2006). Consequently, the terrain surrounding the ejecta is lower than the surface was at the time of impact, so that the ejecta appears thicker than expected. The excess ejecta may be composed purely of a sublimation lag deposit left from the former icy substrate, or it may also contain some fraction of the original ice (Black and Stewart, 2008).

The model for Pr formation proposed by Meresse et al. (2006) follows a sequence similar to that interpreted to have occurred during the production of EE (Black and Stewart, 2008), beginning with an impact that penetrated an ice-rich deposit superposed on a silicate-rich regolith and excavated the regolith material. The resulting lobate ejecta is distributed in the region proximal to the crater rim crest and interior, on top of the ice-rich layer. After impact, the crater interior acts as a trap for debris, and is slowly infilled by the eolian transport of material, as well as by nearby impact ejecta and possible deposition from the atmosphere. If the crater is sufficiently small, the infilling will raise the elevation of the crater floor above the elevation of the surrounding terrain. Meanwhile, thermal variations and wind deflation respectively sublimate and erode the icy surface layer. The changes in temperature may be due to orbital changes (i.e. eccentricity and obliquity) and/or seasonal effects. The Pr ejecta deposits, however, have low thermal inertia (Meresse et al., 2006), possibly due to a thin insulating layer of fine-grained material. As a result, the ejecta is preferentially protected from the thermal fluctuations, helping to preserve the ice content of the ejecta. Although the ejecta itself is also subject to eolian erosion, it is removed at a much lower rate than the intercrater plains. The result is a crater that has both its ejecta and crater interior perched above the surrounding terrain (Meresse et al., 2006).

In the general proposed Pd formation model (Kadish et al., 2009), an impact occurs into a layer of ice and snow, mixed with dust, but the excavation cavity does not necessarily reach the underlying silicate regolith. The impact event distributes ejecta and possibly impact melt on and around the crater rim; due to the composition of the target material, the ejecta itself is likely to be largely ice and snow. The surface proximal to the crater becomes indurated in some manner as a result of the impact process (Arvidson et al., 1976; Osinski, 2006; Schultz and Mustard, 2004; Skorov et al., 2001; Wrobel et al., 2006). The resulting armored surface can extend to a distance of multiple crater radii, exceeding the lateral extent of the ejecta deposit. Subsequent obliquity-driven climate change leads to the sublimation of volatiles from the unarmored intercrater terrain, lowering the elevation of the plains. The armoring, however, inhibits sublimation from beneath the hardened pedestal surface. This produces a symmetrical, circular scarp around the edge of the armored crater and its ejecta. The result is a crater centered on a pedestal that is composed of the initial icy layer that was deposited on the silicate regolith. In this model, the crater interior is usually above the elevation of the surrounding terrain, and infilling of the crater interior can occur, raising the elevation of the crater above that of the pedestal surface (Kadish et al., 2009).

It should be noted that other models for Pd formation have been proposed (e.g. Arvidson et al., 1976; McCauley, 1973). These studies suggested that Pd resulted from impacts into dry, fine-grained material. An armoring mechanism indurated the proximal surface, allowing eolian deflation to remove the nonarmored intercrater terrain while preserving the pedestal material. This left the Pd perched above the surrounding plains (Arvidson et al., 1976; McCauley, 1973). In both the ice-rich and dry models, a host of

armoring mechanisms have been proposed. These include increased ejecta mobilization caused by volatile substrates (e.g. Osinski, 2006), a coarse lag deposit (Arvidson et al., 1976), a veneer of impact melt (Schultz and Mustard, 2004), dust insulation (Skorov et al., 2001), or a thermally indurated soil consisting of a layer of fine-grained, volatile-poor dust and/or salts (Wrobel et al., 2006). For a discussion of these armoring mechanisms, see Kadish et al. (2009).

In comparing this range of characteristics and these proposed formation mechanisms, it is clear that the processes may be similar, particularly between EE and Pr. In both of these cases, the initial impact excavates the underlying regolith, and the distributed ejecta is primarily responsible for inhibiting the sublimation of the proximal volatiles during erosion of the intercrater terrain, leading to the anomalously large ejecta volumes. The only significant distinction between the geomorphological outputs identified in the process models is the infilling of the crater interiors; all EE are necessarily fresh, having deep crater cavities, whereas Pr have always undergone extensive infilling, yielding shallow crater interiors. Pr are also more likely to show modification of their ejecta deposits, possibly due to eolian deflation (Meresse et al., 2006). As will be discussed later, this may imply that Pr are simply modified EE which have been degraded and/or covered by post-emplacement deposits.

Based on the limited extent of Pd ejecta deposits, which are not always present on the pedestal, it is very likely that Pd have experienced a different process by which the ice-rich material becomes preserved. As previously mentioned, several mechanisms have been proposed that could be capable of armoring such a large surface area relative to the size of the crater interior, but none have been proven (Arvidson et al., 1976; Osinski,

2006; Schultz and Mustard, 2004; Skorov et al., 2001; Wrobel et al., 2006). The absence of ejecta associated with many Pd supports the interpretation that the impacts that form Pd, unlike EE and Pr, do not excavate a significant volume of the underlying silicate regolith. As such, the ejecta would consist primarily of the ice-rich layer, making it easily erodible, and would have a very small, if any, rock fraction. Using the depth-diameter relationship for simple craters of $d=0.21D^{0.81}$, where d is the depth and D is the diameter (Garvin et al. 2003), it is clear that the impacts resulting in Pd (1-3 km diameter craters) tend to excavate only 200 to 500 m below the rim crest. This depth will vary due to the strength of the impact material (Garvin et al., 2000). Because the impact excavation depth is only slightly thicker than the material that is eventually removed due to sublimation and deflation, most Pd have their crater basins and any detectable ejecta perched above the elevation of the intercrater plains. By strict definition, this would allow them to be classified as Pr. However, as we will emphasize in the following section, while some Pd may technically qualify as Pr, the two morphologies are not identical, having several distinguishing physical and topographic features.

4. Physical Attribute Comparison

4.1. Crater Diameter and Ejecta/Pedestal Thickness

One of the significant physical distinctions between these crater types is the variation in diameter ranges (Fig. 9). As previously mentioned, the initial studies of EE and Pr revealed that they tend to be approximately the same size range. Although these studies did not survey craters of all diameters, the distribution of sizes in confirmed

examples suggests that the majority of EE and Pr are between 4 and 10 km in diameter, with extreme cases extending the range from 2 to 23 km (Black and Stewart, 2008; Boyce et al., 2005; Meresse et al., 2006). Conversely, Pd typically range from <0.5 to 6 km in diameter, with a median of 1.2 km (Kadish et al., 2009). These distributions show that the lower size limit for EE and Pr overlaps only slightly with the upper size limit of Pd (Fig. 9). As such, if all three crater types form from impacts into the same icy paleodeposits, then this distinction in crater sizes suggests that the primary factor influencing the initial morphology of the observed craters is the excavation depth (Barlow et al., 2001), which is largely due to the size of the impactor.

The validity of the above assumption relies on the notion that each crater type results from distinct impacts into the same thickness of ice-rich paleodeposits, rather than being produced by impacts into deposits of different thicknesses that were present at different times. To assess this, we can compare the thicknesses of the excess ejecta, perched ejecta, and pedestals (Fig. 9). If these morphologies do form from the same icy layers of the same thickness, then their proposed formation mechanisms predict that the ejecta/pedestals will have similar thicknesses.

As previously mentioned, Black and Stewart (2008) found that EE range from 27 to 108 m in excess thickness based on the expected thickness of the ejecta for a given crater size. They identified a mean excess thickness of approximately 50 m. In their study of Pr, Meresse et al. (2006) noted that the DLE of an average Pr is 35-140 m thicker than that of a normal crater. Lastly, Kadish et al. (2010) showed that the vast majority of the pedestals of Pd are 20 to 110 m in thickness, with a mean of 46 m. These measurements were made on the pedestal, but outside of the outer margins of any visible ejecta, so they

act as a proxy for the thickness of the icy paleolayer, comparable to the physical significance of the excess ejecta measurements for EE and Pr (Kadish et al., 2010). The similarity of the thicknesses of each of the three morphologies is remarkable (Fig. 9); these results strongly support our interpretation that EE, Pr, and Pd all formed from impacts into ice-rich deposits of similar thicknesses. Furthermore, these data suggest that the deposits were, on average, several tens of meters thick, and in some cases exceeded 100 meters in thickness.

This finding may also explain the apparent lack of EE and Pr larger than 20 km. Boyce et al. (2005) note that Pr larger than 10 km in diameter would not be common due to the difficulty of completely infilling such a voluminous cavity. This, however, would not affect the size range of EE, which have not been identified larger than 18 km in diameter despite the fact that Black and Stewart (2008) extended their survey of fresh craters up to 50 km in diameter. From a process perspective, given the method by which EE and Pr are interpreted to have formed, a size limitation imposed by the thickness of the icy target layer would be expected. Because the ice-rich deposit has a fixed thickness, the volume of excess ejecta will become proportionately smaller as the fresh crater size increases. This will reduce the $V_{\text{above}}/V_{\text{cavity}}$ ratio below the necessary 3σ value of 2.5 required for EE classification. Additionally, it is likely that the heat generated from larger impacts would more completely melt the volatile fraction of the proximal icy layer upon impact, further reducing the proportion of excess ejecta. This melting has been shown to occur for Sinton crater, a large impact that is interpreted to have formed on a plateau icefield (Morgan and Head, 2009). Essentially, large impacts resulting in craters greater

than about 25 km would overwhelm the tens of meters of ice-rich material at the surface, resulting in a negligible change to the ejecta volume.

4.2. Topography and Morphology of Ejecta

A second apparent distinction between these three crater types is the texture and topographic profile of their ejecta (Figs. 1-7). Both in images and in profile, the ejecta of EE closely resembles that of typical crater ejecta (Garvin et al., 2000); without supporting volumetric measurements of the ejecta and crater interior, it would be extremely difficult to distinguish an EE from a normal fresh crater with DLE (Figs. 1,2). The typical DLE of EE slopes gradually downward from the well-defined crater rim crest, with the steepest slopes occurring in the transition between the inner and outer layers of the ejecta. As previously mentioned, some EE exhibit a concentric topographic depression on the inner layer ejecta bordering the crater rim crest. This moat-like trait is typical of most DLE, and is interpreted to be a primary feature resulting from the supersonic nature of the outward flow responsible for producing the inner ejecta layer (e.g. Boyce and Mougini-Mark, 2006). Topographically, the outer ejecta layer merges almost seamlessly with the surrounding plains. However, images of EE ejecta usually exhibit rough textures and often reveal surfaces that have clear radial striations. This characteristic roughness contrasts sharply with the smooth texture of the plains in Utopia (Figs. 1,2).

The ejecta of Pr is similar to that of EE, with a few notable distinctions. Similar to the crater interior associated with Pr, the ejecta often shows evidence of having been covered by debris. Although the texture maintains a rough appearance, which is confirmed in the topographic profiles, it is usually somewhat more subdued than that of

the fresh ejecta associated with EE, as are the radial striations that are present on most Pr ejecta (Figs. 3-5). Unlike EE ejecta, Pr ejecta sometimes has a terminal rampart, especially in DLE cases. The ejecta of most Pr, however, gradually slopes down to the surrounding plains. This is always the case in SLE examples of Pr. Topographic profiles of Pr can give the false impression that Pr ejecta is quite distinct from EE ejecta. This interpretation of the ejecta is influenced by the absence of a deep crater interior and an eroded crater rim, which in some cases makes the ejecta difficult to distinguish from the crater. Variations in vertical exaggeration (Fig. 1-7) also make Pr ejecta appear deceptively rough when compared to EE ejecta. Morphological assessments, however, suggest that Pr ejecta most often represents a subdued/degraded version of EE ejecta. It should be noted that, despite these common differences between Pr and EE ejecta, the two can sometimes be practically indistinguishable; in these cases, Pr appear to be EE with a filled-in crater interior (Fig. 2).

A detailed discussion of typical Pd ejecta is difficult because the presence of ejecta on the pedestal surface is so uncommon. When SLE is present, it is almost always thin, contributing only a slight halo of roughness to the otherwise smooth flat pedestal surface (see Fig. 7 in Kadish et al., 2010). The texture of Pd ejecta is often so subtle that it is detectable only in high resolution (MOC, CTX, HiRISE) images, and even then its distal perimeter cannot always be distinguished from the pedestal surface. Topographic profiles of typical Pd are distinct when compared to EE and Pr in that Pd always have a well-defined scarp at the margin of their pedestal (Figs. 6,7). This scarp should not be confused with a characteristic of the ejecta, however, as the pedestal and ejecta are distinct features. Variations in elevation due to the presence of ejecta are difficult to

discern using MOLA topography due to the ~300 m spacing between data points (e.g. Smith et al., 2001). As such, Pd topographic profiles show that the pedestal is by far the most prominently expressed feature. Depending on the freshness of the Pd, the crater rim and crater interior may be well-defined like that of EE, or significantly subdued like that of Pr.

5. Age Comparison

Superposed impact crater size-frequency distributions can be used to estimate the ages of craters and their ejecta deposits, despite small sample sizes and counting areas. Crater counting on the ejecta/pedestal of EE, Pr, and Pd can provide estimates of the ages of individual craters. If this method is repeated on many distinct small surfaces, it is possible to produce a preliminary age range. In addition, preservation states can be used to make inferences about the relative ages of crater populations. It is therefore useful to provide a general description of age estimates for the populations in order to place the formation mechanisms within the context of the climate history of Mars. In this section, we provide crater counts on ejecta for individual crater ages, as well as lower limits for population ages; calculating the age of a crater population using the conventional size-frequency distribution technique is difficult because the method dates the age of the surface, which is not necessarily the individual crater formation age. However, using the diameters of a crater population and the area on which it is present will yield the minimum duration of time necessary to form that population.

Black and Stewart (2008) calculate the apparent retention age of their fresh crater population in Utopia to establish that the EE population has an apparent age of 100 to 200

Myr. It should be noted that this is not the age of any specific crater, but rather the time interval required to form the EE population when the necessary icy deposit was emplaced. The time needed to form the observed population is necessarily greater than ~200 Myr because the ice-rich material is not currently present and a robust solution for the last 20 Myr of martian obliquity history shows low obliquity periods for the last 3-5 Myr, and potentially widely variable obliquity for the last 250 Myr (Laskar et al., 2004). Given the rarity of EE – only 10 of the 572 fresh craters measured by Black and Stewart (2008) qualified – and the 200 Myr formation timescale, Black and Stewart (2008) suggest that EE production is associated with an episodic phenomenon. They conclude that EE ages are likely to have spanned the Amazonian period, forming in conjunction with multiple distinct ice-emplacement episodes, and that the fresh appearance of EE supports the interpretation that they are young (Black and Stewart, 2008).

The dating of Pr is complicated by the fact that the ejecta deposits have undergone noticeable modification, including mantling, burial and morphologic degradation. If the crater interior has been filled by a significant volume of sediment, then it is reasonable to believe that material has also accumulated on the ejecta deposits. This process also infills and erases craters, leading to the calculation of artificially young ages. Because of this, the age range of Pr is not well defined. Their degraded states strongly imply that they are older than EE. Boyce et al. (2005) used stratigraphic relationships between Pr and the Vastitas Borealis Formation to determine that Pr are likely Late Hesperian or Early Amazonian in age.

The timescale of formation of Pd was calculated using the mid-latitude Pd population and the corresponding area on which they formed. Similar to the EE time

interval, this method leads to a derived formation timescale of approximately 100 Myr (Kadish et al., 2009). Using the same logic outlined for the accumulation of EE, this result implies that Pd are likely to have formed throughout the Amazonian during episodic periods of mid-latitude ice-rich deposits. The episodic emplacement of Pd has also been confirmed by stratigraphic relationships in which one Pd is partially draped over another Pd (Kadish et al., 2010). Additional work on dating 50 individual pedestal surfaces revealed that 70% of those measured are younger than 250 Myr. These individual ages are, however, lower-limit calculations due to modification and resurfacing of the pedestals. In addition, 20% of the pedestal surfaces were calculated to be more than 1 Gyr in age. These examples appear significantly more degraded, and show evidence of infilling of their crater interiors, similar to the morphology of Pr.

The combination of these dating efforts for each of the three crater types provides a general timeline for their formation. The probable recurrence of the ice-rich paleodeposit from which EE, Pr, and Pd form suggests that none of the populations resulted from a single phase. In addition, multiple crater types may have formed from the same phase. Despite these possible overlaps and extended formation timescales, it is likely that Pr are generally the oldest of the three morphologies. Pr consistently display the most degradation, and the observation that some show partial burial by the Vastitas Borealis Formation implies a Hesperian age. Pd appear to be generally young (tens to a few hundred Myr), but some individual examples show that they can be much older (a few Gyr). As a population, EE are necessarily fresh and are likely to be the youngest of the crater types.

6. Geographic Distribution Comparison

The initial survey for EE by Black and Stewart (2008) noted that, within the study region, nine of the ten EE identified were located in Utopia Planitia (Fig. 10). The only other EE was located in Acidalia Planitia. Black and Stewart (2008) also identified nine moderately excess ejecta craters (MEE), with $V_{\text{above}}/V_{\text{cavity}}$ between 2 and 2.5, five of which were in Utopia, three in Acidalia, and one in Isidis. Due to the common modification of craters near the poles from mantling, high latitudes were not included in the study. As such, the limited latitudinal range at which EE were identified, primarily between 32°N and 44°N, is not a comprehensive assessment of the distribution of EE. Black and Stewart (2008) specifically note that it is likely that other EE have formed in their study region, but have subsequently been modified and/or degraded, and that many EE may exist outside their survey area.

Surveys detailing the distribution of Pr also covered regions exclusively in the northern hemisphere (Boyce et al., 2005; Meresse et al., 2006). These studies found that the highest concentrations of Pr are in Utopia, Acidalia, and Arcadia Planitia between 40°N and 55°N (Fig. 10), but they have been identified as far south as 25°N. Given the sheer number of confirmed Pr – 414 in the limited survey area of Boyce et al. (2005) – it is clear that they are significantly more common than EE. Figure 10 shows that both Pr and EE are most heavily concentrated in Utopia and somewhat less so in Acidalia, with only Pr being present in Arcadia. As we will show in the following section, both EE and Pr are present, but less common, in the southern hemisphere of Mars.

The distribution of more than 2300 Pd larger than 0.7 km in diameter has been well established between 60°S and 60°N (Kadish et al., 2009). This study shows that, like

EE and Pr, the highest populations of northern hemisphere Pd are in Utopia and Acidalia. Pd are also concentrated in Arcadia (Fig. 10). Of the Pd measured, four times as many exist in the northern hemisphere than in the southern hemisphere. Those that are present south of the equator tend to be focused in Malea Planum, with much smaller populations in Terra Cimmeria and Terra Sirenum. Latitudinally, Pd extend as far equatorward as 33°N and 40°S. Subsequent high-latitude studies have confirmed that Pd are common near the poles, and can even form on the polar caps (Kadish et al., 2011). These data confirm that, of the three crater morphologies, Pd are the most common and widespread (Fig. 10).

7. New Examples of Excess Ejecta Craters

Due to the geographic limitations of previous surveys for EE and Pr, as outlined in section 2, we expanded the search for these crater morphologies into the southern hemisphere. This was necessary in order to provide a more complete geographic comparison of the locations in which EE, Pr, and Pd are capable of forming, an observation that is a key aspect of understanding the relationship between the crater types. We performed a survey from 0° to 70°S using a THEMIS IR mosaic and MOLA altimetry. The combination of images and topography allowed us to select fresh craters, as well as some that had both the crater interior and ejecta perched above the surrounding plains.

Fresh craters with clear ejecta were generally included down to 2 km in diameter unless good quality CTX coverage was available, and then we were able to measure some smaller examples. This cutoff was necessary because, without high resolution images of

small craters, it is not possible to confirm that they are fresh. Some craters that would classify as both Pr and Pd were previously identified in the southern hemisphere from the Kadish et al. (2009) survey for Pd. We expanded the search for new examples of Pr that would not be classified as Pd. Overall, our analysis revealed that EE, like Pd, are much rarer in the southern hemisphere, and Pr are similarly uncommon.

Using high resolution HRSC DTMs and interpolated MOLA data, we created eight profiles of each fresh crater we studied, and then detrended the profiles by subtracting the regional topographic slopes. Averaging these profiles for each individual crater allowed us to measure the crater depth and width and the average excess ejecta thickness. Crater depths were confirmed using MOLA shot data. We then measured the areal extent of the ejecta and multiplied this by the average excess ejecta thickness to get the excess ejecta volume (V_{ejecta}). We approximated the crater volume (V_{cavity}) as a paraboloid, using the crater depth below the elevation of the surrounding plains and the crater diameter at the elevation of the plains. Using these values, we were able to confirm the presence of four craters with $V_{\text{cavity}}/V_{\text{ejecta}}$ greater than 2.5 (Fig. 11; Table 2). It should be noted that, by using the techniques set forth by Black and Stewart (2008), we assume that the typical $V_{\text{cavity}}/V_{\text{ejecta}}$ is not significantly different for craters in the southern hemisphere, and thus a value of 2.5 is still 3σ from the average.

Interestingly, no EE were identified that had a diameter greater than 3 km (Table 2). Because Black and Stewart (2008) only measured fresh craters larger than 4 km, these new EE are considerably smaller than those previously analyzed. There is, however, one EE of comparable size, named Vaduz, which has been analyzed in detail by Schaefer et al. (2011). Because these craters are so small, they are readily susceptible to erosion. As

such, the rarity of their presence, having survived the sublimation and removal of the surrounding ice-rich target layer, is not surprising. The new EE, in addition to having small diameters, also have relatively thin excess ejecta (16-26 m) compared to measurements by Black and Stewart (2008). The ejecta of these EE examples is always of the DLE type and is remarkably extensive compared to the sizes of the craters (Fig. 11). The small volumes of the crater cavities and large extents of their ejecta yield high $V_{\text{cavity}}/V_{\text{ejecta}}$ values, reaching up to 28.5 (Table 2). Unlike the northern hemisphere examples, these EE appear to have relatively smooth ejecta, although this interpretation may be hindered by limitations of the image resolution; some portions of the ejecta do appear rougher than others, and there are signs of sublimation pits on the surface of at least one of the new EE ejecta deposits (Fig. 11a).

The newly identified EE are located exclusively between 45°S and 65°S, and are all in the eastern hemisphere, which is where the vast majority of southern hemisphere Pd are located (Fig. 10). These EE are not, however, within close proximity of each other. Each is located in or near a Pd field (within 100s of km), and we have identified one example that is only tens of km from two Pr (Fig. 11b). This distribution is consistent with the findings of the northern hemisphere geographic distribution, as discussed in the previous section; each of the three morphologies tends to occur and be concentrated in the same regions, and multiple morphologies are often seen within the same image (Figs. 2,5).

As noted in the Pd survey by Kadish et al. (2009), Pd are much more common in the northern hemisphere (Fig. 10). Our finding that both Pr and EE are also rarer in the southern hemisphere supports the interpretation that the morphologies are genetically

related; having comparable relative population concentrations globally suggests that the crater types are similarly inhibited from forming in certain regions while other regions are conducive to the formation of each morphology. The lack of any identified large EE in the southern hemisphere is consistent with the finding by Kadish et al. (2010) that the pedestals of Pd are, on average, thinner (not as tall) in the southern hemisphere. In general, the smaller number of each morphologic crater type (EE, Pd, Pr), their geographic distribution (Fig. 10), and their thinner ejecta deposits/pedestals in the southern hemisphere imply that the ice-rich target material was less common in the southern highlands; specifically, these pieces of evidence support the interpretation that the ice-rich paleodeposits in the southern hemisphere were thinner and not as geographically widespread. In other words, although southern hemisphere ice-rich deposits may have accumulated just as frequently as those in the northern hemisphere, the southern hemisphere deposits may not have reached the same thicknesses, may have sublimated more quickly, and/or may have been much more constrained to localized regions.

8. Discussion

The comparison of EE, Pr, and Pd yields some striking similarities as well as some key distinguishing traits (Table 3). This survey expands on the previous understanding of EE and Pr, both in terms of their geographic extents (Fig. 10) and physical sizes (Fig. 9). This information, in conjunction with prior detailed Pd studies, provides the necessary context from which we can draw a more comprehensive analysis of the potential relationship between these morphologies. In terms of physical size (Fig.

9), the survey does show that EE and Pr can occur at smaller diameters than found in previous measurements by Black and Stewart (2008) and Boyce et al. (2005). We measured one EE that was 1.5 km in diameter, and some of the Pd that are less than 2 km in diameter qualify as Pr. However, the majority of EE tend to be greater than 5 km, and the majority of Pr are greater than 3 km. We were unable to find any new examples of EE or Pr that exceeded the size of the largest examples identified by Black and Stewart (2008) and Boyce et al. (2005), respectively; nonetheless, their studies showed that both of these morphologies can reach approximately 20 km in diameter. Pd, on the other hand, can be much smaller, with many examples less than 1 km in diameter. In addition, Pd generally do not exceed 6 km.

If we combine this outline of the diameter ranges with the fact that each morphology exhibits almost identical excess ejecta/pedestal thicknesses (Fig. 3), with averages around 50 m in all cases, then the data suggest that morphologic variations are initially based on excavation depth relative to the thickness of the ice-rich target layer; each morphology protects/insulates the same layer thickness, but the size of the impactor (and possibly other characteristics including impact velocity, impact angle, and target material strength) determines the crater depth. If the impact penetrates through the ice-rich material and excavates regolith, it creates a significant ejecta deposit. If not, it can result in a smooth armored pedestal that has a minimal ejecta deposit, or lacks ejecta altogether (Fig. 8).

This interpretation is supported by both the geographic distribution and morphologic characteristics of EE, Pr, and Pd. Specifically, the fact that the morphologies are all located in the same geographic regions within the same restricted latitudinal bands

in mid to high latitudes (Fig. 10) supports the interpretation that they all require the same target material, which appears to accumulate in response to a climate-related mechanism. Our expansion of the EE and Pr surveys into the southern hemisphere shows that they occur where Pd are present. This confirms that the highest concentrations of each crater type occur in the same regions in both hemispheres. What would cause the much larger population of Pd craters? Given the fact that smaller impacts occur more frequently based on the size-frequency distribution of the impactor population, one would expect that the Pd population would grow most rapidly during periods when the ice-rich material was emplaced.

From a morphological perspective, the smoothness of pedestal surfaces, and the fact that most lack ejecta, is consistent with induration of a flat paleodeposit. Most of the ejecta would have been icy material given the thickness of the ice-rich deposit and the shallow excavation depths of small impacts. This ice-rich ejecta would have sublimated when the intercrater terrain sublimated and deflated. Regarding EE and Pr, the presence of DLE, radial striations, and rough surface textures suggests the presence of rocky material included in the ejecta, which must have been sourced from the underlying regolith. This requires that the impacts penetrated through the entire icy surface layer.

The ages of these morphologies, with EE being necessarily young (Amazonian) and Pr being usually older (Late Hesperian to Early Amazonian) suggests a possible evolution from EE to Pr. These two morphologies are located in the same geographic regions, and have the same diameter size ranges and ejecta characteristics. There are also many more Pr than EE (Fig. 10). These data suggest that EE are able to maintain the ice-rich content in their ejecta for geologically long timescales, on the order of tens to

hundreds of millions of years. As EE age and become degraded, their crater interiors become infilled, and they become Pr (Fig. 2). The absence of fresh Pr and degraded EE supports the interpretation that at least some EE transform into Pr as they are mantled and eroded. Pd, being primarily young but having some old examples, experience a unique age progression that involves erosion of the pedestal from the scarp back to the crater rim through sublimation pitting along the margin (Kadish et al., 2010).

9. Conclusions

This study establishes associations between three distinctive crater morphologies (Table 3) that were previously studied independently. Through the assessment of excess ejecta craters (Black and Stewart, 2008), perched craters (Boyce et al., 2005; Meresse et al., 2006), and pedestal craters (Arvidson et al., 1976; Barlow et al., 2000; Kadish et al., 2009), we have established significant evidence for a genetic relationship between the crater types. Our expansion of previous surveys reveals that EE and Pr are present in the southern hemisphere in the same geographic locations as Pd. We have also shown that, in rare cases, EE and Pd can be smaller than the examples identified by previous studies.

These new survey results, in conjunction with the direct comparison of each morphology, lead us to conclude that:

1) EE and Pr are genetically related, and are likely to have formed from the same general mechanism – ejecta armoring of an icy substrate (Fig. 8). The primary difference between these morphologies is simply that Pr have experienced post-impact infilling, resulting in extremely shallow crater depths and subdued ejecta textures.

2) Given the diameter ranges of EE and Pr (Fig. 9), and the estimated thickness of the mid-latitude ice-rich deposit during periods of high obliquity (10s to 100s of meters), these impacts overwhelmed the ice-rich layer, penetrating to the underlying martian silicate regolith. This resulted in the excavation of rock that formed the blocky ejecta necessary to preserve the ice-rich deposits.

3) The smaller size of Pd, and the significant differences from Pr and EE in topographic profile due to the absence of ejecta, requires that Pd result from a slightly different process. The fact that the pedestals of Pd have the same average thickness as the excess ejecta of EE and Pr (Fig. 9), and form in the same geographic regions (Fig. 10) implies that they result from impacts into the same type of ice-rich target material. However, Pd differ in that they do not penetrate through the icy surface layer, and thus do not generate a rocky silicate-rich ejecta covering. Instead, an indurated, dusty lag deposit appears to protect the underlying ice-rich material.

4) The ages of EE, Pr, and Pd suggest that ice-rich material has been repeatedly deposited at mid latitudes in both hemispheres throughout the Amazonian. The geographic distribution of EE, Pr, and Pd, with significantly higher concentrations in the northern hemisphere (Fig. 10), suggests that the lowlands may be superposed more frequently by these ice-rich deposits. Stratigraphic, morphologic, and crater counting evidence supports the interpretation that there have been multiple generations of these crater populations. This would require the episodic emplacement of icy paleodeposits, which are likely to have accumulated and sublimated at mid latitudes due to obliquity-driven climate variations.

Acknowledgments

The authors would like to thank the HiRISE, CTX, and HRSC teams, without whom this study could not have been completed. The authors are grateful for financial support from NASA Mars Data Analysis Program (MDAP) grant NNX09A14GG to JWH.

References

- Arvidson, R.E., Coradini, M., Carusi, A., Coradini, A., Fulchignoni, M., Federico, C., Funicello, R., Salomone, M., 1976. Latitudinal variation of wind erosion of crater ejecta deposits on Mars. *Icarus* 27(4), 503-516, doi:10.1016/0019-1035(76)90166-4.
- Barlow, N.G., 2005. A New Model for Pedestal Crater Formation. Workshop on the Role of Volatiles and Atmospheres on Martian Impact Craters, LPI Contribution No. 1273, 17-18.
- Barlow, N.G., Koroshetz, J., Dohm, J.M., 2001. Variations in the onset diameter for Martian layered Ejecta morphologies and their implications for subsurface volatile reservoirs. *Geophys. Res. Lett.* 28(16), 3095-3098.
- Barlow, N.G., Boyce, J.M., Costard, F.M., Craddock, R.A., Garvin, J.B., Sakimoto, S.E.H., Kuzmin, R.O., Roddy, D.J., Soderblom, L.A. 2000. Standardizing the nomenclature of Martian impact crater ejecta morphologies. *J. Geophys. Res.* 105(E11), 26733-26738.

Black, B.A., Stewart, S.T., 2008. Excess ejecta craters record episodic ice-rich layers at middle latitudes on Mars. *J. Geophys. Res.* 113, E02015, doi:10.1029/2007JE002888.

Boyce, J.M., Mouginis-Mark, P., 2006. Martian craters viewed by the Thermal Emission Imaging System instrument: Double-layered ejecta craters. *J. Geophys. Res.* 111, E10005, doi:10.1029/2005JE002638.

Boyce, J.M., Mouginis-Mark, P., Garbeil, H., 2005. Ancient oceans in the northern lowlands of Mars: Evidence from impact crater depth/diameter relationships. *J. Geophys. Res.* 110, E03008, doi:10.1029/2004JE002328.

Forget, F., Haberle, R.M., Montmessin, F., Levrard, B., Head, J.W., 2006. Formation of glaciers on Mars by atmospheric precipitation at high obliquity. *Science* 311, 368-371.

Garvin, J.B., Sakimoto, S.E.H., Frawley, J.J., 2003. Craters on Mars: Global Geometric Properties from Gridded MOLA Topography. Sixth International Conference on Mars, abstract #3277.

Garvin, J.B., Sakimoto, S.E.H., Frawley, J.J., Schnetzler, C., 2000. North polar region craterforms on Mars: Geometric characteristics from the Mars Orbiter Laser Altimeter. *Icarus* 144, 329-352.

Head, J.W., Marchant, D.R., 2009. Inventory of Ice-related Deposits on Mars: Evidence for Burial and Long-Term Sequestration of Ice in Non-Polar Regions and Implications for the Water Budget and Climate Evolution. Lunar and Planet. Sci. Conf. XL, abstract #1356.

Head, J.W., Marchant, D.R., 2003. Cold-based mountain glaciers on Mars: Western Arsia Mons. *Geology* 31, 641-644, doi:10.1130/0091-7613

Head, J.W., Mustard, J.F., Kreslavsky, M.A., Milliken, R.E., Marchant, D.R., 2003. Recent ice ages on Mars. *Nature* 426, 797-802.

Kadish, S.J., Head, J.W., 2011. Preservation of Layered Paleodeposits in High-Latitude Pedestal Craters on Mars. *Icarus*, under review.

Kadish, S.J., Head, J.W., Barlow, N.G., 2010. Pedestal Crater Heights on Mars: A Proxy for the Thicknesses of Past, Ice-Rich, Amazonian Deposits. *Icarus* 210, 92-101, doi:10.1016/j.icarus.2010.06.021.

Kadish, S.J., Barlow, N.G., Head, J.W., 2009. Latitude Dependence of Martian Pedestal Craters: Evidence for a Sublimation-Driven Formation Mechanism. *J. Geophys. Res.* 114, E10001, doi:10.1029/2008JE003318.

Kadish, S.J., Head, J.W., Barlow, N.G., Marchant, D.R., 2008. Martian pedestal craters: Marginal sublimation pits implicate a climate-related formation mechanism. *Geophys. Res. Lett.* 35, L16104, doi:10.1029/2008GL034990.

Kreslavsky, M., Head, J.W., 2002. Mars: Nature and evolution of young latitude-dependent water-ice-rich mantle. *Geophys. Res. Lett.* 29, doi:10.1029/2002GL015392.

Laskar, J., Correia, A.C.M., Gastineau, M., Joutel, F., Levrard, B., Robutel, P., 2004. Long term evolution and chaotic diffusion of the insolation quantities of Mars. *Icarus* 170(2), 343-364.

Lefort, A., Russell, P., Thomas, N., McEwen, A., Dundas, C.M., Kirk, R., 2009. Observations of periglacial landforms in Utopia Planitia with the High Resolution Imaging Science Experiment (HiRISE). *J. Geophys. Res.* 114, doi:10.1029/2008JE003264.

Levrard, B., Forget, F., Montmessin, F., Laskar, J., 2004. Recent ice-rich deposits formed at high latitudes on Mars by sublimation of unstable equatorial ice during low obliquity. *Nature* 431, 1072-1075.

Levy, J., Head, J.W., Marchant, D.R., 2010. Concentric crater fill in the northern mid-latitudes of Mars: Formation processes and relationships to similar landforms of glacial origin. *Icarus* 209, 390-404, doi: 10.1016/j.icarus.2010.03.036.

Madeleine, J.-B., Forget, F., Head, J.W., Levrard, B., Montmessin, F., Millour, E., 2009. Amazonian northern mid-latitude glaciation on Mars: A proposed climate scenario. *Icarus* 203, 390-405.

McCauley, J.F., 1973. Mariner 9 Evidence for Wind Erosion in the Equatorial and Mid-latitude Regions of Mars. *J. Geophys. Res.* 78, 4123-4137, doi:10.1029/JB078i020p04123.

Melosh, H.J., 1989. *Impact Cratering: A Geological Process*. Oxford Univ. Press, New York.

Meresse, S., Costard, F., Mangold, N., Baratoux, D., Boyce, J.M., 2006. Martian perched craters and large ejecta volume: Evidence for episodes of deflation in the northern lowlands. *Meteorit. Planet. Sci.* 41, 1647-1658.

Morgan, G.A., Head, J.W., 2009. Sinton crater, Mars: Evidence for impact into a plateau icefield and melting to produce valley networks at the Hesperian-Amazonian boundary. *Icarus* 202, 39-59.

Mustard, J.F., Cooper, C.D., Rifkin, M.K., 2001. Evidence for recent climate change on Mars from the identification of youthful near-surface ground ice. *Nature* 412, 411-414.

Osinski, G.R., 2006. Effect of volatiles and target lithology on the generation and emplacement of impact crater fill and ejecta deposits on Mars. *Meteorit. Planet. Sci.* 41(10), 1571-1586.

Schaefer, E.I., Head, J.W., Kadish, S.J., 2011. Vaduz, an unusual fresh crater on Mars: Evidence for impact into a recent ice-rich mantle. *Geophys. Res. Lett.*, accepted.

Schultz, P.H., Mustard, J.F., 2004. Impact melts and glasses on Mars. *J. Geophys. Res.* 109, doi:10.1029/2002JE002025.

Skorov, Y.V., Markiewicz, W.J., Basilevsky, A.T., Keller, H.U. 2001. Stability of water ice under a porous nonvolatile layer: Implications to the south polar layered deposits of Mars. *Planet. Space Sci.* 49, 59-63, doi:10.1016/S0032-0633(00)00121-5.

Smith, D.E., et al., 2001. Mars Orbiter Laser Altimeter: Experiment summary after the first year of global mapping of Mars. *J. Geophys. Res.* 106, doi:10.1029/2000JE001364.

Stewart, S.T., Valiant, G.J., 2006. Martian subsurface properties and crater formation processes inferred from fresh impact crater geometries. *Meteorit. Planet. Sci.* 41, 1509-1537.

Wrobel, K., Schultz, P., Crawford, D., 2006. An atmospheric blast/thermal model for the formation of high-latitude pedestal craters. *Meteorit. Planet. Sci.* 41(10), 1539-1550.

Tables

Table 1. Commonly used abbreviations and respective definitions.

EE	Excess Ejecta Crater(s)	Fresh craters that have ejecta volumes above the pre-impact surface that are at least 2.5 times the volume of the crater cavity.
Pr	Perched Craters(s)	All craters whose current cavity floors and ejecta deposits are at or above the elevation of the surrounding terrain.
Pd	Pedestal Craters(s)	Craters characterized by having the crater interior located near the center of a pedestal that is surrounded by an outward-facing scarp.
SLE	Single-Layer Ejecta	Ejecta consisting of only one layer of material.
DLE	Double-Layer Ejecta	Ejecta consisting of two layers of material. The inner layer has a smaller diameter and is superposed on the outer layer.

Table 2. Locations and physical attributes of the four newly identified excess ejecta craters.

Crater #	Latitude (°S)	Longitude (°E)	Crater Diam. (km)	Avg. Ejecta Thickness (m)	Ejecta Area (km ²)	V _{cavity} (km ³)	V _{ejecta} (km ³)	V _{ejecta} / V _{cavity}
1	63.6	88.4	1.5	16	38	0.046	0.608	13.2
2	55.6	46.3	2.2	23	440	0.448	10.120	22.6
3	46.1	160.3	3.0	26	173	1.017	4.498	4.4
4	49.1	135.7	2.3	18	151	0.096	2.718	28.5

Table 3. General comparison of the three crater morphologies.

	Excess Ejecta Craters	Perched Craters	Pedestal Craters
Typical crater diameter	5 to 18 km	3 to 23 km	<0.5 to 6 km
Typical thickness	27-108 m, with a mean of ~50 m	35 to 140 m	20-110 m, with a mean of 46 m
Ejecta type/texture	Usually DLE with a rough rocky texture	SLE or DLE with a subdued rough texture	No ejecta or SLE with a smooth texture
Distribution	10s of known examples, present at mid latitudes in both hemispheres	100s of known examples, present at mid latitudes in both hemispheres	2300+ known examples, present at mid latitudes in both hemispheres
Age	Late Amazonian	Late Hesperian to Early Amazonian	Most are Late Amazonian, but some examples are Hesperian

Figure Captions

Figure 1 – An excess ejecta crater (EE) located at 38.5°N, 99.2°E, shown as a CTX mosaic with HRSC HiRes DTM data. The black north-south trending line across the crater shows the path of the topographic profile beneath the image, which has a vertical exaggeration of 30x. This EE, which has a $V_{\text{above}}/V_{\text{cavity}}$ of 3.4, is 18.7 km in diameter, and the crater interior is approximately 1.2 km deep. The crater exhibits clear double-layer ejecta (DLE), with a moat-like depression directly outside of the crater rim. The outer layer of the ejecta is quite rough, making it easily distinguishable from the surrounding plains. The crater interior contains a prominent central peak, visible both in the image and topographic profile, derived from gridded MOLA data.

Figure 2 - An excess ejecta crater located at 32.8°N, 107.4°E, shown as a CTX mosaic with HRSC HiRes DTM data. The black SW-NE trending line across the crater shows the path of the topographic profile beneath the image, which has a vertical exaggeration of 10x. This EE, which has a $V_{\text{above}}/V_{\text{cavity}}$ of 5.2, is 5.5 km in diameter and the crater interior is approximately 0.8 km deep. This fresh crater exhibits rough single-layer ejecta (SLE) that has a well-defined margin where it gently slopes down into the plains. The crater interior shows only minor evidence of infilling. The second crater in the image has similar ejecta morphology and, although the crater rim looks quite young, the crater interior has been almost completely infilled. This crater qualifies as a perched crater. The proximity of these examples suggests that the Pr may have been infilled by the ejecta of the EE.

Figure 3 – A 4.3-km-diameter perched crater shown as a CTX mosaic with gridded MOLA topography. The black SW-NE trending line across the crater shows the path of the topographic profile, which has a vertical exaggeration of 51x. The crater interior exhibits clear concentric crater fill (CCF); due to the extensive infilling, the floor of the crater is now at the same elevation as the surface of the ejecta. The eastern half of the crater rim crest is still quite prominent, as can be seen in the image and the profile, but overall the rim appears to be considerably degraded. The ejecta, which itself contains small infilled craters, still has a distinguishable inner and outer layer. The radial striations are faintly visible, interrupted by the extremely rough surface texture. The margins of the ejecta are well-defined, creating a clear contrast with the relatively smooth surrounding plains.

Figure 4 – A 4.8-km-diameter perched crater, shown as a CTX mosaic with HRSC HiRes DTM data. The black west-east trending line across the crater shows the path of the topographic profile, which has a vertical exaggeration of 73x. CCF has completely filled the crater interior, bringing the elevation of the crater basin level with the ejecta. The ejecta itself is DLE, with a rougher inner layer and a smoother outer layer that ends in a discontinuous rampart at its margin. Note that this ejecta is interacting with the ejecta of another crater to the northeast.

Figure 5 – A particularly interesting example of what could be classified as a heavily degraded 8.8-km-diameter perched crater, shown as a CTX mosaic with HRSC HiRes DTM data. The crater interior has undergone extensive infilling, and the fill material,

which is heavily pitted, is now the highest part of the crater. Extensive sublimation/deflation of the ejecta is readily apparent, although both layers of the DLE can be identified, with slightly rougher texture on the inner layer. A moat-like pit, resembling scallops, extends around almost the entire margin of the outer ejecta, and is likely to be due to sublimation of the ice content of the ejecta. This sublimation and erosion is so advanced that, in some places where the plains have variable local topography, the ejecta is actually beneath the elevation of the plains. Other Pr/Pd are visible near the top and bottom of the image.

Figure 6 – Pedestal crater examples shown as CTX mosaics with gridded MOLA topography and corresponding profiles from MOLA shot data. Both of these craters show significant infilling of their crater interiors. Although they lack visible ejecta deposits, and both have a well-defined marginal scarp, which is a distinctive trait of Pd, by definition they both qualify as Pd. A) A 2.1-km-diameter Pd located at 48.1°N, 101.3°E. B) A 2.8-km-diameter Pd located at 57.2°S, 36.0°E. C) A profile of the Pd in (A), showing the individual MOLA points. The vertical exaggeration of the profile is 67x. D) A profile of the Pd in (B), showing the MOLA shot data. The vertical exaggeration of the profile is 40x. Modified from Kadish et al. (2010).

Figure 7 – Two examples of pedestal craters with marginal pits, shown as CTX mosaics with MOLA topography and corresponding profiles from MOLA shot data. Infilling of the crater interiors is visible in both cases. Neither crater shows clear ejecta on its smooth pedestal surface, but the topographic profiles reveal that both craters qualify as perched

craters by strict definition. The marginal pits represent evidence of sublimation of ice from the pedestal material along the exposed scarps. A) A 2.6-km-diameter Pd located at 60.2°N, 102.5°E B) A 3.9-km-diameter Pd located at 62.4°N, 99.4°E. C) A profile showing the MOLA shot data of the Pd in (A). The vertical exaggeration of the profile is 44x. D) A profile of the Pd in (B), derived from MOLA shot data. The vertical exaggeration of the profile is 67x. Modified from Kadish et al. (2009).

Figure 8 –Schematic illustrations highlighting the primary steps in the formation of excess ejecta craters (left), perched craters (middle), and pedestal craters (right). These process models for EE, Pr, and Pd have been adapted from Black and Stewart (2008), Meresse et al. (2006), and Kadish et al. (2009), respectively. Note the primary commonalities between the models, which include: 1) An impact into an ice-rich surface layer overlying the regolith. In the EE and Pr models, this impact completely penetrates through icy deposit to the underlying regolith, but this does not occur in the Pd model. 2) Sublimation/deflation of the ice-rich layer from the intercrater terrain, resulting in the lowering of the elevation of the surrounding plains. 3) Preservation of the icy layer proximal to the crater interior, either due to ejecta cover or related armoring processes. This results in the anomalously high volume of material around the crater in the form of excess ejecta or a pedestal. The only notable difference between the EE and Pr models is that, in the Pr model, the crater interior becomes infilled to the point that the floor of the basin is above the elevation of the surrounding terrain.

Figure 9 – A graph of the crater diameter and thickness values for EE (green square), Pr (blue triangle), and Pd (red circle). Locations of the data points show the approximate average values for each crater population while the error bars indicate the range of values, as identified by Black and Stewart (2008), Boyce et al. (2005), Meresse et al. (2006), and Kadish et al. (2009). These data exclude extreme cases – for example, the new EE found in this study show that some examples can be much smaller in diameter than the population identified by Black and Stewart (2008). This visualization of the typical physical characteristics the crater morphologies clearly shows the similarity between their thicknesses (vertical error bars). The diameters (horizontal error bars) show that there is an overlap between larger Pd and smaller EE and Pr, but Pd tend to be smaller while EE and Pr are similar in size.

Figure 10 – The top map shows the geographic distribution of excess ejecta craters (green dots) and moderately excess ejecta craters (red dots) from Black and Stewart (2008), perched craters (blue dots) from Boyce et al. (2005), pedestal craters (black dots) from Kadish et al. (2009), and newly identified excess ejecta craters in the southern hemisphere (yellow squares). The bottom map, which shows MOLA topography, identifies significant regions of interest. Due to the limited geographic extent of previous surveys for EE and Pr, we have outlined the general region over which they were identified with a purple box. Note, however, that neither the EE nor the Pr survey included the entire area of the purple box; the EE survey covered only 86-163°E and 308-355°E for the latitudes shown (Black and Stewart, 2008), while the Pr survey was limited to distinct rectangular regions based on the available MOLA 1/128° DEM (Boyce et al.,

2005). In addition, both the EE and Pr studies ignored craters smaller than 4 and 6 km in diameter, respectively. Despite these limitations, the distribution shows clear similarities in where EE, Pr, and Pd form, with the highest concentrations in Utopia and Acidalia Planitia, and the new southern hemisphere EE are all located in regions where Pd are present. In terms of population density, these data show that Pd are the most widespread, while EE are the least common.

Figure 11 – Images of three of the newly identified excess ejecta craters in the southern hemisphere. Each example is less than 3 km in diameter, and exhibits DLE. A) Crater #2 in Table 2, shown in CTX image P15_007030_1238. This crater has the largest ejecta area of the four EE identified in this study. The ejecta shows evidence of sublimation pitting, especially near the margins of its outer layer. B) Crater #4 in Table 2, shown in CTX image P16_007264_1326. This EE is located within tens of km from two Pr, seen in the top left and bottom right of the image. The ejecta of this crater does show some signs of smoothing due to erosion, but it is notably fresher than that of the two Pr, and it maintains long lobes and radial striations. C) Crater #1 in Table 2, shown in CTX image B11_013819_1162. Although this crater is still considered fresh, it shows the most abundant evidence of erosion of any of the new EE examples. Both layers of the DLE are visible, but the texture appears subdued.

Figure 1

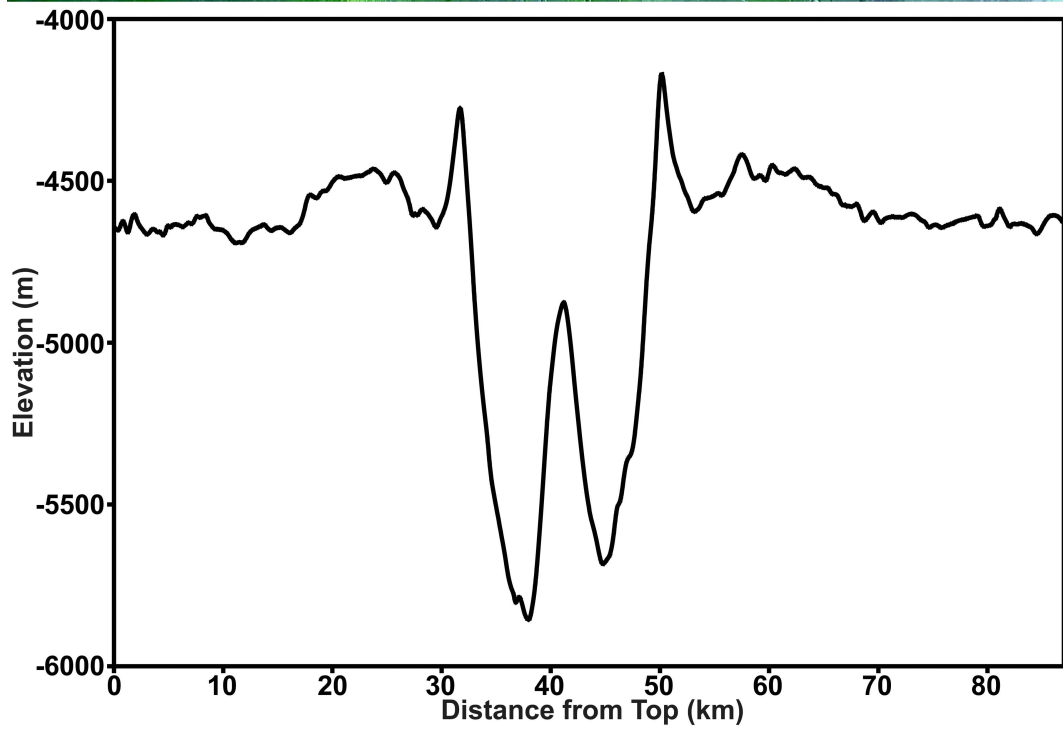
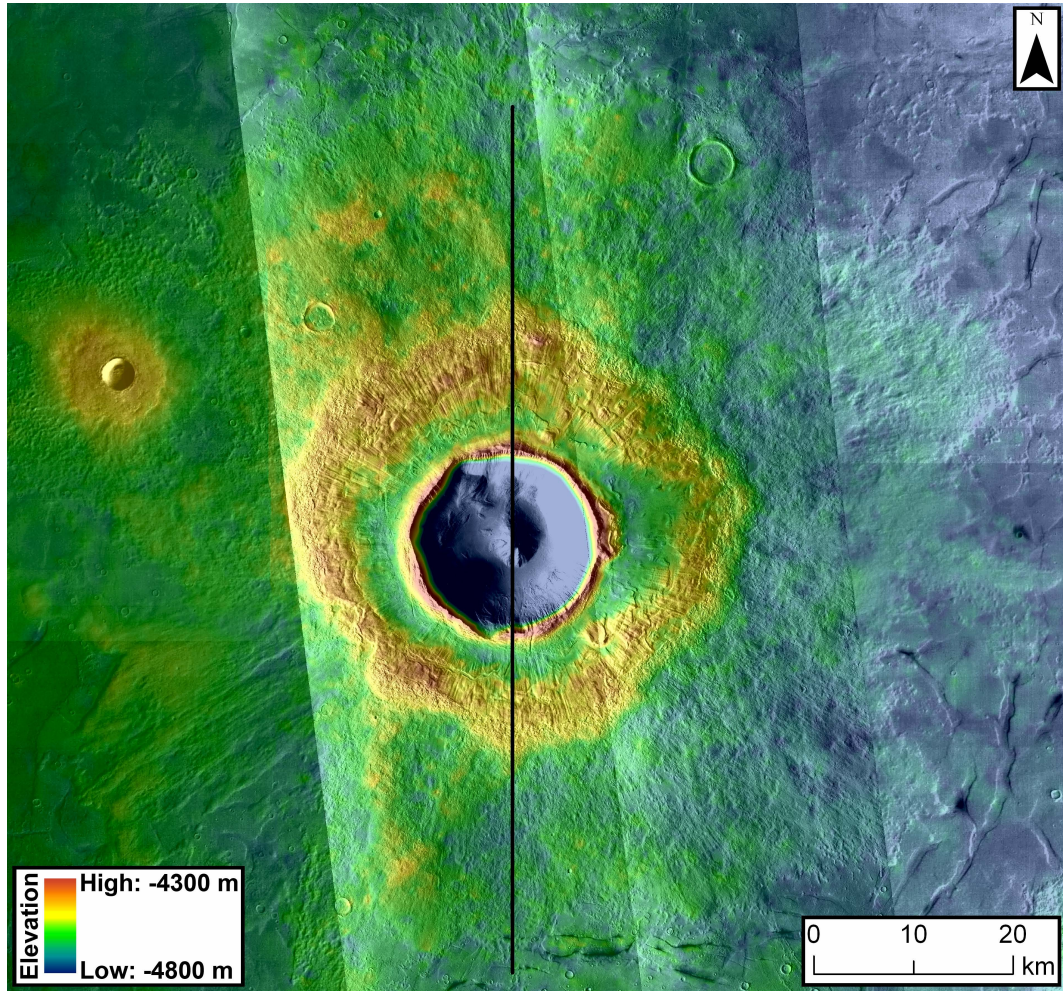


Figure 2

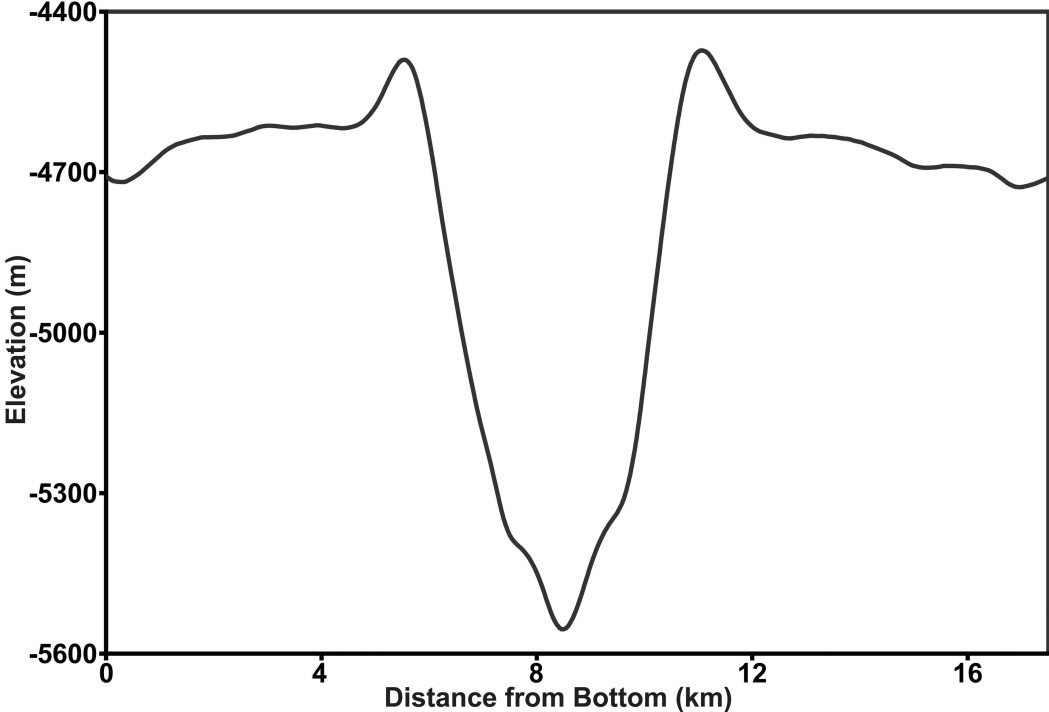
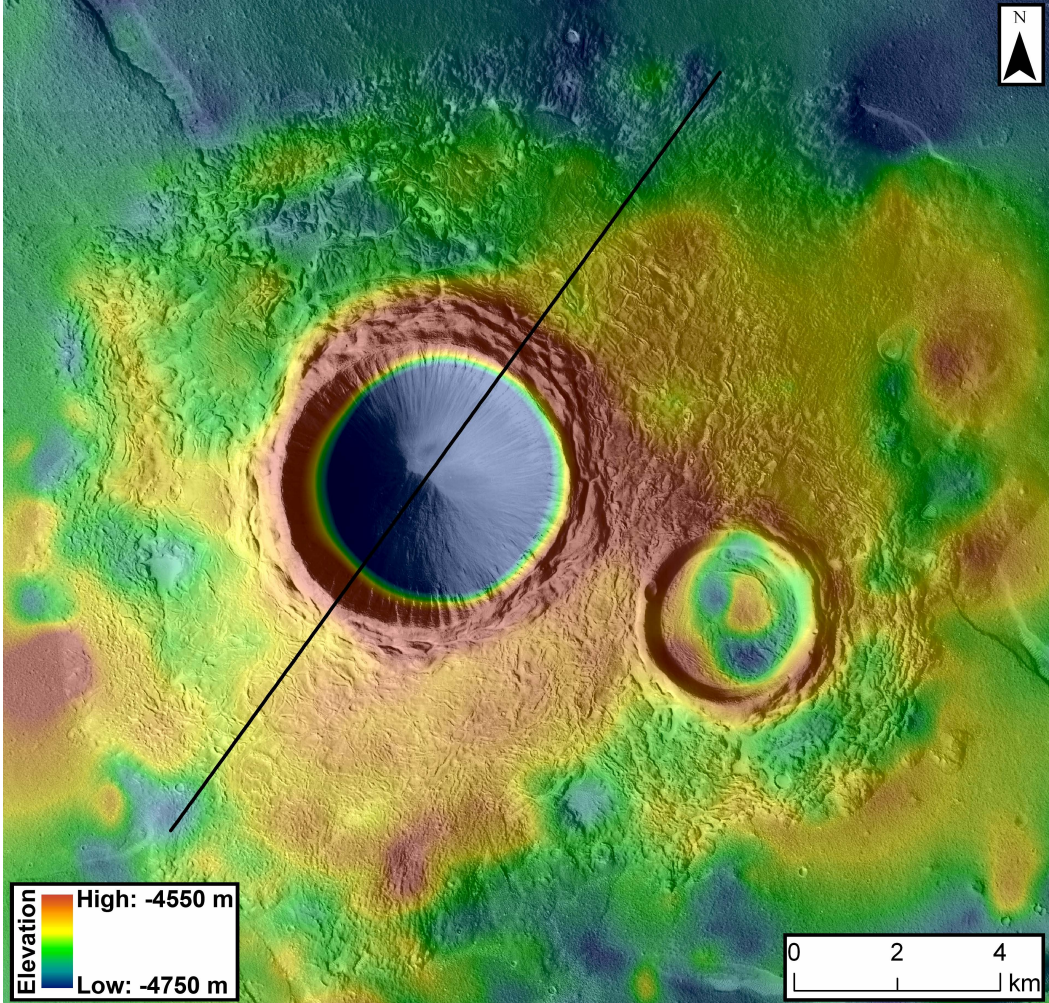


Figure 3

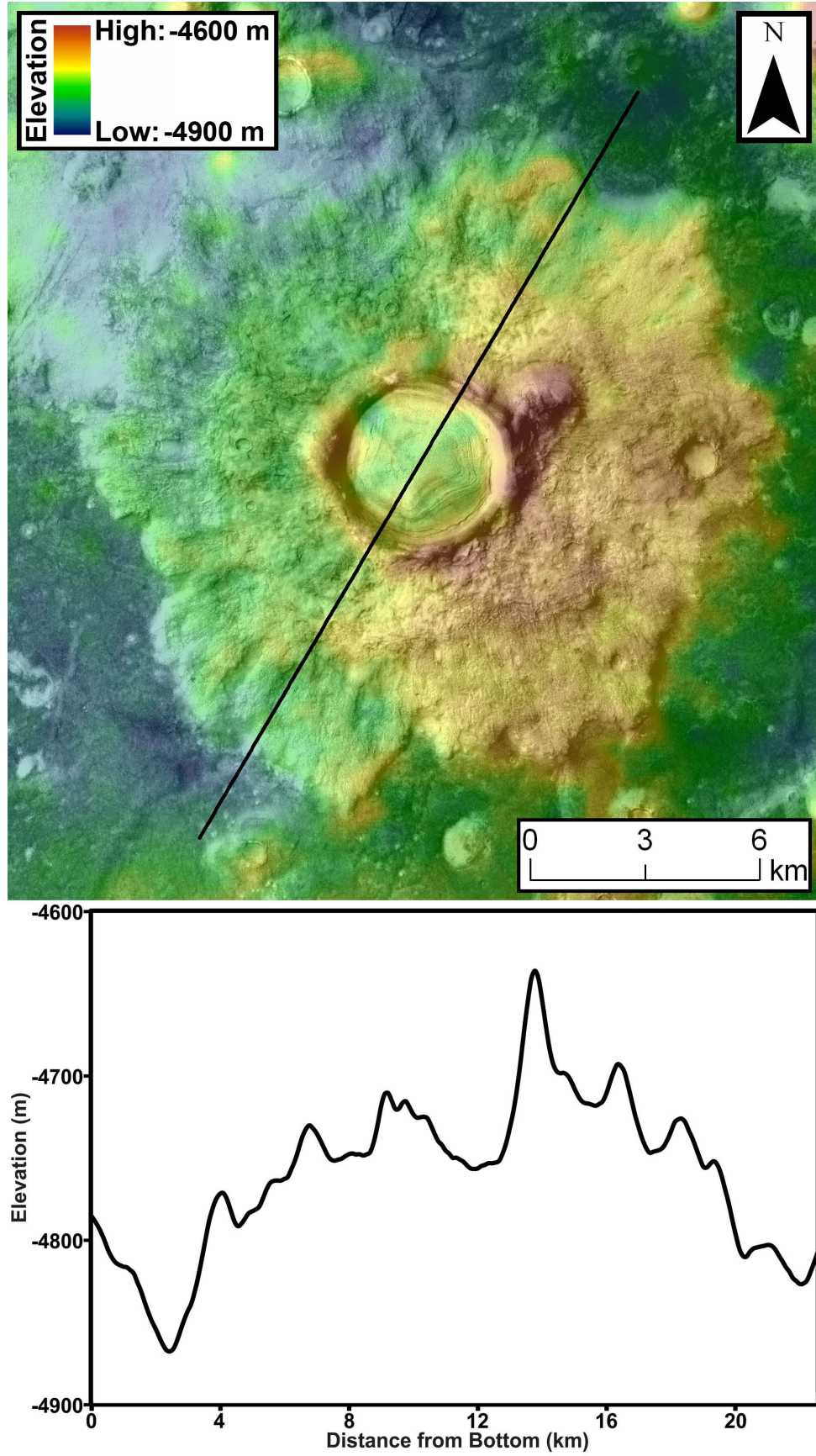


Figure 4

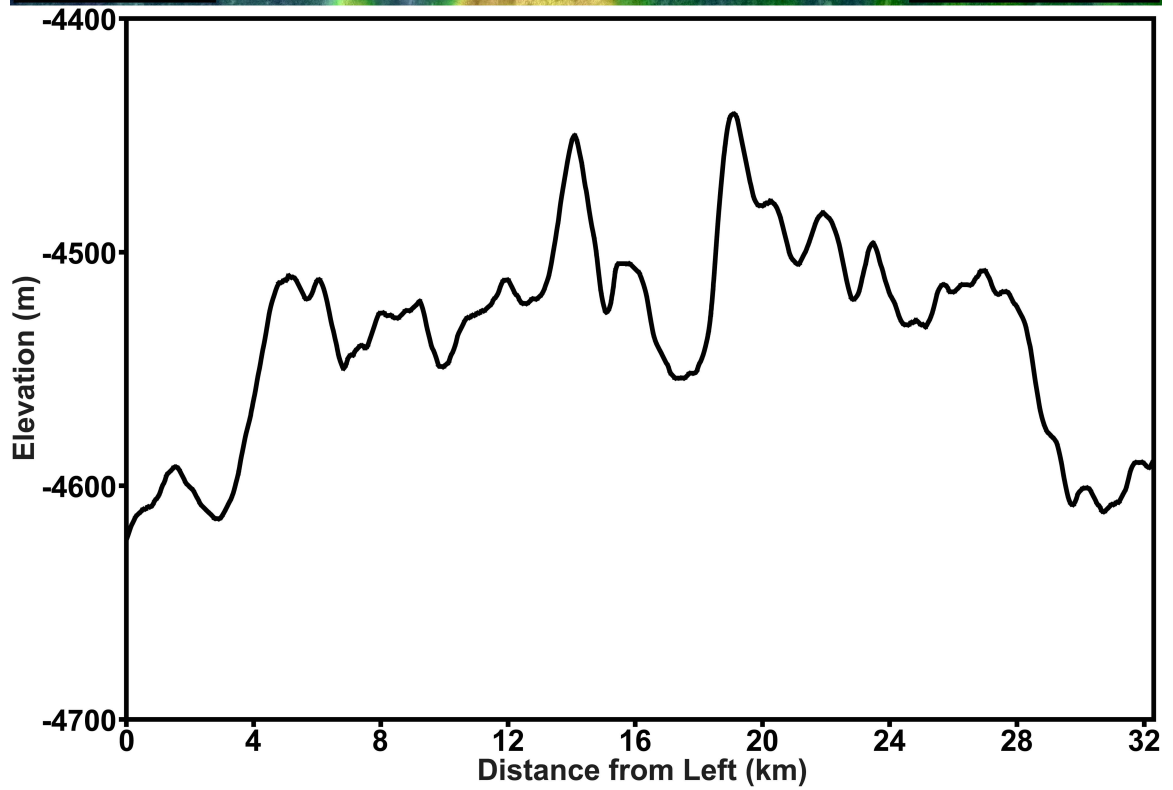
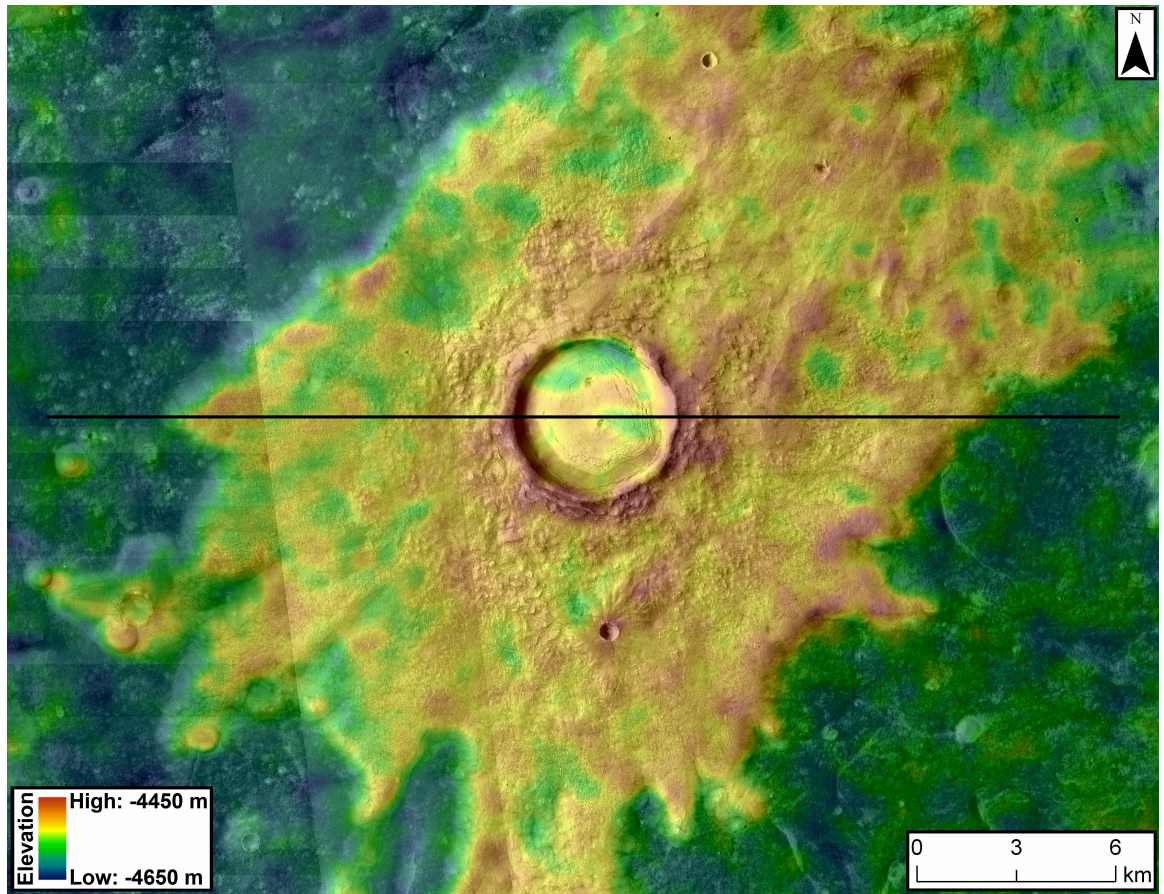


Figure 5

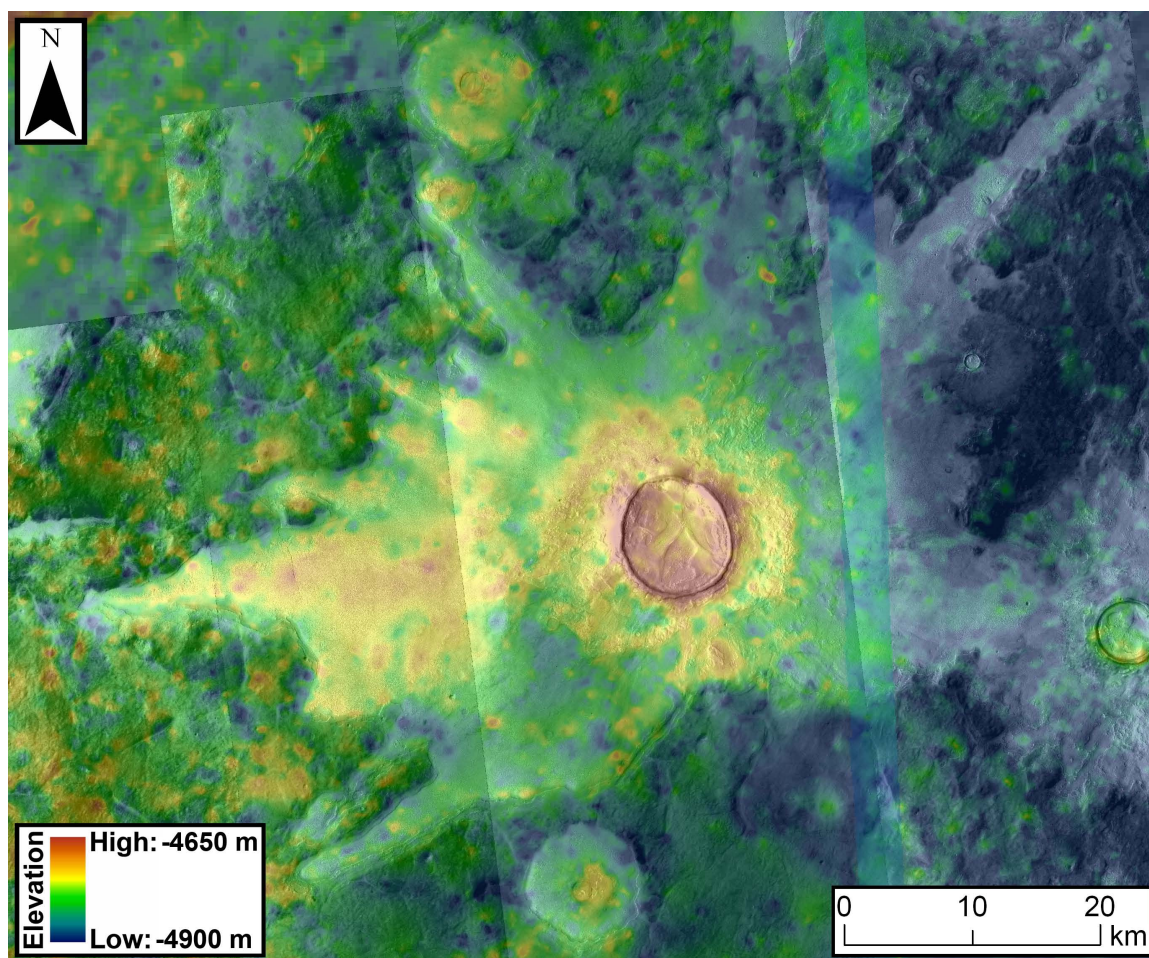


Figure 6

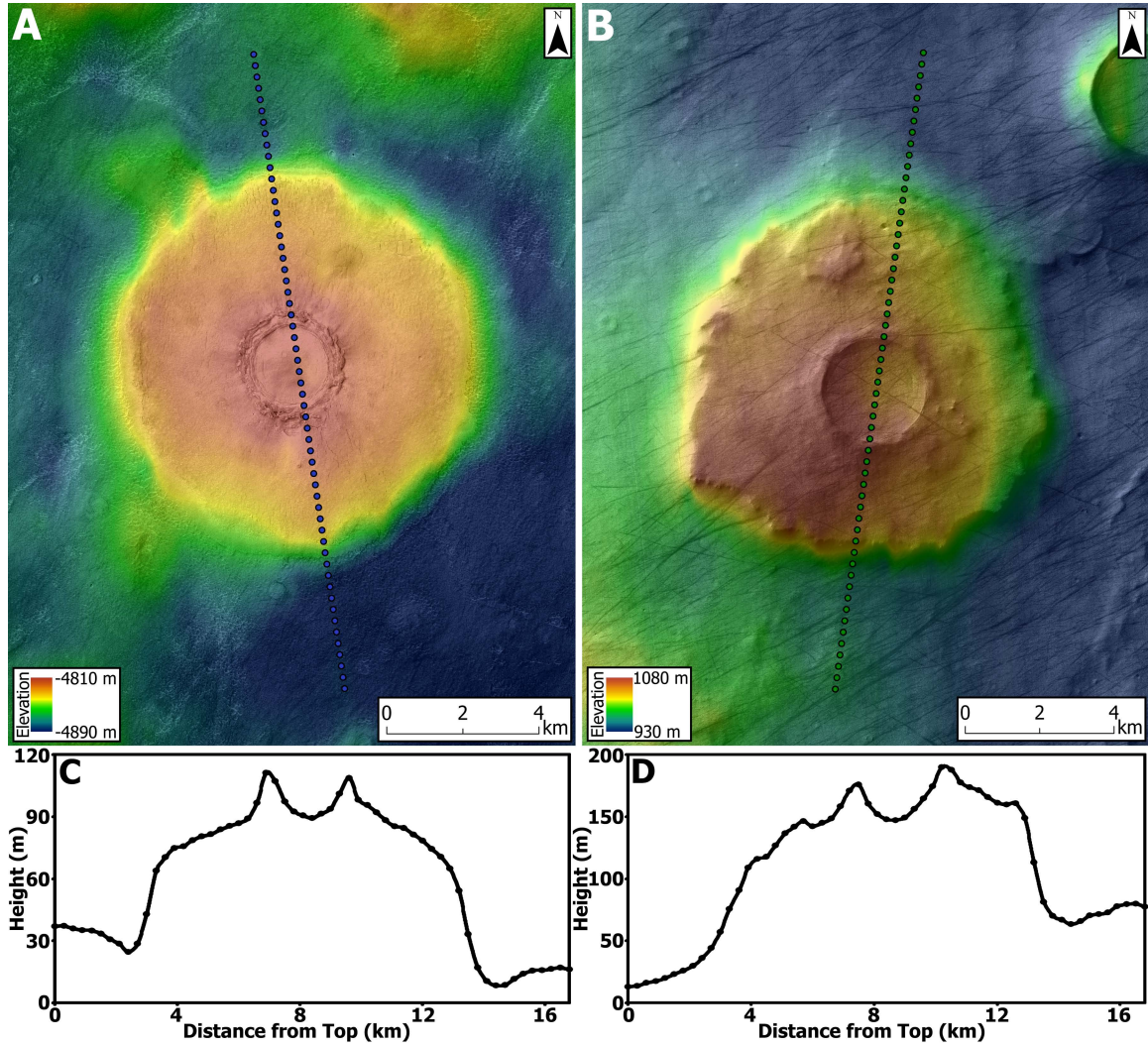


Figure 7

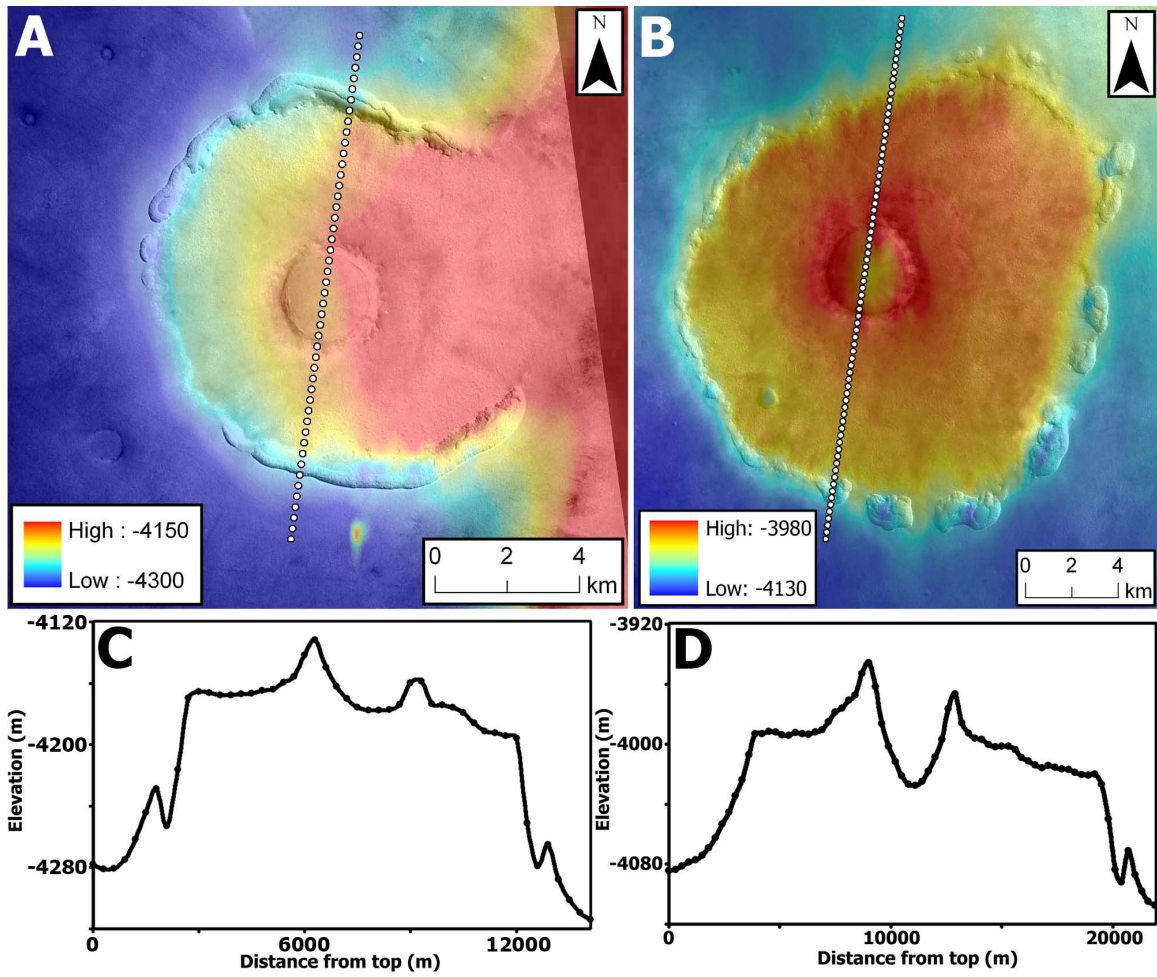


Figure 8

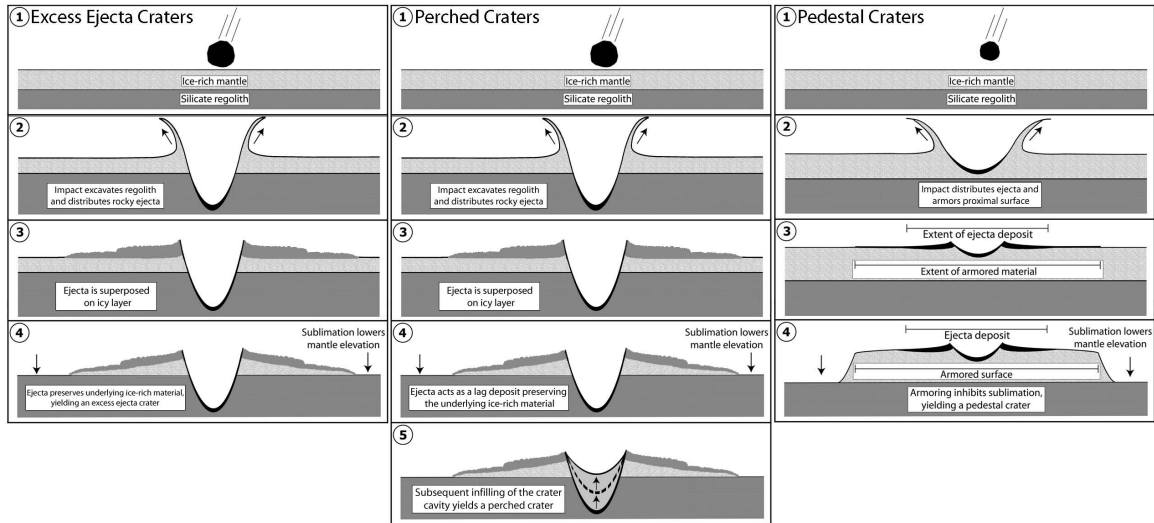


Figure 9

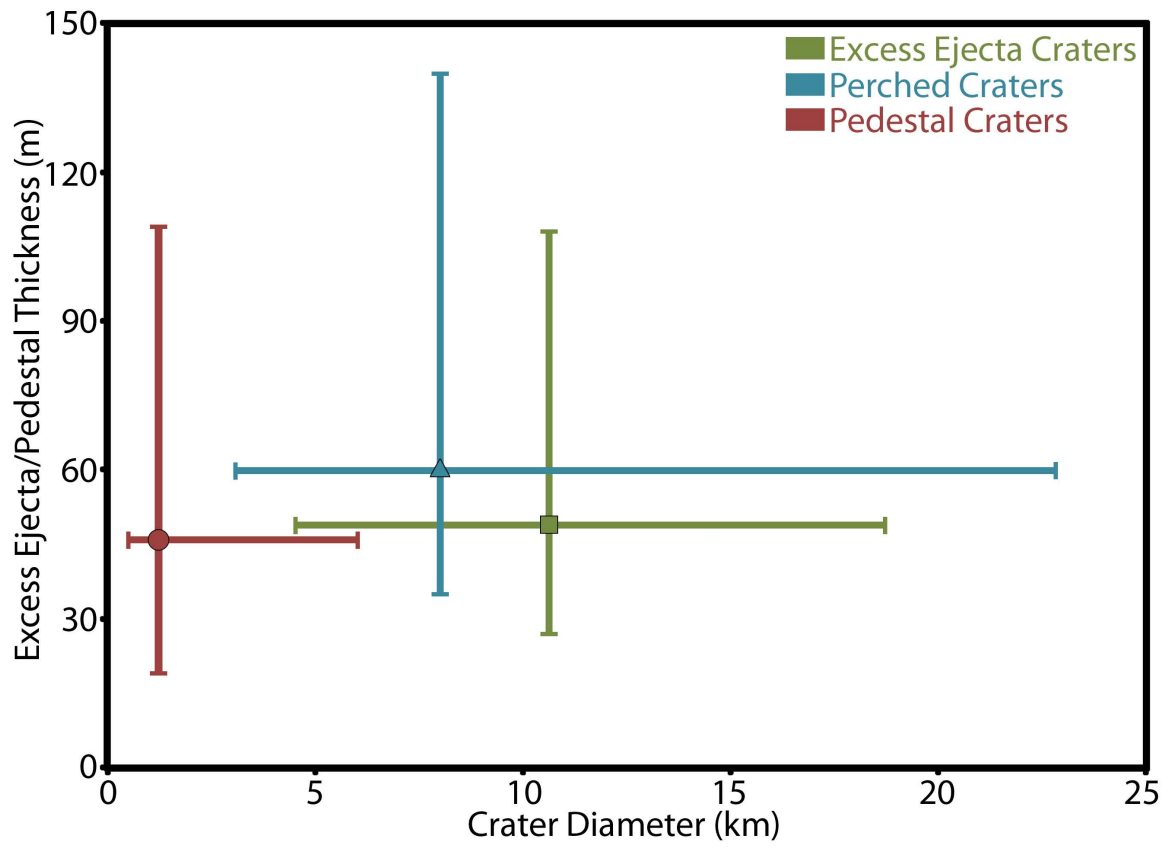


Figure 10

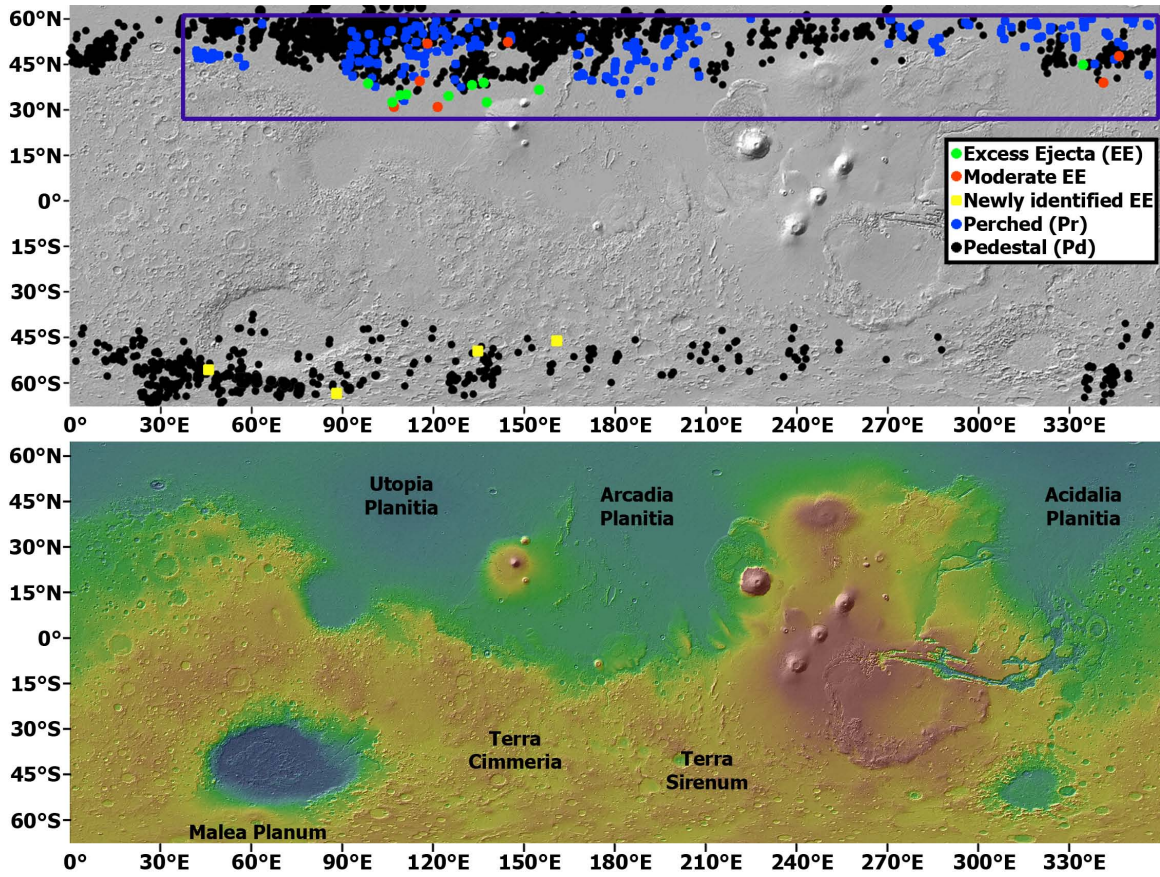
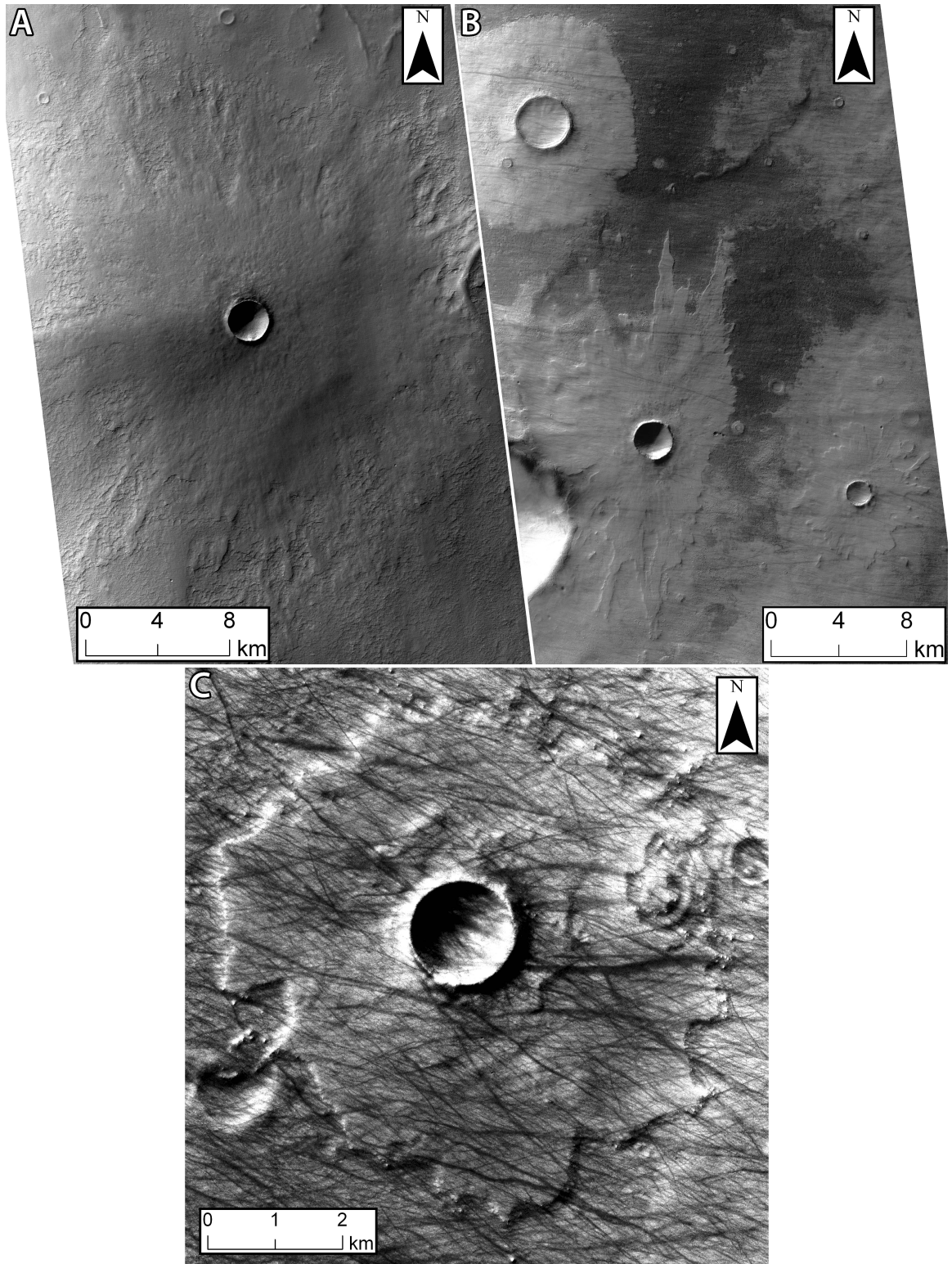


Figure 11



CHAPTER FIVE:

The Periodicity and Transport Pathways of Amazonian Ice-Rich Paleodeposits at Low to Mid Latitudes on Mars

Seth J. Kadish^a and James W. Head^a

^aDepartment of Geological Sciences, Brown University, Providence, RI 02912 USA

To be Submitted:

Icarus, April 2011

Abstract

There is significant geomorphologic evidence for the past presence of deposits composed of ice-rich material at mid and low latitudes on Mars. The time during which these various deposits were emplaced and how the ice migrated from the polar regions to form the deposits is still highly debated. Using new and revised ages and periodicity calculations for mid-latitude pedestal craters and low-latitude tropical mountain glaciations, we explore the timing and pathways of non-polar ice-rich deposits emplaced during the Amazonian period on Mars. We then apply these in the context of the relationship between obliquity and latitudinal ice stability to place constraints on the obliquity history of Mars over the past 200 Myr. In particular, we find that pedestal craters have formed frequently (at least every 15 Myr) over this time period, but the formation age of the population is only 90 Myr, meaning that ice-rich material was only transiently deposited at mid latitudes, rather than continuously. Glaciations at the Tharsis Montes, however, have not reached their full extent since ~130 Ma (with minor glaciations around 65 Ma), but must have been in existence for durations as long as hundreds of Myr in order to form the recessional drop moraines (ridged facies) at Arsia Mons. These data suggest that there has been frequent exchange of ice between the high, mid, and low latitudes, with ice being emplaced for longer durations of time at low latitudes than at mid latitudes prior to ~130 Ma, when the tropical mountain glaciers were fully developed. Mid-latitude deposits, however, are likely to have occurred more frequently and recently than low-latitude deposits. This implies an obliquity history that oscillates between 35° and $\geq 45^\circ$ prior to ~130 Ma, exchanging ice between the mid and low latitudes in order to create the Tharsis glaciations and some pedestal craters. The

obliquity history then oscillated between $\sim 35^\circ$ and $\leq 25^\circ$ over the past ~ 130 Ma, transporting volatiles between the mid latitudes and the polar regions, which formed the youngest pedestal craters. The Tharsis Montes glaciations and mid-latitude pedestal crater population, however, represent only a fraction of the non-polar climate signatures on Mars. The dating and analysis of additional ice-related and periglacial morphologies will place further restrictions on the timing, pathways, and obliquity scenarios discussed here.

1. Introduction

The climate history of Mars involves a host of variable factors including the solar constant, spin-axis/orbital parameters, atmospheric properties, and characteristics of the planetary surface (e.g. Head et al., 2003; Read and Lewis, 2004). Each factor has contributed to the long-term evolution of the climate of Mars. Deconstructing the dynamic interplay between these inputs has been at the forefront of Mars research since the 1960s, when the Mariner spacecraft obtained the first close-up images of the surface (e.g. McCauley et al., 1972). Despite the limitations of having no human missions or sample return missions, planetary scientists have made significant progress toward an understanding of the climate history using a combination of datasets gathered by orbiters, landers, and rovers, as well as meteorites from Mars. In particular, our knowledge has been bolstered by high-resolution and multispectral images (e.g. Bibring et al., 2005; McEwen et al., 2007; Murchie et al., 2007) and altimetry data (e.g. Smith et al., 1999) of the surface of Mars, atmospheric measurements (e.g. Zurek et al., 1992), and climate modeling (e.g. Forget et al., 2006; Haberle et al., 2003). As Mars research continues to place constraints on the multitude of possible climate histories, new data will play a crucial role in redefining the boundaries.

The behavior of recent climate change remains debated as evidence mounts for a variety of ice-rich surface features at mid and low latitudes (e.g. Head and Marchant, 2008) (Fig. 1); the current presence of polar ice caps on Mars (e.g. Phillips et al., 2008) with minimal quantities of surface ice at mid and low latitudes suggests a complex exchange of volatiles over the past few hundred Myr (e.g. Tanaka, 2000). In an effort to improve the current understanding of Late Amazonian climate change, we perform

geomorphological analyses to assess the distribution and characteristics of non-polar ice-related deposits and crater counting analyses to assess their ages. By definition, the Late Amazonian Epoch began between 300 and 600 Myr ago (Hartmann and Neukum, 2001), and we will generally refer to the Late Amazonian as the past few hundred Myr of martian history. This research includes original investigations as well as revisions of previous analyses using newly available image data. Specifically, we combine the study of pedestal craters (mid and high latitude) with tropical mountain glaciers (equatorial) (Fig. 1). Using knowledge of the role that ice played in creating these features in conjunction with our calculated individual ages and population formation age for them, we are able to define new constraints for the history of Late Amazonian climate change. Through this analysis, we seek to answer the following outstanding questions: (1) What has been the timing and periodicity of ice-rich paleodeposits at mid and low latitudes, particularly in the last 200 Myr? (2) What is the physical pathway that snow/ice takes from the polar regions to the equatorial regions and back during excursions to high obliquity? (3) What constraints can we place on Mars' obliquity history during the past 200 Myr?

2. Mid-Latitude Pedestal Craters

Recent analyses support the hypothesis that pedestal craters (Pd) on Mars form via sublimation of ice-rich deposits (Kadish et al., 2008a, 2009, 2010) (Fig. 2). Our research favors a model that calls on impact into volatile-rich targets to produce Pd during periods of higher obliquity, when mid- to high-latitude substrates were characterized by thick layers of snow and ice. The area proximal to the crater becomes

armored during the impact event. During return to lower obliquity, the regional ice-rich unit sublimated, except below the protective cover of the armored pedestal surfaces. These intervening volatiles eventually migrated either equatorward or poleward, away from the mid latitudes. In this model, the ages of individual Pd and the formation age of the Pd population have significant implications for the timing and recurrence of the accumulation of ice-rich material at mid latitudes. In this study, we provide evidence that Pd are young (usually Mid to Late Amazonian) and formed from multiple episodes of emplacement of ice-rich material at mid latitudes.

2.1. Morphologic and Stratigraphic Observations

Pedestal craters (Fig. 2) are generally morphologically fresh, with well-preserved crater rims and minimal degradation of pedestal surfaces (Barlow et al., 2000; Kadish et al., 2009). Although some Pd show evidence of infilling in their crater bowls, most are relatively unmodified by filling processes; the elevation of the bottom of the crater bowl is usually between the elevation of the pedestal surface and elevation of the surrounding terrain. While these attributes support the interpretation that Pd are young, one particular feature, pits in the marginal scarps of some Pd (Kadish et al., 2008a), are interpreted to implicate recent sublimation of the ice-rich material composing the pedestal. These pits (Fig. 2), which are morphologically similar to scallops, represent loss of material from the pedestal itself; topographic profiles confirm that the pits do not extend below the elevation of the surrounding terrain. They are not seen on the pedestal surface, which supports the interpretation that the armoring is weaker along the pedestal margins, allowing ice to sublimate from the scarp and form the pits. Given our current

understanding of the diffusive exchange of water between the regolith and the atmosphere (e.g. Mellon et al., 2004), it is possible that marginal pits represent an active sublimation process and are still developing, forming connected pits and moat-like structures around some individual Pd (Kadish et al., 2008a, 2010).

From a stratigraphic perspective, a significant portion of the Pd population is located on Amazonian-aged units in the northern lowlands and in the north polar region (e.g. Tanaka et al., 2003, 2008). In particular, Pd are concentrated on the Arcadia and Elysium Formations, as well as several other young plains units. This superposition of Pd on young surfaces requires that the Pd are also young; any resurfacing of the surrounding terrain would have destroyed or drastically altered the Pd, and as such, Pd must be younger than the units on which they are emplaced. There are also many Pd located on Hesperian-aged units. These Pd do not necessarily appear older than those superposed on Amazonian-aged units, suggesting that the mid-latitude deposits required to form Pd can be completely removed via sublimation and deflation without resetting the age of the regional surface.

In addition to stratigraphic relationships between Pd and the intercrater terrain, we have identified several instances of Pd which are partially draped over the scarps or completely superposed on the surfaces of other Pd (Kadish et al., 2009, 2010) (Fig. 2b,c). Although these examples do not provide absolute Pd ages, they do support the interpretation of a recurring ice-rich deposit at mid latitudes. Cases of partially draped Pd reveal that they are topographically influenced by the underlying Pd scarp. This requires one Pd to form completely, followed by an impact into a subsequent deposit that contours to the topography of the underlying Pd; if the two Pd formed from the same paleodeposit

at different periods during its accumulation (and thus different thicknesses), the pedestals would overlap, but both would be flat, preserving the level topography of the paleodeposit (see Figs. 8 and 9 from Kadish et al., 2010).

2.2. Population Formation Age

Crater counting (Fig. 3) cannot provide an absolute age for the entire Pd population due to the fact that not all pedestals formed at the same time. It can, however, provide a lower limit for how long the population took to form, assuming continuous presence of the mid-latitude, ice-rich deposit. In other words, plotting all the Pd diameters on a size-frequency distribution plot will establish the amount of time it would take to accumulate that particular crater population (Fig. 4). Kadish et al. (2009) calculated this value using a subset of the Pd database ($N=1,363$), which yielded a best-fit of ~ 50 Myr. They used this value to extrapolate a minimum population formation age of 100 Myr, based on the fact that they had only used approximately one half of the total Pd population (Kadish et al., 2009), and that a constant crater flux can be assumed for young surfaces (Neukum et al., 2001). We have since completed the diameter measurements of all mid-latitude Pd in the catalog ($N=2,287$), allowing for a revised population formation age calculation. Using the full Pd population database and the corresponding area on which they form, we derive a best-fit for the population formation age of ~ 90 Myr based on Hartmann (2005) isochrons (Fig. 4). The best fit line for the size-frequency distribution is steeper than the isochrons for crater sizes greater than about 3 km. This is due to the fact that the sizes of Pd are restricted by the thickness of the target ice-rich deposit, which inhibits the formation of large Pd, converting them into excess ejecta

craters due the excavation of regolith target material below the ice-rich mantle (Kadish et al., 2011).

As noted by Kadish et al. (2009), the time period over which the observed population formed is necessarily greater than 90 Myr because the ice-rich deposit is not currently present. In addition, a robust solution for the last 20 Myr of martian obliquity history (Laskar et al., 2004) shows low obliquity periods for the last 3-5 Myr, and potentially widely variable obliquity for the last 250 Myr (Fig. 5). This guarantees that the ice-rich material has not been continuously present across the mid-latitudes throughout the Late Amazonian, and therefore the necessary cumulative 90 Myr during which the ice-rich material was present is likely to have taken place over several episodes throughout the Amazonian. As we will later discuss, because Pd can be eroded and removed, 90 Myr is a lower limit for the total time period during which ice has been emplaced at mid latitudes. However, the Pd used to calculate this 90 Myr timescale match the production function defined by Hartmann (2005), supporting the accuracy of this value. We explore this issue further in the discussion where we show that, although the 90 Myr timescale is a lower limit, the actual value cannot be significantly different.

2.3. Individual Pedestal Ages

In order to identify specific time periods when ice-rich material was present at mid latitudes, we have counted craters on the surfaces of 50 individual mid-latitude pedestals using HiRISE (25 cm/pix) and CTX (6 m/pix) image data (Table 1); HiRISE data were necessary for accurate counts on the smaller pedestal areas ($<100 \text{ km}^2$). The pedestals on which we counted are not randomly selected – we counted on those that had

100% coverage of clear HiRISE or CTX data – and therefore do not represent a random sampling of the total population (Fig. 6). It is important to note that the crater counting is limited to the pedestal surface, and does not include the pedestal crater bowl (Figs. 7,8). This ensures that we are dating the age of the preserved paleodeposit and not younger crater fill. Although crater counts on small areas are prone to uncertainties due to the statistics of small numbers, secondary craters, and erosion/removal of small craters, crater counting on numerous pedestal surfaces can provide robust results; groups of Pd with the same age provide insight into the timing and frequency of ice-rich deposition at mid latitudes. The best fits for these data yield an age range of ~1 Myr to ~3.6 Gyr and a median of ~140 Myr (Fig. 9). These ages are necessarily lower limits due to the possibility of the pedestal surfaces being mantled by subsequent deposits. Because this is still a relatively small subset of the total Pd population, we are cautious about extrapolating small groups with the same age to imply the occurrence of large-scale paleodeposit accumulations.

We do, however, see some significant trends in the ages of the 50 individual pedestals (Fig. 9; Table 1). First, 70% of the pedestal ages are less than 250 Myr. This may be due to erosion of older Pd, which would preferentially skew the total population to include more young Pd. This erosion is notable when viewing individual size-frequency distributions, which show a paucity of small superposed craters, resulting in slopes that are shallower than the Hartmann (2005) isochrons (Figs. 7,8). Second, during the 150 Myr between 25 Ma and 175 Ma, there is at least one pedestal that has formed every 15 Myr; in other words, over this time period, there is never a gap of more than 15 Myr between individual Pd ages (Figure 9; Table 1). This suggests either frequent

accumulation of mid-latitude ice-rich paleodeposits, or that the deposits are maintained for long (tens to hundreds of millions of years) time periods. Finally, although there is no statistically significant trend between the age and area of a given pedestal ($R^2 = 0.0128$), none of the nine pedestals older than 1.5 Gyr is $>100 \text{ km}^2$ in area, and only one of the fifteen pedestals older than 250 Myr is $>100 \text{ km}^2$ in area. By comparison, seven of the 35 pedestals less than 250 Myr are $>100 \text{ km}^2$ in area. This supports the interpretation of Kadish et al. (2010) that older pedestals are being eroded from the margins inward to become smaller. As we will show, these trends in individual pedestal ages have significant implications for the periodicity of ice-rich paleodeposits at mid latitudes during the Late Amazonian.

3. Ages of the Tropical Mountain Glacier Fan-Shaped Deposits

Fan-shaped deposits (FSDs) extending to the northwest of the Tharsis Montes on Mars (Fig. 10) are the remnants of Amazonian-aged, cold-based, tropical mountain glaciers (TMGs). The glacial origin for these deposits was first recognized on the basis of their facies (Head and Marchant, 2003; Kadish et al., 2008b; Milkovich et al., 2006; Shean et al., 2005; Shean et al., 2007; Williams, 1978). The most prominent units include concentric ridges tracing the distal margin of the FSDs and a knobby facies distributed over much of the FSDs. These have been interpreted as drop moraines and sublimation till, respectively. The recessional drop moraines form at the end of the glacier, where debris is deposited and builds up during periods of glacial equilibrium (Boulton and Eyles, 1979). The knobs are interpreted to form when supraglacial material is deposited during rapid sublimation/down-wasting of the glacier. Subsequent studies have used

atmospheric general circulation models (Forget et al., 2006) to show that ice/snow will accumulate on the western flanks of the Tharsis Montes during periods of high obliquity ($>45^\circ$). GCMs have been used in conjunction with ice-sheet flow models (Fastook et al., 2008) to reproduce possible histories for the growth and retreat of the glaciers.

The ages of the Tharsis Montes and Olympus Mons have been established in previous studies using both stratigraphic relationships and crater counting. These stratigraphic relationships had been previously assessed and, in accordance with Viking crater counting data, Tanaka (1986) assigned each of the Tharsis Montes a Late Amazonian age. Based on their observations and the resulting paleostratigraphic reconstruction, Scott and Tanaka (1981, 1986) argued that the Tharsis Montes' FSDs are approximately the same age as the youngest flows coming from each of the volcanoes. Subsequent regional mapping has been conducted (e.g. Scott and Zimbelman, 1995; Scott et al., 1998) which verifies that the FSDs were emplaced throughout the Mid- to Late-Amazonian. Scott and Zimbelman (1995) assign separate Amazonian ages for the distinct units within the Arsia Mons FSD. Scott et al. (1998) identify ages for lava flows on the shield of Pavonis Mons, arguing that the majority are Early Amazonian in origin while Late Amazonian flows are limited in extent; the FSD formed concurrently with these latter flows.

Our efforts to date the Ascraeus FSD (Kadish et al., 2008b), as well as efforts by Shean et al. (2005, 2006) to date the Pavonis and Arsia FSDs, help to place the glaciations into the time framework of non-polar ice deposition in the Amazonian (Head and Marchant, 2008; Head et al., 2009). Crater counting has confirmed Amazonian ages for the Tharsis Montes (e.g. Hartmann et al., 1999; Hartmann and Neukum, 2001) and

their respective FSDs (Shean et al., 2005; Shean et al., 2006; Kadish et al., 2008b), as well as for Olympus Mons (e.g. Basilevsky et al., 2005; Grier et al., 2001; Hartmann and Neukum, 2001; Head et al., 2005). In this section, we use recent high-resolution image data to provide updated crater counts for each of the Tharsis Montes FSDs.

3.1. Ascraeus Mons

Kadish et al. (2008b) undertook an analysis of the impact crater size-frequency distribution over a near-complete (>99% coverage) THEMIS IR mosaic (100 m/pix) of the ~13,000 km² Ascraeus Mons FSD. These images were supported by a partial THEMIS VIS mosaic (18 m/pix) that covered 83% of the FSD. Only craters that were too small to be seen in the IR data were counted using the VIS data, although the diameters of the larger craters were checked using the VIS data. Craters were counted down to 350 m in the IR mosaic. Plotting the VIS and IR craters on the same isochrons showed that the data flattened out for diameters less than 350 m, crossing the isochrons (Hartmann, 2005). This implies that the deposit has undergone modification and possible resurfacing since its deposition; the flattening of the plot at low diameters suggests that craters <350 m in diameter are being eroded or infilled at the same rate that they are being produced. Because of this, Kadish et al. (2008b) used craters that had diameters >500 m in order to calculate an absolute age; the data from N(.5)-N(2) yielded a best fit age of approximately 250 Myr based on the Hartmann (2005) isochrons.

We have recounted the craters in the Ascraeus Mons FSD (Fig. 11) using newly available CTX images (6 m/pix), which provide 100% coverage of the deposit. This revision allowed us to improve the accuracy of previous diameter measurements, include

new craters, and exclude craters that are clearly parts of secondary chains. When plotted on the isochrons, the new crater counts show that the data roll over at craters <700 m in diameter (Fig. 11). Using the data from N(.7)-N(2), which includes 14 craters, provides a revised best fit age of approximately 220 Myr based on the Hartmann (2005) isochrons, which is 12% younger than the previous calculation by Kadish et al. (2008b) (Fig. 11). This updated age brings it closer to the ages of the Arsia and Pavonis FSDs, as will be discussed in the following sections.

3.2. Pavonis Mons

Shean et al. (2005) used THEMIS IR and VIS data to establish a Late Amazonian age for the ~74,000 km² Pavonis Mons FSD (Fig. 10), between 10 and 200 Myr based on isochrons from Hartmann and Neukum (2001). Plotting their data on the Hartmann (2005) isochrons produces a best fit age of approximately 110 Myr. They note, however, that limited coverage of the area and a poor statistical distribution make this absolute age somewhat uncertain; a young crater-retention age is expected due to (1) modification of the units of the FSD since their deposition and (2) erosion and infilling of smaller craters (Shean et al., 2005). Additionally, some craters observed may be impacts into the Tharsis lava plains, which underlie the FSD units; counting these craters would result in an overestimate of the age (Shean et al., 2005).

In a manner similar to the Ascraeus revision discussed above, we utilized CTX images that were released since the Shean et al. (2005) study, which provide 100% coverage of the FSD. The new crater counts (Fig. 12) confirm that, similar to the Ascraeus FSD, craters <700 m in diameter are being eroded at a rate comparable to the

rate at which they are forming, resulting in a rollover of the data on the size-frequency distribution; this erosion is likely to be eolian in nature, and smaller craters may also be completely infilled by the thick regional dust deposits (e.g. Christensen, 1986). Using the 49 craters counted from N(.7)-N(4) yields a revised best fit age of 125 Myr (Fig. 12). This new age is about 14% older than the Shean et al. (2005) calculation.

3.3. Arsia Mons

Using THEMIS VIS and HRSC images, Shean et al. (2006) concluded that a Mid- to Late-Amazonian age for the ~166,000 km² Arsia Mons FSD is the most likely. They calculated a lower boundary for the absolute age of >25 Ma (90% confidence) by counting only the fresh craters on the deposit and an upper boundary of <650 Ma (90% confidence) by counting all craters on the deposit. This upper boundary population included craters that had experienced infilling and modification, indicating that they were either older than the FSD deposit or emplaced on an underlying flow (Shean et al., 2006). Plotting the Shean et al. (2006) data of all craters >700 m in diameter within the FSD on Hartmann (2005) isochrons yields a best fit age of approximately 175 Myr.

Using a combination of HRSC and CTX data, we created a seamless mosaic of the Arsia FSD at 10 m/pix resolution. Counting on this mosaic, we identified 65 craters that are >700 m in diameter, 12 more than were found in the Shean et al. (2006) survey. Plotting the new catalog of 764 craters in the Arsia FSD >250 m in diameter (Fig. 13) confirms that the rollover in the data occurs around 700 m diameter, making this the appropriate lower limit cut off for establishing an absolute age. The resulting best fit age

from the new data, using N(.7)-N(10) and Hartmann (2005) isochrons, is about 210 Myr, which is 20% older than the Shean et al. (2006) age (Fig. 13).

In addition to dating the entire Arsia FSD, we also calculated the ages of three distinct sections of the ridged facies, which is composed of recessional drop moraines (Fig. 14). Because the Arsia FSD contains the largest sequence of ridges of any of the tropical mountain FSDs, it is the ideal candidate for identifying any potential trends in the progression of the ages of the ridges as a function of radial distance from the flank of the mountain. Dating an individual ridge is not possible due to the low crater density in the area and the extremely thin width of each ridge. However, by dividing the ridges into sections, we can create countable areas and establish a sequence of ages. These ages can then be used to provide clues as to when and how quickly the glacier(s) receded.

Using the revised crater database for the Arsia deposit, we defined three sections of ridges using the most prominent continuous ridges as the basis for subdivision (Fig. 14); we refer to the sections as the outer (farthest from the mountain), middle, and inner (closest to the mountain) sections. It is important to note that, because the regions were defined based on specific geomorphic boundaries, they are not all the same size, nor do they contain the same number of ridges. Because the age determination via crater counting accounts for the area of the dated surface, the differences in the areas of the regions should not affect the chronology. Although individual ridges can merge or suddenly disappear, we were able to count the number of ridges in each section along several different radial crossings to provide robust values. We found that the outer, middle, and inner sections contained approximately 80, 40, and 65 ridges, respectively. Although we display all craters larger than 90 m in the size-frequency distributions from

these ridged areas (Figs. 15-17), there is a clear rollover in the data for craters <700 m. This is expected given that our dating of the entire FSDs also showed that the crater populations did not match the expected production functions for craters <700 m. As such, only craters >700 m in diameter were used to calculate best-fit ages for the ridged sections. The best-fit ages, based on Hartmann (2005) isochrons, are 725 Myr (Fig. 15), 475 Myr (Fig. 16), and 345 Myr (Fig. 17) for the outer, middle, and inner sections, respectively.

As we will discuss in the following section, this chronology shows that the ridges are certainly the oldest facies within the FSDs. Further, the time that elapsed between the formation of each section suggests that an individual ridge may take hundreds of kyr or even a few Myr to form. In the following discussion, we explore this possibility using the cross-sectional area of the ridges and the expected glacial flow rates (Fastook et al., 2008), and assess the implications that this ridge formation rate has on the movement of ice during the Mid and Late Amazonian.

4. Discussion

4.1. Timing and Periodicity of Ice-Rich Paleodeposits

The notion of a recurring mid-latitude, ice-rich deposit is supported by the known variations in martian obliquity over the past 20 Myr (Laskar et al., 2004). The obliquity of Mars over the last 5 Myr has oscillated between 15° and 35°, and during the previous 15 Myr, it oscillated between 25° and 45° (Fig. 5). Given the modeled exchange of volatiles between the poles, mid latitudes, and equatorial regions at these obliquities (e.g. Forget et al., 2006; Madeleine et al., 2009; Mischna et al., 2003), and the high frequency

of the recent obliquity variations (e.g. Levrard et al., 2004; Laskar et al., 2004; Head et al., 2009), it is expected that ice-rich material has been repeatedly deposited and removed at mid latitudes throughout the Late Amazonian. For a summary of the morphologies that result from the recurring deposition of ice-rich material at mid latitudes (Fig. 1), see Head and Marchant (2008). Briefly, from a geomorphological standpoint, this repeated deposition and removal cycle has been shown in the form of both desiccation of the latitude-dependent mantle (e.g. Head et al., 2003; Mustard et al., 2001) and widespread mid-latitude glaciations at the dichotomy boundary (e.g. Head et al., 2005, 2006). In this section, we discuss our morphological and crater counting analyses in the context of when and how frequently ice-rich deposits may have accumulated at the mid and low latitudes.

In a study intended to explore the climatic scenarios regarding mid-latitude glaciations – particularly lobate debris aprons and lineated valley fill in the Deuteronilus and Protonilus Mensae regions – Madeleine et al. (2009) derived a net accumulation rate of ~10 mm/yr across vast regions in the northern mid-latitudes. Although this rate was intended to understand the growth of lobate debris aprons, the predicted accumulation also occurs across the areas in which mid-latitude pedestal craters are identified (see Fig. 7 in Madeleine et al. 2009). At a net accumulation rate of 10 mm/yr, it would take on the order of 5 kyr to form a deposit thick enough to produce an average pedestal (~50 m in height), and even the tallest mid-latitude pedestals (<200 m) could form from deposits that accumulated in 20 kyr. It should be noted that the 10 mm/yr accumulation rate (Madeleine et al., 2009) is specific to the mid latitudes, but is robust within a factor of two for all climate parameter settings that result in accumulation at the mid latitudes. As

such, although the accumulation rate may be different for high- and low-latitude scenarios, it is likely to be correct to within an order of magnitude. This is supported by the accumulation rates identified by Forget et al. (2006) for the TMGs of 30 to 70 mm/yr. The TMGs, predicted to reach maximum thicknesses of 2-3 km (Shean et al., 2005), could thus accumulate in tens to a hundred kyr. These accumulation timescales are very short in comparison to the amount of time that we predict the deposits were emplaced. As such, throughout this discussion, we will assume that deposits can be rapidly emplaced and removed, allowing deposits to occur transiently.

Although the crater counting ages on the surface of pedestals are lower limits due to possible erosion and mantling (Figs. 7,8), the relative surface ages are robust because the pedestal surfaces are being exposed to the same degradation processes, such as sublimation and eolian removal of material. Consequently, the database of 50 pedestal crater ages has important implications for how frequently ice is emplaced at the mid latitudes (Fig. 9). In particular, our finding that, even with the limited subsample size, at least one pedestal has formed every 15 Myr between 25 Ma and 175 Ma (Table 1), suggests relatively frequent recurrence of the accumulation of the ice-rich paleodeposit. We find this explanation to be more plausible than the alternative, which would be that the deposit is continuously maintained at mid latitudes for time periods exceeding 100 Myr. As discussed, the formation age of the entire Pd population is only 90 Myr; if the deposit were continuously emplaced between 25 Ma and 175 Ma, we would expect a much larger Pd population based on the current cratering rate (Hartmann, 2005). For example, if the deposit were emplaced for the entire 150 Myr span, we would expect to see 67% more pedestal craters than we currently observe. Additionally, because we have

dated pedestals that are older than 175 Myr (Table 1), we know that the deposit was present at these times earlier in the Amazonian, and we would therefore expect an even larger population of Pd to exist at that time. Finally, the presence of fresh, partially superposed Pd (Fig. 2c) strongly supports the interpretation that the deposit has been emplaced, completely removed, and emplaced again (Kadish et al., 2010). This further supports the interpretation that the emplacement of the deposit has been a recurring process during the Late Amazonian, rather than a completely continuous one.

It is important to note the potential impact of the erosion of Pd on this analysis. We know pedestals are being highly degraded and are likely to have been completely removed due to sublimation/deflation on the basis of prior morphological observations of sublimation pits/moats and debris haloes surrounding pedestal scarps (Kadish et al., 2008a, 2010). As previously noted, none of the oldest pedestals analyzed have large surface areas, but because all pedestals erode over time, the oldest examples were likely to have been much larger when they initially formed. Despite the evidence of erosion of individual Pd, the removal rate is not fast enough to alter our previous conclusion about the Pd population size – namely that if the mid-latitude paleodeposit were emplaced for continuous periods lasting as long as 150 Myr, then the current Pd population is too small. In other words, even if we account for the erosion and complete removal of Pd, the current observed Pd population argues against the continuous presence of ice-rich material at mid-latitudes for periods of 150 Myr. This is confirmed by the location of the rollover in the size-frequency distribution of the Pd population formation age, which occurs at approximately 750 m in diameter (Fig. 4); if the erosion and removal of Pd were affecting larger examples, we would expect to see a rollover in the size frequency

distribution at larger Pd sizes. It should also be noted that the formation of large Pd (greater than approximately 4 km in diameter) is inhibited due to penetration of the impactor through the ice-rich surface layer and excavation of significant volumes of regolith, which usually results in an excess ejecta crater (Black and Stewart, 2008; Kadish and Head, 2011). Examining the Pd population between 1 and 3 km in diameter (Fig. 4), which accounts for approximately 77% of the total Pd population, reveals that this size range matches the expected production function (Hartmann, 2001). We use this range for identifying a best-fit because the erosion/removal and inhibition of formation of Pd only have a statistically significant effect on Pd that are $<\sim 750$ m and $>\sim 4$ km in diameter, respectively. The remaining 23% of the Pd population that is not significantly influenced by erosion or target thickness equates to more than 1750 craters that are used to establish the population formation age, ensuring that 90 Myr is an accurate value and not a significant underestimate (Fig. 4).

Because Pd erode and can be removed due to sublimation/deflation over long time periods, the decline in the relative number of older pedestals is not an indication that ice-rich paleodeposits were emplaced less frequently in the Early Amazonian or Hesperian. The presence of 10 Pd dated to between 1 and 3.6 Gyr in age (Fig. 9) guarantees that the accumulation of ice-rich material at mid latitudes has periodically occurred during the Amazonian and possibly the Hesperian. The scarcity of these older Pd is likely to be an indication of the effectiveness of the degradation process. It is, however, possible that Pd formed much less frequently in the past, and that large populations of Hesperian-aged Pd never existed. Our current data do not allow us to distinguish between these two scenarios.

The ages of the fan-shaped deposits (FSDs) (Fig. 10), as discussed previously, have important implications for when ice was present in the equatorial region. Our crater counting yields ages of 220 Myr, 125 Myr, and 210 Myr for the Ascraeus, Pavonis, and Arsia FSDs respectively (Figs. 11-13). However, these are derived from the total superposed crater population and entire surface area within each FSD. We know, based on our dating of the Arsia ridged sections (Figs. 10-13), that the facies are not all the same age; the distribution of craters within the Arsia FSD suggests that the ridged section is the oldest region, with younger surfaces exposed in the inner parts of the FSD. For example, a size frequency distribution for the Arsia FSD excluding the ridged facies yields a best-fit age of approximately 130 Myr, which is 80 Myr younger than the age derived for the whole deposit. As discussed previously, eolian modification and dust deposition within the FSDs may be erasing small craters. As such, we have used only craters >700 m in diameter, whose size frequency distribution matches the production function, in calculating this 130 Myr best-fit age. This inner-deposit age still appropriately exceeds the minimum age of at least 45 Ma established by Shean et al. (2006) on the basis of dated lava flows that are superposed on the Arsia FSD. Other young surfaces have been dated within the FSDs, as shown in work by Shean et al. (2007) that offers evidence for more recent small-scale glaciations occurring in graben on the western flank of Arsia. The fill material left by the accumulation of ice is calculated to be ~35-115 Myr, with a model age of 65 Myr (Shean et al., 2007). In addition, at the Pavonis FSD, Shean et al. (2005) identified a smooth facies that may represent debris-covered ice, implying that some glacial remnants are still present at these low latitude regions. Finally, Neukum et al. (2004) dated lobate glacial deposits at the base of

Olympus Mons (Milkovich et al., 2006) and derived ages of 130 to 280 Myr for the larger units, but 20 to 60 Myr for some subunits (Neukum et al., 2004).

Due to the cold-based nature of these glaciers (e.g. Head and Marchant, 2003; Kadish et al., 2008b; Shean et al., 2005), it is difficult to discern how many distinct glaciations have occurred. Confirmed observations of crisscrossing and merging moraines support the interpretation that multiple glaciations, or phases in single glacial periods, have occurred at each of the Tharsis Montes. When a glacier is emplaced, the ice would protect the underlying regolith from smaller impacts, producing artificially young ages for the FSDs. Because of this and the variable ages of the facies within the deposits, we are cautious about using the derived ages of the FSDs as time periods when ice was certain to have been present at the equator. Despite this complication, the young ages of the FSDs are still extremely important because they ensure at the very least that ice has been present in the equatorial region at some point during the Late Amazonian. The morphological observations of the ridges, as well as of several inward facing scarps (Shean et al., 2005; Kadish et al., 2008b) support the interpretation that the glaciers have been recurring or that they have experienced significant oscillations between advance and retreat while being emplaced. The available morphological evidence is not sufficient to establish whether completely distinct glaciations have occurred, but we find this recurrence likely given the discussed history of the exchange of volatiles between high, mid, and low latitudes over hundreds of Myr.

Dating the Arsia ridged facies (Fig. 14) places more definite constraints on the timing and duration of glacial emplacement. Because the ridges are a single facies near the outer edge of the FSD, they are less likely to show the effects of artificially young

ages due to covering by glacial ice. In addition, because we understand how glacial moraines form, we know these to be recessional moraines and can therefore establish a chronology with the outer ridges being the oldest and the inner ridges being the youngest. As previously mentioned, the sequence of ages for the sections of the ridged facies and the remaining non-ridged area of the Arsia FSD is 725 Myr, 475 Myr, 345 Myr, and 130 Myr (Figs. 15-17). Because the glacier is likely fluctuating/pulsating as it retreats (Fastook et al., 2008), we cannot definitively state that the outer section of ridges took 250 Myr to form (the difference between the ages of the outer and middle ridged sections). However, because the entire sequence occurred over hundreds of millions of years and produced almost 200 ridges, we can use the differences in ages and the number of ridges in each section to calculate an average for the amount of time necessary to produce a typical ridge. Not surprisingly, when we ratio the time periods for each section (250 Myr, 130 Myr, and 215 Myr) to the number of respective ridges in each section (80 ridges, 40 ridges, and 65 ridges), we find strikingly consistent values for the average amount of time needed to form a ridge (3.13 Myr/ridge, 3.25 Myr/ridge, and 3.31 Myr/ridge).

To assess the validity of a million-year-timescale of ridge formation, we performed a 1D calculation of the debris thickness superposed on the glacier that would be necessary to form a ridge given the cross sectional area of a ridge, the glacial flow rate, and the time allowed to form the ridge (Table 2). This model assumes that debris is emplaced along a line extending radially away from flank of Arsia, and is being transported to the terminus of the glacier along the glacier's surface, where it is deposited to form a ridge, which has a triangular cross section (Fig. 18). We made this calculation

for a minimum, median, and maximum sized ridge. It is important to note that the cross-sectional area is directly proportional to the resulting debris thickness. As such, even if the ridges are ice-cored (perhaps as much as 60% pure ice), the effect will be negligible because we are concerned with orders of magnitude for the debris thickness and not exact values. For time periods, we used four orders of magnitude (1 kyr, 10 kyr, 100 kyr, and 1 Myr) to ensure that any reasonable possibilities would be considered. Finally, we applied two possible glacial flow rates (0.01 m/yr and 0.1 m/yr) to account for the range of values predicted by the glacial models of Fastook et al. (2008). It should be noted that the resulting values for the debris thickness are time-averaged; we would expect this thickness to fluctuate considerably during the extent of its emplacement, especially given the possible 100 kyr to 1 Myr timescale and spin axis/orbital variations that occur over these timescales (Fig. 5).

This set of variables (Fig. 18) produces 24 outcomes for the debris thickness, ranging from 5 mm to 9 km (Table 2). If we examine the eight possible outcomes for a typical (median) ridge, the range is 8 cm to 800 m. As mentioned, some years may produce anomalously large debris quantities, especially during massive eruptions, but these time-averaged values must have been physically possible for tens to hundreds of Myr to form the entire extensive sequence of ridges. If we consider typical eruption fluxes (e.g. Wilson et al., 2001) and the limitations imposed by the maximum fluxes allowed without completely melting the glacier (Wilson and Head, 2009), it is clear that debris thicknesses on the order of 1 m or larger, which must have been sustained for thousands of years, are extremely unlikely. Even under the fast glacial flow scenario (0.1 m/yr), building a typical ridge in 10 kyr would require a debris thickness of 8 m.

Allowing 100 kyr to form the ridge yields a thickness of 0.8 m, which is still quite high given the time period for which it must have been emplaced. As can be ascertained from the results shown in Table 2, this model strongly supports the million-year formation timescale for typical ridges. This result is further supported by the age difference between the outer ridged section (725 Myr) and the non-ridged portion of the FSD (120 Myr), which suggests that glaciers have been present for hundreds of Myr, cumulatively, to create the differences in crater density.

In the context of the timing and periodicity of ice-rich deposits at mid and low latitudes, the ages of the FSDs and the time required to form the moraines provide two important constraints: (1) Large volumes of ice have been present at low latitudes within the last few hundred Myr, and at mid latitudes within the past tens of Myr. (2) If the moraines cumulatively took ~600 Myr to form, then ice must have been present for a longer duration in the Late Amazonian at low latitudes, in the form of TMGs, than at mid latitudes, as established by the relatively brief 90 Myr population formation age of the Pd. As we will discuss, these conclusions have significant implications for how ice-rich material migrates from the polar region to mid and low latitudes (Head and Marchant, 2008).

4.2. Transport Pathways for Ice-Rich Material

The path that snow/ice takes from the poles to mid and low latitudes during periods of high obliquity has remained somewhat unclear (Fig. 19). Recent work based on geomorphological evidence (e.g. Head et al., 2003) suggests that ice can take a top-down path at obliquities of 30 to 35°, moving from the poles to mid latitudes to the

equatorial region, mimicking the typical development of terrestrial ice ages. The ice-rich deposits recede in the reverse order, sublimating first from the lower latitudes and then the mid latitudes (Head et al., 2003). Climate models (e.g. Forget et al., 2006; Levrard et al., 2007; Madeleine et al., 2009; Mischna and Richardson, 2005; Montmessin et al., 2007), have suggested another potential path. Specifically, Forget et al. (2006) show that ice can be transported directly from the polar regions to low latitudes at an obliquity of 45° . Upon return to lower obliquity (25° - 35°), the ice-rich material is removed from the lower latitudes and is transitorily deposited at the mid latitudes before eventually returning to the polar regions (Levrard et al., 2004; Madeleine et al., 2009; Montmessin et al., 2007). The accumulation of these widespread mid-latitude deposits, which act as the target material for Pd formation, is highly dependent on having high dust opacity in the atmosphere (Haberle et al., 2003; Madeleine et al., 2009), and is also very sensitive to the season and location of Mars in its orbit (i.e. perihelion or aphelion) (Mischna et al., 2003). Here, we use the previously presented age and timescale data to provide new insights into these models for the transport pathways.

As mentioned, small quantities of ice are still likely to be present within both the mid- and low-latitudinal bands, being preserved under a rocky covering in the form debris-covered glaciers, lobate debris aprons, and lineated valley fill, or under some other armoring in the form of Pd and smooth facies (Head et al., 2005, 2006; Kadish et al., 2009; Shean et al., 2005). For the purpose of the following discussion, however, we are not concerned with these relatively small volumes that have been trapped; rather, we are concerned with identifying how large quantities of ice-rich material travel between the poles, mid latitudes, and low latitudes. In other words, we aim to understand how large

quantities of ice are transported during shifts in obliquity-driven climate change, particularly when surface ice becomes stable in non-polar regions. The conclusions from the previous section indicate that, in large quantities, ice has been present at mid latitudes more recently than at low latitudes. It is, however, possible that recent cold-based glaciations at low latitudes, in the absence of any debris source from erupting volcanoes, simply left behind no geomorphologic trace. In addition, over the past ~ 1 Gyr, ice has been present for a longer duration of time at low latitudes than at mid latitudes.

What do these timing constraints suggest about the migration paths of ice? To assess this, we will consider each of the two preceding conclusions separately. First, we consider the interpretation that ice-rich deposits have been emplaced more recently at mid latitudes than at low latitudes. Two pedestal surfaces have ages of < 10 Myr, and 13 pedestal surfaces have ages of ≤ 65 Myr (Table 1), which is the model age of the lobate fill material left by the recent glaciations on the flank of Arsia (Shean et al., 2007). Furthermore, the spacing of pedestal ages (≤ 15 Myr between 25 and 175 Ma), may imply that multiple episodes of the accumulation of ice-rich material at mid latitudes have occurred since the last formation of the TMGs. These data imply one of two possible outcomes, which are not mutually exclusive: (1) When ice sublimates from the TMGs, it is transiently deposited at the mid latitudes before returning to the polar regions. (2) Ice can be transported between the poles and mid latitudes without reaching the low latitudes. At least one of these statements must be true in order to produce ice-related morphologies at the mid latitudes that are younger than the youngest evidence for glaciations at low latitudes.

It is certainly possible that both of the previous statements are true. The spacing of pedestal ages (Fig. 9; Table 1), contrasting with the relatively short population formation age of the pedestal craters (Fig. 4), requires frequent periodic emplacement of ice-rich material at mid latitudes during the past ~250 Myr. However, the FSDs do not show significant evidence of such frequent episodic glaciations over that time period. This implies that ice-rich material is frequently but briefly being removed from the polar regions and emplaced at mid latitudes and then returning to the poles, which would confirm the second statement. If this is the case, it would preclude us from being able to confirm the first statement (that ice is transiently deposited at mid latitudes on its way from the TMGs to the poles), because we are unable to distinguish between mid-latitude ice-rich deposits that have been sourced from the polar regions versus those sourced from the low latitudes; ice sublimating from the TMGs may be transitorily deposited at mid latitudes, but the pedestals resulting from these deposits would be indistinguishable from those that formed from ice-rich deposits sourced from the polar regions (Fig. 19).

To investigate further the plausibility of these pathways, we can consider the second conclusion in section 4.1 – that ice has been present for a longer overall period of time at the low latitudes than at the mid latitudes during the past ~1 Gyr. As discussed, the formation age of the pedestal crater population implies that ice-rich deposits have only been emplaced at mid latitudes for ~90 Myr (Fig. 4). This is significantly less than the ~600 Myr required to form the ridged facies (recessional moraines) in the Arsia FSD (Figs. 10-13). As previously stated, these data support the observation of climate models (e.g. Madeleine et al., 2009; Mischna et al., 2003) that obliquity excursions can lead to

surface ice stability at mid or low latitudes, but the ice is generally not stable at both mid and low latitudes at the same time.

In the context of pathways, this logical conclusion does not rule out the possibility that ice being transported equatorward from the poles or poleward from the low latitudes is briefly deposited at mid latitudes. On the contrary, the interpreted high frequency of the mid-latitude ice-rich deposits in conjunction with ice being emplaced longer at low latitudes than at mid latitudes indicates that: (1) excursions to higher obliquity generally move the ice stability zone to low latitudes rather than mid latitudes, and (2) the mid latitudes are a frequent stopping point for ice as it migrates back and forth between the polar and equatorial regions. Simply put, our data support the interpretation that ice is exchanged between the poles and mid latitudes, and between the mid latitudes and low latitudes (Fig. 19). Given the oscillatory nature of Mars' obliquity (Laskar et al., 2004) (Fig. 20), periods of higher average obliquity are likely to have led primarily to the stable emplacement of TMGs, with brief transitions to ice-rich deposits at mid latitudes, then back to the TMGs or polar regions. This exchange of volatiles between mid and low latitudes is an important consequence of our frequency and timescale results, allowing the mid latitudes to have more frequent glaciations and the low latitudes to maintain ice for a longer overall duration of time. As we will discuss in the following section, the periodicity and timescale of ice deposition at mid and low latitudes also provides important guidelines for the recent history of the obliquity of Mars.

4.3. Implications for Mars' Obliquity History in the Late Amazonian

As previously discussed, Laskar et al. (2004) published a series of fifteen possible spin-axis obliquity histories for Mars for the last 250 Myr (although hundreds more were derived) (Fig. 20a). These obliquity histories are identical for the past 20 Myr (Fig. 5). However, due to extreme sensitivity to initial conditions, they vary considerably during the period from 20 Ma to 250 Ma (Laskar et al., 2004). Fortunately, we can use our understanding of the ages and periodicities of Pd and TMGs to identify necessary periods of high and/or low obliquity and the frequency of fluctuations. In particular, the proposed obliquity history (Fig. 20f) should climatically allow for the key observations made throughout the previous section regarding the pathways that ice takes (Fig. 19). In this section, we add to constraints placed by Fastook et al. (2008) and Head et al. (2009) in an effort to refine further the possible history of Mars' obliquity over the past 200 Myr.

Fastook et al. (2008) model growth and retreat of the Arsia TMG using possible obliquity histories from Laskar et al. (2004) as a climate driver for their ice-sheet model. Comparing the subsequent reconstructions with calculated ages of the FSDs (e.g. Shean et al., 2005), Fastook et al. (2008) identify three acceptable obliquity scenarios (P000, N001, and N006). These scenarios all have high obliquity excursions ($>45^\circ$) between 100 and 200 Ma. This requirement is consistent with our revised FSD ages; although the obliquity histories do not extend far enough to compare to our ages for the ridged sections, the age of the non-ridged portion of the Arsia FSD (130 Myr) and the age of the Pavonis FSD (125 Myr) both suggest a collapse of large-scale glaciations around that time, with smaller glaciations occurring more recently (Shean et al., 2007). In order for

the glaciers to be emplaced and forming moraines, periods of high obliquity must have occurred prior to ~130 Myr, as shown by Fastook et al. (2008).

Head et al. (2009) compiled the ages of the FSDs along with mid-latitude glacial events to constrain the obliquity history. They first identify four mean baselines in order to classify the fifteen obliquity histories (Laskar et al., 2004). As described by Head et al. (2009), these baselines are: (1) $\sim 25^\circ$, which is the current mean obliquity, producing robust water-ice polar caps and high-latitude ground ice (Boynton et al., 2002). Under this regime, surface ice is unstable at mid and low latitudes (Mellon and Jakosky, 1995). (2) $\sim 15^\circ$, which is a very low mean obliquity. Under this regime, the CO_2 atmosphere collapses and condenses at the poles (Kreslavsky and Head, 2005). (3) $\sim 35^\circ$, which is an intermediate mean obliquity. This may be sufficient to sublimate the polar cap (Levrard et al., 2007) and produce mid-latitude ice-rich deposits if the dust opacity is sufficiently high (Madeleine et al., 2009). (4) $\sim 45^\circ$, which is a high mean obliquity. Upon reaching this tilt in the spin-axis, the dominant reservoir for ice on Mars will be located at low latitudes (Forget et al., 2006), likely in the form of TMGs (e.g. Head and Marchant, 2003; Kadish et al., 2008b; Shean et al., 2005).

Using these baselines as a framework for classification, Head et al. (2009) separate the scenarios into groups in which the obliquity is generally low, high, or variable/intermediate. Then, using FSD and mid-latitude glaciation ages, they suggest that scenario N001 is the only option that is plausibly consistent with all the ages considered. They do note that, because the published scenarios are not deterministic, N001 is not necessarily the correct solution. Rather, their methodology provides a means for eliminating candidates that contradict the known ages, and constrains the remaining

possibilities (Head et al., 2009). This work, as well as that by Fastook et al. (2008), creates a considerable foundation for our own analysis, which strongly agrees with their interpretations. However, as previously stated, our new and revised ages allow for further specifications regarding the possible obliquity history.

Our data provide the three following guidelines for the recent obliquity history of Mars (Fig. 14a,b): (1) Between 20 and 130 Ma, the obliquity should primarily be fluctuating between 25° and 35° (baselines 1 and 3). This would allow for the frequent accumulation of mid-latitude ice-rich deposits to form the young Pd population, but would not produce a fixed deposit at mid latitudes. This obliquity behavior would be similar to, but perhaps slightly less than, the known obliquity from 5 to 20 Ma, which oscillated between 25° and 45° with a mean at 35° (Laskar et al., 2004). (2) There must be at least one brief excursion to mean high obliquity (baseline 4) in the past 130 Myr (perhaps around 65 Ma) to explain the small glaciation on the flank of Arsia Mons (Shean et al., 2007). (3) Just before ~ 130 Ma, there should be a shift to a mean high obliquity (baseline 4) that would allow for the growth of massive TMGs. This obliquity regime should fluctuate such that it frequently but briefly drops to 35° (baseline 3), allowing for the continued formation of the Pd population.

With these guidelines in hand, we can evaluate the obliquity scenarios selected by Fastook et al. (2008) and Head et al. (2009). We find N006 to be impossible due to its permanence above baseline 4 between 50 and 200 Ma (Fig. 20). This would not allow for the frequent formation of Pd at mid latitudes. In contrast, scenario N001, with a mean obliquity between baselines 3 and 4 for almost the entire 200 Myr period, is not plausible because it would produce too many Pd; this scenario would yield >100 Myr of mid-

latitude ice-rich deposits. Consequently, we prefer a scenario similar to P000, perhaps translated down by $\sim 5^\circ$ with a brief spike to baseline 4 added around 65 Ma (Fig. 20). This obliquity history would be capable of producing the closely spaced Pd ages without creating too large a Pd population. It would also allow for the accumulation of the TMGs prior to 130 Ma and would then have them suddenly collapse with only a limited recurrence around 65 Ma.

This proposed obliquity history is, of course, only one of many possible options that conform to our data. However, as shown by Fastook et al. (2008) and Head et al. (2009), an important result of introducing the ages of new glacial events at specific latitudes is the ability to eliminate many of the generated obliquity scenarios (Laskar et al., 2004). Our TMG and Pd ages provide new constraints for this approach as well. Specifically, our results nullify scenarios for the past 250 Myr in which: (1) the obliquity is maintained at baseline 3 (35°) for >100 Myr, (2) the obliquity stays at baseline 4 (45°) within the past 130 Myr, and (3) the obliquity does not reach baseline 4 (45°) prior to ~ 130 Ma. As additional mid and low latitude glaciations and ice-rich deposits are dated, further restrictions will be added, allowing for the eventual reconstruction of the Late Amazonian obliquity history of Mars.

5. Conclusions

The preceding analyses of pedestal craters (Pd) (Fig. 2) and tropical mountain glaciers (TMGs) (Fig. 10) provide new insights into when and where ice-rich material has been located on Mars during the Late Amazonian. We use a combination of individual ages and population formation ages to explore possible pathways for the ice as it was

transported between latitudinal bands. These data place important constraints on the obliquity history of Mars during the past 200 Myr.

Our analysis of Pd (Fig. 2), which includes morphologic and stratigraphic observations as well as crater counting efforts, leads us to conclude the following: (1) Pd are morphologically fresh, and marginal sublimation pits may represent recent or active sublimation of the pedestal material, implying a young ice-rich deposit. (2) Pd are superposed on Amazonian-aged units, and must be younger than those units. (3) Instances where Pd are completely superposed or partially draped over other Pd require multiple episodes of emplacement of an ice-rich deposit at mid latitudes. (4) Crater counting techniques for the entire Pd population suggest a minimum timescale of formation of ~ 90 Myr (Fig. 4). Given that the ice-rich deposit has not been continuously present for this duration, the timescale of formation is necessarily longer than ~ 100 Myr. (5) Crater counting on individual Pd surfaces (Figs. 2-4) provides an age range of ~ 1 Myr to ~ 3.6 Gyr, with a median of ~ 140 Myr. In addition, 70% of the pedestal ages are less than 250 Myr (Table 1; Fig. 9). (6) During the 150 Myr between 25 Ma and 175 Ma, there is at least one pedestal that has formed every 15 Myr. This suggests that the ice-rich paleodeposit accumulated frequently during that time period.

Our analysis of the Tharsis Montes fan-shaped deposits (FSDs) (Fig. 10) has yielded revised ages and a new understanding of the chronology regarding the formation of the ridged facies in the Arsia FSD. The updated crater counting establishes best-fit ages of 220 Myr, 125 Myr, and 210 Myr for the Ascreaus, Pavonis, and Arsia FSDs, respectively (Figs. 11-13). The best-fit age of the non-ridged section of the Arsia FSD is 130 Myr. We have also divided the ridged facies at Arsia into three sections (outer,

middle, and inner) (Fig. 14), and dated these, yielding respective ages of 725 Myr, 475 Myr, and 345 Myr (Figs. 15-17). When we ratio the age differences between the sections – 250 Myr (outer to middle), 130 Myr (middle to inner), and 215 Myr (inner to non-ridged area) – to the number of respective ridges in each section (80 ridges in outer, 40 ridges in middle, and 65 ridges in inner), we find the average amount of time needed to form a ridge. These ratios are 3.13 Myr/ridge, 3.25 Myr/ridge, and 3.31 Myr/ridge, suggesting that, as an order of magnitude calculation, the ridges require approximately a million years to form rather than tens or even hundreds of thousands of years. This million-year formation timescale is supported by 1D model calculations of the debris thickness necessary to form a ridge (Table 2); in order to produce a typical ridge even under a fast glacial flow regime, debris thicknesses are unrealistically high – 0.8 m for a 100 kyr scenario to 80 m for a 1 kyr scenario – unless we allow for a million-year formation timescale. In this case, the necessary time-averaged debris thickness drops to a much more reasonable value of 0.08 m. We emphasize that these are time-averaged values, as it is likely that the thickness varied considerably during the million-year time periods. Finally, the difference in ages between the outer ridged section (725 Myr) and the non-ridged portion of the FSD (120 Myr) suggests that TMGs have been present for hundreds of Myr, cumulatively, to create the observed differences in crater density.

Combining the above Pd and TMG results, we shed new light on the questions that we initially posed. First, what has been the timing and periodicity of ice-rich paleodeposits at mid and low latitudes, particularly in the last 200 Myr? The TMG and Pd ages suggest that large volumes of ice have been present at the low latitudes within the last few hundred Myr, with the last major glaciation ending around ~130 Ma. At the mid

latitudes, the widespread ice-rich deposits necessary to form Pd were emplaced within the past tens of Myr and likely within the past few Myr (Table 1). Additionally, if the ~200 moraines in the Arsia FSD individually form on million-year-timescales, then they cumulatively took hundreds of millions of years to form, perhaps as much as ~600 Myr, as extrapolated from the 3 Myr average for the formation of a single moraine. Consequently, ice must have been present for a longer duration in the Late Amazonian at low latitudes, in the form of TMGs, than at mid latitudes, as established by the relatively brief 90 Myr population formation age of the Pd.

Second, what is the physical pathway (Fig. 19) that snow/ice takes from the polar regions to the equatorial regions and back during excursions to high obliquity? The relatively short formation age of the Pd population (~90 Myr) (Fig. 4) compared to that of the moraines left by the TMGs (hundreds of Myr) suggests that excursions to higher obliquity generally move the ice stability zone to low latitudes. However, in order to accommodate the short spacing between the ages of the Pd, the mid latitudes must have been a frequent stopping point for ice as it migrated back and forth between the polar and equatorial regions; our data suggest that ice is exchanged between the poles and mid latitudes, and between the mid latitudes and low latitudes. In this scenario, periods of higher average obliquity are likely to have led to the stable emplacement of TMGs, with brief transitions to ice-rich deposits at mid latitudes, then back to TMGs or polar ice caps. This would allow the mid latitudes to have more frequent glaciations and the low latitudes to maintain ice for a longer overall duration of time.

Third, what constraints can we place on Mars' obliquity history during the past 200 Myr? Between 20 and 130 Ma, the obliquity should primarily be fluctuating between

25° and 35°, with a mean around 30° (Fig. 20). This would allow for the frequent accumulation of mid-latitude ice-rich deposits to form the young Pd population, but would not produce a fixed deposit at mid latitudes. During this period, there must be at least one brief excursion to mean high obliquity (perhaps around 65 Ma) to explain the small glaciation on the flank of Arsia Mons (Shean et al., 2007). Just before ~130 Ma, there should be a shift to a mean high obliquity that would create a stable climate for the TMGs. This obliquity regime should fluctuate such that it frequently but briefly drops to ~35°, allowing for the continued formation of the Pd population. Our results also argue against the plausibility of certain scenarios for the past 200 Myr, including those in which the obliquity is maintained at ~35° for >100 Myr, the obliquity stays at 45° within the past 130 Myr, and the obliquity does not reach 45° prior to ~130 Ma.

This work helps to develop a more refined understanding of climate change during the Late Amazonian on Mars. The Tharsis Montes glaciations and mid-latitude pedestal crater population, however, represent only a fraction of the non-polar climate signatures on Mars (Head and Marchant, 2008) (Fig. 1). The dating and analysis of additional ice-related and periglacial morphologies will place further restrictions on the timing, pathways, and obliquity scenarios discussed here. These efforts will be accompanied by improved climate modeling, which will enhance our understanding of the link between obliquity and the movement of ice on Mars. This crucial combination of morphological/dating analyses working in tandem with climate model research will lead to the complete decoding of climate signals and reconstruction of Amazonian climate change on Mars.

Acknowledgments

The authors would like to thank the HiRISE, CTX, and HRSC teams, without whom this study could not have been completed. The authors are grateful for financial support from NASA Mars Data Analysis Program (MDAP) grant NNX09A14GG to JWH.

References

- Arvidson, R.E., Coradini, M., Carusi, A., Coradini, A., Fulchignoni, M., Federico, C., Funicello, R., Salomone, M., 1976. Latitudinal variation of wind erosion of crater ejecta deposits on Mars. *Icarus* 27(4), 503-516.
- Barlow, N.G., Boyce, J.M., Costard, F.M., Craddock, R.A., Garvin, J.B., Sakimoto, S.E.H., Kuzmin, R.O., Roddy, D.J., Soderblom, L.A. 2000. Standardizing the nomenclature of Martian impact crater ejecta morphologies. *J. Geophys. Res.* 105(E11), 26733-26738.
- Basilevsky, A.T., et al., 2005. Morphology and geological structure of the western part of the Olympus Mons volcano on Mars from the analysis of the Mars Express HRSC imagery. *Solar Syst. Res.* 39, 85-101.
- Bibring, J.-P., et al., 2005. Mars Surface Diversity as Revealed by the OMEGA/Mars Express Observations. *Science* 307, 1576-1581.

Black, B.A., Stewart, S.T., 2008. Excess ejecta craters record episodic ice-rich layers at middle latitudes on Mars. *J. Geophys. Res.* 113, E02015, doi:10.1029/2007JE002888.

Boulton, G.S., Eyles, N., 1979. Sedimentation by valley glaciers: a model and genetic classification. In *Moraines and Varves*. Schluchter, C. (ed.). Balkema, Rotterdam, 11-23.

Boynton, W.V., et. al., 2002. Distribution of Hydrogen in the Near Surface of Mars: Evidence for Subsurface Ice Deposits. *Science* 297, 81-85.

Christensen, P.R., 1986. Regional dust deposits on Mars: Physical properties, age, and history. *J. Geophys. Res.*, 91, doi:10.1029/JB091iB03p03533.

Fastook, J.L., Head, J.W., Marchant, D.R., Forget, F., 2008. Tropical mountain glaciers on Mars: Altitude-dependence of ice accumulation, accumulation conditions, formation times, glacier dynamics, and implications for planetary spin-axis/orbital history. *Icarus* 198, 305-317, doi:10.1016/j.icarus.2008.08.008.

Forget, F., Haberle, R.M., Montmessin, F., Levrard, B. Head, J.W., 2006. Formation of Glaciers on Mars by Atmospheric Precipitation at High Obliquity. *Science* 311, 368-371.

Grier, J.A., Bottke, W.F., Hartmann, W.K., Berman, D.C., 2001. Mars: Chronological Studies of the Large Volcanoes in Tharsis. *Lunar Planet. Sci.* XXXII, abstract 1823.

Haberle, R.M., Murphy, J.R., Schaeffer, J., 2003. Orbital change experiments with a Mars general circulation model. *Icarus* 161, 66-89, doi:10.1016/S0019-1035(02)00017-9.

Hartmann, W.K., 2005. Martian cratering 8: Isochron refinement and the chronology of Mars. *Icarus* 174, 294-320.

Hartmann, W.K., Neukum, G., 2001. Cratering Chronology and the Evolution of Mars. *Space Sci. Rev.* 96, 165-194.

Hartmann, W.K., Malin, M., McEwen, A., Carr, M., Soderblom, L., Thomas, P., Danielson, E., James, P., Veverka, J., 1999. Evidence for recent volcanism on Mars from crater counts. *Nature* 397, 586-589.

Head, J.W., Marchant, D.R., 2003. Cold-based mountain glaciers on Mars: Western Arsia Mons. *Geology* 31, 641-644.

Head, J.W., Mustard, J.F., Kreslavsky, M.A., Milliken, R.E., Marchant, D.R., 2003. Recent ice ages on Mars. *Nature* 426, 797-802.

Head, J.W., et al., 2005. Tropical to mid-latitude snow and ice accumulation, flow and glaciation on Mars. *Nature* 434, 346-351.

Head, J.W., Nahm, A.L., Marchant, D.R., Neukum, G., 2006. Modification of the dichotomy boundary on Mars by Amazonian mid-latitude regional glaciation. *Geophys. Res. Lett.*, 33, doi:10.1029/2005GL024360.

Head, J.W., Marchant, D.R., 2008. Evidence for Non-Polar Ice Deposits in the Past History of Mars. *Lunar Planet. Sci.* XXXIX, abstract 1295.

Head, J.W., Marchant, D.R., Forget, F., Laskar, J., Madeleine, J.-B., Fastook, J.L., 2009. Deciphering the Late Amazonian Climate History of Mars: Assessing Obliquity Predictions with Geological Observations and Atmospheric General Circulation Models. *Lunar Planet. Sci.* XL, abstract 1349.

Kadish, S.J., Head, J.W., Barlow, N.G., Marchant, D.R., 2008a. Martian pedestal craters: Marginal sublimation pits implicate a climate-related formation mechanism. *Geophys. Res. Lett.* 35, L16104, doi:10.1029/2008GL034990.

Kadish, S.J., Head, J.W., Parsons, R.L., Marchant, D.R., 2008b. The Ascræus Mons fan-shaped deposit: Volcano-ice interactions and the climatic implications of cold-based tropical mountain glaciation. *Icarus* 197, 84-109, doi:10.1016/j.icarus.2008.03.019.

Kadish, S. J., Barlow, N.G., Head, J.W., 2009. Latitude Dependence of Martian Pedestal Craters: Evidence for a Sublimation-Driven Formation Mechanism. *J. Geophys. Res.* 114, E10001, doi:10.1029/2008JE003318.

Kadish, S.J., Head, J.W., Barlow, N.G., 2010. Pedestal Crater Heights on Mars: A Proxy for the Thicknesses of Past, Ice-Rich, Amazonian Deposits. *Icarus*, doi:10.1016/j.icarus.2010.06.021.

Kadish, S.J., Head, J.W., 2011. Impacts into Non-Polar Ice-Rich Paleodeposits on Mars: Excess Ejecta Craters, Perched Craters and Pedestal Craters as Clues to Amazonian Climate History. *Icarus*, under review.

Kreslavsky, M.A., Head, J.W., 2005. Mars at very low obliquity: atmospheric collapse and the fate of volatiles. *Geophys. Res. Lett.* 32, L12202, doi:10.1029/2005GL022645.

Laskar, J., Correia, A.C.M., Gastineau, M., Joutel, F., Levrard, B., Robutel, P., 2004. Long term evolution and chaotic diffusion of the insolation quantities of Mars. *Icarus* 170, 343-364.

Levrard, B., Forget, F., Montmessin, F., Laskar, J., 2004. Recent ice-rich deposits formed at high latitudes on Mars by sublimation of unstable equatorial ice during low obliquity. *Nature* 431, 1072-1075.

Levrard, B., Forget, F., Montmessin, F., Laskar, J., 2007. Recent formation and evolution of northern Martian polar layered deposits as inferred from a Global Climate Model. *J. Geophys. Res.* 112, E06012, doi:10.1029/2006JE002772.

Madeleine, J.-B., Forget, F., Head, J.W., Levrard, B., Montmessin, F., Millour, E., 2009. Amazonian northern mid-latitude glaciation on Mars: A proposed climate scenario. *Icarus* 203, 390-405.

McCauley, J.F., et al., 1972. Preliminary Mariner 9 report on the geology of Mars. *Icarus*, 17, 289-327.

McEwen, A.S., et al., 2007. Mars Reconnaissance Orbiter's High Resolution Imaging Science Experiment (HiRISE). *J. Geophys. Res.*, 112, doi:10.1029/2005JE002605.

Mellon, M.T., Jakosky, B.M., 1995. The distribution and behavior of martian ground ice during past and present epochs. *J. Geophys. Res.* 100, 11781–11799, doi:10.1029/95JE01027.

Mellon, M.T., Feldman, W.C., Prettyman, T.H., 2004. The presence and stability of ground ice in the southern hemisphere of Mars. *Icarus* 169, 324-340.

Milkovich, S.M., Head, J.W., Marchant, D.R., 2006. Debris-covered piedmont glaciers along the northwest flank of the Olympus Mons scarp: Evidence for low-latitude ice accumulation during the Late Amazonian of Mars. *Icarus* 181(2), p. 388-407.

Mischna, M.A., Richardson, M.I., 2005. A reanalysis of water abundances in the Martian atmosphere at high obliquity. *Geophys. Res. Lett.* 32, L03201, doi:10.1029/2004GL021865.

Mischna, M.A., Richardson, M.I., Wilson, R.J., McCleese, D.J., 2003. On the orbital forcing of Martian water and CO₂ cycles: A general circulation model study with simplified volatile schemes. *J. Geophys. Res.* 108, 5062, doi:10.1029/2003JE002051.

Montmessin, F., Haberle, R.M., Forget, F., Langevin, Y., Clancy, R.T., Bibring, J.-P., 2007. On the origin of perennial water ice at the south pole of Mars: A precession-controlled mechanism?. *J. Geophys. Res.*, 112, doi:10:1029/2007JE002902.

Murchie, S., et al., 2007. Compact Reconnaissance Imaging Spectrometer for Mars (CRISM) on Mars Reconnaissance Orbiter (MRO). *J. Geophys. Res.* 112, doi:10:1029/2006JE002682.

Neukum G., Ivanov, B.A., Hartmann, W.K., 2001. Cratering records in the inner solar system in relation to the Lunar reference system. In *Chronology and Evolution of Mars*, edited by R. Kallenbach, J. Geiss, and W. K. Hartmann, 87-104, International Space Science Institute, Bern.

Neukum, G., and 10 colleagues, 2004. Recent and episodic volcanic and glacial activity on Mars revealed by the High Resolution Stereo Camera. *Nature* 432, 971-979.

Phillips, R.J., et al., 2008. Mars north polar deposits: Stratigraphy, age, and geodynamical response. *Science* 320, 1182-1185.

Read, P.L., Lewis, S.R., 2004. *The Martian Climate Revisited*. Praxis Publishing Ltd, Chichester, UK.

Scott, D.H., Tanaka, K.L., 1981. Mars - Paleostratigraphic restoration of buried surfaces in Tharsis Montes. *Icarus* 45, 304-319.

Scott, D.H., Tanaka, K.L., 1986. Geological Map of the Western Equatorial Region of Mars. U.S. Geol. Surv. Misc. Invest. Ser. Map, I-1802-A.

Scott, D.H., Zimbelman, J.R., 1995. Geological Map of Arsia Mons Volcano, Mars. U.S. Geol. Surv. Misc. Invest. Ser. Map, I-2480.

Scott, D.H., Dohm, J.M., Zimbelman, J.R., 1998. Geologic map of Pavonis Mons Volcano, Mars. U.S. Geol. Surv. Misc. Invest. Ser. Map, I-2561.

Shean, D.E., Head, J.W., Marchant, D.R., 2005. Origin and evolution of a cold-based tropical mountain glacier on Mars: The Pavonis Mons fan-shaped deposit. *J. Geophys. Res.* 110., E05001, doi: 10.1029/2004JE002360.

Shean, D.E., Head, J.W., Kreslavsky, M., Neukum, G., HRSC Co-I Team, 2006. When Were Glaciers Present in Tharsis? Constraining Age Estimates for the Tharsis Montes Fan-shaped Deposits. *Lunar Planet. Sci.* XXXVII, abstract 2092.

Shean, D.E., Head, J.W., Fastook, J.L., Marchant, D.R., 2007. Recent glaciation at high elevations on Arsia Mons, Mars: Implications for the formation and evolution large tropical mountain glaciers. *J. Geophys. Res.* 112, E03004, doi: 10.1029/2006JE002761.

Smith, D.E., et al., 1999. The Global Topography of Mars and Implications for Surface Evolution. *Science*, 284, 1495-1503, doi:10.1126/science.284.5419.1495.

Tanaka, K.L., 1986. The stratigraphy of Mars. *J. Geophys. Res.* 91(B13), E139-E158.

Tanaka, K.L., 2000. Dust and Ice Deposition in the Martian Geologic Record. *Icarus* 144, 254-266.

Tanaka, K.L., Skinner Jr., J.A., Hare, T.M., Joyal, T., Wenker, A., 2003. Resurfacing history of the northern plains of Mars based on geologic mapping of Mars Global Surveyor data. *J. Geophys. Res.* 108(E4), 8043, doi:10.1029/2002JE001908.

Tanaka, K.L., Rodriguez, J.A.P., Skinner Jr., J.A., Bourke, M.C., Fortezzo, C.M., Herkenhoff, K.E., Kolb, E.J., Okubo, C.H., 2008. North polar region of Mars: Advances in stratigraphy, structure, and erosional modification. *Icarus* 196(2), 318-358.

Williams, R.S., 1978. Geomorphic processes in Iceland and on Mars: A comparative appraisal from orbital images. *Geol. Soc. Am. Abstr. Programs*, 10, 517.

Wilson, L., Head, J.W., 2009. Tephra deposition on glaciers and ice sheets on Mars: Influence on ice survival, debris content, and flow behavior. *J. Volcanol. Geoth. Res.*, 185, 290-297.

Wilson, L., Scott, E.D., Head, J.W., 2001. Evidence for episodicity in the magma supply to the large Tharsis volcanoes. *J. Geophys. Res.*, 106, 1423-1433.

Tables

Table 1. The data for the 50 pedestal surfaces dated in this study using crater counting techniques. Note the frequency of ages between 25 Ma and 175 Ma, with pedestals forming at least every 15 Myr.

Pedestal #	Best Fit Age (Myr)	# of superposed craters	Pedestal Area (km ²)	Diameter of largest superposed crater (km)
1	1.3	23	2.4	0.02
2	2.9	8	68.5	0.10
3	25	23	232.9	0.16
4	32	22	65.4	0.20
5	34	5	265.9	0.27
6	49	22	34.79	0.09
7	49	9	43.5	0.15
8	50	24	26.7	0.25
9	50	5	22.49	0.16
10	52	4	68.5	0.23
11	61	5	18.756	0.15
12	64	8	61.227	0.38
13	65	7	27.6	0.24
14	66	12	44.26	0.23
15	70	17	76.34	0.48
16	78	8	60.78	0.24
17	85	14	105.5	0.34
18	92	19	6.33	0.09
19	98	12	171.2	0.50
20	105	14	75.1	0.22
21	111	8	56.0	0.30
22	114	6	36.896	0.21
23	123	5	12.32	0.08
24	130	9	43.5	0.14
25	138	18	34.09	0.21
26	143	9	65.2	0.36
27	152	11	160.5	0.36
28	166	10	116.5	0.44
29	195	10	150.866	0.52
30	196	7	63.2	0.26
31	199	8	28.75	0.30
32	200	5	35.8	0.47

33	222	7	55.84	0.26
34	245	4	27.97	0.18
35	249	14	53.928	0.47
36	353	9	50.97	0.32
37	470	5	66.2	0.43
38	497	9	96.5	0.38
39	798	12	79.8	0.39
40	846	9	40.1	0.55
41	1260	55	384.34	1.18
42	1685	2	22.199	0.36
43	1772	12	43.65	0.70
44	1917	8	70.09	0.50
45	2106	7	58.6	0.60
46	2721	15	35.56	0.58
47	2873	5	31.43	0.63
48	2949	23	56.42	0.72
49	3552	7	7.5	0.67
50	3592	3	31.79	0.71

Table 2. Our 1D calculation for the formation of ridges (drop moraines) in the Arsia Mons fan-shaped deposit. This model considers three ridge sizes, four formation timescales, and two glacial flow rates. The resulting time-averaged debris thicknesses would need to be maintained for their associated formation timescales in order to produce the observed ridges.

Ridge Cross-Sectional Area (m ²)	Formation Timescale (yrs)	1D Flux (m ² /yr)	Glacial Flow Rate (m/yr)	Debris Thickness (m)
500	1000	0.5	0.01	50
500	10000	0.05	0.01	5
500	100000	0.005	0.01	0.5
500	1000000	0.0005	0.01	0.05
500	1000	0.5	0.1	5
500	10000	0.05	0.1	0.5
500	100000	0.005	0.1	0.05
500	1000000	0.0005	0.1	0.005
8000	1000	8	0.01	800
8000	10000	0.8	0.01	80
8000	100000	0.08	0.01	8
8000	1000000	0.008	0.01	0.8
8000	1000	8	0.1	80
8000	10000	0.8	0.1	8
8000	100000	0.08	0.1	0.8
8000	1000000	0.008	0.1	0.08
90000	1000	90	0.01	9000
90000	10000	9	0.01	900
90000	100000	0.9	0.01	90
90000	1000000	0.09	0.01	9
90000	1000	90	0.1	900
90000	10000	9	0.1	90
90000	100000	0.9	0.1	9
90000	1000000	0.09	0.1	0.9

Figure Captions

Figure 1 – The distribution of morphologies related to non-polar ice deposits. These features include tropical mountain glaciers (#8) at low latitudes and pedestal craters (#10) at mid latitudes. Modified from Head and Marchant (2008).

Figure 2 – A synthesis of pedestal crater images. A) A 3D perspective sketch of a pedestal crater, highlighting the limited distribution of ejecta on the pedestal surface, the significance of the pedestal height, and the ice-rich material that composes the pedestal. B) A subscene of THEMIS image V21415004 (57.1°N, 78.5°E). This example shows the limited extent of the rough-textured ejecta deposit superposed on the smooth pedestal surface; the pedestal surface has a greater radial extent than the ejecta deposit in all directions. A small marginal pit exists on its eastern scarp. C) A mosaic of V18046009 and V18358008 (61.0°S, 71.0°E). The larger crater has marginal pits along its eastern perimeter. The smaller crater is draped over this scarp, truncating one of the pits. D) A perspective view (VE = 10x) of a pedestal crater in Utopia Planitia with marginal pits in its outward-facing scarp (CTX image P01_001555_2430 with MOLA altimetry data). The 3.9-km-in-diameter crater is elevated ~100 m above the surrounding plains. The pits, which are ~1-3 km in length and 20 m deep, result from the sublimation of ice from the volatile-rich material underlying the indurated surface of the pedestal crater.

Figure 3 – A set of graphs showing the significant elements of incremental crater size-frequency distributions. A) A plot highlighting the boundaries between the significant epochs in martian history. B) An idealized plot of a crater size-frequency distribution whose slope matches that of the isochrons at large sizes (>2 km in diameter), signifying that the distribution of crater sizes is unmodified from the expected production function. The rollover at smaller sizes (<2 km in diameter) is due to erosion and removal of small craters. C) A crater size-frequency distribution showing the effects of resurfacing at some point in the crater population's history. For example, this would result if a Late Amazonian lava flow resurfaced a Mid Amazonian lava flow, removing crater below a certain diameter, but leaving larger craters intact. This is often referred to as a kink in cumulative plots. D) A typical crater size-frequency distribution with a characteristic rollover in the data at small sizes and a paucity of craters at large sizes. This is observed in the pedestal crater population due to erosion of smaller pedestal craters and the inhibition of the formation of large pedestal craters.

Figure 4 – A size-frequency distribution of the complete database of mid-latitude pedestal craters ($N=2,287$). Pedestal craters with diameters smaller than 1 km are being eroded at a rate much faster than they are being produced, creating a rollover in the data. The formation of pedestal craters larger than 4 km in diameter is inhibited by the limited thickness of the ice-rich target material; larger impacts that penetrate completely through the ice-rich surface layer excavate silicate regolith, creating large ejecta blankets that lead to the formation of excess ejecta craters (Black and Stewart, 2008; Kadish et al., 2011). If we consider pedestal craters between 1 and 4 km in diameter, which accounts for 2/3 of

the total population, we see that they match the production function, yielding a best-fit population formation age of 90 Myr.

Figure 5 – The obliquity history of Mars between 20 Myr ago and 10 Myr from now. The obliquity underwent a transitional period between 3 and 5 Myr ago, when it shifted from a mean obliquity of $\sim 35^\circ$ to a mean obliquity of $\sim 25^\circ$. This is likely to have shifted the latitudinal ice stability from the mid latitudes to the low latitudes. Modified from Laskar et al. (2004).

Figure 6 – The distribution of pedestal craters (black dots) as mapped by Kadish et al. (2009), and the subpopulation of pedestal surfaces (pink dots) dated in this study. The pedestals selected for age dating were based on available HiRISE and CTX coverage, and are thus not a random sample.

Figure 7 – An example of a pedestal crater whose surface was dated (Crater #4 in Table 1). The region highlighted in green was the counting area, which does not include the pedestal crater bowl. The blue circles highlight craters that are superposed on the pedestal surface, which were used to establish the age of the pedestal. The size-frequency distribution shows a best-fit age of 32 Myr (Late Amazonian).

Figure 8 – A second example of a pedestal crater examined for the dating of individual pedestal surfaces (Crater #17 in Table 1). This pedestal has clear marginal pits. The green shading represents the counting area and the blue circles delineate superposed craters.

Note that the contiguous pedestal crater on the eastern side of the image is not included in the count. The best-fit age is 85 Myr (Late Amazonian), as shown in the corresponding size-frequency distribution.

Figure 9 – Histograms showing the distribution of the 50 pedestal surfaces dated in this study. A) The entire set of 50 pedestal ages. Although the majority (70%) of pedestals is less than 250 Myr in age, ten pedestals are determined to be more than 1 Gyr in age. B) A closer examination of the pedestals that formed during the Late Amazonian. This histogram shows that at least one pedestal has formed in every 15 Myr bin over the past 200 Myr. These data are sourced from Table 1, which explicitly shows that at least one pedestal has formed every 15 Myr between 25 and 175 Ma.

Figure 10 – A context map of MOLA data (hillshade and altimetry) showing the Tharsis Montes. The fan-shaped deposits are delineated, extending to the northwest of the flanks of each volcano.

Figure 11 – A crater size-frequency distribution showing the revised best-fit age of 220 Myr for the Ascraeus Mons fan-shaped deposit. Note that the data rollover at diameters of less than 700 m.

Figure 12 – A crater size-frequency distribution showing the revised best-fit age of 125 Myr for the Pavonis Mons fan-shaped deposit.

Figure 13 – A crater size-frequency distribution showing the revised best-fit age of 210 Myr for the Arsia Mons fan-shaped deposit.

Figure 14 – A CTX and HRSC mosaic of the Arsia Mons fan-shaped deposit. The ridged sections (outer, middle, and inner) have been mapped in blue, green, and yellow, respectively. These boundaries between these sections were defined on the basis of particularly large, continuous ridges. The ridges in the inner section are discontinuous, resulting in an area that is not contiguous. At their widest extents, the outer, middle, and inner regions have 80, 40, and 65 ridges, respectively. Because ridges merge and can be buried, ridges were counted across multiple transects.

Figure 15 – A crater size-frequency distribution for our crater counting on the outer ridged section in the Arsia Mons fan-shaped deposit. The rollover of the data occurs at diameters less than 700 m. The resulting best-fit age is 725 Myr.

Figure 16 – A crater size-frequency distribution for our crater counting on the middle ridged section in the Arsia Mons fan-shaped deposit. The resulting best-fit age is 475 Myr.

Figure 17 – A crater size-frequency distribution for our crater counting on the inner ridged section in the Arsia Mons fan-shaped deposit. The resulting best-fit age is 345 Myr.

Figure 18 – A schematic diagram showing the key elements of our 1D model for moraine formation. This illustrates the set of variables considered in the model (ridge cross-sectional area, glacial surface flow rate, and formation timescale). The cross-sectional area is divided by the formation timescale to derive a debris flux; the debris is likely sourced from volcanic eruptions. The debris flux is then divided by the glacial surface flow rate to derive a time-averaged thickness of debris necessary to form the moraine.

Figure 19 – A diagram of three proposed scenarios for the pathways that ice-rich material takes during obliquity excursions. Note that the pathways are only shown in the northern hemisphere, but the actual pathways would be symmetric in both hemispheres. In each case, shifts to higher obliquity lead to increased insolation on the poles, causing volatiles to migrate equatorward. Subsequent shifts back to lower obliquity result in the volatiles returning to the poles.

Figure 20 – A set of obliquity histories for Mars. In all cases, obliquity (in degrees) is on the y-axis and age (in Myr) is on the x-axis. A) A set of 15 possible obliquity histories published by Laskar et al. (2004). The solutions are highly sensitive to initial conditions. As such, only the past 20 Myr are robust. B) The robust solution for Mars' obliquity history over the past 20 Myr from Laskar et al. (2004). C-E) Scenarios P000, N001, and N006 from Laskar et al. (2004). These are the preferred scenarios identified by Fastook et al. (2008) on the basis of glacial models for the Tharsis Montes tropical mountain glaciations. Head et al. (2009) used a host of geomorphologies to determine that a scenario like N001 is the most probable, but is not necessarily unique or correct. In this

study, we find that a scenario similar to P000 best fits our ages and proposed pathways for ice-rich material. F) A modified version of scenario P000, which best explains our observations. This scenario accounts for frequent but transitory mid-latitude deposits to produce the pedestal crater population, a brief low-latitude glaciation to produce the 65 Myr lobate flows at Arsia and Olympus Mons, and an extended period at high obliquity prior to 130 Myr to produce the massive tropical mountain glaciers.

Figure 1

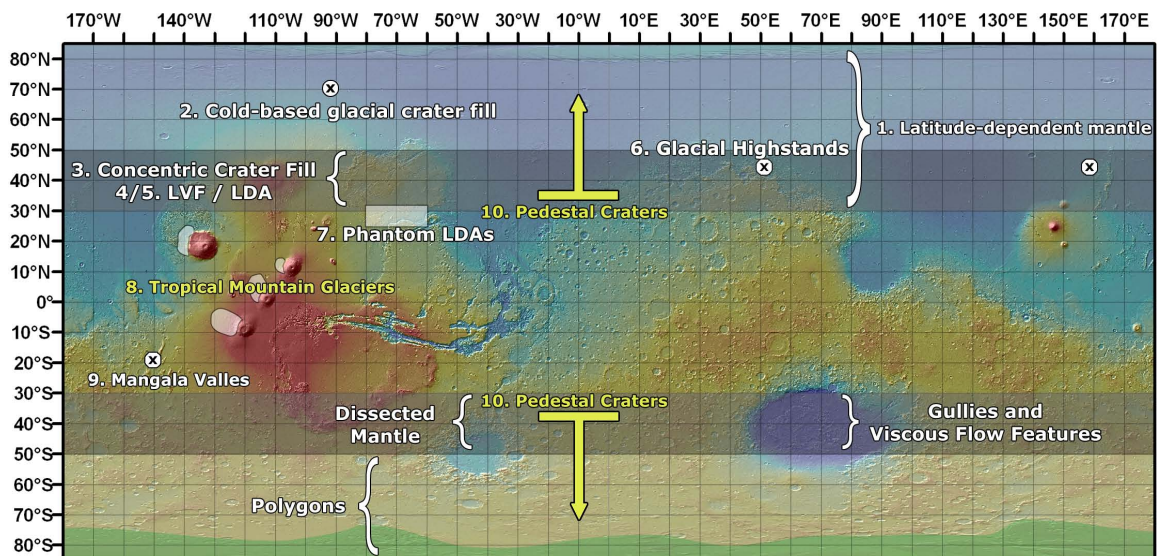


Figure 2

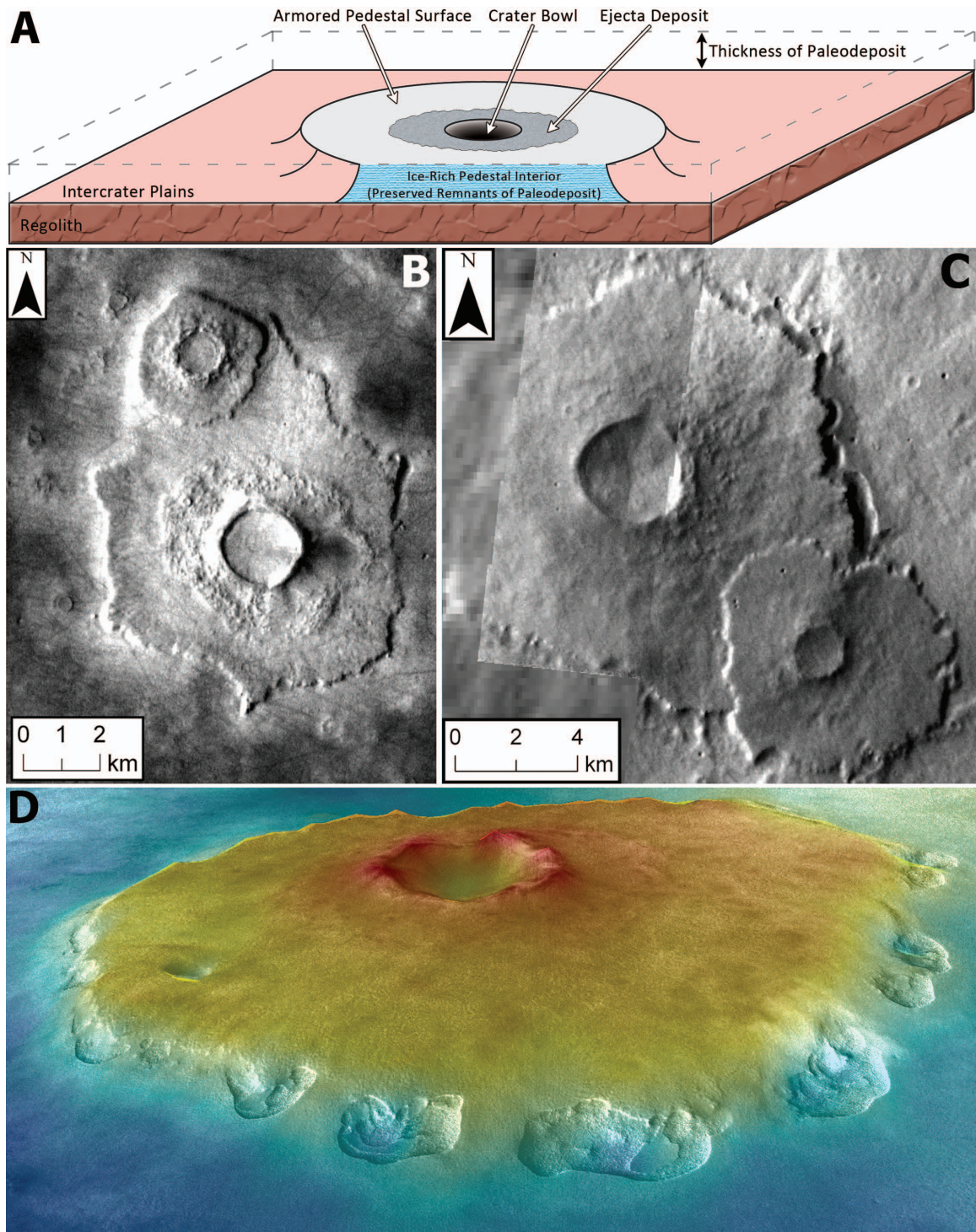


Figure 3

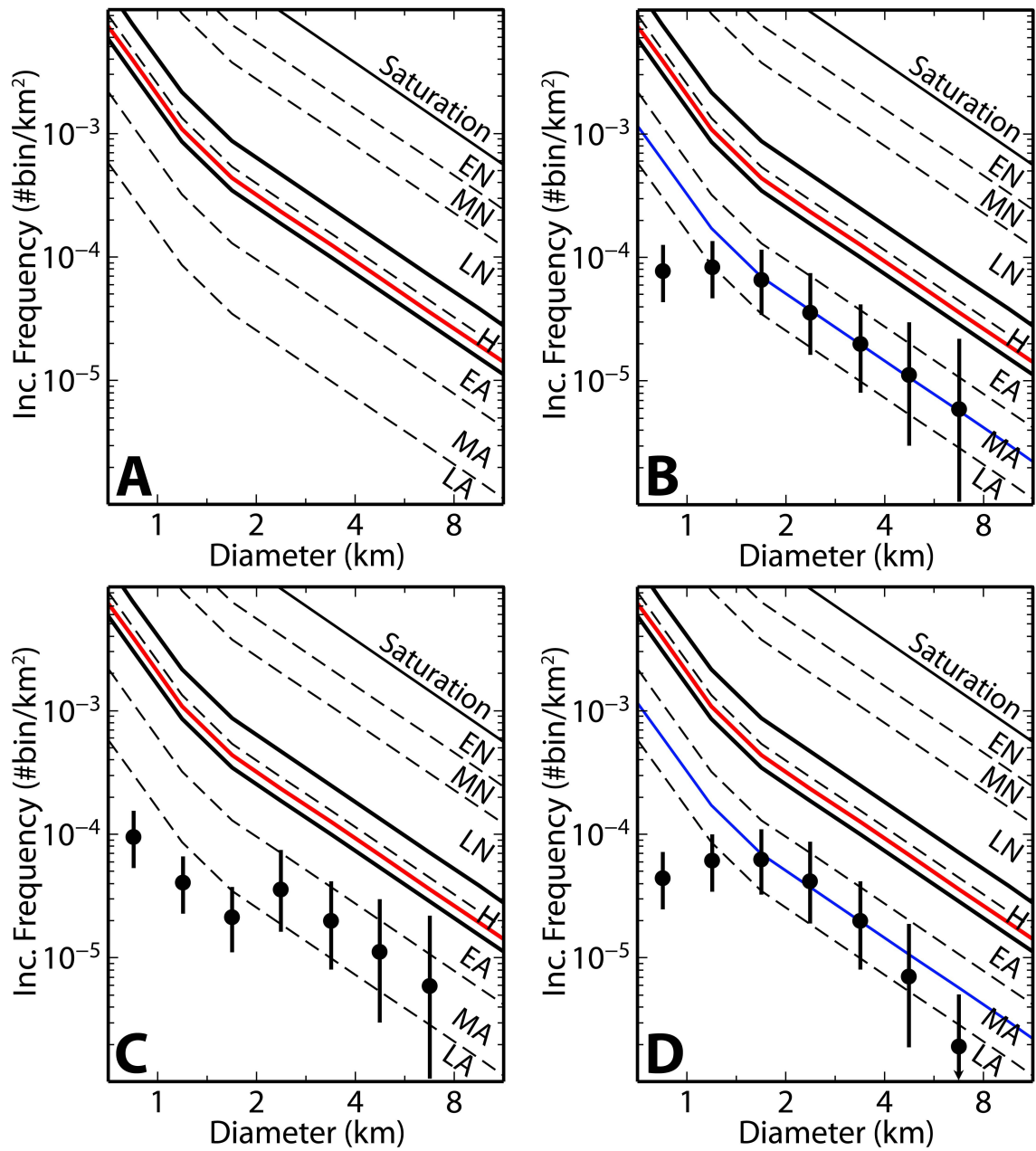


Figure 4

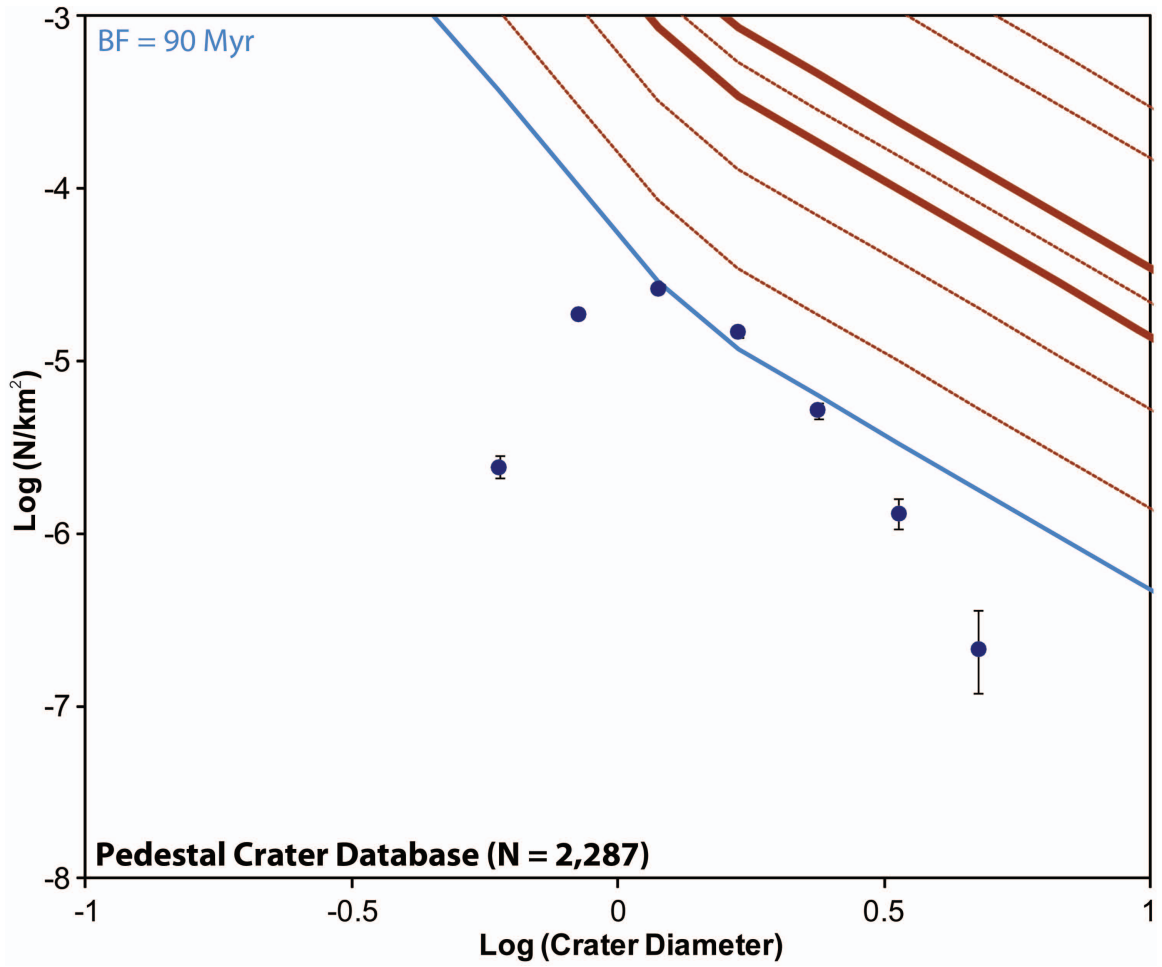


Figure 5

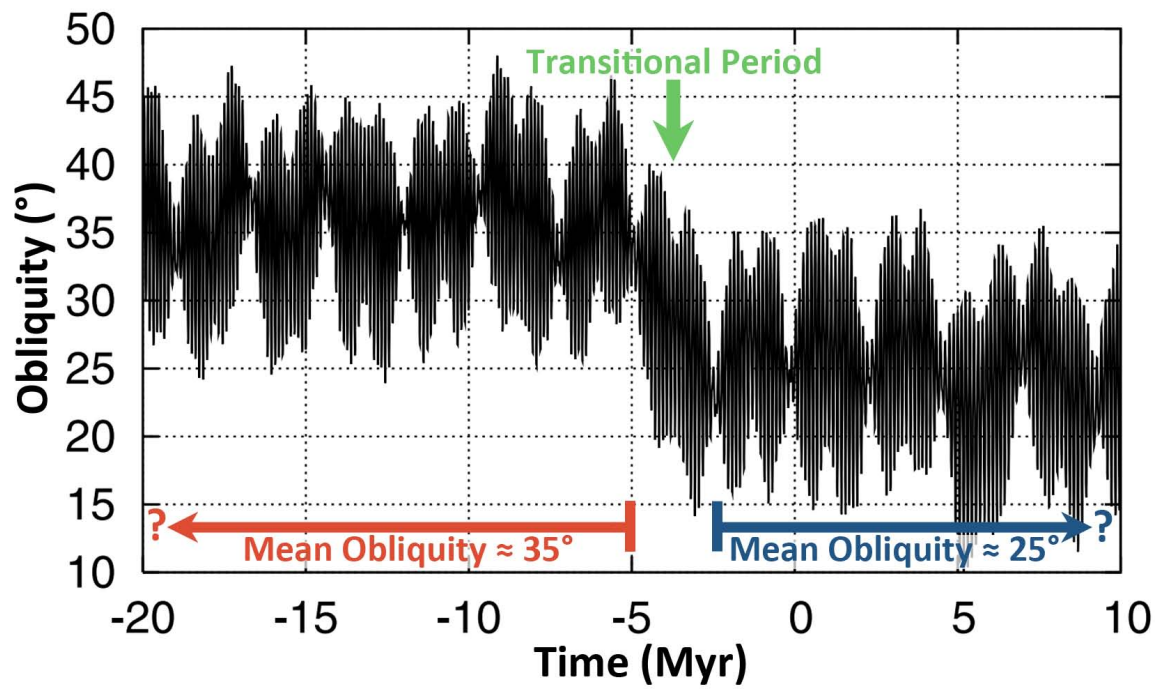


Figure 6

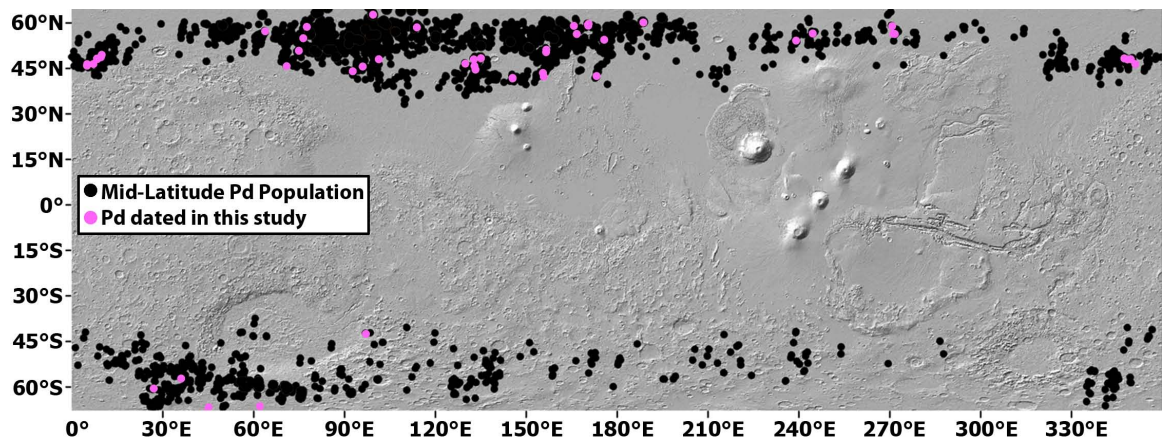


Figure 7

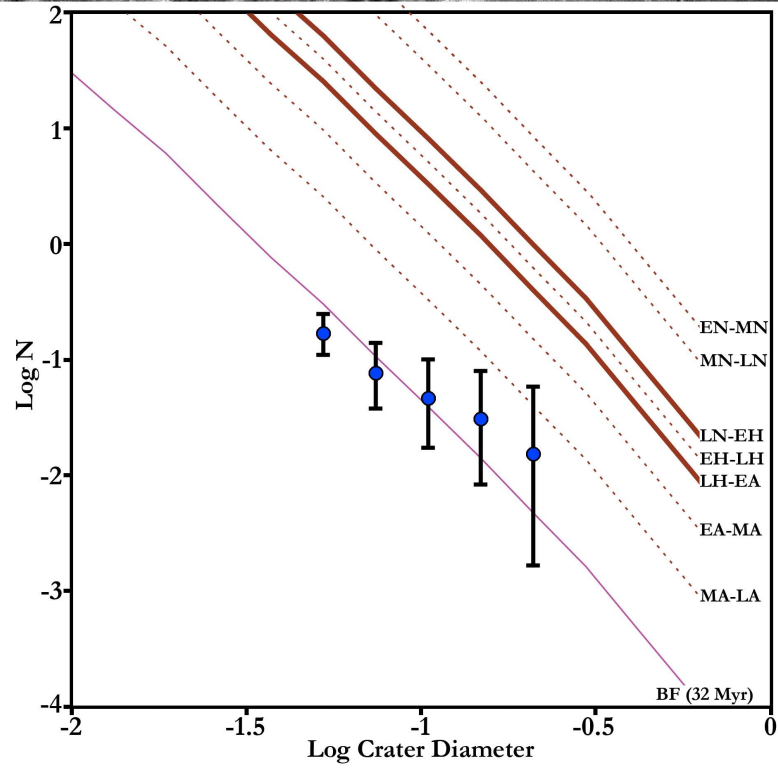
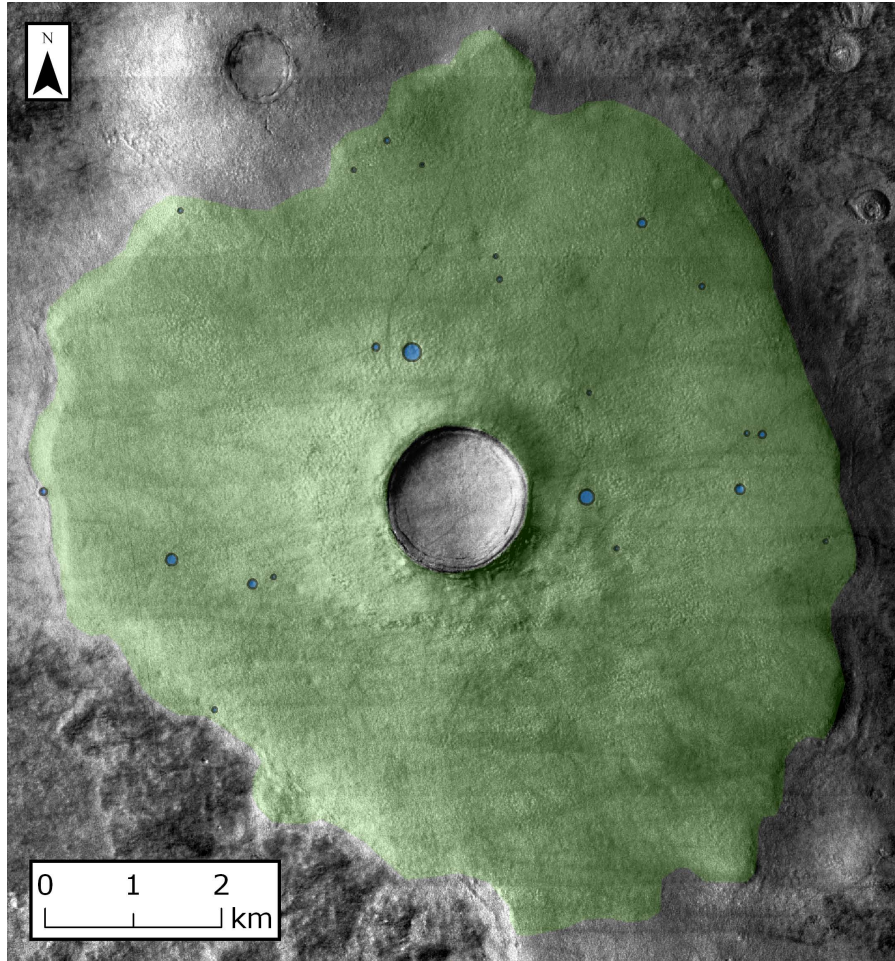


Figure 8

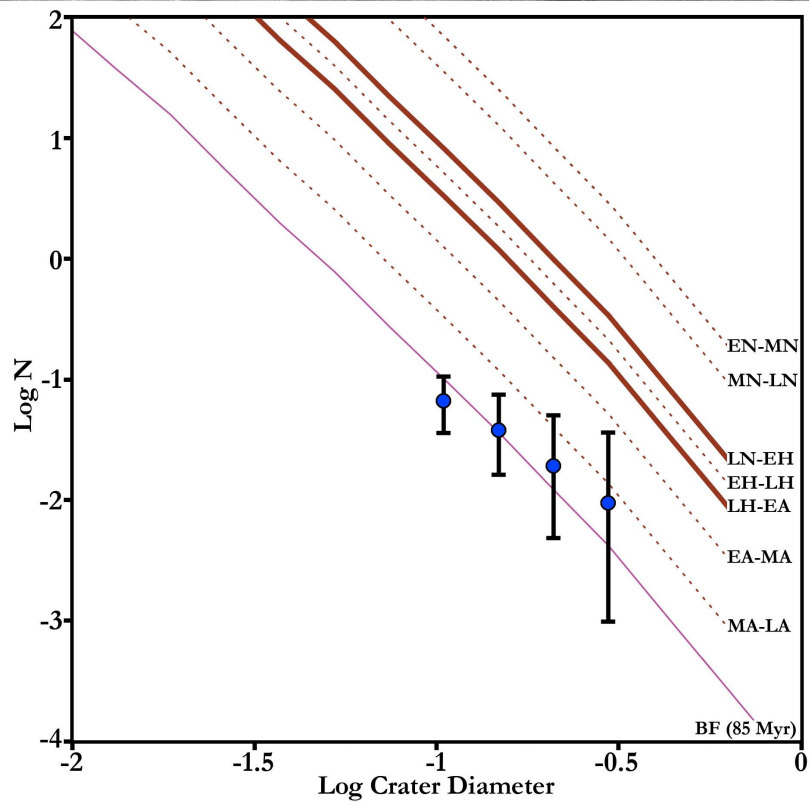
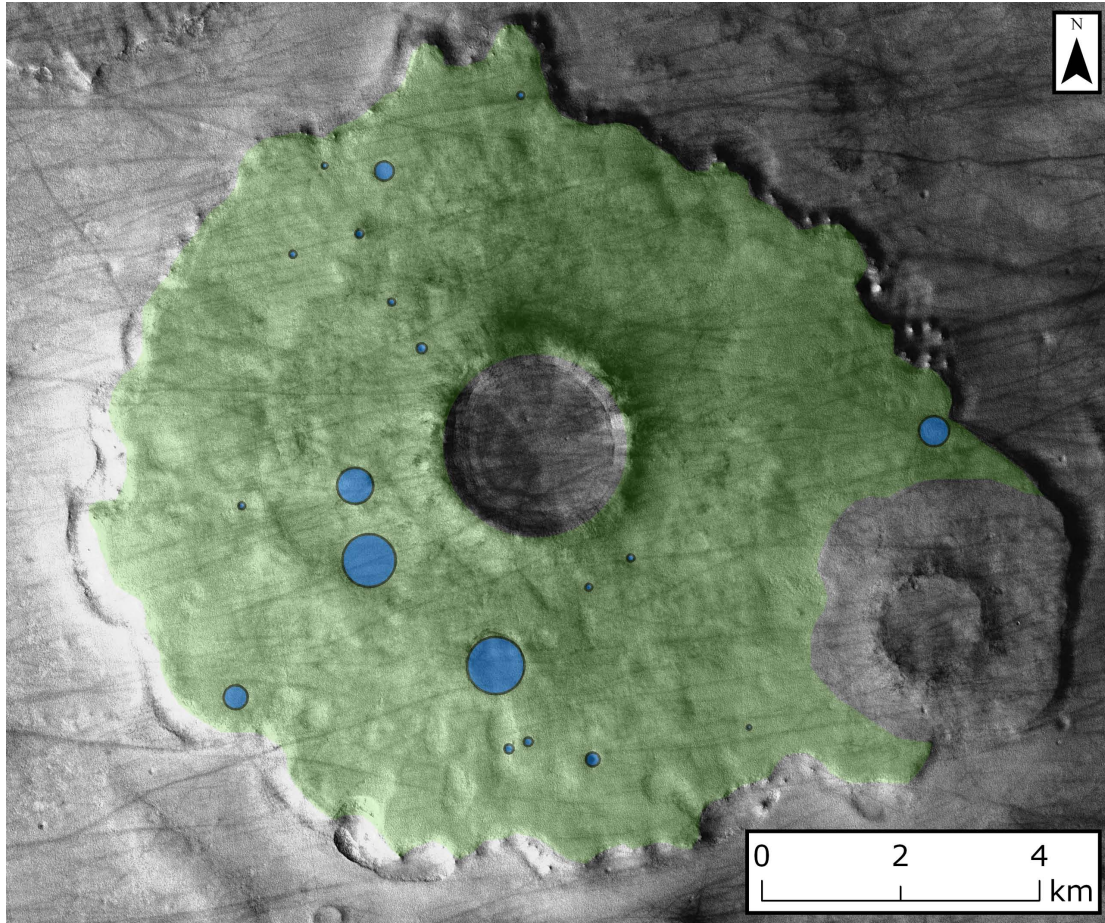


Figure 9

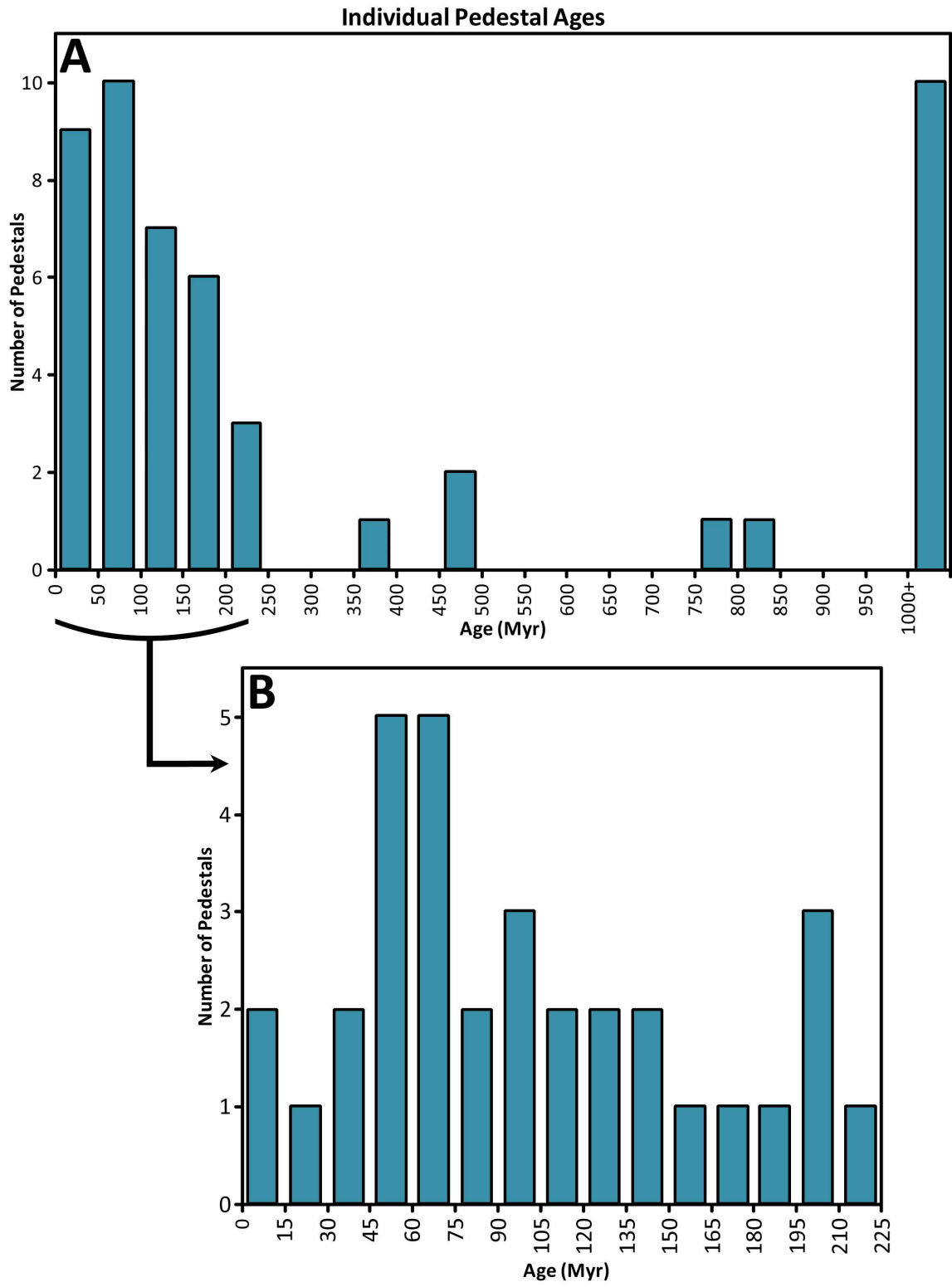


Figure 10

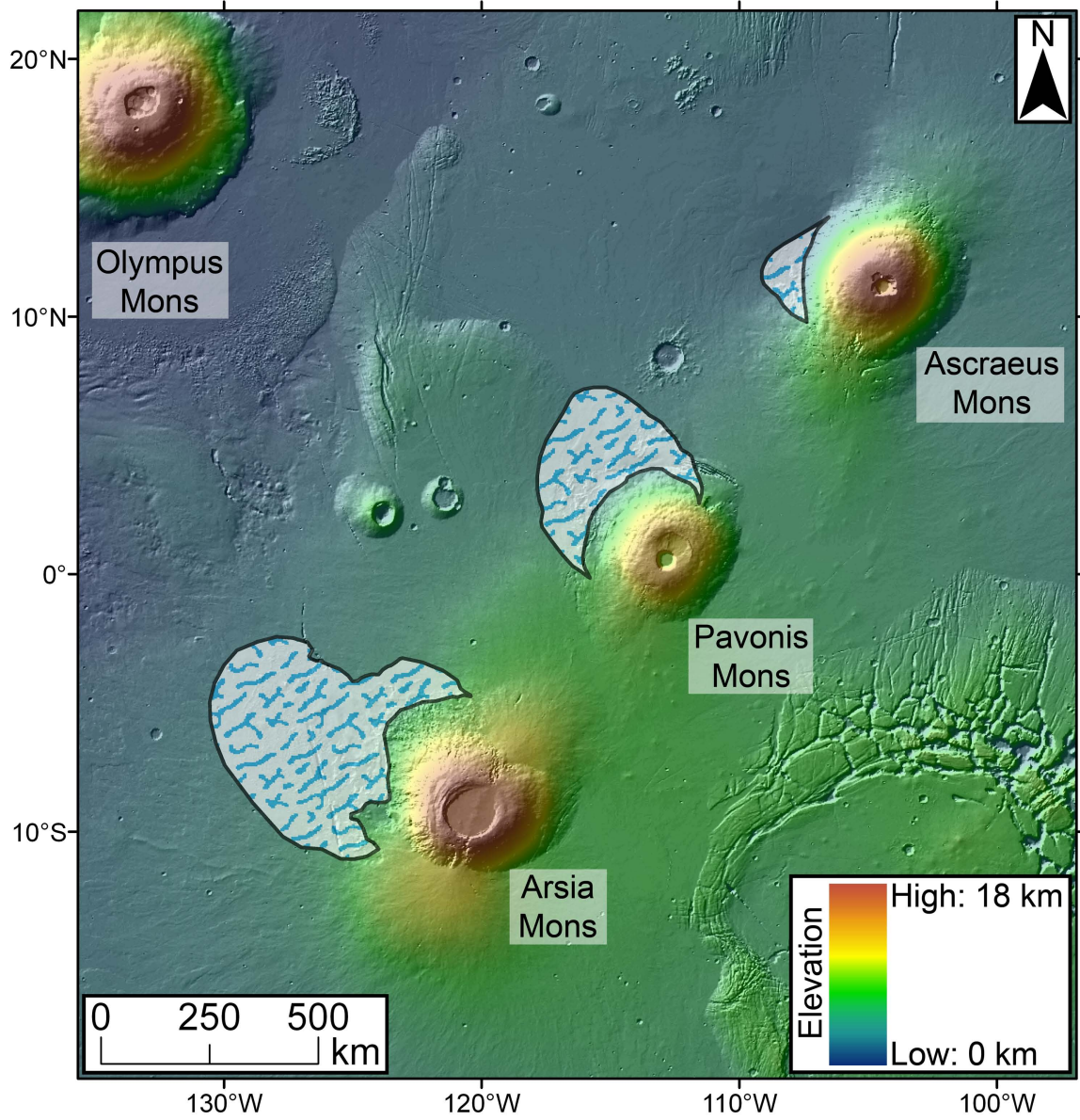


Figure 11

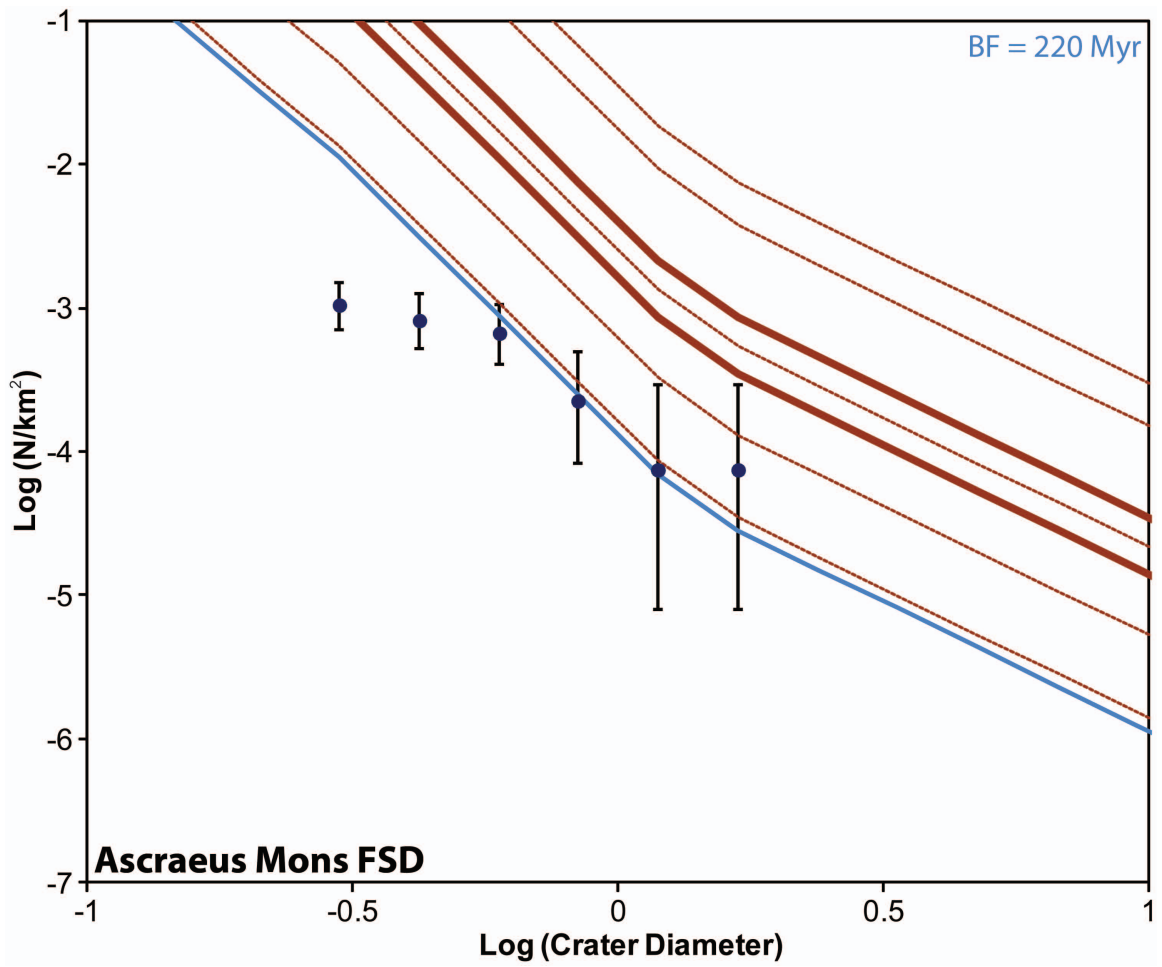


Figure 12

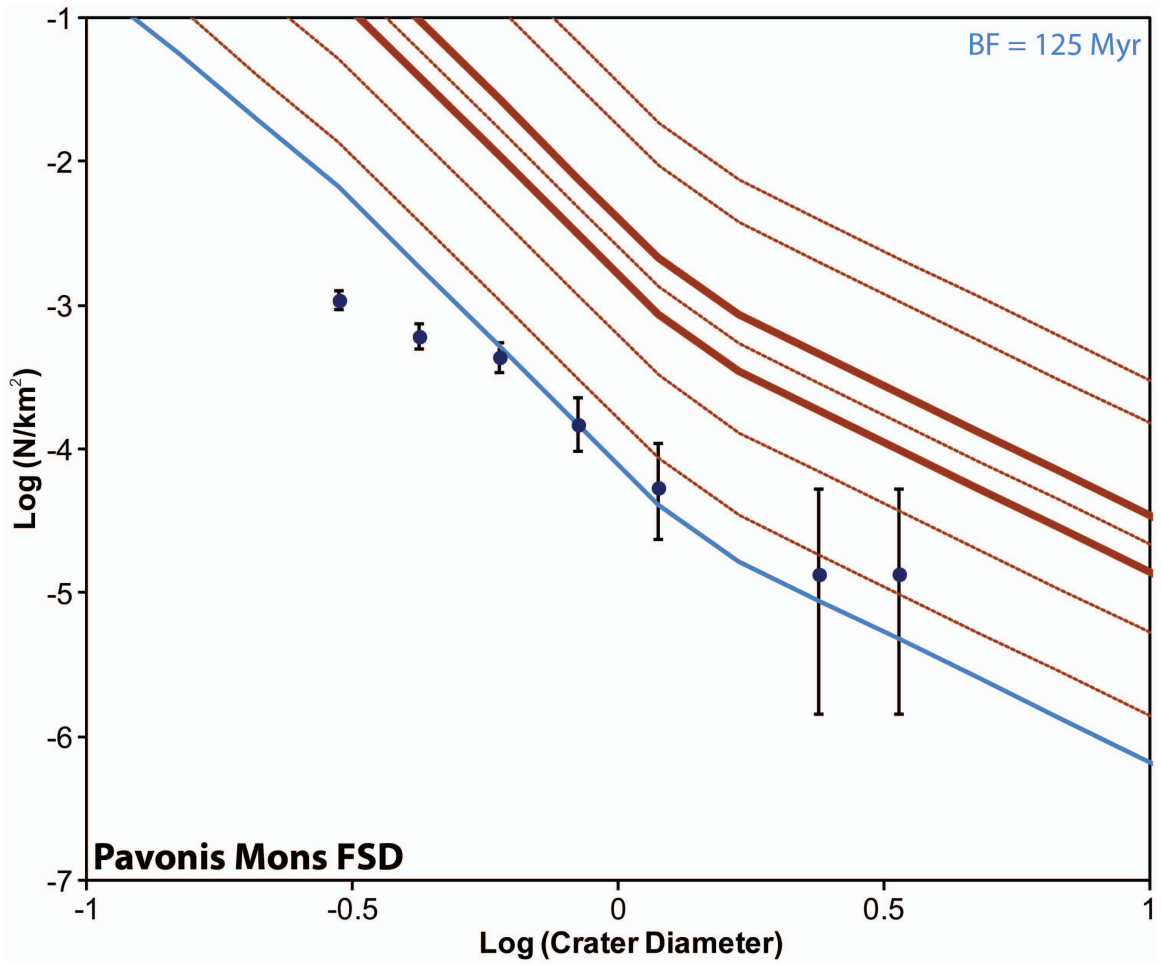


Figure 13

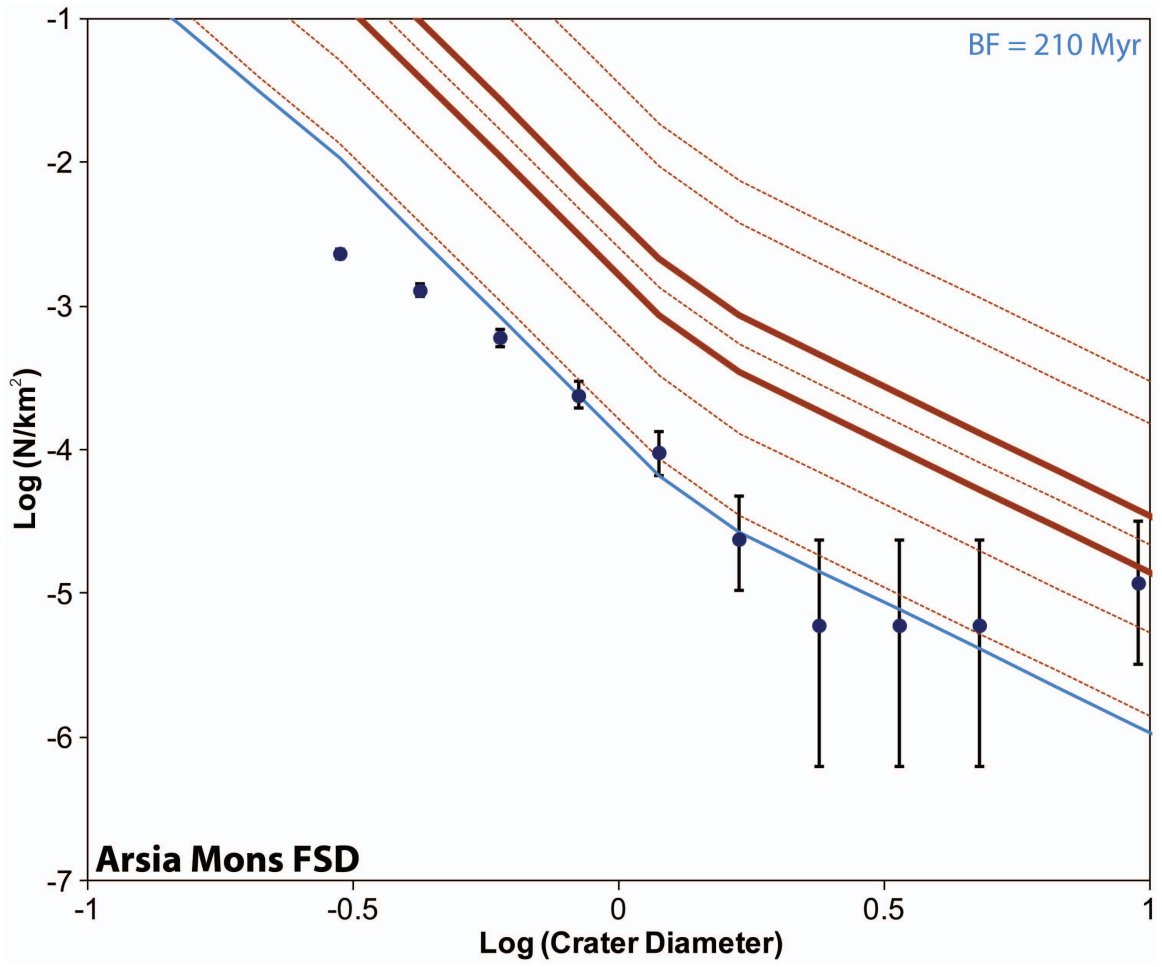


Figure 14

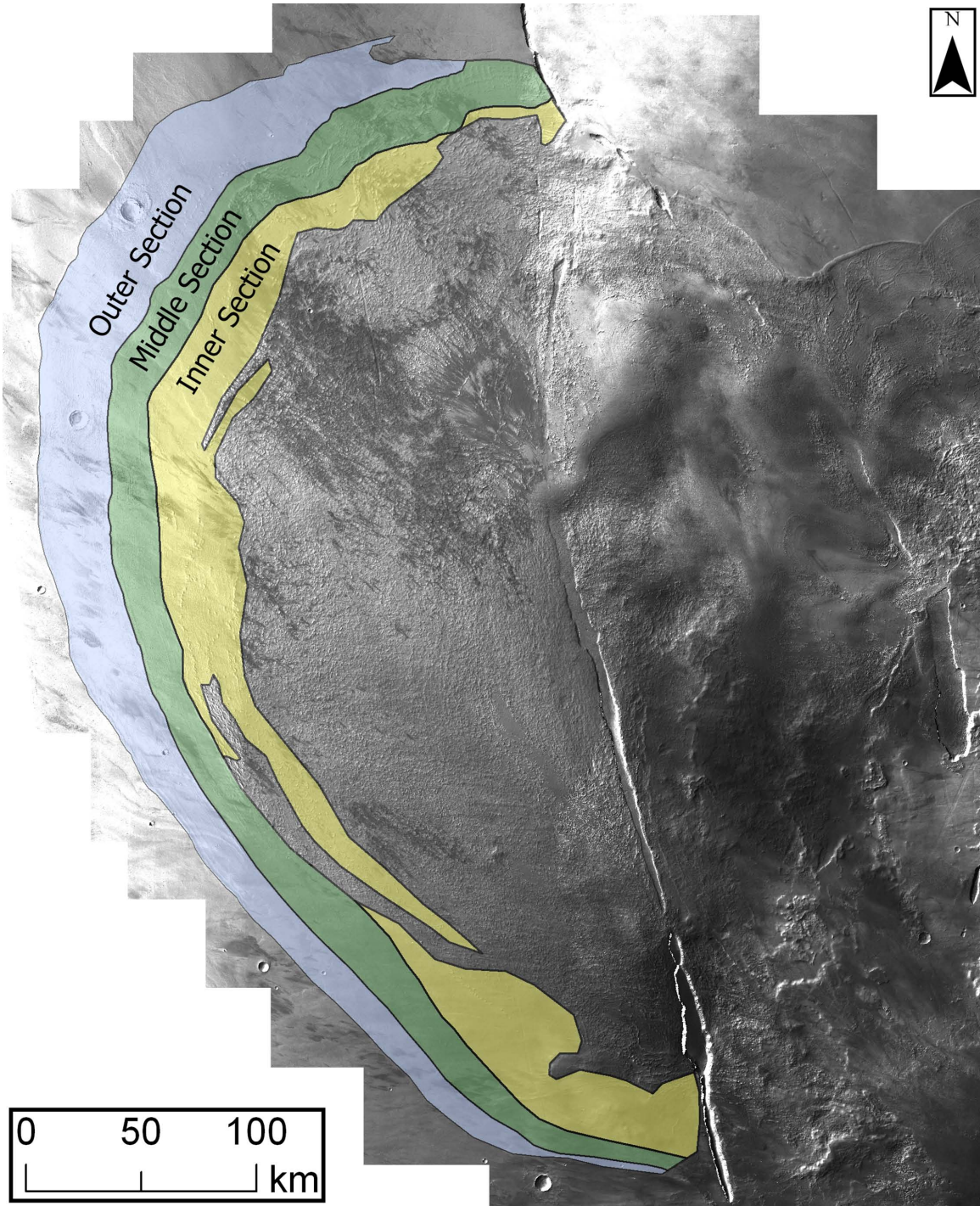


Figure 15

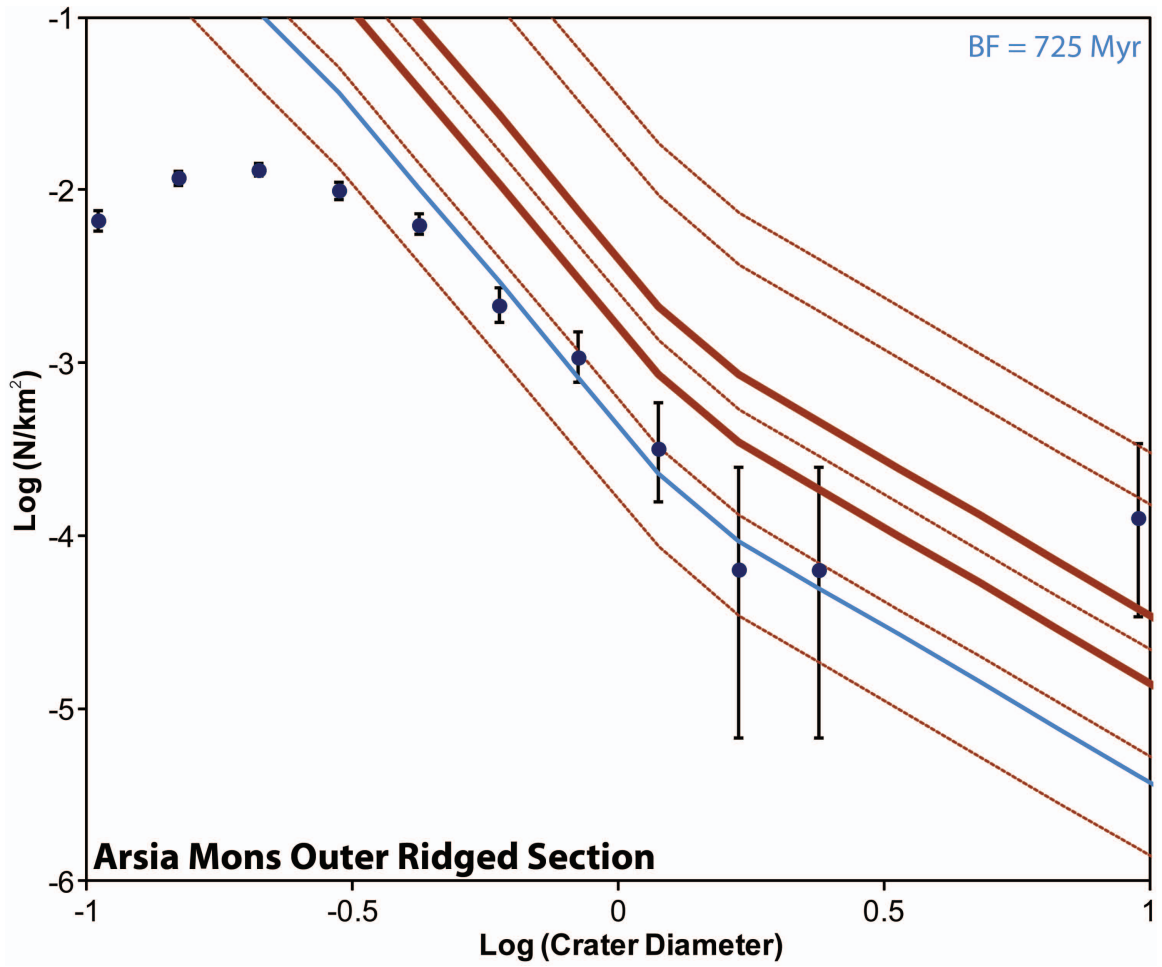


Figure 16

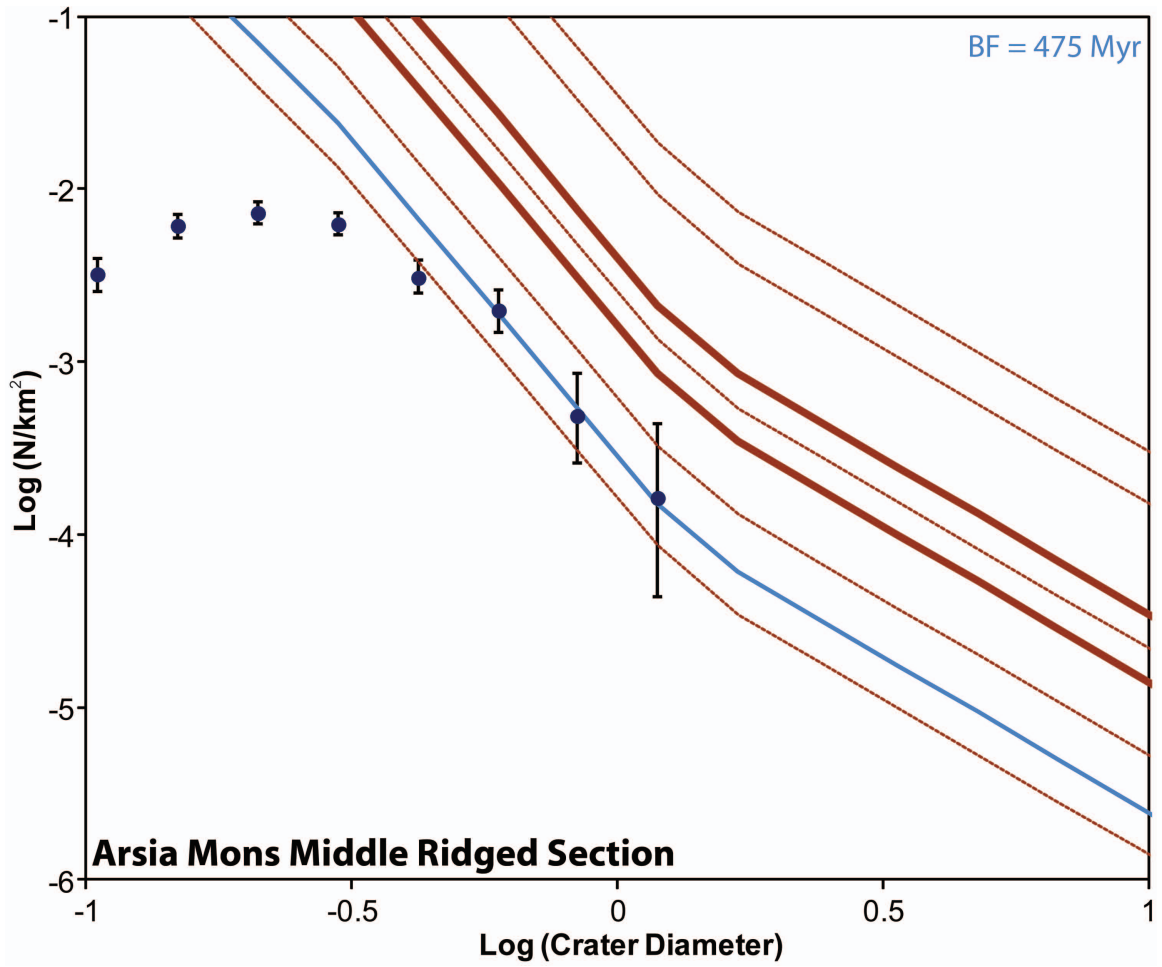


Figure 17

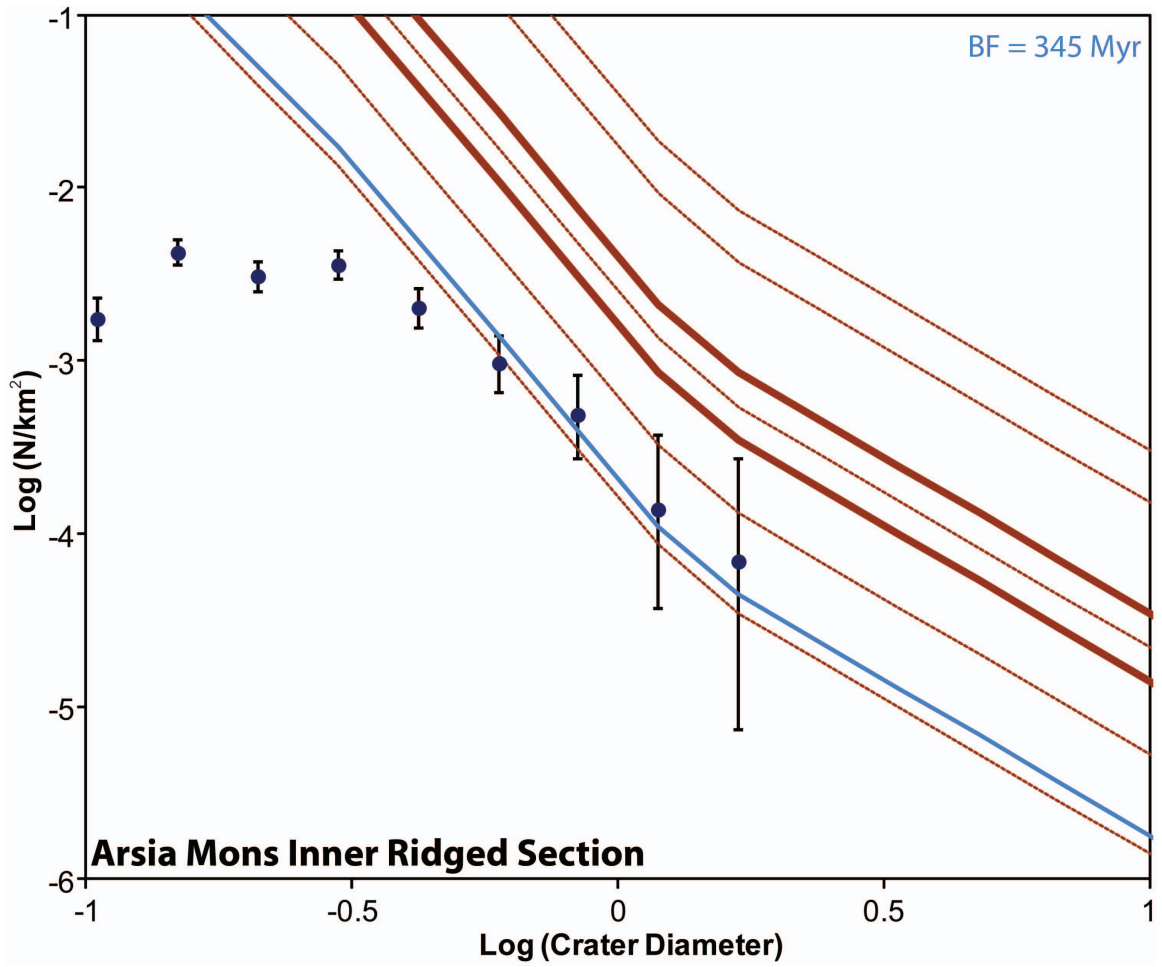
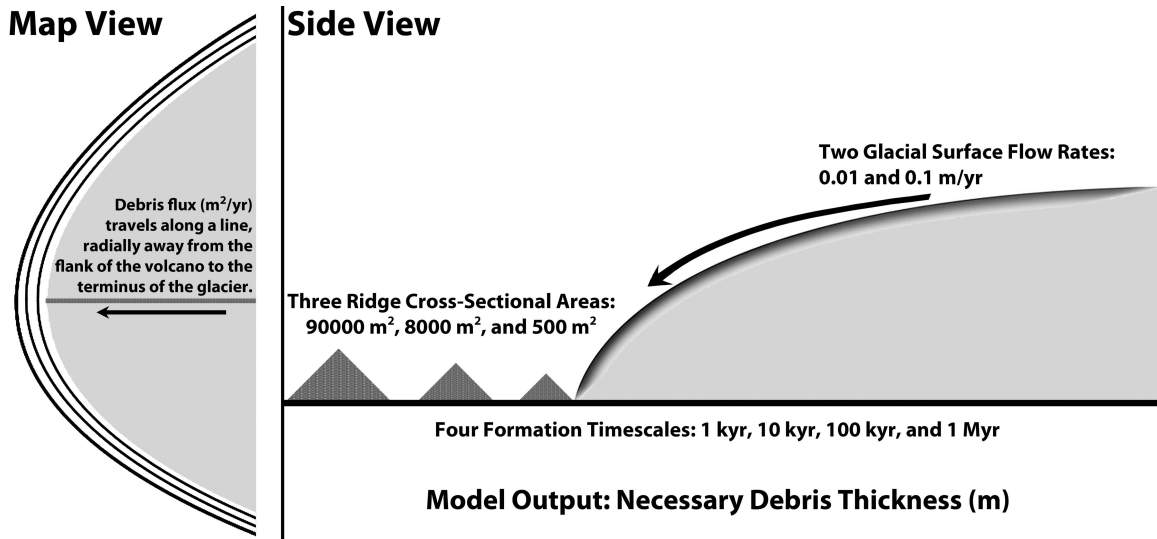


Figure 18



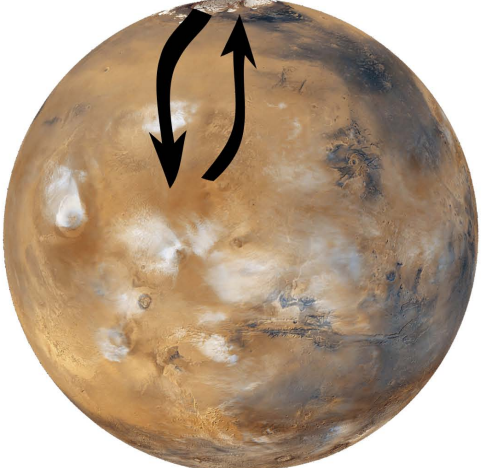
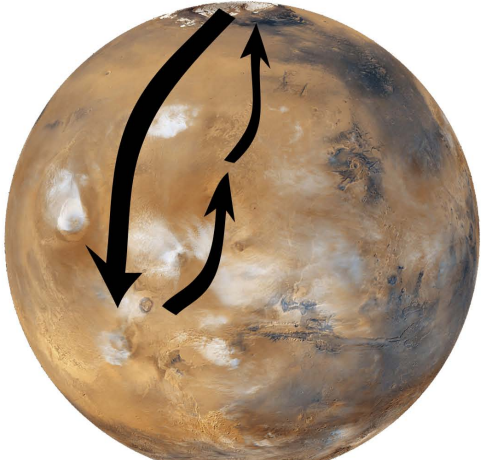
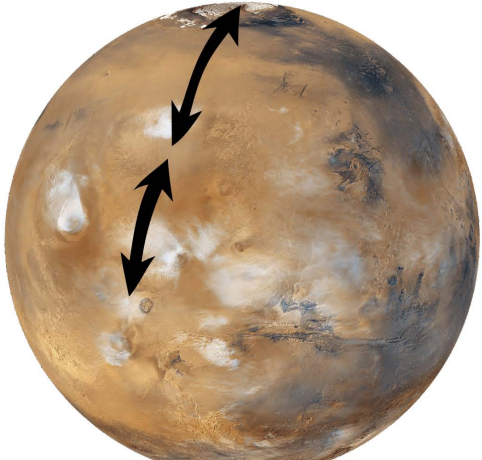
<p>Head et al. 2003</p>	 <p>A diagram of Mars showing ice transport from high latitudes to mid-latitudes. Two curved arrows originate from the polar regions and point towards the mid-latitudes, indicating the direction of ice movement.</p>	<p>Proposed scenario: A shift to $\sim 35^\circ$ obliquity induces a Martian ice age. The increased insolation on the polar caps sublimates ice from the high latitudes. As a result, ice-rich deposits are emplaced symmetrically down to latitudes of $\sim 30^\circ$ in both hemispheres.</p>
<p>Forget et al. 2006 Madeleine et al. 2009</p>	 <p>A diagram of Mars showing ice transport from polar caps to the Tharsis Region. Two curved arrows originate from the polar regions and point towards the Tharsis Region, indicating the direction of ice movement.</p>	<p>Proposed scenario: Using a climate model, Forget et al. (2006) showed that, at an obliquity of $\sim 45^\circ$, ice is transported directly from the polar caps to the Tharsis Region. Madeleine et al. (2009) used the model with an equatorial ice source to produce widespread accumulation of dust-ice-rich deposit across the mid-latitudes.</p>
<p>This Study</p>	 <p>A diagram of Mars showing ice exchange between high, mid, and low latitudes. Two curved arrows originate from the polar regions and point towards the mid-latitudes, indicating the direction of ice movement.</p>	<p>Proposed scenario: Our morphologic observations and crater count ages imply that ice is readily exchanged between the high, mid, and low latitudes. In this scenario, ice has remained at low latitudes for a longer time period than at mid latitudes, but is more frequently deposited at mid latitudes.</p>

Figure 20

